

**Surface-functionalized latex particles as additives
in the mineralization of zinc oxide:
influence on crystal growth and properties**

Dissertation
zur Erlangung des Grades

Doktor der Naturwissenschaften

am Fachbereich Chemie,
Pharmazie und Geowissenschaften
der Johannes Gutenberg-Universität Mainz

vorgelegt von

Rafael Muñoz-Espí
geboren in Ontinyent (València)

Mainz, 2006

Die vorliegende Arbeit wurde in der Zeit von Oktober 2002 bis Dezember 2005 unter der Betreuung von Prof. Dr. G. Wegner am Max-Planck-Institut für Polymerforschung durchgeführt.

Dekan: Prof. Dr. P???? L???????

1. Berichterstatter: Prof. Dr. G?????? W?????

2. Berichterstatter: Dr. habil. F???? R???

Datum der mündlichen Prüfung: 2. 3. 2006

Übersicht

Polystyrolatexteilchen, modifiziert an der Oberfläche mit unterschiedlichen hydrophilen Gruppen, wurden durch Miniemulsionspolymerisation hergestellt und zur Kontrolle der Zinkoxid-Kristallisation in wässrigem Medium verwendet. Effekte der Latexfunktionalisierung und -konzentration auf das Kristallwachstum, die Morphologie, die Struktur und die Eigenschaften des Zinkoxids wurden untersucht. Durch die Benutzung unterschiedlicher Latexadditive gewinnt man Kristalle im Mikron- und Submikron-Bereich mit einer breiten morphologischen Vielfalt. Latexteilchen, deren Oberfläche mit Carboxylgruppen funktionalisiert waren, eignet sich besonders gut für weitere quantitative Untersuchungen. In diesem Fall nimmt mit steigender Additivkonzentration das Aspektverhältnis der Kristallen ab. Es wird angenommen, dass Latexteilchen vorzugsweise an den schnell wachsenden {001}-Flächen des Zinkoxids adsorbieren, wobei sie mit den Wachstumszentren in Wechselwirkung stehen und die Wachstumsrate in [001] reduzieren.

Wenn Zinkoxid in Gegenwart von Latex hergestellt wird, werden die Polymerpartikel in die wachsende Kristalle eingebaut und polymer-anorganische Hybridmaterialien dabei erhalten. Solche Materialien bestehen aus einer weitgehend ungestörten anorganischen Matrix, in der die organischen Latexteilchen eingebettet sind. Steigende Mengen von Latex werden eingebaut, wenn die Gesamtlatekonzentration erhöht wird.

Photolumineszenzspektren wurden gemessen, um Information über Defektzentren zu bekommen. Emissionsspektren aller Proben zeigten einen schmalen UV-Peak und ein breites Band im grün-gelbes Spektralbereich. Die ersterwähnte Emission wird der Exziton-Rekombination zugeschrieben, während die zweite mit tiefen Donatorniveaus zusammenzuhängen scheint. Latex zeigt sich als Löscher der sichtbaren Emission in Zinkoxid. Somit zeigen ZnO-Latex Hybride eine deutlich geringere Photolumineszenzintensität (im Vergleich mit reinem Zinkit) im sichtbaren Bereich des Spektrums. Unter kontinuierlicher Photoanregung wird ein erkennbares dynamisches Verhalten der Photolumineszenz beobachtet, das in Zusammenhang mit einer Photodesorption von adsorbiertem Sauerstoff stehen kann. Solche oberflächenadsorbierten Sauerstoffspezies scheinen eine Rolle in den optischen Eigenschaften der Materialien zu spielen. Sie können das Tunneln der Elektronen vom Leitungsband zu bereits bestehenden tiefen Störstellen vermitteln, die wahrscheinlich mit intrinsischen Defekten (Sauerstoff-Fehlstellen oder Zink in Zwischengitterplätze) in Verbindung stehen.

Polymerteilchen können die Stellen, an denen Sauerstoffadsorption stattfindet, blockieren und damit zu der beobachteten Löschung der sichtbaren Emission beitragen.

Elektronenparamagnetische Resonanz (EPR) ergab weitere Informationen über Kristalldefekte mit ungepaarten Elektronen. Spektren der Proben weisen ein einzelnes Signal bei $g \approx 1.96$ auf, typisch für Donatoren nahe der Bandkante („shallow donors“). Im Gegensatz zu Ergebnissen anderer Autoren, korrelierten die EPR-Signale und die sichtbare Photolumineszenz nicht, was darauf hinweist, dass die verantwortlichen Zentren für die sichtbare Emission und die EPR-Signale unterschiedlichen Ursprungs sein müssen.

Abstract

Polystyrene latex particles modified at the surface with different hydrophilic functional groups were prepared by miniemulsion polymerization and applied to control the crystallization of zinc oxide in aqueous medium. The effects of both latex structure and concentration on the crystal growth, morphology, crystalline structure, and properties of the resulting zinc oxide were analyzed. Depending on the latex additive used, micro- and submicro-sized crystals with a broad variety of morphologies were obtained. Among the studied latexes, the carboxyl-derived particles were shown to be a convenient system for further quantitative investigations. In this case, as the additive concentration increases, the aspect ratio of the crystals decreases systematically. Latex particles are assumed to adsorb preferentially onto the fast growing {001} faces of ZnO, interacting with the growth centers and reducing the growth rate in [001].

When zinc oxide is precipitated in the presence of latex, the polymer particles become incorporated into the growing crystals and polymer-inorganic hybrid materials are obtained. These materials are composed of an inorganic and largely undisturbed crystalline matrix in which organic latex particles are embedded. Increasing amounts of latex become incorporated into the growing crystals at increasing overall concentration in the crystallizing system.

Photoluminescence (PL) spectra were measured to obtain information on defect centers. Emission spectra of all samples showed a narrow UV peak and a broad band in the green-yellow spectral region. The former emission is attributed to exciton recombination, whereas the latter seems to be related with deep-level donors. Latex appears to be a quencher of the visible emission of zinc oxide. Thus, compared to pure zincite, ZnO-latex hybrid materials show a significantly lower PL intensity in the visible range of the spectrum. Under continuous photoexcitation, a noticeable dynamic behavior of the PL is observed, which can be related to a photodesorption of adsorbed oxygen. These surface-adsorbed oxygen species seem to play a crucial role for the optical properties of the materials and may mediate the tunneling of electrons from the conduction band to preexisting deep-level traps, probably related to intrinsic defects (oxygen vacancies or interstitial zinc). The polymer particles can block the sites where oxygen adsorbs, and the disappearance of the "electron-shuttle" species leads to the observed quenching of the visible emission.

Electron paramagnetic resonance (EPR) provided additional information about crystal defects with unpaired electrons. Spectra of all samples exhibit a

single signal at $g \approx 1.96$, typical for shallow donors. Contrary to the results of other authors, no correlation was possible between the EPR signal and the visible range of PL spectra, which suggests that centers responsible for the visible emission and the EPR signal are different.

Acknowledgments

This work would not have been possible without the contributions—in one or other way—of many people, to whom I express my sincere gratitude.

First of all, I thank my advisor and “scientific father”, Professor G. Wegner, for his constant teaching and his confidence during the last three years. I appreciate as well the invaluable support—scientific and nonscientific—of my “Valencian boss”, C. M. Gómez, who has followed the progress of my thesis very closely.

I. Lieberwirth, project leader of the “mineralization team”, is acknowledged for the numerous scientific discussions and for all of the advice since my arrival at the MPIP.

A very special “*merci beaucoup!*” is addressed to L. Herschke, who was a teacher for me. He was always there when I looked for help.

G. Jeschke is thanked for his readiness and involvement in the measurement of EPR spectra and in the investigations on the defect structure of the prepared materials. The discussions with G. Floudas and his remarks were also very useful for the better understanding of the physical properties. I am as well thankful to F. Laquai for the measurement of the time-resolved spectra.

F. Renz is acknowledged not only for accepting to referee the thesis, but also for his useful comments and suggestions, which helped to improve the final version.

Furthermore, I wish to show my appreciation to P. Castignolles, for the hundreds of wise tips during the time sharing laboratory and, especially, for the corrections and comments on Chapter 2.

B. Minch is gratefully acknowledged for the careful reading and correction of the whole manuscript. A. Chandra has to be thanked for the comments on Chapter 4 and for the discussions about X-ray diffraction.

The assistance in the everyday work of the engineers and technical staff of the institute cannot be forgotten. In particular, I would like to thank the following people: H. Menges, for the willingness and continuous assistance in the measurement of optical spectra; G. Jentzsch, for help with some lab issues; and G. Glaßer, for providing the instruction for the scanning electron microscope.

During his stay in Mainz, J. García-Turiel was a good friend and a great scientific colleague, and the interaction with him brought fruitful ideas for the further development of the work.

I also would like to thank O. I. Vinogradova and the people of her group for the willingness to scientific collaboration. Although, finally, they were not included in the thesis, the experiments carried out with D. Golovko helped in the understanding of the interaction between latex particles and ZnO surfaces.

H.-D. Werner is thanked for offering the possibility to conduct the X-ray diffraction measurements with the equipment of the Institute of Geosciences at the University of Mainz, as well as for the scientific advice in the interpretation of some data. The friendly technical assistance of R. Meffert is also acknowledged.

The Deutsche Akademische Austauschdienst (DAAD), the Foundation “la Caixa”, the European Commission (Marie Curie Fellowship Program), and the Max Planck Society are acknowledged for financial support. B. Schiewe, scientific administrator of the International Max Planck Research School for Polymer Materials Science, is also thanked for the tips, the administrative support, and the organization of seminars and summer/winter schools.

Certainly, I am very grateful to all my office and laboratory mates; we shared not only work and scientific problems, but also a part of our life. In addition to those already mentioned and without forgetting the rest, I wish to especially thank J.-Y. Kim, M. Faatz, and M. M. Demir. S. Hinz has also my best thanks for her friendship and for the thousand of stimulating discussions during the breaks. And, of course, I cannot skip the members of the “International Lunch and Cappuccino Community”: thanks to all of you for the nice time we have had together.

Finally, but in the first place of my mind, I thank those who have been emotionally closest to me—including my family—for their love and for being always on my side in the ups and downs that involved this work.

Table of contents

1 GENERAL INTRODUCTION.....	1
1.1 Motivation	1
1.2 Structure and scope of the thesis	2
1.3 Fundamentals of crystallization processes	3
1.3.1 Crystallization from supersaturated solutions	3
1.3.2 The nucleation step	4
1.3.3 Crystal growth	6
1.3.4 Ripening	9
1.3.5 Defects in solids	10
1.3.6 Effect of impurities	11
1.3.7 Processes influencing the crystal morphology.....	14
1.4 Polymer-controlled crystallization	15
2 SYNTHESIS AND CHARACTERIZATION OF SURFACE-FUNCTIONALIZED LATEX PARTICLES.....	17
2.1 Introduction.....	17
2.2 Fundamentals of miniemulsion polymerization	19
2.2.1 Definitions.....	19
2.2.2 Free-radical polymerization in miniemulsion	20
2.2.2.1 Initiation and initiators.....	22
2.2.2.2 Particle nucleation mechanisms	23
2.2.3 Stability of miniemulsions	24
2.3 Theoretical background of techniques for characterization of latex particles.....	26
2.3.1 Dynamic light scattering (DLS)	26
2.3.2 Electrokinetics: surface charge and zeta potential	29
2.3.3 Electrophoresis	30
2.4 Synthesis of surface-functionalized latexes	31
2.4.1 Formulation and choice of the components	32
2.4.2 Polymerization and structure of latex particles	35
2.5 Characterization of latex particles	36
2.5.1 Determination of particle size	37
2.5.2 Determination of surface charge density by polyelectrolyte titration.....	40
2.5.3 Measurement of zeta potential by microelectrophoresis	46

2.6	Conclusions.....	47
2.7	Experimental section	48
3	LATEX-CONTROLLED PRECIPITATION OF ZINC OXIDE	51
3.1	Introduction.....	51
3.2	Fundamentals of the precipitation of zinc oxide.....	53
3.2.1	Solubility and precipitation	53
3.2.2	Thermodynamical aspects.....	55
3.3	Precipitation of ZnO in the absence of additives	57
3.4	Latex particles as morphology controlling agents.....	59
3.4.1	Effect of the chemical nature of the functionalizing groups	59
3.4.2	Effect of the surface charge density.....	62
3.4.3	Effect of the pH.....	64
3.4.4	Effect of the latex ingredients.....	66
3.4.5	Effect of the latex concentration	67
3.5	Poly(styrene–acrylic acid) latex as a model for systematic studies	69
3.6	Conclusions.....	73
3.7	Experimental section	74
4	CRYSTAL CHARACTERIZATION AND GROWTH KINETICS OF ZNO PRECIPITATED IN THE PRESENCE OF LATEXES	77
4.1	Introduction.....	77
4.2	Crystal structure of zinc oxide.....	77
4.2.1	X-ray diffractometry of ZnO	78
4.2.2	Lattice dynamics of ZnO: vibrational spectroscopies.....	80
4.3	Estimation of latex content by thermogravimetric analysis.....	82
4.4	Crystal structure in the absence of additives	83
4.5	Crystal structure versus latex-surface chemistry	85
4.5.1	Effect of the independent monomers	87
4.6	Crystal structure versus latex concentration	89
4.7	Effect of thermal annealing on the crystal structure	92
4.8	Kinetic considerations: morphogenesis of ZnO crystals in the presence of latexes.....	93

4.9	Conclusions.....	96
4.10	Experimental section	97
5	INFLUENCE OF LATEX ON THE PHYSICAL PROPERTIES OF ZINC OXIDE: A SPECTROSCOPIC INVESTIGATION	99
5.1	Introduction.....	99
5.2	Fundamentals of defects in solids	100
5.2.1	Point defects in zinc oxide	100
5.2.1.1	Concentration of point defects.....	101
5.2.1.2	Defect equilibria in ZnO	102
5.2.2	Investigation of defects by photoluminescence spectroscopy.....	104
5.2.2.1	Basics of photoluminescence spectroscopy	104
5.2.2.2	Excitonic transitions and UV emission in ZnO	107
5.2.2.3	Visible emission in ZnO.....	107
5.2.3	Investigation of defects by electron paramagnetic resonance	109
5.3	Optical properties of ZnO–latex hybrid materials.....	110
5.3.1	Room-temperature photoluminescence spectra	110
5.3.2	Dynamic behavior of the photoluminescence	117
5.3.3	Temperature dependence of the photoluminescence	122
5.3.4	Time-resolved spectroscopy.....	126
5.4	EPR investigation of ZnO–latex hybrid materials	129
5.5	Conclusions.....	132
5.6	Experimental section	133
6	GENERAL CONCLUSIONS AND OUTLOOK	137
	References	141
	List of abbreviations and symbols.....	152
	Index.....	156

Chapter 1

General introduction

1.1 Motivation

Commonly in nature, formation of inorganic crystals is controlled by the presence of biogenic macromolecules. Calcium carbonate, present in coral and shells of sea creatures, or calcium phosphates, present in bones or teeth, are typical examples of this phenomenon. Many research groups focus on the investigation of such processes, working in the area of biomineralization.^[1-3] However, the study of mineralization phenomena and the growth mechanisms involved is not only interesting for the life sciences, but it has also industrial importance. The control of crystal growth features of inorganic materials has become an active research field in the last two decades, because of the increasing interest in obtaining materials with homogeneity and specificity of both crystal shape and size distribution, crucial in many applications.^[4-7]

Imitating nature, polymers with different structures have been used as additives in crystallization of inorganic and organometallic (e.g., metal oxalates) compounds. In particular, double-hydrophilic block and graft copolymers have been shown to be very effective in the control of crystal growth of materials obtained in aqueous media. The effects observed with hydrophilic polymers prompt the investigation of a system with functional groups anchored to the surface of spherical latex particles. Such particles, prepared by miniemulsion polymerization, provide an interesting approach to control crystal growth, as indicated by preliminary results^[8] and confirmed by subsequent works.^[9-12]

Miniemulsion latex particles are versatile, as the particle size and the local concentration of functional groups attached to the surface can be controlled. Whereas the synthesis of double-hydrophilic block and graft copolymers may be cumbersome, the synthesis of latex particles is convenient and reproducible, and structures of defined size with surfaces of various chemical compositions can be obtained quickly from simple monomers.

From the mechanistic point of view, zinc oxide is quite an ideal system for studies regarding controlled crystallization. Due to its high insolubility in water, ZnO can be easily precipitated from aqueous solution and only one modification

(zincite) is obtained. In addition, micro- and nanostructures of zinc oxide are interesting for various applications, such as catalysts, cosmetics, pigments, varistors, optoelectronic devices, and gas sensors. Although the properties of ZnO has been known for a long time, the effort devoted to the investigation of this II–VI semiconductor has grown surprisingly in the last years. A wide—and tunable by doping—band gap (~ 3.3 eV at room temperature), a large binding energy of 60 meV, thermal and chemical stability, polarity of the unit cell along the c -axis, non-toxicity, and an inexpensive production are some of the characteristics that explain the research interest for this material. Especially promising is its use as basis material for the fabrication of UV-to-blue and visible light-emitting diodes, room-temperature lasers, solar cells (as an alternative to TiO_2), or transparent conducting films.^[13–15]

In this work, polystyrene latex particles (diameter of 60–100 nm) modified at the surface with different hydrophilic functional groups are prepared by miniemulsion polymerization and used as controlling agents in the crystallization of zinc oxide from aqueous medium. The aim is to analyze the effect of both chemical nature of the latex surface and latex concentration on the growth, morphology, crystalline structure, and physical properties of the prepared zinc oxide.

1.2 Structure and scope of the thesis

Each chapter of this thesis, with the logical exception of the general introduction (*Chapter 1*) and the conclusive chapter (*Chapter 6*), is organized in the same way: a theoretical part, which reviews important theoretical concepts and the fundamentals of the experimental methods, is followed by the discussion of the results and the main conclusions; the experimental details are given at the end of the chapter.

The first part of the work (*Chapter 2*) focuses on the preparation and characterization of the surface-functionalized latex particles used in the following chapters as controlling agents for the crystallization of ZnO. After reviewing the fundamentals of miniemulsion polymerization, the synthetic pathway and formulation used are described. Next, the determination of the particle size (by electron microscopy and dynamic light scattering) and the estimation of the surface charge density (by polyelectrolyte titration and microelectrophoresis) are discussed.

Previous work^[9,10] had shown that the crystallization of ZnO in the presence of poly(styrene–acrylic acid) latex particles results in organic–inorganic hybrid

materials incorporating the latex particles in the zincite crystals. An aim of this work was to extend the studies to latex particles with different chemical nature and investigate the influence of their structure on the morphology of the resulting crystals. This is central to the discussions of *Chapter 3*, where it is shown how the morphology depends on both the surface chemistry and the latex concentration. Whether or not the observed morphological differences have a correspondence in the long-range crystal perfection is treated in *Chapter 4*, in which the characterization of the prepared crystals by X-ray diffractometry and vibrational spectroscopies (FTIR and Raman) is analyzed.

The morphology, the crystal quality, and the defects of crystalline materials determine many of their physical properties, such as optical, electric, and magnetic properties. Our ZnO–latex hybrid materials were studied by photoluminescence spectroscopy and electron paramagnetic resonance (EPR) to obtain information on defect centers. In *Chapter 5*, the results of these investigations are correlated with the defect structure of the obtained zincite.

1.3 Fundamentals of crystallization processes

This section provides the general theoretical background of the thesis and reviews the most important concepts of crystallization processes from a supersaturated solution. The steps of the crystal formation are considered, making special emphasis on crystal defects and on the effect of impurities, which is crucial in this work, as zinc oxide is synthesized in the presence of additives.

1.3.1 Crystallization from supersaturated solutions

The crystallization of a substance from an aqueous solution implies a precipitation reaction governed by a solubility equilibrium. For a general solubility equilibrium of a compound $A_{\nu_A} B_{\nu_B}$,



the Gibbs free energy of dissolution is given by

$$\Delta G = RT \ln \frac{Q}{K_{\text{eq}}} = RT \ln \frac{\{A^{\nu_B+}\}^{\nu_A} \{B^{\nu_A-}\}^{\nu_B}}{\{A^{\nu_B+}\}_{\text{eq}}^{\nu_A} \{B^{\nu_A-}\}_{\text{eq}}^{\nu_B}} \quad (1.2)$$

where R is the gas constant, T is the absolute temperature, Q is the reaction quotient, K_{eq} is the equilibrium constant, $\{i\}$ is the actual activity of the species i , and $\{i\}_{\text{eq}}$ is the activity of i in equilibrium. If the *ion activity product* (IAP) is

defined as

$$\text{IAP} = \{A^{v_B^+}\}^{v_A} \{B^{v_A^-}\}^{v_B} \quad (1.3)$$

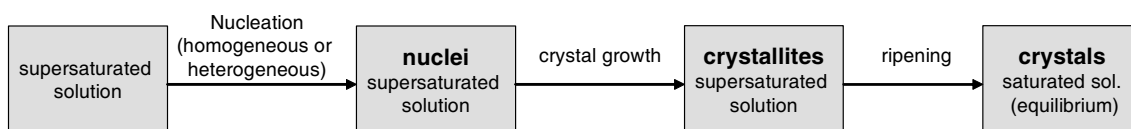
then eq. (1.2) can be written as

$$\Delta G = RT \ln \frac{\text{IAP}}{K_{s0}} = RT \ln S \quad (1.4)$$

where K_{s0} is the solubility product and the quotient $S = \text{IAP}/K_{s0}$ is the *saturation level* (or *saturation ratio*). If $\text{IAP} > K_{s0}$, the free energy of dissolution, ΔG , is positive and the solution is *supersaturated* (or *oversaturated*); if $\text{IAP} = K_{s0}$, $\Delta G = 0$, and the solution is *saturated*, that is, in equilibrium; if $\text{IAP} < K_{s0}$, then $\Delta G < 0$ and the solution is *undersaturated*.

In general, the formation of crystals from a supersaturated solution includes three steps, as represented in Scheme 1.1: nucleation, crystal growth, and ripening.

- *Nucleation* is the formation of centers (*nuclei*) from which spontaneous growth can occur. Metastable phases (such as amorphous hydrous phases) are frequently invoked as the initial nucleation products of crystalline compounds.^[16] The nucleation can be *primary*, if occurring in systems that do not contain crystalline matter, or *secondary*, if the nuclei are generated in the vicinity of crystals present in a supersaturated system. The primary nucleation can occur *homogeneously* (spontaneously) or *heterogeneously* (induced by foreign particles).^[17] Actually, the nucleation leading to crystal formation is frequently heterogeneous.
- The *crystal growth* is constituted by the processes of deposition of material on the formed nuclei.
- *Ripening* is the process through which larger crystals (less soluble) are formed at the expense of smaller ones (more soluble).

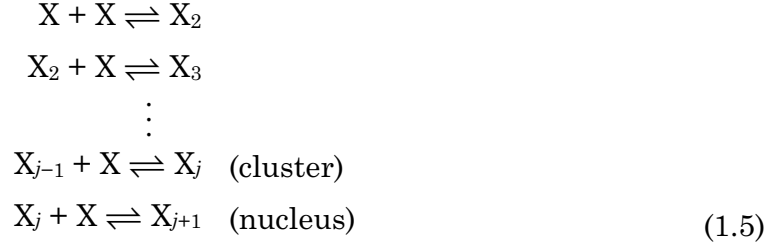


Scheme 1.1. Steps of the crystal formation.

1.3.2 The nucleation step

A *nucleus* is the result of the interaction of species (ions or molecules) to form a *cluster* of critical size. The number of molecules required for a stable nucleus can

vary from about ten to several thousands. The formation of a nucleus could be considered as a sequence of bimolecular additions:^[17]



The formation of stable nuclei requires overcoming an energy barrier that can be calculated as follows. The free energy change associated with the formation of a nucleus, ΔG_j , is the sum of two contributions: (i) the free energy of the bulk material (sometimes referred as volume excess free energy), that is, the energy to form a solid or, more correctly, the energy difference between the bulk material (a very large particle with $r = \infty$) and the solute in solution; and (ii) the surface excess free energy, that is, the work required to create a surface. For spherical nuclei of radius r , this can be expressed as^[18]

$$\Delta G_j = \Delta G_{\text{bulk}} + \Delta G_{\text{surf}} = \frac{4}{3}\pi r^3 \Delta G_v + 4\pi r^2 \gamma \tag{1.6}$$

where ΔG_v is the difference of the free energy between both phases (solution/melt and solid phase) per unit volume and γ is the interfacial tension. ΔG_v , negative for a supersaturated solution, can be written as

$$|\Delta G_v| = \frac{k_B T \ln S}{v} \tag{1.7}$$

where k_B is the Boltzmann constant, S is the saturation ratio [as defined in eq. (1.4)], and v is the volume of a nucleus.[†]

The representation of ΔG_j as a function of the nucleus radius, r , goes through a maximum with coordinates $(r^*, \Delta G_j^*)$. When the nucleus achieves the critical nucleation radius (r^*), with the critical nucleation energy (ΔG_j^*), the growth of the crystal occurs, and the free energy of the system decreases, as it is shown in Figure 1.1. The maximum of this function can be calculated differentiating eq. (1.6) and equating to zero:

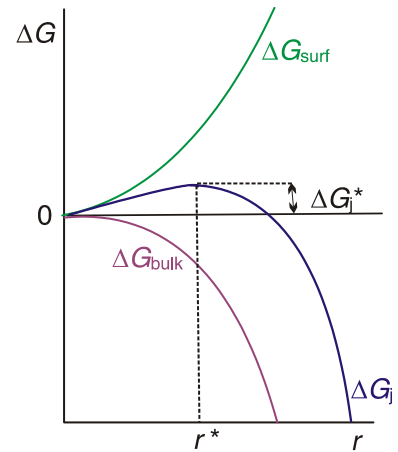


Figure 1.1. Variation of the free energy in the formation of a nucleus of radius r .

[†] Note that ΔG_v could be also written as a function of the *molar* volume V ($V = v \cdot N_A$, where N_A is Avogadro's number): $\Delta G_v = RT \ln S / V$.

$$r^* = -\frac{2\gamma}{\Delta G_v} \quad (1.8)$$

The value of ΔG_j^* is obtained from eqs. (1.6) and (1.8):

$$\Delta G_j^* = \frac{16\pi\gamma^3}{3(\Delta G_v)^2} = \frac{4\pi\gamma}{3}(r^*)^2 \quad (1.9)$$

Substituting eq. (1.7) in eq. (1.9), it can also be written

$$\Delta G_j^* = \frac{16\pi\gamma^3 v^2}{3(k_B T \ln S)^2} \quad (1.10)$$

The rate of nucleation (number of nuclei formed per unit time per unit volume), J , can be expressed by the Arrhenius equation:

$$J = A \exp\left(-\frac{\Delta G_j^*}{k_B T}\right) \quad (1.11)$$

where A is a factor related to the efficiency of collisions of ions/molecules. Applying eqs. (1.7) and (1.9), eq. (1.11) can be rewritten as

$$J = A \exp\left[-\frac{16\pi\gamma^3 v^2}{3k_B T^3 (\ln S)^2}\right] \quad (1.12)$$

A final consideration regarding the nucleation should be made. It has been known since early experimental work that, when rapidly cooling some aqueous solutions of inorganic salts, crystals of a form less stable than that which normally crystallizes can deposit first.^[17] The so-called *Ostwald's rule of stages* (named in honor of Ostwald, who tried to generalize this behavior), postulates that the precipitate with the highest solubility (i.e., the least stable solid phase) will form first in a consecutive precipitation reaction. This can be explained because the nucleation of a more soluble phase is kinetically favored with respect to a less soluble. However, many exceptions have been found to Ostwald's rule.^[19]

1.3.3 Crystal growth

The growth of crystals is a very complex matter and many different theories have been developed to explain how crystals are formed. Roughly speaking, these theories can be classified in two groups: surface energy theories and diffusion theories.

The *surface energy theories* are essentially based on the principle that the final shape of a crystal is determined by the minimization of the surface energy; in

other words, the crystal adopts the shape with minimum surface energy. This is a quite naive approach to the problem, and nowadays such theories are in disuse.

The basis of the *diffusion theories* is that the matter is deposited continuously on a crystal face at a rate proportional to the difference in concentration between the point of deposition and the bulk of the solution.^[17] One of the initial diffusion theories was postulated by Volmer,^[20] who using a thermodynamic reasoning proposed that the crystal growth occurs discontinuously by a layer-by-layer deposition. Building units (atoms, ions, or molecules) arriving to the crystal lattice can migrate on the growing crystal face (*surface diffusion*) and there is an equilibrium between the species forming the layer and in the bulk of the solution. The building units become fixed in positions where the attractive forces are maximal, the so-called *active sites*. In this theory it is assumed that a *surface nucleus* should form before the crystal can continue growing (*surface or two-dimensional nucleation*). A thermodynamic treatment analogous to that presented for the three-dimensional nucleation in the previous section can be considered. A critical size and a free-energy barrier should be achieved before the surface nucleation takes place. The free energy of formation of a surface nucleus, assumed to be a disc of radius r and height h , can be written as^[17]

$$\Delta G_j = v\Delta G_v + a\gamma = \pi r^2 h \Delta G_v + 2\pi r h \gamma \quad (1.13)$$

where a and v are the area and the volume of a nucleus and ΔG_v can be expressed in the same way as in eq. (1.7). With considerations analogous to §1.3.2, the critical size r^* is given by

$$r^* = -\frac{\gamma}{\Delta G_v} \quad (1.14)$$

and the barrier free energy by

$$\Delta G_j^* = -\frac{\pi h \gamma^2}{\Delta G_v} \quad (1.15)$$

Substituting eq. (1.7) in eq. (1.15), we obtain

$$\Delta G_j^* = \frac{\pi h \gamma^2 v}{k_B T \ln S} \quad (1.16)$$

A relatively high local supersaturation is necessary for two-dimensional nucleation, but comparing eqs. (1.10) and (1.15), it can be said that this supersaturation is lower than that required for three-dimensional nucleation under the same conditions.

A typical picture of the growing layers is given by the model proposed by Kossel^[21,22] and Stranski,^[23] according to which a flat crystal surface is composed of monoatomic layers containing one or more *kink* sites (see Figure 1.2). The building units are incorporated to the crystal at a kink and the kink moves along a *step*. A new step should begin by surface nucleation, frequently at the corners, but the steps required for growth can only be produced, on a perfect crystal surface, under a highly supersaturated environment. However, in reality growth takes place also under much lower supersaturation than predicted theoretically. Burton, Cabrera, and Frank^[24] pointed

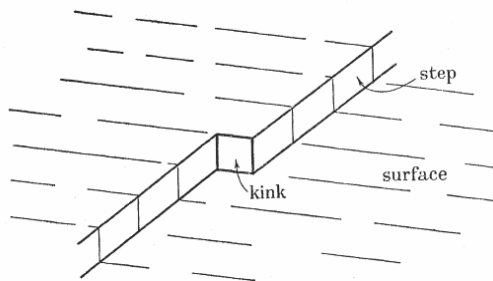


Figure 1.2. Schematic representation of a kink in a step on a crystal surface (Reprinted from Ref. [25], Copyright 1951, with permission from the Royal Society.)

out: “No one seems to have noticed that the assumption that the growth of crystals from the vapor takes place in this way (by two-dimensional nucleation in the crystal surface) implies a rate of growth which is negligible at small supersaturations.” Therefore, they concluded that “the growth of crystals can only be explained by recognizing that the crystals which grow are not perfect, and their imperfections (in particular, dislocations terminating in the surface with a screw component) will provide the steps required for growth, making two-dimensional nucleation unnecessary.”^[25] A *screw dislocation* (see definition in the next section) originates a *growth spiral*, as illustrated by Figure 1.3, the curvature of which cannot exceed a maximum value, determined by the critical radius for two-dimensional nucleation under the supersaturation conditions of the growing medium. Growth may continue in spiral shape indefinitely. The three mentioned authors developed a kinetic theory of growth,^[25] nowadays known as *Burton–Cabrera–Frank theory* (BCF theory), which correlates the curvature of the growing spiral and, thereby, the width of consecutive ledges with the level of supersaturation.

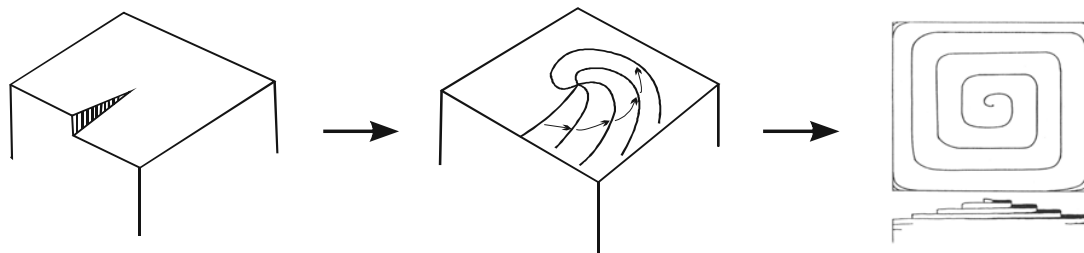


Figure 1.3. Development of a growth spiral starting from a single screw dislocation. (Left and central figures drawn after Ref. [17], Copyright 2001, with permission from Elsevier. Right figure reprinted from Ref. [25], Copyright 1951, with permission from the Royal Society.)

1.3.4 Ripening

Small particles have the tendency to dissolve and “transfer” the solute to larger particles; thus, small particles disappear and large particles grow. This phenomenon, typically referred as *Ostwald ripening* (following the name given by Liesegang^[26]) or simply *ripening*, is explained by the higher solubility of smaller particles with respect to larger ones, as given by the Gibbs–Thomson equation,^[17]

$$\ln \left[\frac{c(r)}{c^*} \right] = \frac{2\gamma V}{\nu R T r} \quad (1.17)$$

where D is the diffusion coefficient of the solute, $c(r)$ is the concentration of solute in the supernatant above particles with small particles of radius r , c^* is the equilibrium saturation concentration in contact with large particles ($r \rightarrow \infty$), γ is the interfacial tension, V is the molar volume of the solute, ν is the number of ions in a formula unit, and R is the gas constant. Applying the Taylor series[†] for $c(r)/c^* \approx 1$ (ripening occurs at very low supersaturation), eq. (1.17) can be written as

$$c(r) - c^* \approx \frac{2\gamma V c^*}{\nu R T r} \quad (1.18)$$

If the growth kinetics of the large particles at the expense of the small follows a diffusion-controlled, first-order kinetics, the radius-change rate is given by^[17]

$$\frac{dr}{dt} = \frac{DV[\bar{c} - c(r)]}{r} \quad (1.19)$$

where \bar{c} is the average bulk solution concentration. Substituting $c(r)$ from eq. (1.18) in eq. (1.19), it yields

$$\frac{dr}{dt} = \frac{DV}{r} \left[(\bar{c} - c^*) - \frac{2\gamma V c^*}{\nu R T r} \right] \quad (1.20)$$

being $c - c^*$ always positive during precipitation. Equating the previous two equations, we obtain the critical size

$$r^* = \frac{2\gamma V c^*}{\nu R T (c - c^*)} \quad (1.21)$$

Particles with size under this critical value will dissolve, and larger particles will grow.

[†] The Taylor expansion of the natural logarithm of x about a point $x = \alpha$ is given by:

$$\ln x = \ln \alpha + \frac{x - \alpha}{\alpha} - \frac{(x - \alpha)^2}{2\alpha^2} + \frac{(x - \alpha)^3}{3\alpha^3} - \dots$$

1.3.5 Defects in solids

It has been discussed that crystal imperfections, especially dislocations, are decisive for the growth. In the following, the different types of defects in solids are briefly described. After their dimensionality, the defects can be classified in point, linear, and planar defects.

Point defects: *Point defects* are atomic defects in the crystal lattice that can occur thermally (*intrinsic defects*, related with entropy-dictated disorder) or arise from external agents (e.g., radiation), but can also be created by the presence of impurities (*extrinsic defects*, see the last paragraph of the next section). Point defects include lattice vacancies, interstitial atoms, substitutional impurity atoms, and interstitial impurity atoms. A detailed study of the point defects, including thermodynamic considerations of their formation and the specific case of zinc oxide, will be found in Chapter 5.

Linear defects (dislocations): *Linear defects* or *dislocations* are faults in the arrangement of the atoms in a line through the crystal lattice. Dislocations are defects present in large numbers (typically in the order of $\sim 10^7 \text{ cm}^{-2}$), even in well annealed metals.^[27]

Dislocations play an important role in crystal growth, but also affect some physical properties, especially the mechanical properties. In semiconductors, they can also influence electrical properties. Dislocations can also play a role in formation or annihilation of native point defects.^[28]

A dislocation is characterized by the so-called *Burgers vector*. This vector is obtained by going to the vicinity of a dislocation, and then traversing a counterclockwise path around it, as represented in Figure 1.4. In a perfect crystal, this path is closed, whereas in the presence of a dislocation it is not. The Burgers vector is the vector required to close the path.^[29]

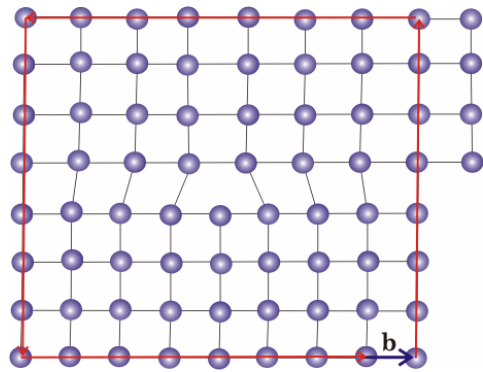


Figure 1.4. Representation of the Burgers vector, \mathbf{b} , for an edge dislocation. A counterclockwise path is constructed by counting the same number of atoms (7 atoms up, 7 to the left, 7 down, and 7 to the right) in the vicinity of the dislocation; the Burgers vector is the vector necessary to close the path.

The two main types of dislocation are *edge* and *screw dislocations*. In an edge dislocation, schematically represented in Figure 1.5a, the crystal is partially displaced in the slip plane ABCD perpendicular to the line FE, called *dislocation line*. The dislocation line is defined as the line at which the disregister between

the atoms in the planes immediately above and below the slip plane is $a/2$, being a the lattice spacing.^[27] In the case of a screw dislocation, illustrated in Figure 1.5b, the displacement occurs parallel to the dislocation line (GH), as indicated by the arrow. In an edge dislocation, the Burgers vector is perpendicular to the dislocation line, while for a screw dislocation it is parallel.

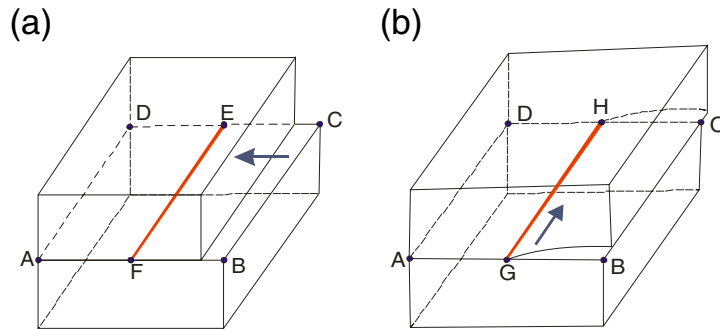


Figure 1.5. Representations of (a) an edge and (b) a screw dislocation. (Drawn after Ref. [27].)

Planar defects: A *planar defect* is a discontinuity in the perfection of the crystal across a plane and is the result of mechanic or thermal stresses or irregular growth. There are many different types of planar defects, among which the most important are crystallographic shear planes, grain boundaries, stacking faults, tilt boundaries, and twin boundaries.

- *Crystallographic shear planes* are planar faults in a crystal that separate two parts of the crystal which are displaced with respects to each other. A shear plane causes a slight change in the composition of the crystal and can cause the elimination of point defects. Some metal oxides such as TiO_{2-x} , VO_{2-x} , and WO_{3-x} can be stabilized in this way by elimination of oxygen vacancies.^[27]
- *Grain boundaries* occur between the crystallites (or “grains”) comprising a polycrystal and separate regions with different orientation (domains).
- A *stacking fault* is a one- or two-layer interruption in the regular stacking sequence of the atom layers.
- A *tilt boundary* is an array of edge dislocation separating two slightly misaligned grains.
- A *twin boundary* is a plane separating two grains that are mirror images of each other. There is no region of disorder and the atoms in the twin boundary can be considered as belonging simultaneously to the both twins.

1.3.6 Effect of impurities

Impurities can affect the crystal formation in different ways. They can influence solubility–precipitation equilibria, nucleation, growth, and Ostwald ripening, or

can also be responsible for the stabilization of certain crystal phases. These features can be intentionally used to control crystal-growth processes and the polymer-controlled crystallization (discussed in §1.4) is placed in this context.

Elemental impurities (foreign ions/atoms incorporated into a crystal lattice) can also influence enormously the physical properties of crystals. In this sense, doping of crystals represents a common issue in solid-state physics and materials engineering.

Effect on the solubility: If a solute A is solved in a solvent B , the addition of a foreign substance C (soluble in B) may cause that the solution becomes supersaturated (decrease of solubility, “salting-out” effect) or unsaturated (increase of solubility, “salting-in” effect) with respect to A . Additionally, C can also react or form a complex with A , diminishing the concentration of A and changing the whole nature of the system.

Effect on the nucleation: Foreign substances may catalyze the nucleation step by reducing the energy barrier ΔG_j^* [eq. (1.9)]. In nature, for instance, inorganic crystals, skeletal particles, sand, or biocolloids can serve as heteronuclei. Surfactants and other materials may adsorb to the active site and inhibit or prevent the nucleation.

In *heterogeneous nucleation* (in the presence of foreign bodies), the term ΔG_{surf} of eq. (1.6) has to be redefined, because the nucleus is formed partially in contact with the solution and partially in contact with the surface of the solid substrate. Now, ΔG_{surf} can be written as^[19]

$$\Delta G_{\text{surf}} = \gamma_{\text{CW}} A_{\text{CW}} + (\gamma_{\text{CS}} - \gamma_{\text{SW}}) A_{\text{CS}} \quad (1.22)$$

where A represents the area; γ is the interfacial energy; and the suffixes CW, CS, and SW refer to cluster–water, cluster–substrate, and substrate–water, respectively. If the interfacial energy between the foreign particle and the particle of interest (γ_{CS}) is smaller than the interfacial energy between the crystal and the solution (γ_{CW}), the nucleation may take place at lower concentration. In an ideal case, $\gamma_{\text{CS}} \rightarrow 0$ and $\gamma_{\text{SW}} = \gamma_{\text{CW}}$; thus eq. (1.22) can be simplified as

$$\Delta G_{\text{surf}} = \gamma_{\text{CW}} (A_{\text{CW}} - A_{\text{CS}}) \quad (1.23)$$

If $\gamma_{\text{SW}} \gg \gamma_{\text{CW}}$, then ΔG_{surf} may even become negative and the activation barrier vanishes (cf. Figure 1.1).

The presence of impurities can also affect the *induction period*, defined as the time elapsing between the achievement of supersaturation and the appearance of crystals.^[17]

Effect on the crystal growth: Since the rate of the growth is frequently controlled at the interface, the adsorption of some foreign substances at the growing sites can affect significantly the crystal growth. Impurities may affect the growth kinetics and enhance or “poison” the growth (they can absorb selectively on different crystal faces and retard their growth rates), determining the final morphology of the crystals. The suppression of growth by an impurity is expected to depend on the size, shape, or orientation (stereochemistry) of impurity molecules.^[30]

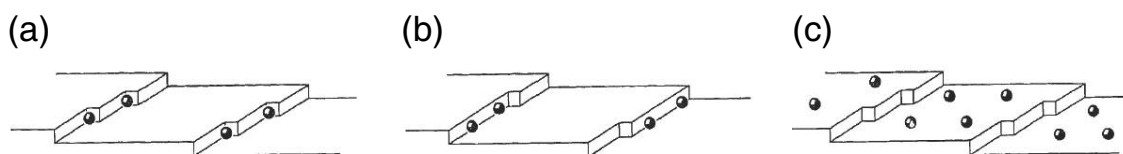


Figure 1.6. Adsorption of impurities on a crystal surface: **(a)** at a kink site, **(b)** at a step, and **(c)** on a ledge. (Reprinted from Ref. [31], Copyright 1976, with permission from Elsevier.)

Following Davey and Mullin,^[17,32] the absorption of the foreign substance can take place at different sites: (i) at a *kink*, (ii) at a *step*, or (iii) at a *ledge* (face) between steps. This is illustrated by Figure 1.6. If the adsorption at kinks is possible, very low concentration of the impurity can have a great effect. Higher concentrations are required, if the impurity adsorb preferentially at step sites, and large amounts can be necessary if the adsorption at ledges is the most important mechanism. Thus, the blockage of active growing sites by the impurity should be related with the impurity concentration. Approaches based on a Langmuir adsorption isotherm has been proposed to model this relationship.^[17,30–33]

Effect on the Ostwald ripening: Considering that the ripening implies the growth of the larger crystals at the expenses of the smaller ones, any additive that affects the crystal growth will also influence the ripening. Adsorption of foreign substances may slow down or suppress growth processes at the surface and, consequently, retard the ripening. Colloidal suspensions are stabilized by addition of substances (e.g., gelatin or carboxymethyl cellulose) that suppress the Ostwald ripening.^[17]

Effect on physical properties: The presence of foreign atoms (ions) in a crystal lattice may alter the original physical properties of the material, especially optical, electric, and magnetic properties. In this context, the impurities can be classified in *compensated* and *noncompensated*.^[29]

- When the foreign element comes from the same column of the periodic table as the host crystal, the impurity is *compensated* or *isoelectronic* (e.g., germanium in a silicon crystal). In this case, the difference in the electron

number is confined to core states and these electrons are bound to the nucleus and inert.

- If the impurity comes from a different column of the periodic table, it is called *noncompensated*, because there is a difference in the electronic structure of valence shell with respect to the host. The impurity acts as a *donor* or *acceptor* of electrons. This is of especial importance in semiconductor physics. For instance, boron has one valence electron less than silicon, and if silicon is doped with boron, an electron is missing in the valence band (i.e., a positive hole is formed); silicon is in this case a *p-type semiconductor* (*p* for positive). If silicon is doped with an element with more valence electrons (e.g., phosphorous), electrons are present close to the conduction band and can be easily promoted; silicon is then an *n-type semiconductor* (*n* for negative).

1.3.7 Processes influencing the crystal morphology

According to the symmetry of their lattice, crystals can be classified in only seven general groups: cubic, tetragonal, orthorhombic, monoclinic, triclinic, rhomboidal, and hexagonal. The shape of a crystal should, in principle, externalize the unit-cell symmetry. However, differences in the growth velocity of crystal faces and aggregation-mediated crystallization justify why a large variety of external shapes is found in both natural and synthetic crystals.

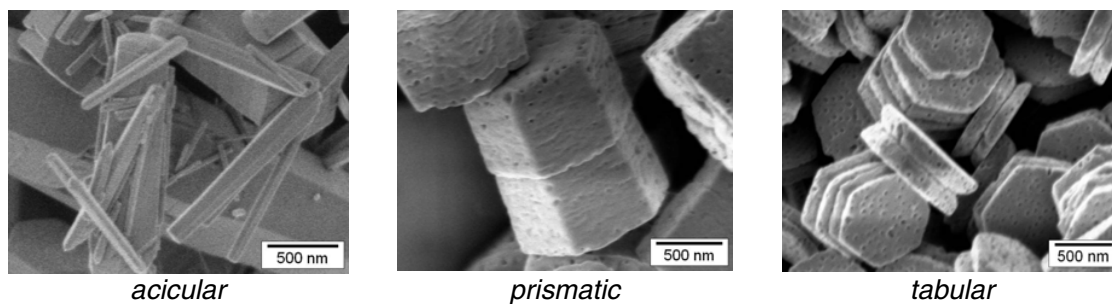


Figure 1.7. Different habits of hexagonal ZnO crystals precipitated from aqueous media in the presence of latex nanoparticles.

Changes in crystal habit: The growth velocity of the different crystal faces can be affected by many parameters, determining the relative sizes of the faces in the resulting crystals and their external appearance or *habit*. The time of crystallization, temperature, degree of supersaturation, solvent, and presence of impurities are some of the parameters that can involve a change in the crystal habit. For example, the presence of impurities can accelerate or poison the growth in certain directions and change the final shape. Considering the case of the hexagonal system, a *prismatic habit* could be probably expected. However, a rapid growth along

the c -axis leads to a needlelike morphology (*acicular habit*). On the contrary, a rapid growth along the other axes or a slow growth in the direction of the c -axis can originate a platelike shape (*tabular habit*). These three typical habits of the hexagonal system are exemplified in Figure 1.7 for the case of zinc oxide.

Formation of composite crystals: The formation of composite crystals is a phenomenon that occurs in both natural and synthetic crystalline systems as a consequence of aggregation and intergrowth; its avoidance is one of the main problems of the scale up of crystallization processes for industrial applications. Composite crystals occur as *clusters* of crystals formed by simple random aggregation or more symmetrically, as in the case of the *parallel growth*. Another common form of composite crystal is the *twin*, composed of two individual crystals. In some cases twins can be *interpenetrant* or *partially interpenetrant*. Figure 1.8 illustrates the previous phenomena considering always examples of ZnO crystals.

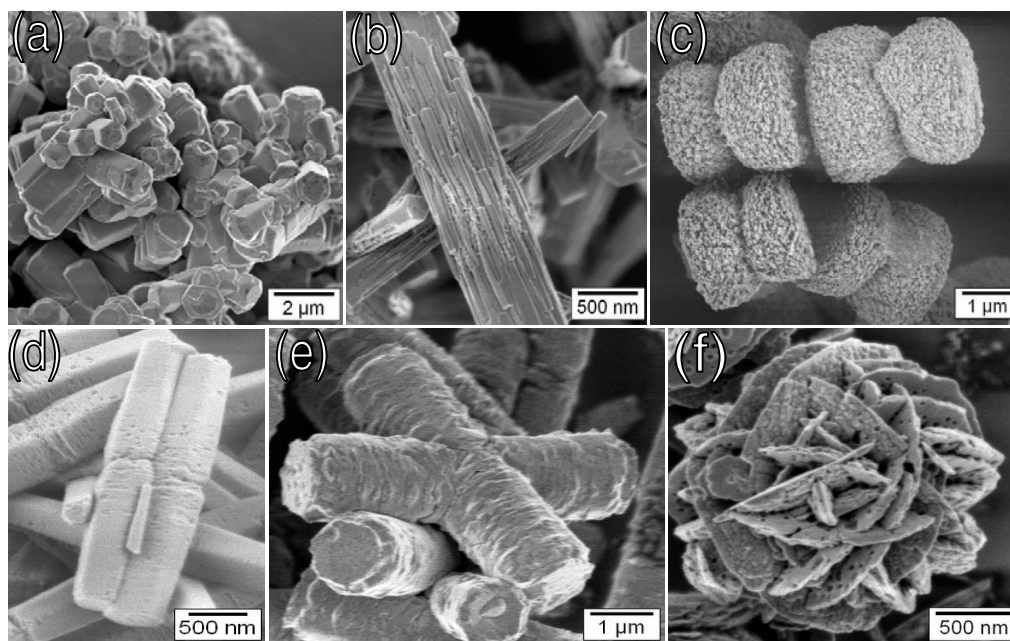


Figure 1.8. Formation of composite crystals in ZnO precipitated from aqueous medium in the presence of different latex additives: (a) clusters formed by aggregation, (b) parallel growth, (c) twins, (d) partially interpenetrant twins, (e) and (f) interpenetration of crystals.

1.4 Polymer-controlled crystallization

It has been shown how “foreign” substances or additives may influence the different steps of the crystal formation, which may be used to control the properties of

a certain crystallized material. Biomimetic strategies have led to use polymers for this purpose. The combination of polymers with inorganic (and organometallic) materials has always been present in nature and has also a long tradition in industry, as exemplified by the use of surfactants and different types of polymers to avoid aggregation of inorganic suspensions, or by the dispersion of pigments in polymeric paints. Polymers have also been used as templates, especially for the generation of inorganic materials via sol–gel processes (see the review of van Bommel et al.^[34]). A peculiar example of polymers for templating purposes was presented by Iskandar et al.,^[35] who used polystyrene latex nanoparticles to produce spherical silica particles containing ordered mesopores. However, the so-called polymer-mediated crystallization implies a completely different approach. In this case, soluble polymers are not used as templates but as specific controlling agents of the crystal formation. Macromolecules may play a role in the nucleation process or can also adsorb selectively at certain crystal faces and control the growth, leading to changes in the habit and determining the final morphology. In some cases, polymers can also stabilize phases that, otherwise, are metastable.

Many types of polymers—including both natural and synthetic—have been applied to control crystallization processes. Some of the applied polymers are, for instance, DNA,^[36,37] starch,^[38] hydroxypropylmethylcellulose,^[39,40] polyaspartates,^[41] poly(allylamine hydrochloride),^[42] polyacrylates,^[43–47] polyvinylpyrrolidone,^[48,49] hyperbranched polyglycerol,^[50] polystyrene sulfonates,^[42,51] dendrimers,^[52–54] graft copolymers (or comb polymers),^[8,55] and block copolymers.^[8,56,57] Among them, double-hydrophilic block copolymers (DHBCs) are by far the most broadly investigated and have been shown to be particularly effective in many different systems: carbonates (CaCO_3 , BaCO_3 , PbCO_3 , CdCO_3 , MnCO_3),^[58–67] zinc oxide,^[8,68–71] cerium oxide and CeOHCO_3 ,^[72] barium sulfate,^[45,73–75] barium chromate,^[76,77] barium titanate,^[47] calcium oxalate dihydrate,^[78] cadmium tungstate,^[79] cadmium sulfide,^[80] and calcium phosphates.^[81] A systematic overview in the different systems in which the crystallization has been controlled by hydrophilic polymers can be found in a recent review published by Yu and Cölfen.^[57]

A less investigated system, but with many potential applications, is provided by functionalized latex particles. The developments during the last years in miniemulsion polymerization allow to synthesize particles with defined and tunable size and chemical nature. So far, latex particles have been applied with relative success to the crystallization of calcium carbonate,^[11] zinc oxide,^[8,9] and zinc phosphates.^[12]

Chapter 2

Synthesis and characterization of surface-functionalized latex particles

To make a synthetic latex . . . is something like having a baby, it's easy to do, it can bring great joy, but it can be impossibly difficult to understand in detail all that went into the process and its subsequent behavior!

—Robert M. Fitch^[82]

2.1 Introduction

The term latex (fluid, in Latin) referred originally to a natural milky fluid produced by cells of various seed plants, as for example of genera *Hevea* and *Ficus*. Natural latex is a polymeric aqueous dispersion containing different substances: resins, tannins, alkaloids, proteins, polysaccharides, etc., and it is the source of rubber (also called caoutchouc—from *caa-o-chu*, “crying wood” in an ancient Amerindian language) and other materials as gutta-percha, chicle, and balata. The words latex and rubber are sometimes confused and used as synonyms, but rubber designates a resulting product, essentially a polymer (natural or synthetic) of isoprene, whereas latex is a more general term and refers to the precursor emulsion. In the production of natural rubber, the emulsions obtained from the plants are coagulated and then prepared as sheets and dried. The imitation of nature, a usual strategy in science, led to the production of synthetic latexes[†] and nowadays the meaning of latex has been extended and it is used for any polymeric emulsion or polymer colloid. This latter term, *polymer colloid*, was coined in the 1970s to refer to latexes and implies an intersection of the properties of polymers and colloids.^[82]

[†] In English, the plural of *latex* may take the etymological form *latices*, from the Latin language, or the form *latexes*, broadly used in specialized literature. In this work we decided to use *latexes*, to avoid confusions with *lattices*, plural form of *lattice*.

Polymer colloids are obtained by heterophase polymerization processes, such as emulsion, mini- and microemulsion, or suspension polymerization. The development of the heterophase polymerization techniques is closely related with the history of rubber and its synthetic production. The first attempts of producing synthetic rubber date back to the First World War and were made in Germany by Luther and Hueck (coworkers of IG Farbenindustrie AG), who developed the first viable emulsion polymerization method.^[83] During the Second World War, the interruption in the delivery of natural rubber coming from Asia accelerated enormously the research and the developments in the production of synthetic rubber, being remarkable the progress in emulsion polymerization. In the last decades, emulsion polymerization has become an important technique for a broad variety of applications, not only in the synthetic rubber, but also in paints, adhesives, paper coatings, floor polishes, sealants, toughened plastics, cement and concrete additives, medical diagnostics, and drug-delivery systems. Conventional emulsion polymerization represents by far the majority of the industrial world production of latexes (more than 20 million tons a year^[84]), but other techniques, specially miniemulsion polymerization, are gaining importance progressively.

Much research has been devoted to latex systems and thousands of papers about the topic have been published. Several reference books,^[82,83,85–87] conference books,^[88–91] and review articles^[84,92–94] compile the cumulated knowledge in emulsion polymerization techniques. The case of *miniemulsion* polymerization has been specifically reviewed in various journal articles.^[95–98]

Miniemulsion polymerization has indeed several advantages among the rest of heterophase polymerization methods. Uniform and monodisperse latexes with particle size in the submicrometer range and much longer stable than those obtained by conventional emulsion can be readily obtained by this technique. Furthermore, the amount of surfactant is lower than in microemulsion polymerization, and this can be important in several applications. Miniemulsion polymerization provides, in addition, a convenient and versatile method to prepare polymer colloids with promising features, for instance the possibility of encapsulating fluorescent dyes^[99] or inorganic pigments.^[100–103]

Because they have spherical shape and it is possible to vary the particle size and surface charge, and because they can be transferred from one fluid medium to another, monodisperse latex particles—as the obtained by miniemulsion polymerization—are ideal model systems for testing colloidal theories.

2.2 Fundamentals of miniemulsion polymerization

2.2.1 Definitions

An *emulsion* is a system consisting of a liquid dispersed in droplets (*dispersed phase*) in another immiscible liquid (*continuous phase*), with or without using an emulsifier. Commonly the dispersed phase is an organic substance and the continuous phase is water; these dispersions are named *oil-in-water* emulsions. However, the opposite case, the so-called *water-in-oil* emulsions (or *inverse emulsions*), is also possible: aqueous droplets are dispersed then in an organic solvent. If a polymerizable monomer is used as a dispersed phase and the necessary conditions are met (i.e., required temperature and presence of initiator), a polymerization reaction can start.

In the context of emulsion polymerization, oil-in-water emulsion systems are classified in three types: *macroemulsions* (conventional emulsions), *miniemulsions*, and *microemulsions*. The main differences between these categories are the size and the stability of the droplets:

- In *macroemulsions*, the droplet size is relatively large (1–100 μm) and the stability is quite short (limited to minutes). The emulsions are kinetically stabilized by using surfactants, and empty and monomer-swollen surfactant micelles coexist in the initial state. Phase separation takes place rapidly, unless the system is well-mixed.
- *Miniemulsions* have an intermediate position between macro- and microemulsions in terms of stability and droplet size. They are critically stabilized systems, have a typical droplet size between 50 and 500 nm, and the stability ranges from days to months. The oil/water interfacial tension is much larger than zero and high shear devices (such as ultrasonicators, microfluidizers, or high pressure homogenizers) are required to achieve the state of miniemulsion. The amount of emulsifier is similar to macroemulsions and lower than in microemulsions. Costabilizers with low molecular weight, such as long chain (≥ 12 carbons) alkanes (e.g., hexadecane) or alcohols (e.g., 1-hexadecanol) are commonly used.
- Finally, *microemulsions* are translucent and the droplet size varies from 10 to 100 nm. They are thermodynamically stable, with an interfacial tension at the oil/water interface close to zero. The emulsifier concentration must be above the required to form spontaneously a thermodynamically stable microemulsion, and these high concentrations lead to a complete coverage of the latex

particles by the surfactant. A short chain (≤ 5 carbons) alcohol (e.g., 1-pentanol) is typically used as costabilizer.

Based on the stability and the droplet size, Sudol and El-Aasser proposed the schematic representation shown in Figure 2.1.^[104] Additionally, some authors have pointed out other differences between the three types of emulsions, in reference to the kinetics and the change of the particle size during polymerization processes. According to Landfester,^[95] “in macroemulsion polymerization, the latex particle does not correspond to the primary emulsion droplet, and the size is established by kinetic parameters,” whereas in miniemulsion polymerization, the size of the droplets “is essentially given by dispersion process and droplet stability, but not by polymerization parameters” and “the latexes are essentially a polymerized copy of the original droplets.” However, this concept of “one-to-one” copy in miniemulsion polymerization (i.e., the particle size of the polymerized latex particles is the same as the initial droplet size) is less clear for other authors. Asua,^[97] for instance, affirms that “the one-to-one copy is a desirable feature of miniemulsion polymerization, but the conditions required to achieve this goal seem to be very difficult to attain in practice.” He indicated that the “one-to-one copy” is not a feature of miniemulsion polymerization, but a “possibility that might be reached,” and recommend to “be cautious about using this concept to analyze miniemulsion data.”

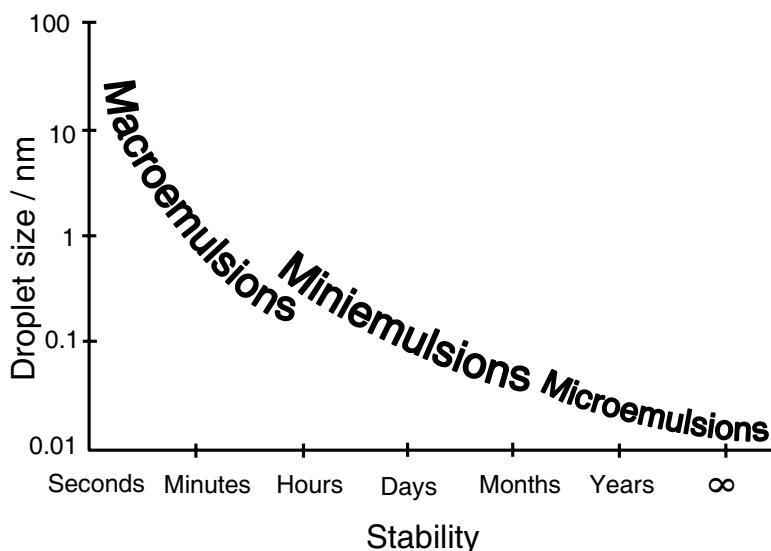
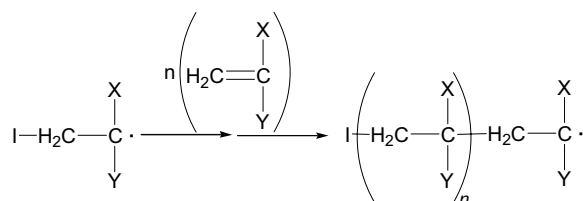
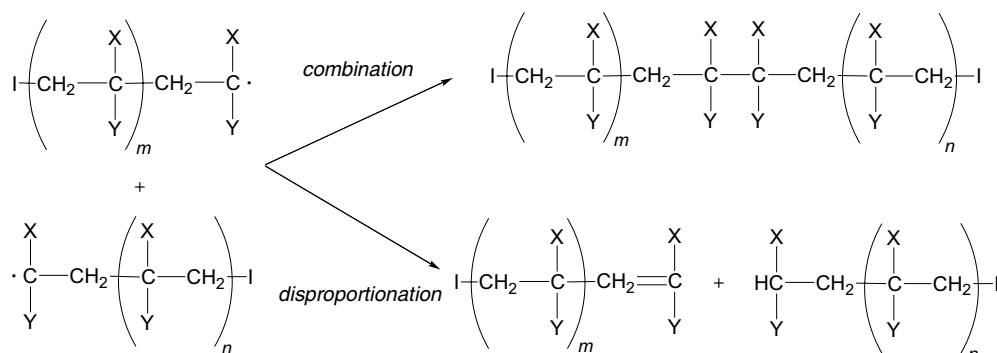


Figure 2.1. Schematic representation of relative stability of emulsions as a function of time according to Sudol and El-Aasser.^[104] (Copyright 1997 by John Wiley & Sons Limited. Reproduced with permission.)

2.2.2 Free-radical polymerization in miniemulsion

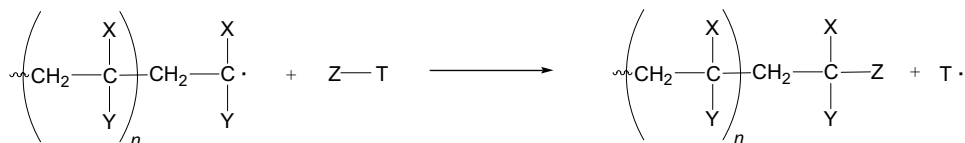
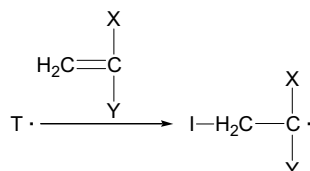
Free-radical polymerization can be conveniently carried out in heterogeneous media and under relatively undemanding conditions, for instance without

removing the stabilizer contained in commercial monomers, or in the presence of oxygen traces. The objective of this section is to review some aspects of the chemistry of free-radical polymerization, focusing on compounds and phenomena significant in this work. Detailed explanations can be found in the excellent book of Moad and Solomon,^[105] on which this section is partially based.

Initiation:**Propagation:****Termination:**

Scheme 2.1. General mechanism of the free-radical polymerization.

The monomers used in free-radical polymerization have the general structure $CH=CR^1R^2$, where R^1 and R^2 are two substituents (in general different, but they may also be identical). Classically, three classes of reactions can be considered, as illustrated in Scheme 2.1: *initiation* (involving generation of radicals), *propagation* (involving addition of radicals to the less substituted end of the double bond), and *termination* (involving disproportionation or combination between two growing chains). However, initiating species are not only formed from initiator decomposition but also indirectly by transfer to monomer, solvent, transfer agent, or impurities. Therefore, a fourth type of reaction has to be considered: *chain transfer* (see Scheme 2.2). The new radical formed in such reaction ($T\cdot$) may lead to *reinitiation* steps.

Chain transfer:**Reinitiation:****Scheme 2.2.** Chain transfer and reinitiation reactions in the mechanism of free-radical polymerization.**2.2.2.1 Initiation and initiators**

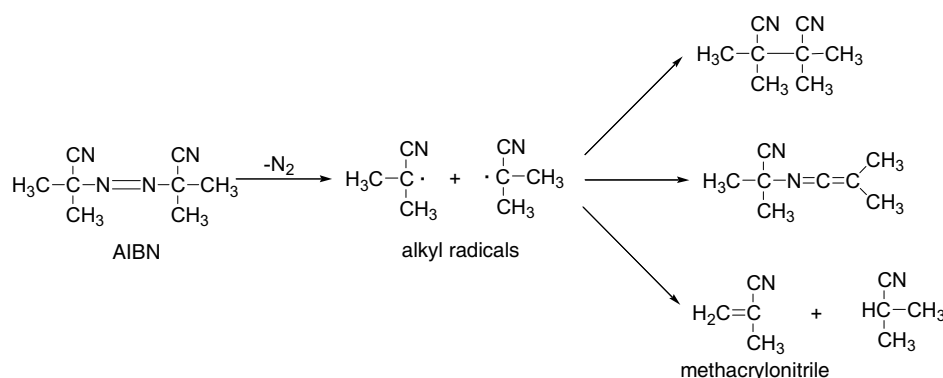
Initiation includes the steps of generation of primary radicals by decomposition of the initiator and the steps of addition of these radicals to the monomer to form initiating radicals (see Scheme 2.1). The most important initiators used in free-radical polymerization are azocompounds (containing $-\text{N}=\text{N}-$) and peroxides (containing $-\text{O}-\text{O}-$). Among the azocompounds, two classes can be distinguished: dialkyldiazenes, with general formula $\text{R}-\text{N}=\text{N}-\text{R}'$, and dialkyl hyponitrites, with general formula $\text{RO}-\text{N}=\text{N}-\text{OR}'$ (R and R' are identical or different groups). Two typical dialkyldiazene initiators, both oil-soluble, are 2,2'-azobis(isobutyronitrile) (AIBN) and 2,2'-azobis(2-methylbutyronitrile) (AMBN).[†] Among the peroxides, water-soluble inorganic peroxides, such as potassium persulfate ($\text{K}_2\text{S}_2\text{O}_8$), are often used in emulsion polymerization. The chemical structure of AIBN, AMBN, and $\text{K}_2\text{S}_2\text{O}_8$, together with their solubilities in water and the structures of the radicals formed by decomposition, are contained in Table 2.1.

Table 2.1. Selected initiators used in free-radical polymerization.

initiator	chemical structure	radicals generated	solubility in water at 20 °C [g L ⁻¹]
AIBN	$\text{H}_3\text{C} - \underset{\text{CH}_3}{\overset{\text{CN}}{\text{C}}} - \text{N}=\text{N} - \underset{\text{CH}_3}{\overset{\text{CN}}{\text{C}}} - \text{CH}_3$	$\text{H}_3\text{C} - \underset{\text{CH}_3}{\overset{\text{CN}}{\text{C}}} \cdot$	insoluble
AMBN	$\text{H}_3\text{CH}_2\text{C} - \underset{\text{CH}_3}{\overset{\text{CN}}{\text{C}}} - \text{N}=\text{N} - \underset{\text{CH}_3}{\overset{\text{CN}}{\text{C}}} - \text{CH}_2\text{CH}_3$	$\text{H}_3\text{CH}_2\text{C} - \underset{\text{CH}_3}{\overset{\text{CN}}{\text{C}}} \cdot$	insoluble
$\text{K}_2\text{S}_2\text{O}_8$	$\text{K}^+ \text{ } ^-\text{O} - \overset{\text{O}}{\parallel} \text{S} - \text{O} - \text{O} - \overset{\text{O}}{\parallel} \text{S} - \text{O}^- \text{K}^+$	$^-\text{O} - \overset{\text{O}}{\parallel} \text{S} - \text{O} \cdot$	52

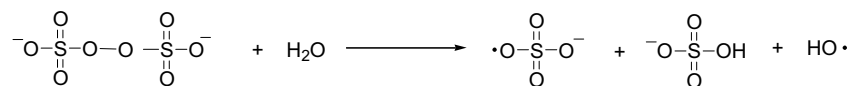
[†] In systematic nomenclature: 2,2'-azobis(2-methylpropanenitrile) and 2,2'-azobis(2-methylbutanenitrile), respectively.

Most thermal (and photochemical) initiators generate radicals in pairs. The *self-reaction* of the radicals to give nonradical species is often the principal pathway, and this is important even at low conversion, with high content of monomer in the medium. Scheme 2.3 shows the possible self-reactions of the alkyl radicals formed by decomposition of AIBN. Analogous reactions occur in the case of AMBN.



Scheme 2.3

In the case of persulfate initiators, their thermal decomposition can be unimolecular, giving two sulfate radical anions, or bimolecular, involving a water molecule and leading to the formation of hydroxyl radicals (see Scheme 2.4).



Scheme 2.4

Due to the many possible by-processes that may occur in the initiation steps, the analysis of the initiation kinetics and, consequently, the polymerization kinetics is very difficult.

2.2.2.2 Particle nucleation mechanisms

Three mechanisms of particle formation are typically proposed in the literature for emulsion polymerization: micellar, homogeneous, and droplet nucleation.

- In *micellar nucleation*, initiator radicals generated in the aqueous phase enter the monomer-swollen surfactant micelles and react with the monomer, beginning the chain propagation reaction. Unentered micelles act as reservoirs and provide surfactant and monomer to the growing particles. This mechanism occurs when the concentration is above the critical micelle concentration (c.m.c.) of the surfactant, as it is the case of microemulsions. Micellar nucleation is not supposed to play an important role in miniemulsion polymerization, where the surfactant concentration is usually below the c.m.c.^[96]

- In *homogeneous nucleation*, radicals generated in the aqueous phase attack monomer units and form water-soluble oligomers, which act as nucleating sites. The monomer is brought to those sites by diffusion, allowing the propagation and growth. This mechanism is important for surfactant-free emulsion polymerization,^[95,96] but it has been found to be of low significance in miniemulsion polymerization of styrene.^[106]
- In the *droplet nucleation* mechanism, radicals enter the monomer droplets as single radicals or oligoradicals, and react with the monomer present there. This mechanism is considered to be predominant in miniemulsion polymerization.^[95,97,107] In an ideal miniemulsion, every single droplet would be nucleated, acting as a polymerization nanoreactor, and the particle number would not change during the polymerization, but this is in general only an ideal situation (see the discussion at the end of §2.2.1).

In case of using oil-soluble initiators (as AIBN or AMBN) in miniemulsion polymerization, the radicals are formed directly in the monomer droplet, being reasonable to assume the droplet nucleation mechanism as preferred. However, there is some controversy at this point. It can be argued that radicals generate also in the aqueous phase from the dissociation of the fraction of the initiator present in that phase (consequence of its partition coefficient). This possibility cannot be completely excluded, but simulation works have indicated that radicals formed in the polymer particles are the main source of effective radicals.^[108]

2.2.3 Stability of miniemulsions

In oil-in-water emulsions, stability refers to the time elapsed before noticeable degradation of the emulsion, indicated by the formation of droplets much larger than in the original emulsion.^[104] Mainly, two processes lead to the destabilization of emulsions: coalescence and Ostwald ripening. Both phenomena are schematically sketched in Figure 1.9.

- *Coalescence* describes the process of collision between two droplets, due to van der Waals attractive forces, to form a new bigger droplet.
- *Ostwald ripening* indicates the process of mass diffusion of the oil phase, from a smaller droplet to a bigger one, due to different Laplace pressure[†] and

[†] The Laplace pressure is the pressure difference, Δp , between the inner and the outer part of a droplet of radius r , given by the Laplace equation,

$$\Delta p = \gamma (2/r)$$

where γ is the surface tension for the oil/water interface. Qualitatively, the surface tension tends to compress the droplet, increasing the internal pressure. The Laplace pressure is balanced by an osmotic pressure (Π), caused by a different chemical potential, and given by the well-known equation proposed by van't Hoff: $\Pi = nRT/V$.

chemical potential. The small droplets disappear through this process, increasing the average droplet size.

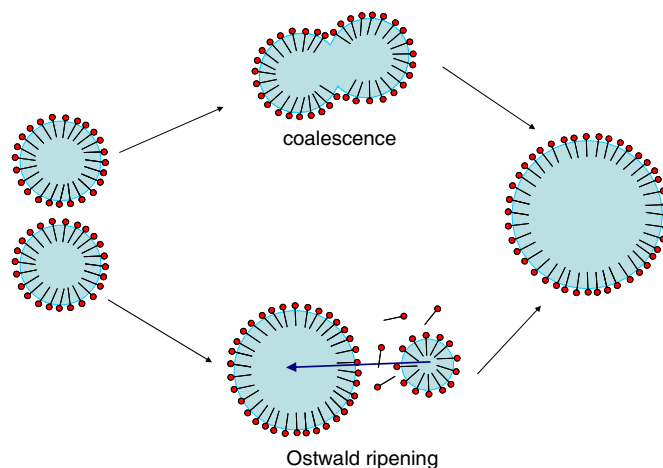


Figure 1.9. Schematic representation of coalescence and Ostwald ripening of particles.

The suppression of both processes, coalescence and Ostwald ripening, is necessary to obtain a stable miniemulsion. The coalescence of the particles is usually avoided by adding surfactants, which decrease the oil/water interfacial tension. The suppression of the Ostwald ripening is possible by adding a *hydrophobic agent*, commonly called *costabilizer* or *cosurfactant*, although some authors consider misleading the latter term and recommend to avoid it.^[95] The costabilizer should have a low molar mass and should be highly water-insoluble and monomer-soluble. Because of its high insolubility in water, the costabilizer cannot easily diffuse from the monomer droplet to the aqueous phase, and the decrease of monomer in a small monomer droplet would cause an increase in the free energy. Consequently, in the presence of a costabilizer, the Ostwald ripening (i.e., monomer diffusion from one droplet to another) is retarded. Hexadecane and cetyl alcohol (1-hexadecanol) are the costabilizers most commonly used in miniemulsion, but many other molecules, such as silanes, siloxanes, or isocyanates may be used. Polymers have also been shown to be effective hydrophobic agents to reduce Ostwald ripening, for instance, polystyrene has been used to stabilize styrene miniemulsions^[109] and poly(methyl methacrylate) has been used in MMA miniemulsions.^[110]

As indicated in §2.2.1, while microemulsions are thermodynamically stable, miniemulsions are critically stabilized systems and only stable for a certain period (metastable systems). The strategies to stabilize emulsions can be classified as electrostatic, steric, or electrosteric. *Electrostatic* repulsion between particles with the same surface charge will tend to avoid the aggregation and to stabilize

the system. Large amounts of ionic initiator (e.g., persulfates) introduce charged groups on the surface of the particles, which stabilize electrostatically the emulsion. The use of charged surfactants leads also to this type of stabilization. A hydrophilic layer onto the surface produces *steric* stabilization. If the latex corona contains charged functional groups (e.g., surface-functionalized latex particles, as those presented in this work), both electrostatic repulsion and steric hindrance will occur; this is called *electrosteric* stabilization. A competition between the electrostatic and the steric stabilizations, on one hand, and the tendency of the system to destabilize, on the other hand, will always take place.

2.3 Theoretical background of techniques for characterization of latex particles

2.3.1 Dynamic light scattering (DLS)

Dynamic light scattering (DLS), also known as photon correlation spectroscopy (PCS) or quasi-elastic light scattering (QELS), is a technique based on the signal fluctuation detected when an incident light beam interacts with particles diffusing in a medium.

Within an emulsion, particles are not static, but in a constant and random movement (*Brownian motion*), due to the effect of the surrounding particles and solvent molecules. Small particles will move faster than larger ones. The Brownian motion is described by the *translational diffusion coefficient* (D), given by the Stokes–Einstein equation:

$$D = \frac{k_{\text{B}}T}{6\pi\eta r} \quad (2.1)$$

where k_{B} is the Boltzmann constant, T is the absolute temperature, η is the viscosity of the medium, and r is the radius of the particles. Note that this equation is only valid for an infinitely diluted solution. The real translational diffusion coefficient will depend not only on the size of the particle core, but also on the electrical double layer (see §2.3.2), influenced by the surface structure and the ionic strength of the medium.

When electromagnetic radiation meets a particle, a part of radiation is scattered. If the scattering particle is moving, the frequency of the scattered radiation will slightly differ from the incident radiation, when viewed by a stationary observer (*Doppler effect*). The intensity I of the scattered light of frequency ω is expressed by an equation with the form of a Lorentzian function,^[111]

$$I(\omega) = A_1 \frac{Dq^2}{(\omega - \omega_0)^2 + (Dq^2)^2} \quad (2.2)$$

where ω_0 is the frequency of the incident radiation, A_1 is a constant, and q is the magnitude of the scattering vector given by the equation

$$q = \frac{4\pi n_0}{\lambda_0} \sin\left(\frac{\theta}{2}\right) \quad (2.3)$$

in which n_0 is the refractive index of the medium, λ_0 is the incident radiation wavelength in air, and θ is the scattering angle. Geometrically, as sketched in Figure 2.2, the scattering vector is defined as the difference between the scattered wave vector (\mathbf{s}_f) and the incident wave vector (\mathbf{s}_i).

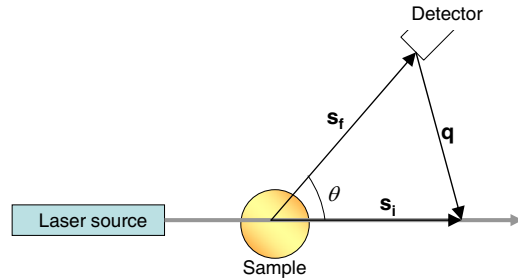


Figure 2.2. Schematic DLS setup with representation of the scattering vector.

The width of the peak at half maximum, Γ , is directly related to the diffusion coefficient according to

$$\Gamma = Dq^2 \quad (2.4)$$

Combining eqs. (2.1) and (2.4), the hydrodynamic radius of the scattered particle may be expressed as

$$r = \frac{k_B T q^2}{6\pi\eta \Gamma} \quad (2.5)$$

Stationary particles would scatter the light with the same intensity as a function of time and would give a stationary scattering pattern. On the contrary, particles undergoing Brownian motion would cause a fluctuation with the time in the detected intensity signal, because of the interference between photons coming from neighboring particles. The detected signal depends on the phase addition of the scattered light. Since the fluctuation of the detected signal is caused by the motion of particles and this is different for particles with different size, the fluctuation rate will depend on the size of the particles. For smaller particles (faster motion) the intensity fluctuates more rapidly than for larger ones. A distribution of frequencies related with the fluctuation of intensities could be obtained according to eq. (2.2). This distribution would have a linewidth Γ that could be substituted in eq. (2.5) to obtain the hydrodynamic radius. However, in DLS (or photon *correlation* spectroscopy) this process is a bit different: a *correlation function* is used to link the different measurements of the fluctuating signal. This

function can be written for a time difference τ (sample time) as

$$G(\tau) = \langle I(t) \cdot I(t + \tau) \rangle \quad (2.6)$$

For a large number of monodisperse particles in Brownian motion, the correlation function follows a simple exponential decay,

$$G(\tau) = A[1 + B \exp(-2\Gamma\tau)] \quad (2.7)$$

where A and B are constants corresponding to the baseline and the intercept of the correlation function, respectively. The parameter Γ corresponds to Γ in eq. (2.4) and can be now substituted in eq. (2.5) to obtain r . For a polydisperse system, the correlation function becomes more complicated and it is expressed as a sum of exponential decays.

In practice, the norm ISO 13321:1996 established a so-called cumulant analysis (used by the software of our equipment) to obtain the particle size distribution from the correlation function. The logarithm of this function, $\ln G(\tau)$, is plotted versus time and fitted to a quadratic expression:^[112]

$$\ln G(\tau) = a + b\tau + c\tau^2 \quad (2.8)$$

In this function, the value b is the Z-average diffusion coefficient. The polydispersity index (PDI), that is, the width of the distribution, is defined as

$$\text{PDI} = \frac{2c}{b^2} \quad (2.9)$$

The obtained particle size distribution is an *intensity distribution*. Assuming spherical morphology and using the Mie theory, this distribution can be converted into a *volume distribution*, and also in a *number distribution*. Consider, as an example, a sample containing the same number of particles of 10 and 100 nm. The number distribution will show two peaks of the same area. Since the volume of a sphere is proportional to the cube of the radius ($V = 4 \pi r^3/3$), in the volume distribution the area of the peak corresponding to the 100-nm particles will be about 1000 times larger than the area of the peak of 10-nm particles. In the intensity distribution, the ratio between both peaks will be 1:10⁶ ($I \propto d^6$, according to the Rayleigh approximation). In the case of a distribution with tails or more than one peak, the volume distribution gives a more realistic approach, while the number distribution implies, in general, great errors and it is not very reliable (small errors in the acquisition of data translate into huge errors in the number distribution).

2.3.2 Electrokinetics: surface charge and zeta potential

A charged particle in an electrolyte solution will be surrounded by a layer of ions with opposite charge. This layer may be considered as composed of two regions: an inner part (*Helmholtz layer*, divided at the same time in the *inner* and the *outer Helmholtz layer*, IHL and OHL), including ions that are bond strongly to the surface of the particle; and an outer part, the *diffuse layer*, in which the distribution is determined by a balance of electrostatic forces and random thermal motion. The potential has a linear behavior in the Helmholtz layer: it reaches a minimum ψ_i in the IHL and then increases[†] in the OHL until ψ_S (Stern potential). In the diffuse layer, the potential tend to zero exponentially.^[113] This model is known as theory of the *electric double layer*, and it is schematically represented in Figure 2.3.

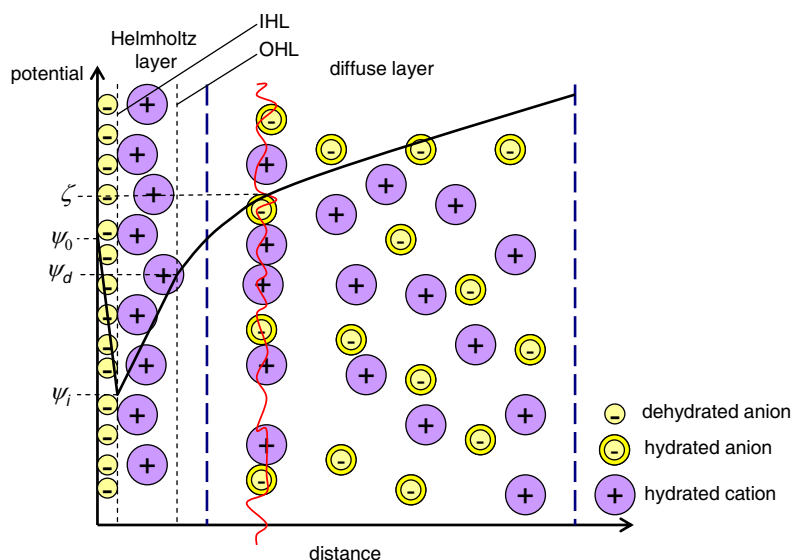


Figure 2.3. Schematic representation of the double layer, with indication of the different parts.

A charged particle will move in the solution together with the fixed (inner) layer and a part of the diffuse layer. This part of the diffuse layer is delimited by an imaginary *shear plane*, which separates the ions associated with the particle (ions “accompanying” the particle) from those of the bulk phase. The potential at the shear plane is known as *electrokinetic potential* or *zeta potential*, ζ .

Even if the surface potential, ψ_0 , could be estimated (in most cases this is not possible), it would not give appropriate information about the colloidal behavior. The important information is given indeed by the *effective charge*, which takes

[†] This is considering a negatively charged particle. For a positively charged particle, the sign would be inverse, and the potential would reach a maximum in the IHL and decreases in the OHL.

into account the surface charge and the double layer. Ideally, it would be helpful to be able to determine the electrostatic potential at the beginning of the diffuse part of the double layer, but experimentally this potential can be only approximated by measuring the ζ -potential.^[114]

The electrokinetic or zeta potential is measured in the practice through the so-called *electrokinetic processes*. These are phenomena in which an asymmetric charge distribution occurs at the interface between two phases, for example the interface of a solid particle and an electrolyte solution. The electrokinetic processes can be classified in four types: electrophoresis, electro-osmosis, streaming potential, and sedimentation potential.

- When an electric field is applied to a solution of charged particles, the particles move toward the oppositely charged electrode. This process is called *electrophoresis*.
- In *electro-osmosis*, the solid phases remain stationary, but the charges in the solution move when the electric field is applied.
- A *streaming potential* is generated when, instead of applying an electric field, the solution is forced through a porous medium or capillary under hydrostatic pressure (the pressure is generated, for instance, pumping a solution through a capillary). Charges of the double layer on the capillary wall will move with the solution in the direction of the stream. This produces an electric stream in the opposite direction of the stream fluid.
- When a suspension of charged particles is settled by gravitation or centrifugation, the resulting particle motion causes a potential difference between the upper and the lower parts of the suspension, called *sedimentation potential*.

Two of these electrokinetic techniques were used in the present work to characterize the latex particles: measurement of *streaming potentials* (used to detect the end point of the polyelectrolyte titration) and *electrophoresis*.

2.3.3 Electrophoresis

Viscous forces tend to oppose the movement of particles toward the electrode of opposite charge in the presence of an electric field. When the equilibrium between the viscous forces and the electrostatic attraction forces is reached, the particles move with a constant velocity v , which is proportional to the applied field E , given by

$$v = \mu_E E \quad (2.10)$$

with μ_E being the electrophoretic mobility, which can be expressed by the modified Stokes law,

$$\mu_E = \frac{Q}{6\pi r \eta} \quad (2.11)$$

where Q is the effective charge on the particle, η is the viscosity of the medium, and r is the particle radius.

The electrophoretic mobility can be related with the ζ -potential by Henry's equation, valid if the charge is low (ζ less than 30 mV).

$$\mu_E = \frac{2\varepsilon\zeta}{3\eta} f(\kappa r) \quad (2.12)$$

where ε is the dielectric constant of the medium and $f(\kappa r)$ is a function of the *Debye length* (κ , reciprocal value of the thickness of the double layer) and the radius of the particle (r). The function $f(\kappa r)$ depends on the particle shape and for a sphere varies between 1 (for small values of κr , *Smoluchowski approximation*) and 1.5 (for large κr , *Hückel approximation*).[†] The Debye length can be calculated with the equation

$$\kappa = \left(\frac{8\pi e^2 N_A}{1000 \varepsilon k_B T} \right)^{1/2} I^{1/2} \quad (2.13)$$

where e is the charge of the electron, N_A is Avogadro's number, ε is the dielectric constant of the medium, k_B is Boltzmann's constant, T is the absolute temperature, and I is the ionic strength.

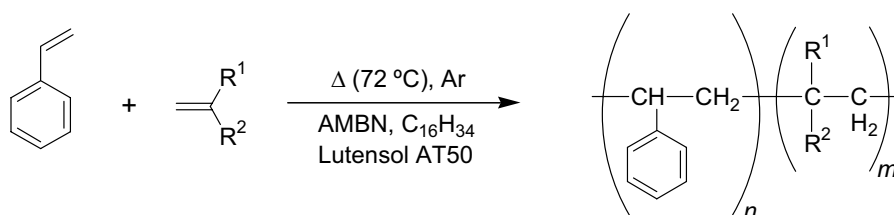
2.4 Synthesis of surface-functionalized latexes

Latex particles of typical radii 30–50 nm were prepared by direct miniemulsion polymerization. In spite of the mechanistic complexity behind the process, whose investigation attracts the attention of many research groups, several reasons led to the choice of the miniemulsion polymerization technique: (i) preceding work has shown the interest of miniemulsion polymers in control of mineralization processes;^[9–12] (ii) this is a convenient and relatively short synthetic process, with high reproducibility, and core–shell functionalized particles varying in the chemical composition of the surface can be quickly obtained from simple

[†] The development of this function can be found in ref. [115].

monomers; (iii) miniemulsions have relatively long-term stability (they may be stable for months); (iv) this technique allows to obtain small particles with high monodispersity; and, finally, (v) the obtained particles are versatile, since the particle size and the local concentration of functional groups attached to the surface can be controlled.

Styrene was the main monomer, and various hydrophilic comonomers were used to modify the surface properties of the latex particles. The general polymerization reaction used in this work can be written as presented in Scheme 2.5.



Scheme 2.5

In the present subchapter, our formulation of the miniemulsion process is justified, and we describe the synthesis process, proposing and justifying a core-shell structure for the surface-functionalized latex particles.

2.4.1 Formulation and choice of the components

Our latexes were synthesized following the basic procedure of Landfester et al.,^[116,117] using ultrasonication as a shear method to achieve the state of miniemulsion. Table 2.2 shows the ingredients and their proportions in our formulation.

Table 2.2. Ingredients and proportions of the miniemulsion formulation used in this work.

phase	ingredient	wt % (with regard to total monomers weight)
oil phase	styrene	92–98
	functional comonomer	2–8
	hexadecane	4.2
	AMBN (initiator)	2

aqueous phase	water	400
	Lutensol AT50 (surfactant)	25

Monomers: Table 2.3 contains the used monomers, their solubility in water and their oil/water partition coefficient.[†] *Styrene* (S), a classic monomer in miniemulsion polymerization and practically immiscible in water, was selected as the main component of the oil phase, in preference to other eligible candidates with higher solubility in water, such as methyl methacrylate (MMA, with a solubility in water of 15 g L⁻¹ at 20 °C, and log P =1.38). The different functionalizing comonomers were chosen from the pool of possible candidates taking into account the knowledge from previous work^[12] and considering the charge and polarity of the functional groups. *Acrylic acid* (AA) derived latexes have been shown to have an interesting effect in the crystallization of ZnO.^[8-10] *Methacrylic acid* (MAA), a derivative of the AA, was also used. *Maleic acid* (MA) was selected as a monomer with double number of carboxylic groups, in comparison to AA. Latexes containing phosphate groups were synthesized by using *ethylene glycol methacrylate phosphate* (EGMP). With *methacrylonitrile* (MAN) and *2-allylphenol* (APh), we pretended to extend the screening to noncharged monomers. Finally, *ar-vinylbenzyl trimethyl ammonium chloride* (VBTMAC) was taken to produce a positively charged latex.

Hydrophobic agent: Hexadecane, a typical costabilizer in miniemulsion polymerization, was used as hydrophobic agent. Landfester et al.^[118] used this costabilizer in styrene miniemulsions, and they reported that it disperses homogeneously in the droplets and does not show any enrichment close to the interface.

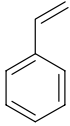
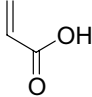
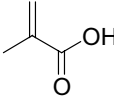

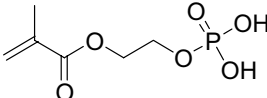
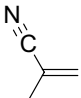
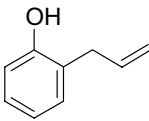
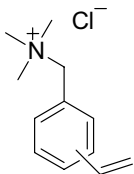
Initiators: An oil-soluble initiator was used in order avoid the polymerization of the hydrophilic comonomers in the aqueous phase. It was desired to start the polymerization inside the droplets, and for this purpose AMBN was preferred to the typical AIBN; both AMBN and AIBN are insoluble in water, but the former one is even more insoluble than the latter. Using AMBN as initiator, the possibility of polymerization in the aqueous phase is practically negligible. In some cases, small portions of a water soluble initiator, potassium persulfate (K₂S₂O₈), were added in an advanced state of the polymerization process to initiate the polymerization of water-soluble comonomers in the aqueous phase and improve their grafting onto the latex corona.

[†] The partition coefficient P is a constant and is defined as the ratio of concentration of compound in aqueous phase (c_{aq}) to the concentration in an immiscible solvent (c_{org}), considering the neutral molecule in the case of ionizable substances:

$$P = c_{\text{org}}/c_{\text{aq}}$$

Usually, the partition coefficient is expressed taking its decimal logarithm, log P . A value of 1 for log P indicates a ratio $c_{\text{org}}/c_{\text{aq}}$ of 10:1; log P = 0 indicates a ratio 1:1; and log P = -1 indicates a ratio $c_{\text{org}} : c_{\text{aq}}$ of 1:10. The value of log P in neutral immiscible liquids runs parallel to their solubilities in water.

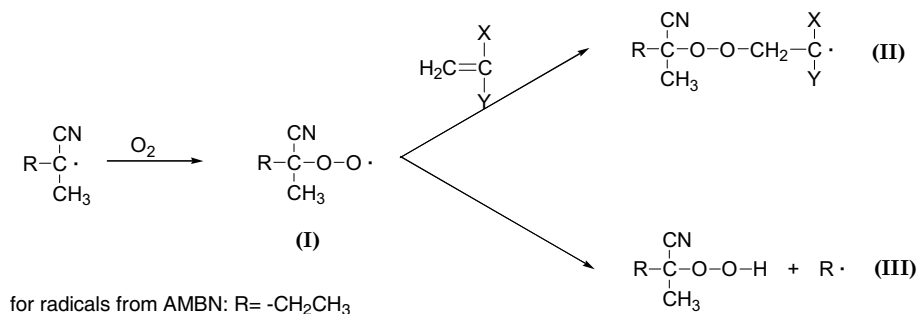
Table 2.3. Monomers used to prepare the surface-functionalized latex particles.

monomer	chemical structure	solubility in water at 20 °C [g L ⁻¹]	partition coefficient log <i>P</i> (o/w)
styrene (S)		0.20	2.96
acrylic acid (AA)		1000 ^[a]	0.35
methacrylic acid (MAA)		soluble	0.93
maleic acid (MA)		788 ^[a]	-0.48
ethylene glycol methacrylate phosphate (EGMP)		-	-
methacrylonitrile (MAN)		25.7	0.68
2-allylphenol (APh)		7	2.91
<i>ar</i> -vinylbenzyl trimethyl ammonium chloride (VBTMAC)		-	-

[a] At 25 °C, instead of 20 °C.

Surfactant: In the context of this work, cationic and anionic surfactants were not considered, because they would introduce functionalization in the latex corona, which may have undesired effects in the inorganic crystallization, in addition to the effect of the intentionally introduced functional groups. Consequently, a nonionic poly(ethylene oxide) derived surfactant was selected: Lutensol AT50 (BASF), a hexadecyl-modified poly(ethylene glycol) with formula (C₁₆H₃₃)(EO)₅₀. The use of Lutensol AT50 in miniemulsion polymerization and the dependence of the particle size with the concentration of this surfactant was studied by Bechthold et al.^[101,119] The final particle size is mainly controlled by the surfactant concentration.

Reaction conditions: The reaction conditions are mainly determined by the nature of the initiator, AMBN. The polymerization reaction was carried out at 72 °C (the “temperature for ten hour half life” for AMBN is 69 °C^[105]) in an inert argon atmosphere. The presence of oxygen in the reaction atmosphere may complicate the initiation process, because the initiator may react with the oxygen to form new radicals. The alkyl radicals resulting of the decomposition of AMBN react with O₂ to give alkylperoxy radicals, as shown in Scheme 2.6. Alkyl peroxy radicals (I) may react with the monomer to form relatively unstable peroxidic end groups (II), and may also abstract hydrogen from polymer, monomer, or other components of the system to form reactive hydroperoxides (III) and new radicals (R·).^[105]



Scheme 2.6. Reaction of alkyl radicals with oxygen.

2.4.2 Polymerization and structure of latex particles

The miniemulsification leads to the formation of small droplets of the oil phase (containing mainly styrene, hexadecane, and the initiator), partially covered by the surfactant, which stabilizes the miniemulsion. The hydrophilic comonomer is outside the droplets in the aqueous phase, but because of its partition coefficient, a small fraction is also present in the oil phase. Thus, copolymerization of the hydrophilic monomer with the styrene may also take place in the droplets. As an example, let us consider acrylic acid (AA) as hydrophilic monomer for the following discussions. There is always an equilibrium between the AA present outside and inside the droplets, and when AA units polymerize in the oil phase, new molecules diffuse from the aqueous to the oil phase. The partitioning of the hydrophilic comonomer between both phases is affected by different factors, such as temperature or pH. As soon as AA becomes incorporated into the growing chain, mainly composed of styrene units, the chain assumes an amphiphilic character and moves toward the interface to expose the carboxyl groups to the water phase. As a consequence, a complex latex corona structure will be formed. As sketched in Figure 2.4, the latex corona is comprised of short segments of the

hydrophilic component of the nonionic surfactant and hydrophilic segments of the copolymer between styrene and AA. A certain concentration of carboxylic groups will be present embedded at various depths inside the corona. It is worthy to mention that some studies have shown that an important amount of carboxylic groups may remain buried inside the particle and not at the surface. The surface coverage increase by increasing the amount of hydrophilic monomer in the comonomer feed.^[120]

We assume that copolymerization processes similar to the one described for the case of the AA occur with the rest of the comonomers used. In the case of methacrylonitrile and 2-allylphenol, with solubilities in water of only 25.7 and 7 g L⁻¹ respectively (at 20 °C), it is to be expected that the segments composed by these monomers will essentially remain inside the latex core, while only a small fraction will be present in the corona.

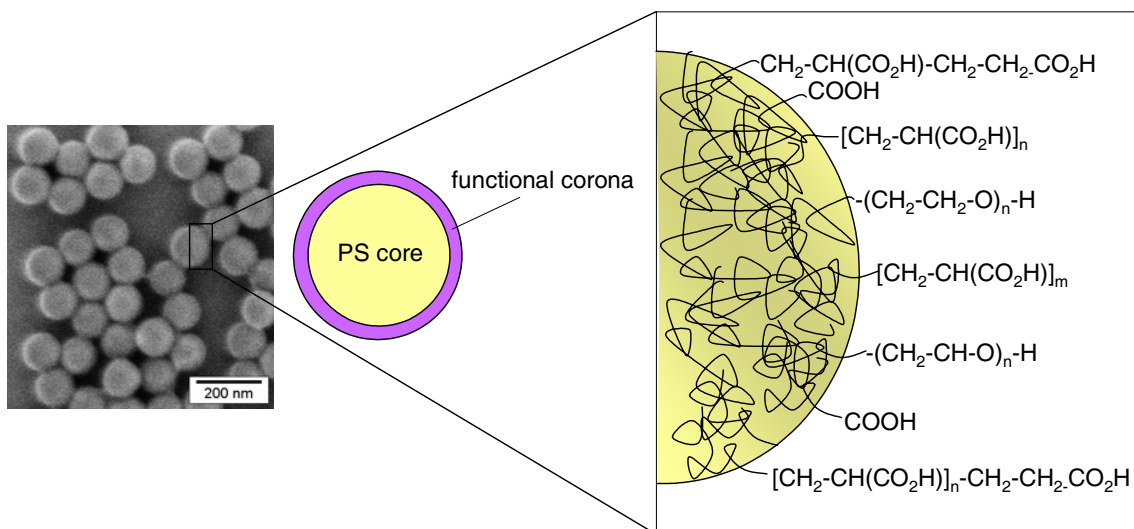


Figure 2.4. SEM micrograph of a poly(styrene–acrylic acid) latex and schematic representation of the chemistry of the surface.

2.5 Characterization of latex particles

The complexity of the effect of hydrophilic monomers in the miniemulsion polymerization processes is translated into a parallel complexity of the resulting latex structure. The details of the structure and properties of the corona in core–shell latexes, formed as a consequence of analogous or similar processes to the used in this work, are not still fully understood and have been object of many studies. Some theoretical considerations have been made for the case of polymer brushes grafted onto spherical colloidal particles.^[121] Experimentally, the radial repartition of the monomers, the surface characteristics and the behavior of core–shell

latexes in solution (i.e., effect of ionic strength and pH) have been analyzed by different techniques: sedimentation,^[122] conductimetric titrations,^[123–125] dynamic light scattering (DLS),^[126,127] static light scattering (SLS) combined with DLS,^[128] combination of light scattering with viscosity measurements,^[129] small-angle neutron scattering (SANS),^[127,130–132] small-angle X-ray scattering (SAXS),^[122,133] transmission electron microscopy (TEM),^[134–137] electrophoresis,^[123,127] solid-state NMR,^[136] atomic force microscopy (AFM),^[137] and other less conventional techniques, such as isothermal titration calorimetry,^[138] single particle light scattering,^[137] or colloidal particle scattering.^[139]

In our case, we are mainly concerned with the particle size and the surface charge density of functional groups that can be addressed by a growing crystal face, assuming that these functional groups need to make contact with the surface in order to control the crystal growth features. Here, the latex diameters were determined by DLS measurements and the number of functional groups per unit area was estimated by titration with an oppositely charged polyelectrolyte (polyelectrolyte titration). The values of the zeta potential, obtained from electrophoretic mobility measurements, were also studied for several latex samples.

2.5.1 Determination of particle size

The particle size and the size distribution are very important characteristics in colloidal systems. The definition of size seems to be quite obvious, but in colloid science it is not a trivial magnitude and is usually defined according to the technique used to measure it. Thus, it is possible to distinguish between geometric, optical, and hydrodynamic size. The *geometric size* is that obtained from optical or electron microscopy, and may be different from the *optical size*, defined as that obtained by inversion of angular intensity light scattering (AILS) data from measurements of a colloid in situ.^[140] The *hydrodynamic size* refers to the size measured from DLS data and it is related with the diffusion of the particle within a fluid; it depends, therefore, on the electrical double layer surrounding the particle, and on the ionic strength.

Electron microscopy (SEM and TEM) offers a good way to obtain particle size distributions of latex samples by statistical treatment of micrographs. This technique allows evaluation of the particle shape and the aggregation present in the system. However, a relatively elaborated sample preparation in comparison with light scattering techniques is required, since the emulsion has to be dried in a substrate to make possible the observation under the electron microscope. The measurement of the sizes and the statistical treatment is a tedious task and very few particles can be examined, leaving the question open whether the selected

subset is representative of the whole sample. For these reasons, the electron microscopy does not appear to be convenient for routine size determination of latex preparations.

A standard alternative in the submicrometer scale, which is the range of the miniemulsion latexes, is provided by DLS, due to the fact that particles with different size will diffuse with different velocities within the emulsion and will show different fluctuations in the detected signal.

In this work, the particle size of latexes were typically determined by using an automatic device Malvern Zetasizer 3000HS, based on DLS measurements at a fixed angle of 90° . The data provided by this device were contrasted with the hydrodynamic radii obtained with a conventional DLS equipment (see Figure 2.5) for a standard polystyrene latex without functionalization on the surface and for a poly(styrene–methacrylic acid) latex. The results are perfectly comparable with differences of <2 nm.

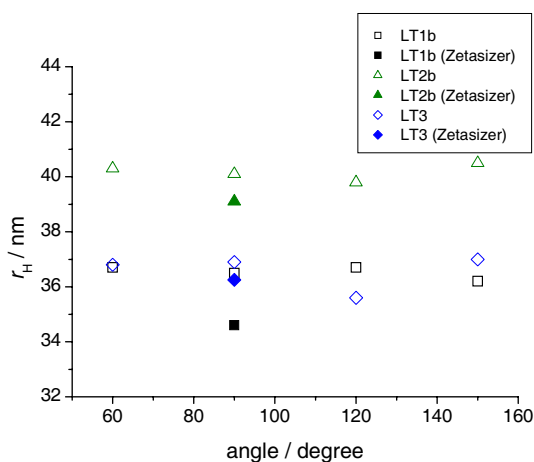


Figure 2.5. Comparison between the hydrodynamic radii, r_H , obtained for latex samples with a conventional DLS equipment at different angles and those obtained with the Malvern Zetasizer at a fixed angle of 90° . The sample LT1 is a polystyrene latex without surface functionalization and the samples LT2b and LT3 are poly(styrene–methacrylic acid) latexes with carboxylic groups on the surface (cf. Table 2.4).

Particles size distributions obtained by the Malvern Zetasizer and by statistical treatment of SEM micrographs were also compared. The distributions for a representative sample, a poly(styrene–acrylic acid) latex, are presented in Figure 2.6. Note, first, the differences between the intensity, volume, and number distributions obtained by DLS; and, second, the differences between the geometric diameter (from SEM) and the hydrodynamic diameter (from DLS), being the former smaller than the latter.

As explained in §2.3.1, DLS provides a distribution based on the intensity, and the volume and number distributions are obtained applying approximations and mathematical calculations. In Figure 2.6, the mean diameter of the number distribution is clearly smaller than the mean diameter of the intensity distribution. If we assume that the conversion between the intensity and the number

distribution provided by the software is correct, these differences can be explained by the fact that larger particles will scatter more light than smaller particles, and a small amount of larger particles in the samples can lead, consequently, to an apparent shift to higher diameters in the intensity distribution.

The difference between sizes obtained with DLS and with SEM is expected, and one has to consider how the measurement is done in each technique. DLS is based on the interaction of light with the matter and the measurement is carried out in solution. In solution, the hairy latex corona, composed by the functional groups and the hydrophilic residues of the surfactant, is expanded and interacts with the medium, forming a layer whose dimensions will influence the result. SEM micrographs result from the interaction of electrons with the matter, and the measurement is done with dried samples under vacuum. Under these conditions, the functional corona is “compressed” and the observed dimensions are essentially the dimensions of the core. Furthermore, although it does not appear to play an important role in our case, the particles can coalesce by drying the samples, and this will also influence the size measured from SEM micrographs.

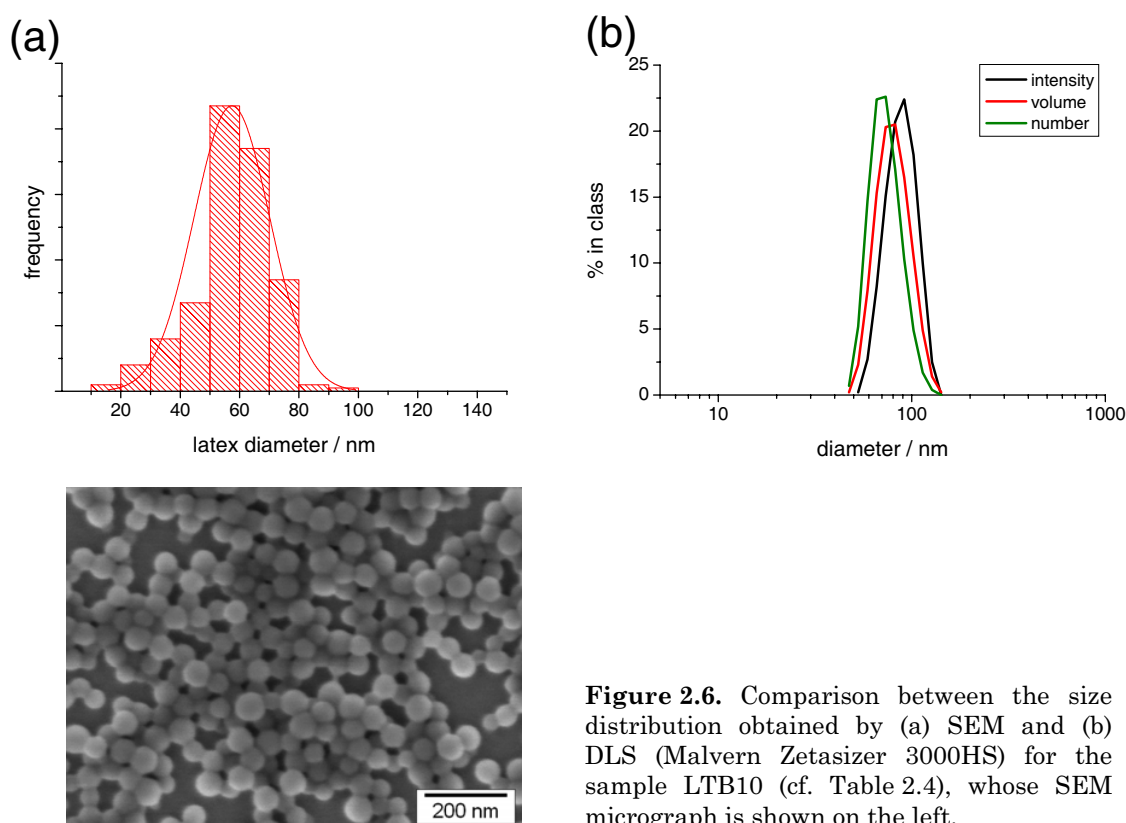


Figure 2.6. Comparison between the size distribution obtained by (a) SEM and (b) DLS (Malvern Zetasizer 3000HS) for the sample LTB10 (cf. Table 2.4), whose SEM micrograph is shown on the left.

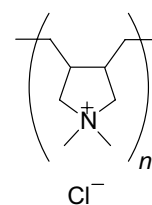
Diameters and polydispersity indices (PDIs) of the latex preparations presented in this work are contained in Table 2.4 (at the end of the next section, p. 45). Diameters, d , were in the range $58 \leq d \leq 97$ nm and the smallest particles

were obtained, as it could be expected, for the polystyrene reference samples without hydrophilic comonomer. In these samples, no functional corona is present and the size corresponds essentially to the polystyrene core, although residues of the surfactant can have as well a slight influence on the measured size. The largest diameters were those of the latexes prepared with noncharged comonomers (MAN and APh). These comonomers are relatively insoluble in water and the formed polymers should mainly be embedded in the core, swelling the particle. Intermediate sizes were obtained for samples prepared with AA, MAA, MA, and EGMP, being the average diameters of the EGMP-derived latexes slightly larger. The EGMP molecule is larger than the rest of monomers and this might explain the latter observation. PDIs range from 0.04 to 0.215. Values under 0.08 indicate nearly monodisperse samples, while values between 0.08 and 0.70 indicate a mid-range polydispersity.^[141] The majority of the samples can be considered as basically monodisperse.

2.5.2 Determination of surface charge density by polyelectrolyte titration

The surface charge density of the latex particles was determined by direct polyelectrolyte titration with poly(diallyldimethylammonium chloride) (poly-DADMAC, Scheme 2.7), detecting the end point with an automatic streaming current detector (SCD), which measures streaming potentials. This technique has been applied to the determination of charge densities of polyelectrolytes and latexes by several authors.^[142–144]

The polyelectrolyte titration (or *colloid titration*, as originally called^[145]) is based on the stoichiometric reaction between the polyelectrolyte of interest and an oppositely charged polymer of known charge density (or equivalent weight). In many cases the reaction occurs with stoichiometry 1:1, but sometimes, copolymers can show deviations from this ratio, especially at high concentrations.^[146] Here, stoichiometry 1:1 was always assumed in the calculations. Typically, the end point of a titration is the inflection point of the curve, which can be precisely determined from the maximum of the first derivative. When the titration is performed by a SCD, the end point can be considered as the point with streaming current equal to zero (referred from here forward as *zero point*); this indicates that all existing charges in the sample have been neutralized. If the potential is unequal to zero, the sign of the measured value indicates whether the charge is positive or negative. The numerical potential value is a relative parameter that



poly-DADMAC

Scheme 2.7

depends on many factors, such as electrical conductivity of the sample, sample viscosity, molecular weight and particle size, dimension of the measuring cell, or temperature.^[147]

In general, the inflection point is almost identical to the zero point. However, some times the inflection point may be more reliable, if for some reason there is an offset in the instrument response that causes the displacement of the apparent zero point.^[143] In our case, the zero point was shown to be very similar to the inflection point; therefore it is taken as a good approximation to the end point. This is shown in Figure 2.7, where the titration curve of a poly(styrene–acrylic acid) latex with poly-DADMAC is presented. The maximum of the numerical derivation of the titration curves allows to find the inflection point, close to the zero point.[†] The difference between the two points is in this case of ca. 0.1 mL, which is not significant, if one considers that two different measurements of the same sample by this technique can give even higher fluctuations.

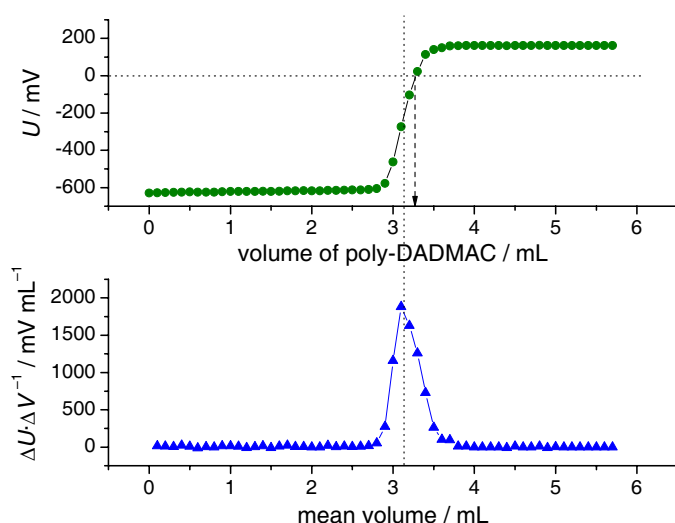


Figure 2.7. Titration of 150 μL of the latex LTB2 (cf. Table 2.4) with poly-DADMAC 0.001 N. The inflection point determined by the numerical derivative (see footnote) is compared with the point of streaming potential equal to zero.

Since the protonation of the functional groups change with the pH, the charge on the latex surface and, therefore, the consumption of poly-DADMAC during the titration will depend also on the pH. The evolution of the streaming potential with the pH was investigated by titration of the latex samples with a NaOH solution (0.01 M). This is represented in Figure 2.8. Here it is observed that in the

[†] Experimentally, the derivative in a titration is calculated as follows. For two consecutive values of the streaming potential, the numerical derivative can be expressed by

$$\frac{\Delta U}{\Delta V} = \frac{U(V + \Delta V) - U(V)}{\Delta V}$$

The values of $\Delta U/\Delta V$ are plotted versus the mean volumes, obtained by

$$\bar{V} = \frac{(V + \Delta V) + V}{2}$$

basic range, the potential reaches a plateau, which indicates that the carboxylic groups present in the latexes are essentially deprotonated and the charge is maximum. Having this in mind, the pH of the latex sample in the titration cell was adjusted at around 9.5 before beginning the titration measurements to ensure that the functional groups were deprotonated.

Typical titration curves for surface-functionalized latexes are presented in Figure 2.9. The first part of this figure (Figure 2.9a) contains curves obtained for four latexes prepared with different amounts of acrylic acid (samples LT20 to LT23, see Table 2.4). Latexes prepared with 1, 2, and 4 wt % (in the initial monomer composition) of AA required an increasing volume of titrating solution

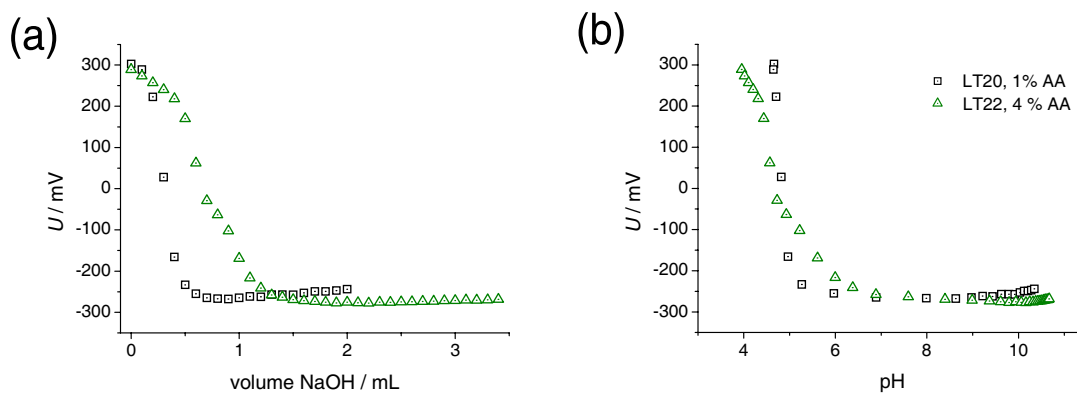


Figure 2.8. Titration of 150 μL of the latex samples LT20 and LT22 (cf. Table 2.4) with a 0.01 M NaOH solution: **(a)** Evolution of the streaming potential with added volume of NaOH. **(b)** Evolution of the potential with the pH in the titration cell.

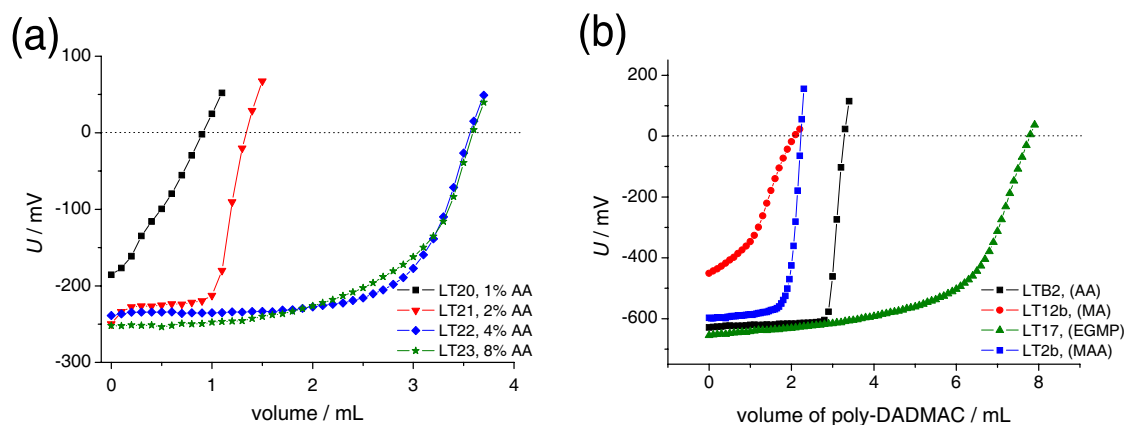


Figure 2.9. Titration of 150 μL of different latex samples (cf. Table 2.4) with a poly-DADMAC solution 0.001 N: **(a)** Comparison of samples LT20–23, prepared with different amounts of acrylic acid in the reaction mixture. **(b)** Comparison of samples LTB2, LT12b, LT17, and LT2b, prepared with 4 wt % of the comonomers AA, MA, EGMP, and MAA, respectively.

until the zero point. The latex prepared with the highest AA concentration of 8% (LT23) showed very similar titration curve as LT22, prepared with 4%, and consumed approximately the same amount of poly-DADMAC. This could indicate that there is a limit in the incorporation of AA in the latex, and the samples LT22 and LT23 have, therefore, a similar surface charge density, regardless of the preparation of the latter with a double amount of AA in the reaction mixture. But this could indicate as well a limitation in the technique used to determine the surface charge density with poly-DADMAC. It cannot

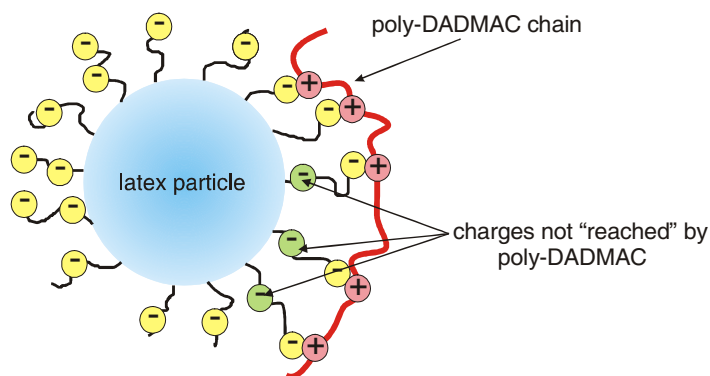


Figure 2.10 Interaction between a negatively charge latex particle and a poly-DADMAC chain. Some charged groups inside the corona may not be "reached" by the positively charged polyelectrolyte.

be excluded that poly-DADMAC chains complex the most exterior carboxyl groups, but do not reach those groups placed in a different depth inside the corona. This situation is sketched in Figure 2.10.

Figure 2.9b shows the titration curves for latexes synthesized with 4 wt % of different functional monomers: acrylic acid (AA), maleic acid (MA), ethylene glycol methacrylate phosphate (EGMP), and methacrylic acid (MAA). From this representation, it can be deduced that incorporation of MA is not as good as for other monomers, and the latex corona present a lower charge density, even if the number of carboxylic groups in the monomer is double. MAA is less oil-soluble than AA; thus, MAA will have a higher tendency to remain inside the hydrophobic latex core than AA. This can easily explain why the consumption of poly-DADMAC is lower in the former case than in the latter. The highest titrating agent consumption is shown by the latex synthesized with EGMP. In this case, it has to be taken into account not only the oxygens of the phosphate group that can be deprotonated, but also the several oxygen atoms of the monomer, which allow the delocalization of the negative charge through the monomer structure. The interaction of oligo- and poly-EGMP chains of the latex corona with poly-DADMAC chains may be complex, but a stoichiometry 1:1 was assumed for the sake of simplicity in further calculations, being aware that this ratio might not be accurate enough.

The surface charge density given in charge groups per unit area, σ_N , of latex particles can be expressed as

$$\sigma_N = \frac{N_{\text{ch}}}{A_t} \quad (2.14)$$

where N_{ch} represents the number of charged groups and A_t is the total surface area of the latex particles. The number of charge groups can be obtained by multiplying the mole number of charged groups (n , obtained from the titration results) by Avogadro's number:

$$N_{\text{ch}} = n \cdot N_A \quad (2.15)$$

The total mass of the titrated latex sample, m_t , is given by the equation

$$m_t = s \cdot V_{\text{emul}} \cdot \rho \quad (2.16)$$

in which s is the solid content of the latex emulsion, V_{emul} is the volume of sample, and ρ is the latex density, considered as approximately 1 g cm^{-3} . In a parallel manner, the mass of a particle, m_{part} , can be calculated assuming a spherical geometry with radius r for the latex particles:

$$m_{\text{part}} = \frac{4}{3} \pi r^3 \rho \quad (2.17)$$

Dividing the total mass by the mass of a particle, it is possible to obtain the total number of particles, N_{part} , allowing the calculation of the total area, A_t :

$$A_t = N_{\text{part}} 4\pi r^2 \quad (2.18)$$

Alternatively, the charge density can also be expressed in coulomb per unit area. In this case, we need to calculate first the specific charge in equivalents per unit mass, q , by applying the equation

$$q = \frac{V \cdot c}{w} \quad (2.19)$$

where V is the consumed volume of titrating polyelectrolyte (poly-DADMAC), c is the concentration of the poly-DADMAC solution in equivalents per unit volume, w is the solid part of the sample or its active substance in mass units. The surface charge density (in coulomb per unit area) is then calculated by

$$\sigma = \frac{q F m_t}{A_t} \quad (2.20)$$

where F is the Faraday constant ($F = 96\,485 \text{ C eq}^{-1}$), and m_t and A_t are given by eqs. (2.16) and (2.18).

Table 2.4 summarizes the characteristics of several latex samples (which will be further referred to in next chapters), including the particle size (discussed in

§2.5.1) and the surface charge density in charged groups per unit area and in coulombs per unit area, calculated using the eqs. (2.14)–(2.20). The charge densities go from 0, in the case of the nonfunctionalized latexes, to 1.9 charged groups·nm⁻² (6.8 mC cm⁻²). For samples prepared analogously with AA (LT20–LT23), MA (LT11–LT13), and EGMP (LT16–LT18), the influence of the initial content of comonomer in the surface charge was screened, and it can be roughly said that a higher hydrophilic monomer percentage leads to higher charge density. However, this is not completely systematic: samples LT22 and LT23 have the same charge density (cf. discussion of Figure 2.9a), and LT23b shows a lower value than LT11, although the quantity of comonomer was double.

Table 2.4. Characteristic data of latex samples obtained by miniemulsion copolymerization of styrene with various comonomers.

sample	formulation ^[a]			diameter [nm]	PDI	σ_N [nm ⁻²]	σ [mC cm ⁻²]
	comonomer	%	K ₂ S ₂ O ₈ ? ^[b]				
LT1b	–	0	no	63.4±0.4	0.172±0.06	0.0	0.0
LT25	–	0	no	58.9±0.9	0.06±0.02	0.0	0.0
LT7	AA	4	no	79.8±0.4	0.154±0.004	1.0	3.5
LT15	AA	4	no	72.0±0.2	0.07±0.01	1.4	5.2
LTB1	AA	4	no	78.7±0.5	0.06±0.01	1.3	5.0
LTB2	AA	4	no	71.4±0.4	0.068±0.009	1.0	3.8
LTB4	AA	4	no	71.4±0.6	0.056±0.003	1.2	3.9
LTB10	AA	4	no	74.0±0.9	0.07±0.02	1.0	3.8
LT20	AA	1	no	77.0±0.2	0.05±0.01	0.3	0.8
LT21	AA	2	no	70.5±0.5	0.09±0.02	0.4	1.1
LT22	AA	4	no	74.0±0.7	0.079±0.004	0.9	2.9
LT23	AA	8	no	74.3±0.2	0.068±0.013	0.9	2.9
LT2b	MAA	4	no	78.1±0.3	0.11±0.01	0.5	1.9
LT3	MAA	4	no	72.5±0.4	0.07±0.01	0.5	1.6
LTB8	MAA	4	no	71.3±0.9	0.06±0.01	0.6	2.1
02LH176	MA	4	yes	75.0±0.4	0.120±0.009	0.5	1.7
LT5	MA	4	yes	80.1±0.3	0.146±0.007	0.6	2.1
LT6	MA	4	no	69.8±0.4	0.09±0.02	0.5	1.8
LTB6	MA	4	no	72.3±0.7	0.04±0.02	0.4	1.4
LT9	MA	4	yes	72.4±0.2	0.11±0.01	0.6	2.3
LT11	MA	2	yes	69.5±0.2	0.08±0.01	0.8	2.9
LT12b	MA	4	yes	69.1±0.4	0.129±0.032	0.5	1.5
LT13	MA	8	yes	68.1±0.3	0.09±0.02	1.7	6.4
02LH178	EGMP	4	yes	86.1±0.2	0.215±0.006	0.6	1.7
LT8	EGMP	4	no	75.3±0.03	0.100±0.001	–	–
LTB5	EGMP	4	no	76.4±0.8	0.099±0.004	0.9	3.5
LT16	EGMP	2	yes	71.2±0.4	0.12±0.01	0.5	1.9
LT17	EGMP	4	yes	80.1±0.1	0.158±0.008	1.9	6.8
LT18	EGMP	8	yes	69.1±0.2	0.111±0.004	1.1	3.8
02LH248	MAN	4	no	97.0±0.5	0.15±0.01	–	–
LT4	MAN	4	no	72.9±0.3	0.088±0.008	–	–
02LH53	Aph	4	no	92.7±0.4	0.141±0.006	–	–
02LH179	VBTMAC	4	yes	80.1±0.9	0.09±0.02	–	–

[a] The samples were prepared with the proportion of the indicated comonomer and the rest of styrene until 100 wt %.

[b] Addition or not of potassium persulfate in an advanced state of the polymerization.

2.5.3 Measurement of zeta potential by microelectrophoresis

Electrophoretic mobilities were measured for representative latex miniemulsions by the so-called light scattering electrophoresis (also known as laser Doppler microelectrophoresis) with the same automatic device used for the particle size determination (Malvern Zetasizer 3000HS). The ζ -potential was calculated from the electrophoretic mobilities according to eq. (2.12), approximating to 1.5 the value of $f(\kappa r)$ (Hückel approximation).

Table 2.5. Electrophoretic mobility and ζ -potential of aqueous solutions (1 g L^{-1}) of representative latexes, prepared with 4 wt % of different comonomers (cf. Table 2.4.).

sample	functional comonomer	$\mu_E / \mu\text{m cm V}^{-1} \text{ s}^{-1}$	ζ -potential / mV
LT25	–	–0.537	–6.8
LT15	AA	–1.671	–21.3
LT3	MAA	–1.202	–15.2
LT5	MA	–1.364	–17.2
LT17	EGMP	–3.080	–39.3
LT4	MAN	–1.078	–13.7
02LH53	APh	+2.488	+31.7
02LH179	VBTMAC	+3.278	+41.8

The electrophoretic mobilities and the related ζ -potential values of a collection of latex samples with different surface chemistry are presented in Table 2.5. The measurements contained in this table were carried out for aqueous solutions of the original emulsions (1 g L^{-1} , considering the solid content of the latex), without any additional adjustment of the pH. These results are in agreement with the results of the previous sections, obtained by polyelectrolyte titration. Since the charge of the functional groups of the latex corona is dependent on the pH, the ζ -potential will be also a function of the pH. This dependence was studied for a series of different poly(styrene–acrylic acid) latexes (the same series whose titration curves are plotted in Figure 2.8) and the results are shown in Figure 2.11. The pH was set by adding aliquots of HCl and NaOH solutions. The further ions (Cl^- , Na^+) introduced by these solutions have the negative effect of influencing the ζ -potential, but this cannot be experimentally avoided. The graph shows how ζ decreases as the pH increases, in correlation with the deprotonation of the carboxylic groups on the latex surface. At higher pH, the ζ -potential increases again, after having reached a minimum. This is caused by the high concentration of Na^+ present in the medium, which affects the double layer surrounding the latex particles. The fact that ζ is not the potential at the surface, but also take into account the electric double layer explains why the value of ζ is

not zero for the latex with surface charge approximately zero (i.e., sample LT25, prepared only with styrene, without addition of any functional comonomer). Furthermore, it can be observed that in the pH range of 8 to 10, the higher the percentage of AA in the monomer composition is, the more negative the ζ -potential becomes. This indicates more carboxylic groups in the surface and a higher charge.

When Figure 2.11 is compared with the results of polyelectrolyte titration of the same samples (Figure 2.8), it is observed that the poly-DADMAC consumption between samples LT20 and LT23 (with 1 and 8 wt % of AA, respectively) is significantly different, but the values of the ζ -potential are, on the contrary, quite similar. The negative values of ζ give a qualitative idea of the negative charge on the latex corona, but the polyelectrolyte titration appears to be a more convenient technique for the surface charge density quantification of latex particles.

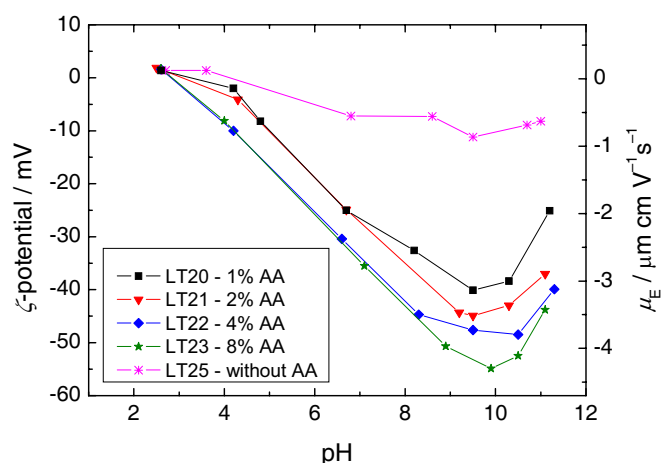


Figure 2.11. Dependence of the ζ -potential on the pH for poly(styrene-acrylic acid) latexes prepared with different acrylic acid content, from 0 to 8% (samples whose titration curves is shown in Figure 2.9a).

2.6 Conclusions

In this chapter, the preparation and the characterization of polystyrene latex particles modified at the surface with different hydrophilic functional groups have been presented. Latex samples with a lower polydispersity and an average diameter <100 nm have been synthesized by miniemulsion polymerization. This technique offers a convenient synthetic pathway and structures varying in chemical composition of the surface can be quickly obtained from simple monomers. The surface functionalization was achieved by including small amount (1 to 8 wt % of the total monomer) of the hydrophilic monomer with styrene in the initial mixture.

The latex particles are assumed to present a core–shell structure: a core of polystyrene is covered by a corona composed of hydrophilic functional groups (originating from the comonomers) and oligo(ethylene oxide) residues (from the surfactant used in the preparation of the miniemulsion).

The diameter of the particles was measured by dynamic light scattering at 90°, technique that allowed a rapid and efficient evaluation of the particle size. Polyelectrolyte titration by detection of the end point by streaming potential measurements provided a good method to determine the surface charge density of the latexes. The final charge (in the range 0–7 mC cm⁻²) was shown to depend on the miniemulsion formulation and the chemical nature of the hydrophilic monomers used in the synthesis.

2.7 Experimental section

Synthesis of latexes

Chemicals with the highest quality supplied by Aldrich were used, unless otherwise stated. The water was always Milli-Q. Latexes were prepared in a similar way to Landfester et al.,^[38,39] via miniemulsion polymerization with styrene (Fluka, puriss., ≥99.5%) and a small amount of a second functional comonomer, among those contained in Table 2.3: acrylic acid, maleic acid (Janssen Chimica, ≥99%), methacrylic acid, ethylene glycol methacrylate phosphate, methacrylonitrile, 2-allylphenol, and *ar*-vinyl benzyl trimethylammonium chloride.

Table 2.6 contains the synthesis parameters of the latex presented in this work. The monomers (styrene and the suitable amount of comonomer, 12 g in total) were mixed with hexadecane (500 mg) and AMBN (commercially known as V59, Wako Pure Chemical Industries; 240 mg). The aqueous phase was prepared dissolving Lutensol AT50 (BASF, 3.0 g) in water (48 g). The indicated quantities correspond to the most typical formulation used in the latex preparation, referred in Table 2.6 as formulation **1**. In some cases the quantities were half (formulation **2**) and in one case (sample LT3) they were multiplied by a factor of 5 to scale up the reaction (formulation **3**). The proportions of the ingredients were in all cases those indicated in Table 2.2. Both oil and aqueous phase were stirred separately for 30 min, and then mixed and stirred for an additional period of 45 min. The miniemulsion was achieved by ultrasonification (US) during the indicated times and intensities (Branson Digital Sonifier 250-D; pulse 1.0 s, pause 0.1 s), cooling down in an ice-water bath to avoid polymerization due to heating. The reaction took place at 72 °C under an argon atmosphere. In some cases,

potassium persulfate was added in an advanced state of the reaction to graft oligomeric hydrophilic free radicals onto the corona.

Typically, the resulting latexes were filtrated and purified by centrifugation in an Ultrafree-15 centrifugal filter device with a membrane Biomax 50 kDa (Millipore).

Table 2.6. Synthesis parameters and final solid content of the latex samples.

sample	formulation ^[a]	K ₂ S ₂ O ₈ mg(h) ^[b]	US min(%) ^[c]	reaction time [h]	solid content [%]
LT1b	2	–	7(80)	14	24.2
LT25	1	–	6(75)	7	23.9
LT7	1	–	7(80)	17	21.9
LT15	1	–	7(80)	15.5	23.8
LTB1	1	–	6(75)	6	23.6
LTB2	1	–	6(75)	6	23.4
LTB4	1	–	6(70)	6	22.1
LTB10	1	–	6(75)	14	22.4
LT20	1	–	6(75)	7	21.5
LT21	1	–	6(75)	7	23.0
LT22	1	–	6(75)	7	23.6
LT23	1	–	6(75)	7	22.0
LT2b	2	–	7(80)	14	23.1
LT3	3	–	7(80)	15	18.7
LTB8	1	–	6(70)	7	23.8
02LH176	2	10(8)	6(75)	9	21.8
LT5	1	10(5)	6(75)	14	23.1
LT6	1	–	6(75)	14	21.2
LTB6	1	–	6(70)	6	23.2
LT9	1	20(5)	6(75)	9	22.5
LT11	1	25(5)	6(75)	14	23.6
LT12b	1	25(5)	6(75)	8	21.0
LT13	1	25(5)	6(75)	14	24.3
02LH178	2	10(8)	6(75)	10	18.5
LT8	1	–	6(75)	17	23.4
LTB5	1	–	6(70)	6	25.6
LT16	1	30(5)	6(75)	18	23.1
LT17	1	30(5)	6(75)	18	22.8
LT18	1	30(5)	6(75)	18	21.6
02LH248	2	–	6(75)	10	19.8
LT4	1	–	7(80)	15	22.1
02LH53	2	–	7(70)	10	10.6
02LH179	2	25(7)	6(75)	10	23.3

[a] All formulations follow the proportions of Table 2.2. The different between the different formulations is the total weight of the ingredients: 12 g of monomers (styrene and comonomer together) in the formulation 1, 6 g in 2, and 60 g in 3; the rest of the ingredients are in proportion with the quantity of monomer.

[b] Quantity of K₂S₂O₈ added, according to the nomenclature “weight(*time*)”, where the weight is expressed in milligrams and *time* is the moment of the reaction in hours when this initiator was added.

[c] Ultrasonication time and intensity, according to the nomenclature “time(*intensity*)”, being the time in minutes and the intensity in percentage.

Characterization of latex particles

Particle sizes and electrophoretic mobilities were measured for diluted solutions (ca. 1% of emulsion in water) with a Malvern Zetasizer 3000HS, previously filtrated with a 0.8- μm membrane syringe filter. DLS measurements shown in Figure 2.5 were carried out in a setup equipped with a correlator ALV 5000, a goniometer ALV-SP81, and a krypton-ion laser (647.1 nm, Spectra Physics, Model Kr 2025).

Solid contents (contained in Table 2.6) were determined by gravimetry drying a portion of emulsion (~ 0.8 g) at 40 °C under vacuum during at least 12 h. SEM micrographs were taken with a field-emission microscope LEO EM1530 Gemini, after preparing a coating of the emulsion on a silicon wafer. Particle size histograms and distributions (as shown in Figure 2.6) were obtained statistically by measuring the radii of not less than 250 particles with help of the software ImageJ (National Institute of Health, USA).

The surface charge density of the latex particles was estimated by polyelectrolyte titration using an automatic titration unit (Metrohm 702 SM Titrino) combined with a particle charge detector (Mütek PCD 03-pH). A pertinent quantity of latex (100–200 μL) dissolved in water was titrated with a $\sim 0.001\text{-N}$ solution of poly-DADMAC (Mütek Analytic, molecular weight distribution in the range 40 000–100 000 g mol^{-1}), after adjusting the pH to ~ 9.5 with a suitable solution of NaOH. The exact concentration of the poly-DADMAC solution was determined by titrating with a 0.001-N solution of the anionic standard sodium polyethensulphonate (Mütek Analytic, 19 100 g mol^{-1}).

Chapter 3

Latex-controlled precipitation of zinc oxide

3.1 Introduction

Shape, morphology, and particle size distribution are key aspects in many industrial applications. For instance, solubility and dispersability of crystals, essential aspects in pigment and cosmetic industry, as well as in biomedicine, depend on the size and on the groups present on the particle surface. Physical properties, such as magnetic properties, photoabsorption or emission, important in electronics or advanced ceramics, may depend on the morphology, the crystal defects, and the particle size. Also in catalysis, the morphology and the size play a decisive role, since they determine the total surface available. Therefore, the understanding of the control parameters of precipitation and crystallization processes has turned into a hot topic in materials science.

Much research has been devoted to the precipitation of ZnO from aqueous media, investigating the changes in morphologies and properties, and trying to understand the controlling parameters. The effect of the synthetic pathway,^[148–151] the reaction parameters (temperature, pH, reaction time, concentration),^[152,153] and the influence of different solvents^[154,155] have been broadly screened. The use of different organic additives to control the morphology of the resulting crystals has been also reported.^[156,157]

As indicated in Chapter 1, following biomimetic strategies, polymers have been used as controlling agents in the crystallization of zinc oxide. The presence of double-hydrophilic block and graft copolymers has been shown to affect the morphology of ZnO crystals obtained from aqueous media.^[8] Öner et al.^[158] studied the effect of a diblock copolymer of ethylene oxide (EO) and methacrylic acid (MAA) with formula $(EO)_{68-b}-(MAA)_8$ on the morphology of precipitated ZnO crystals, comparing the influence of the copolymers with the influence of poly(ethylene oxide) (PEO) and poly(methacrylic acid) (PMAA) homopolymers. In comparison with samples prepared without additive, PEO homopolymers were shown to present no effect when used as crystallization additives, while PMAA showed a strong influence. The observations for the P(EO-*b*-MAA) copolymers were explained as a combination of the principal effect of the PMAA block (“anchor block”), which adsorbs on the ZnO growing faces, and the secondary

effect of the PEO block (“solution block”), which merely takes care of the solubility and prevents the crystal aggregation. Öner et al. proposed a preferential adsorption of the anchor block on the {001} ZnO faces that would block the active growing sites and retard the growth in this face. The action of this block copolymer was further investigated by Taubert et al.,^[38,68–71] who studied the effect of the block length and investigated also block copolymers of EO with styrene sulfonic acid (SSH). Chemical structure of the polymers used by Taubert et al., including the one used by Öner et al., are presented in Figure 3.1, together with the indication of their synthetic pathway. Taubert et al. found that the morphology, size, and mean-size distribution of the ZnO crystals are affected by the chemical nature of the anchor block, the molecular weight of the polymer, and the ratio of the solution block and the anchor block lengths.

Baum^[55] investigated the effect of double-hydrophilic graft copolymers (or comb polymers) composed of a PMAA or poly(vinyl sulfonate) (PVS) backbone and PEO side chains. Copolymers with vinyl-sulfonate groups were shown to be much more active in the control of crystal growth than copolymers containing MAA at the same mole fraction.

Carboxyl-modified latex particles have also been applied to the crystallization of zinc oxide. An initial reason for using such particles was to investigate whether the polymer was incorporated into the ZnO crystal structure or simply adsorbed onto the surface. Early results^[8] demonstrated the incorporation into the crystals, but also showed that latex particles prepared by miniemulsion polymerization could provide an interesting approach to control the crystal growth. In her doctoral thesis, Qi^[9] analyzed the effect of poly(styrene–acrylic acid) [P(S–AA)] latex particles varying in size and surface charge density. She assumed an adsorption of the latex particles to the faces {001} zincite according to a Langmuir isotherm and proposed a quantitative relation linking the aspect ratio

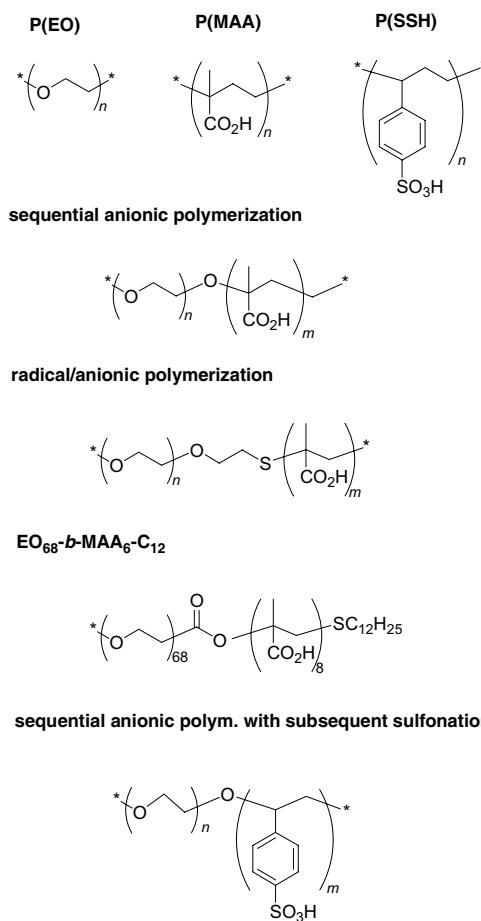


Figure 3.1. Polymers (with indication of the polymerization method) used by Taubert et al. as additives in the control of the ZnO precipitation. (Reproduced with permission from Ref. [69]. Copyright 2002. American Chemical Society.)

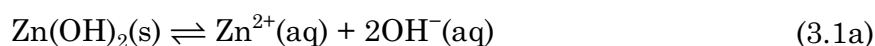
to the latex concentration at constant diameter and surface chemistry. Furthermore, Qi modeled the dependence of the aspect ratio on the charge density of the latex by an algorithm in which attractive forces between the latex particle and the ZnO surface are balanced against repulsive forces of osmotic nature. Also using miniemulsion latex as crystallization additives, Palms^[10] reported a peculiar effect produced by P(S-AA) latexes encapsulating magnetite (Fe₂O₃) inside the particles.

In this chapter, the previous investigations on P(S-AA) latexes are complemented and extended to latex particles with the different surface functionalities presented in Chapter 2. The surface chemistry of the latexes is shown to strongly affect the final morphology of the precipitated zinc oxide.

3.2 Fundamentals of the precipitation of zinc oxide

3.2.1 Solubility and precipitation

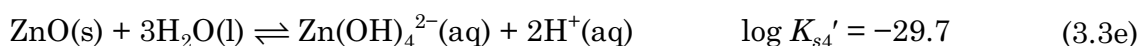
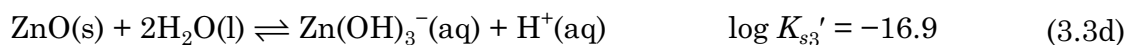
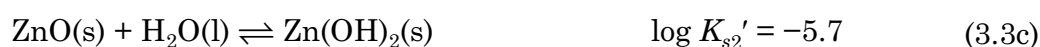
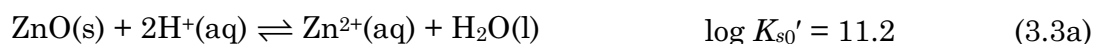
Zinc oxide is a very water-insoluble metal oxide that can be easily precipitated as a crystalline material from an aqueous solution. Several solid phases are possible in the system Zn²⁺-H₂O: amorphous Zn(OH)₂; α-, β₁-, β₂-, γ-, δ-, and ε-Zn(OH)₂; and ZnO.^[159] The precipitation of zinc oxide competes with the precipitation of the zinc hydroxide polymorphs, and the Zn²⁺ ions are in equilibrium with the OH⁻ ions according to



Considering the approximation that the ionic activity of the species is equal to the concentration, the solubility product, K_{s0} , is given by

$$K_{s0} = \{\text{Zn}^{2+}\}\{\text{OH}^{-}\} \cong [\text{Zn}^{2+}][\text{OH}^{-}] \quad (3.2)$$

Often the solubility of metal oxides is expressed taking into account the reaction with protons, and then the solubility equilibria of ZnO in aqueous media can be expressed as^[16]



The solubility constants governing these equilibria, expressed as K'_{si} , are related with the conventional solubility constants [e.g., the given by eq. (3.2)], K_{si} , by the equation

$$K'_{si} = \frac{K_{si}}{K_w} \quad (3.4)$$

in which K_w is the ion product of water. The reactions (3.3) show the amphoteric character of ZnO, that is, it can take or deliver protons, forming different species whose concentrations are given by

$$[\text{Zn}^{2+}] = K'_{s0} [\text{H}^+]^2 \quad (3.5a)$$

$$[\text{ZnOH}^+] = K'_{s1} [\text{H}^+] \quad (3.5b)$$

$$[\text{Zn(OH)}_2] = K'_{s2} \quad (3.5c)$$

$$[\text{Zn(OH)}_3^-] = K'_{s2} [\text{H}^+]^{-1} \quad (3.5d)$$

$$[\text{Zn(OH)}_4^{2-}] = K'_{s4} [\text{H}^+]^{-2} \quad (3.5e)$$

The representation of the logarithm of the concentrations

$$\log[\text{Zn}^{2+}] = \log K'_{s0} - 2\text{pH} \quad (3.6a)$$

$$\log[\text{ZnOH}^+] = \log K'_{s1} - \text{pH} \quad (3.6b)$$

$$\log[\text{Zn(OH)}_2] = \log K'_{s2} \quad (3.6c)$$

$$\log[\text{Zn(OH)}_3^-] = \log K'_{s2} + \text{pH} \quad (3.6d)$$

$$\log[\text{Zn(OH)}_4^{2-}] = \log K'_{s4} + 2\text{pH} \quad (3.6e)$$

versus the pH gives the species diagram, shown in Figure 3.2.

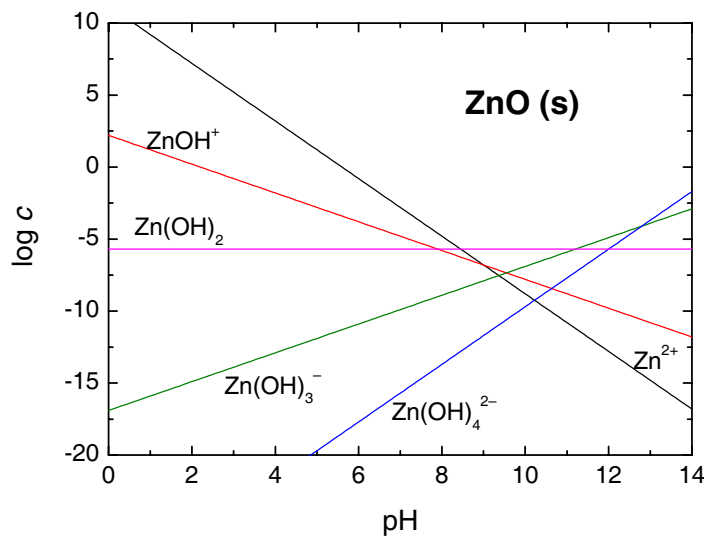
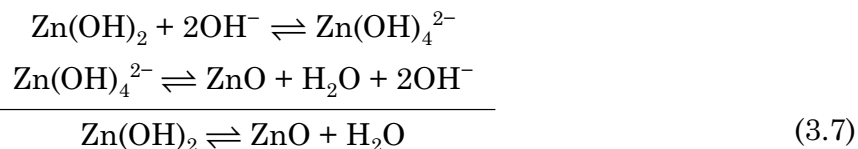


Figure 3.2. Species diagram for the ZnO–H₂O system, calculated according to the eqs. (3.6).

In basic media, Zn(OH)_4^{2-} (and perhaps $\text{Zn}_2(\text{OH})_6^{2-}$) are formed,^[160] and the transition between zinc hydroxide and zinc oxide can be written as a sum of the following equilibria:



Zinc oxide is more stable than the different possible zinc hydroxides, of which the $\varepsilon\text{-Zn(OH)}_2$ is the most insoluble and the most stable. Table 3.1, which contains the solubility products of ZnO and the Zn(OH)_2 polymorphs, shows that ZnO is the most insoluble solid species of the $\text{Zn}^{2+}\text{-H}_2\text{O}$ system.

Table 3.1. Solubility products of zinc oxide and zinc hydroxide polymorphs at 25 °C.

solid phase	log K_{s0}	
	Schindler et al. ^[161] (experimental, $I = 0.2^{\text{[a]}}$)	Baes & Mesmer ^[160] (calculated, $I = 0.0^{\text{[a]}}$)
amorphous Zn(OH)_2	12.70	12.45
$\beta_1\text{-Zn(OH)}_2$	11.98	11.73
$\beta_2\text{-Zn(OH)}_2$	12.02	11.77
$\gamma\text{-Zn(OH)}_2$	11.96	11.71
$\delta\text{-Zn(OH)}_2$	12.07	11.82
$\varepsilon\text{-Zn(OH)}_2$	11.75	11.50
ZnO (active, precipitated)	11.56	11.31
ZnO (inactive, ignited)	11.39	11.14

[a] I represents the dimensionless ionic strength of the solution.

3.2.2 Thermodynamical aspects

In §1.3 it was shown that the spontaneous dissolution of a crystal depends on the temperature and on the saturation level [see eq. (1.4)]. In addition, the solubility of crystals is also affected by the particle size: small particles have higher solubility than larger crystals. Small crystals are thermodynamically less stable and recrystallize to larger ones. For particles $<1 \mu\text{m}$ or with a specific area greater than a few square meters per gram, the surface energy becomes large and the surface properties are influenced. For particles at constant temperature and pressure with a total molar surface S , the Gibbs free energy related with an infinitesimal surface change, ds , can be written as^[162]

$$dG = \mu_0 dn + \bar{\gamma} ds \quad (3.8)$$

where μ_0 is the chemical potential of the bulk material, n is the number of moles, and $\bar{\gamma}$ is the mean solid–liquid interfacial tension. Dividing this expression by dn , we have the expression of the overall chemical potential of the crystal, μ :

$$\frac{dG}{dn} = \mu = \mu_0 + \bar{\gamma} \frac{ds}{dn} \quad (3.9)$$

If v , ρ , and M are volume, density, and molar mass of the crystalline material, respectively, eq. (3.9) can be rewritten as

$$\mu = \mu_0 + \frac{M}{\rho} \bar{\gamma} \frac{ds}{dv} \quad (3.10)$$

The volume (v) and the surface (s) of a crystal are given by the equations

$$v = lx^3 \text{ and } s = kx^2 \quad (3.11)$$

where x is the characteristic dimension of the crystal and k and l are geometric constants dependent on the shape and not on the size of the crystal. Differentiating eqs. (3.11) with respect to x , we obtain

$$\frac{dv}{dx} = 3lx^2 \text{ and } \frac{ds}{dx} = 2kx \quad (3.12)$$

The division of these expressions gives

$$\frac{ds}{dv} = \frac{2}{3} \frac{kx}{lx^2} \left(\frac{x}{x} \right) = \frac{2s}{3v} \quad (3.13)$$

Substituting (3.13) in (3.10)

$$\mu = \mu_0 + \frac{M\bar{\gamma}}{\rho} \frac{2s}{3v} \quad (3.14)$$

and taking into account that the molar surface is $S = Ns$ and the molar volume is $V = Nv = M/\rho$ (where N is the number of particles per mol and s is the surface of a single particle), the overall chemical potential is given by

$$\mu = \mu_0 + \frac{2}{3} \bar{\gamma} S \quad (3.15)$$

For the considered substance, the chemical potential in solution μ' is given by

$$\mu' = \mu'_0 + RT \ln Q \quad (3.16)$$

where μ'_0 is the standard chemical potential and Q is the reaction quotient. In equilibrium, eqs. (3.15) and (3.16) can be equated and, in addition, Q corresponds to the equilibrium constant. Thus,

$$\mu_0 + \frac{2}{3} \bar{\gamma} S = \mu'_0 + RT \ln K_{s_0} \quad (3.17)$$

If S tends to zero (i.e., the characteristic crystal dimension, x , tends to infinity), the second term on the left can be neglected and therefore

$$\mu_0 = \mu'_0 + RT \ln K_{s_0} \quad (3.18)$$

From eqs. (3.17) and (3.18) we obtain

$$(\log K_{s0})_S = (\log K_{s0})_{S=0} + \frac{2}{3} \cdot \frac{\bar{\gamma} S}{2.303RT} \quad (3.19)$$

Finally, the Gibbs free energy involved in the subdivision of a coarse solid in solution in fine particles of molar surface S may be written as

$$\Delta G = 2.303RT[(\log K_{s0})_S - (\log K_{s0})_{S=0}] = \frac{2}{3} \bar{\gamma} S \quad (3.20)$$

Eq. (3.19) was used by Schindler et al.^[159] to explain the stability of the zinc hydroxide polymorphs. They found that the critical size of the critical ZnO nuclei in saturated solutions of the different hydroxides follows the order



which is the same order of the solubility given in Table 3.1. If the ZnO nucleus is smaller, the solubility is higher and the equilibrium of conversion of the metastable Zn(OH)_2 into ZnO, $\text{Zn(OH)}_2 + \text{H}_2\text{O} \rightleftharpoons \text{ZnO}$, is more displaced to the right, that is, the corresponding zinc hydroxide is less stable.

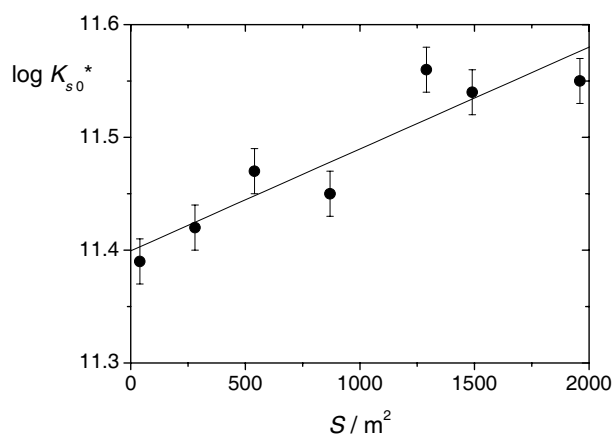
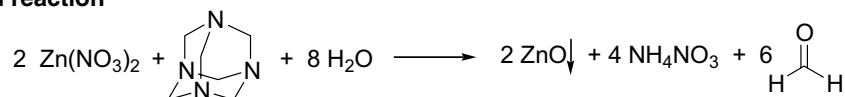
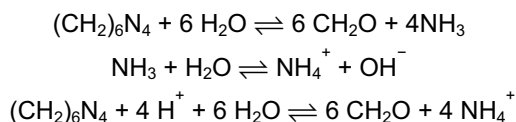


Figure 3.3. Dependence of the solubility of ZnO on the molar surface, which is inverse proportional to the particle size. (Replotted with data from Schindler et al.^[159])

3.3 Precipitation of ZnO in the absence of additives

In the present work, zinc oxide has been precipitated from an aqueous solution of zinc nitrate by adjusting the pH via the thermal decomposition of hexamethylenetetramine (HMTA, urotropine) to give ammonia and formaldehyde at the reaction temperature of 95 °C. The general reaction and the decomposition reactions of HMTA are presented in Scheme 3.1.

General reaction**Decomposition of HMTA and related reactions**

Scheme 3.1. Precipitation reaction of ZnO via thermal decomposition of HMTA and related reactions.

In a conventional precipitation in the absence of any additive (*reference sample*), long hexagonal prismatic crystals are formed. This morphology, reproduced in Figure 3.4, implies that different crystal faces grow with different velocities. It can be deduced that the basal face (001) is a rapid growing face and the lateral faces $\{hk0\}$ are slow growing, and because of that, the result is a needlelike crystal. The micrograph shows a high probability of occurrence of starlike growth features that are the result of nucleation of several individual crystals from the same nucleation center. Small needlelike crystals resulting from secondary nucleation processes are observed. The formation of twins occurs in almost all cases; this may be a consequence of the instability of one of the polar faces of the zincite structure. A representation of this twin formation is sketched in Figure 3.4b.

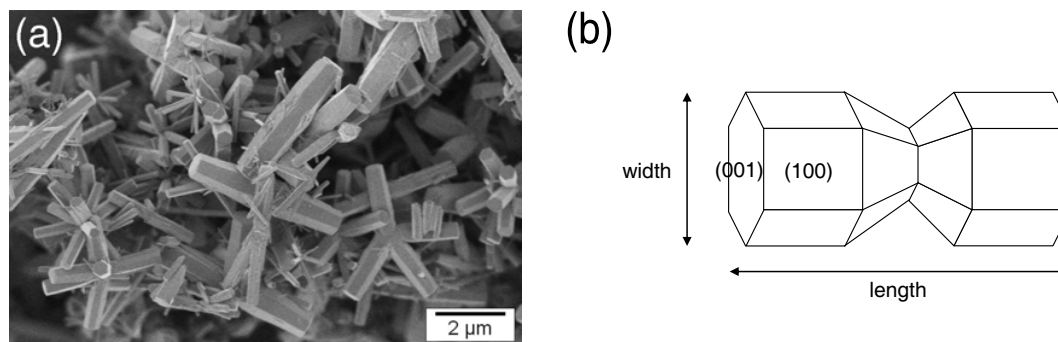


Figure 3.4. (a) Typical sample of ZnO precipitated in the absence of any additive. (b) Representation of twin formation in precipitated zincite.

Typically, zinc oxide is the only reaction product, as deduced from the X-ray diffraction patterns (see Chapter 4), but under certain circumstances, hydroxide species, which have a lamellar structure, can be present. For instance, lower temperatures can lead to the formation of hydroxides. Figure 3.5 shows the products obtained in an experiment in which, due to experimental problems, the temperature was not constant and lower than 90 °C. Lamellar structures are observed, together with the ZnO crystals. It can be assumed that under these

conditions the decomposition of the HMTA was not completed and the reaction did not develop properly. Therefore, hydroxide species, which are metastable and would convert in ZnO in an optimal reaction, can be found in the final product.

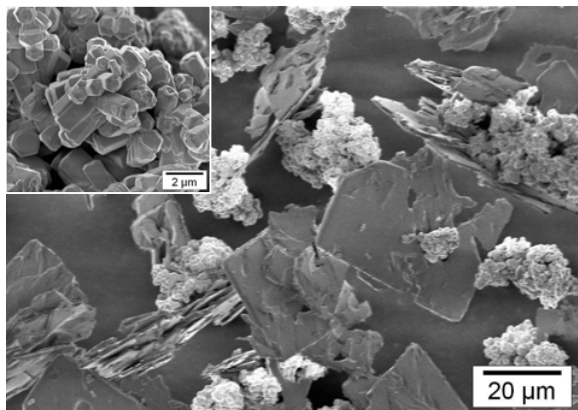


Figure 3.5. SEM micrograph of a sample showing a mixture of zinc oxide and hydroxide species. ZnO shows the typical hexagonal morphology, while hydroxide species show laminar structure. (XRD pattern of this sample is shown in Figure 4.5.)

3.4 Latex particles as morphology controlling agents

3.4.1 Effect of the chemical nature of the functionalizing groups

In a first step, the effect of the chemical nature of the latexes was screened by precipitating the ZnO in a medium containing 1 g L^{-1} of latex (content of solid latex in the total volume, calculated considering the solid content of the miniemulsion), which represents a particle density of ca. $2 \times 10^{13} \text{ cm}^{-3}$ (considering an average radius of 35 nm and approximating the density of the solid latex to 1 g cm^{-3}). In general, the latex particles become incorporated into the growing crystal, being embedded in the structure and giving ZnO–latex hybrid materials. If desired, the latex can be removed by dissolving with suitable organic solvents or, more effectively, by calcination.

The resulting morphology of the crystals was investigated by scanning electron microscopy (SEM). SEM micrographs of the various experiments are compared in Figure 3.6. A brief description of the main observations of the screening experiments follows:

- a) Upon addition of a pure *polystyrene* (PS) latex, without addition of functional groups to its surface, the crystals show essentially the same morphology as the reference sample, composed of hexagonal prismatic crystals of widely differing length-to-cross-section ratio. A few of the latex particles remain adsorbed on the surface.
- b) With *poly(styrene–acrylic acid)* [P(S–AA)] latex, crystals with lower polydispersity in the dimensions are obtained. The crystals are densely covered by

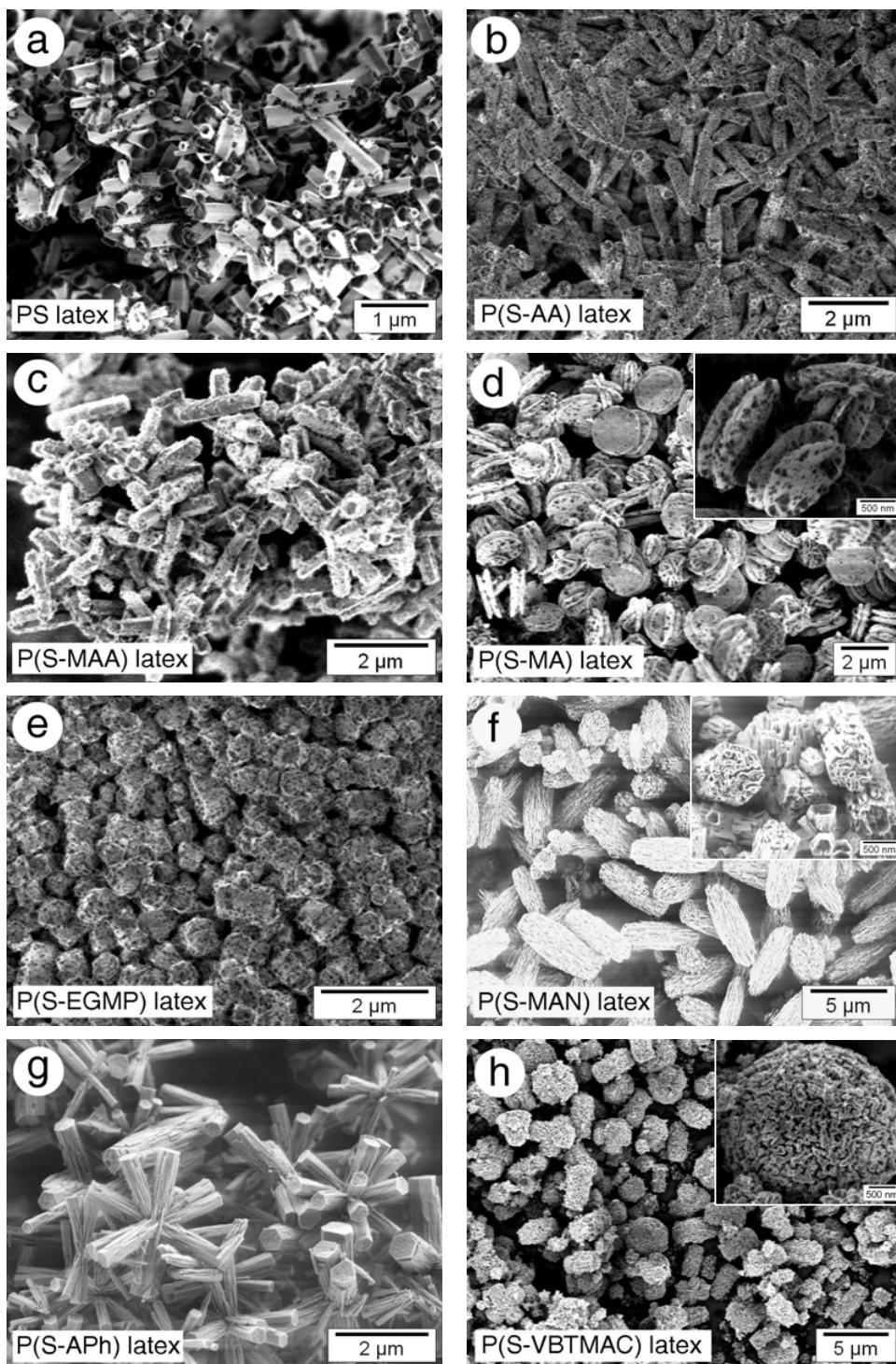


Figure 3.6. SEM micrographs of ZnO samples crystallized in the presence of 1 g L^{-1} of latexes with different surface functionalization, as indicated in the captions. The samples shown in (f) and (h) were calcinated at $600 \text{ }^\circ\text{C}$ to remove the polymer.

latex particles that could not be removed by simple washing, as was the case for the PS latex. This indicates a strong interaction between the surface groups of the latex particles and the zinc oxide.

- c) A very similar morphology to the obtained in the presence of the P(S-AA) latex is obtained in the presence of a *poly(styrene-methacrylic acid)* [P(S-MAA)] latex. However, the incorporation of the polymer to the crystal appears to be lower than in the MAA-derived latex than in the P(S-AA) latex.
- d) The addition of *poly(styrene-maleic acid)* [P(S-MA)] latex, with two carboxylic groups in the functional monomer, leads to crystals with a completely different morphology. The crystals show a platelike shape and no clear borders are formed; the hexagonal structure essentially disappears. However, the twinning and the starlike growth of the crystals from a common nucleation center are present as in previous samples. A relatively high number of latex particles remain in the crystals after washing.
- e) With *poly(styrene-ethylene glycol methacrylate phosphate)* [P(S-EGMP)] latex, the obtained prismatic crystals were shorter and wider, with a more isometric morphology, that is, with similar length and width. The interaction of the latex particles with ZnO appears to be strong, as in the case of the P(S-AA) latex, and the crystals are densely covered with the polymeric nanoparticles.
- f) Very large amounts of aggregated *poly(styrene-methacrylonitrile)* [P(S-MAN)] latex were observed upon using this additive, and the analysis of the crystal morphology was only possible after calcinating the polymer. Figure 3.6f shows peculiar “canal structures” observed in the resulting crystals after pyrolysis at 600 °C (10 °C min⁻¹, from room temperature to 600 °C).
- g) In the presence of the *poly(styrene-2-allylphenol)* [P(S-APh)] latex, starlike hexagonal crystals are again obtained, and no residual polymer is observed. This indicates that the latex does not adsorb onto the crystals and it is completely removed during the centrifugation and washing processes.
- h) As in the case of the P(S-MAN) latex, the analysis of the morphology of the crystals obtained in the presence of the positively charged latex based on *vinylbenzyl trimethylammonium chloride* [P(S-VBTMAC)] was only possible after removal of the latex by calcination. Very porous crystals, with similar canal structures, are shown in Figure 3.6h.

In the case of the latexes used in the samples shown in images (d), (e), and (h) of Figure 3.6, small amounts of potassium persulfate (KPS) was added in advanced states of the polymerization reaction to improve the grafting of hydrophilic oligomers onto the latex corona (see discussion about initiators in

p. 33). The improvement of the latex efficiency when adding KPS was studied by the following example: ZnO was similarly precipitated in the presence of a P(S-AA) latex prepared with KPS and in the presence of a completely analogous latex prepared in the absence of KPS. The product obtained in the former case has been shown in Figure 3.6d, and the one obtained in the latter case is shown in Figure 3.7. Note the inhomogeneity in shape and size of the sample obtained in



Figure 3.7. ZnO precipitated in the presence of 1 g L^{-1} of the latex LT6 (cf. Table 2.4), which was prepared without addition of $\text{K}_2\text{S}_2\text{O}_8$ in advanced states of the polymerization.

the presence of the non-KPS latex. The KPS residues can also be present in the corona of the latex and may have an influence on the ZnO crystallization. Although it is difficult to separate such an effect from the effect derived from the improving on grafting of the hydrophilic oligomer onto the surface, it can be concluded that the addition of KPS improves clearly the efficiency of the latexes.

3.4.2 Effect of the surface charge density

A systematic study of the effect of the surface charge density of poly(styrene-acrylic acid) latexes on the ZnO crystallization was carried out by Qi,^[9] who suggested a quantitative relationship linking the number of carboxylic groups per area with the aspect ratio of the resulting crystals. The aim of this section is not to provide such a quantitative analysis, but a qualitative screening of the effect of the initial amount of hydrophilic comonomer in the miniemulsion formulation, which—together with the synthesis parameters—determines the amount of incorporated comonomer units onto the latex corona and, therefore, the final surface charge density, as it was reported in Chapter 2. The results presented here helped to optimize the miniemulsion for our application in polymer-controlled crystallization.

In Figures 2.10 and 2.12 (Chapter 2), latex samples prepared with 1, 2, 4, and 8 wt % of acrylic acid (AA) in the initial monomer composition were compared. The surface charge densities determined by polyelectrolyte titration with poly-DADMAC were found to be 0.8, 1.1, 2.9, and 2.9 mC cm^{-2} , respectively (cf. samples LT20 to LT23 in Table 2.4). The titration gave similar results for the samples prepared with 4 and 8%, but the ζ -potential differed slightly at $\text{pH} > 8$ for the two latex preparations. Precipitation of ZnO in the presence of 1 g L^{-1} of

each of these samples was carried out and the SEM images of the obtained products are shown in Figure 3.8. The latexes with 1 and 2% of AA contain less carboxyl groups on the corona and the electrosteric stabilization of the miniemulsion is less important. Thus, the particles can aggregate and the latex preparation destabilizes. These latexes do not appear to be efficient in the control of the morphology and homogeneity of the ZnO crystals. The samples are polydisperse and large amounts of latex forming aggregates are observed. This is especially remarkable in the sample crystallized in the presence of the 1%-AA latex. The ZnO samples obtained with the 4%- and 8%-AA latexes are similar, as it could be expected from the similar surface charge density. The 4%-AA sample seems to be optimal in terms of monodispersity and absence of polymer aggregates.

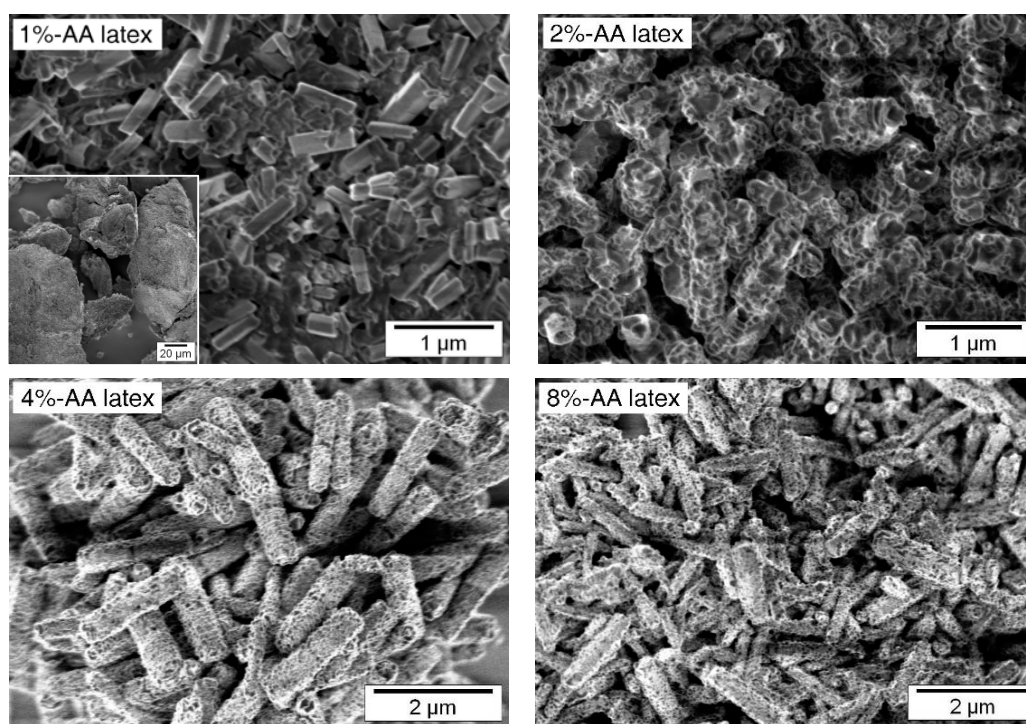


Figure 3.8. SEM images of the products crystallized in the presence of the latexes LT20–LT23 (cf. Table 2.4), whose formulation contained different amounts of acrylic acid.

The influence of the content of hydrophilic comonomer in the miniemulsion formulation was also studied for latexes synthesized with maleic acid (MA) and ethylene glycol methacrylate phosphate, and the results showed also an optimum value of 4% of functional comonomer. Lower contents gave poorly stabilized latexes with lower surface charge densities, which were not efficient as crystallization additives; higher contents did not lead necessarily to an improved control, but sometimes to worse results. As an example, Figure 3.9 compares two ZnO

samples obtained in the presence of 1 g L^{-1} of latexes prepared with 2 and 8% of MA (a sample crystallized in the presence of a 4%-MA latex has been shown in Figure 3.6d). The 8%-MA latex has a strong effect and laminar structures similar to those obtained with high concentration of latex—as it will be described in §3.4.5—are observed. However, the morphology is poorly defined and the polydispersity is high.

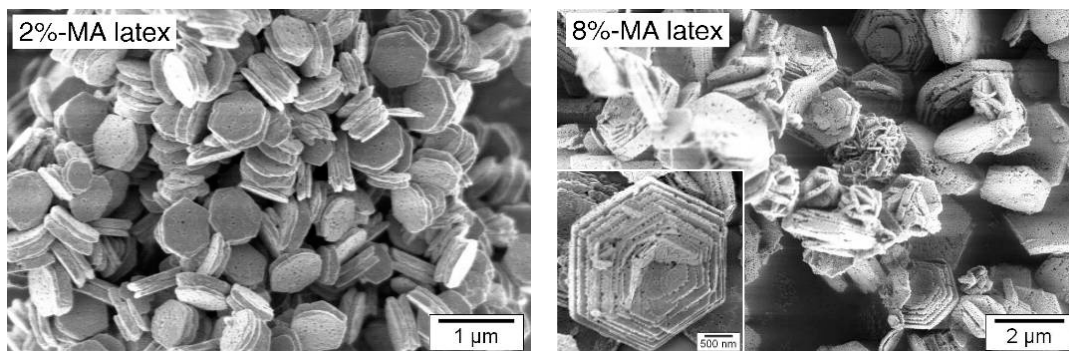


Figure 3.9. SEM images of the products crystallized in the presence of the latexes LT11 and LT13 (cf. Table 2.4), whose formulation contained 2 and 8% of maleic acid, respectively. The latex has been eliminated by calcination at $600 \text{ }^{\circ}\text{C}$.

3.4.3 Effect of the pH

Since the deprotonation of the functional groups attached to the latex surface depends on the pH of the medium, the effect of the latexes on the ZnO crystallization may also depend on the pH during the reaction. This was studied for the case of a P(S-AA) latex, which contains carboxylic groups on the corona. In a first step, the pH was measured at the beginning and at the end of the precipitation reaction for a series of samples prepared with an increasing concentration of the AA-derived latex. The variation of the measured values is presented in Figure 3.10. Before the start of the reaction (i.e., before the addition of HMTA), the pH had an initial value of 5.2 in the absence of additive, and it decreases as the latex concentration increases. However, independently of the initial pH, the buffer effect produced by HMTA leads to a constant final pH

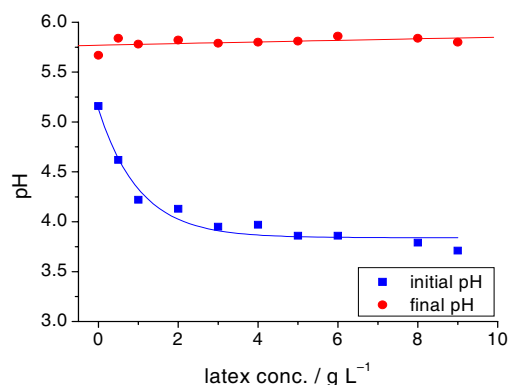


Figure 3.10. Initial and final pH in the crystallization reactor (i.e., at times 0 and 90 min) for a series of ZnO samples crystallized in the presence of different concentrations of the P(S-AA) latex LTB2 (cf. Table 2.4). The continuous lines show an exponential and a linear fitting for the initial and the final pH, respectively.

around 5.8, that is, around 1.5 units over the pH in the presence of 1 g L^{-1} of the latex (of ca. 4.2, as it can be read in Figure 3.10). This pH is achieved short time after the addition of HMTA and it is kept nearly constant until the end of the reaction.

Further experiments were carried out to check the influence of a variation in the pH at the start point. From titration analysis, it was determined that the charge of the corona is maximum for a pH value of ~ 6 – 7 (see Figure 2.8 and respective discussions in §2.5.2). An optimum deprotonation of the carboxylic groups of the particles could be achieved by increasing the initial pH by addition of a base (e.g., NaOH). However, if the pH is too high, the precipitation of ZnO begins before the addition of HMTA. In the sample shown in Figure 3.11a, crystallized in the presence of 1 g L^{-1} of a P(S-AA) latex, the initial pH was adjusted with a NaOH solution to a value of 5.7. The pH was approximately the same after the addition of the HMTA and remained nearly constant during the whole reaction. In the SEM micrograph it can be observed that the final morphology is relatively similar to the obtained without any additional adjustment of the pH. This indicates that, since the medium will be buffered due to the HMTA at $\text{pH} \approx 6$, the adjustment of the initial pH at ~ 6 does not bring any considerable effect.

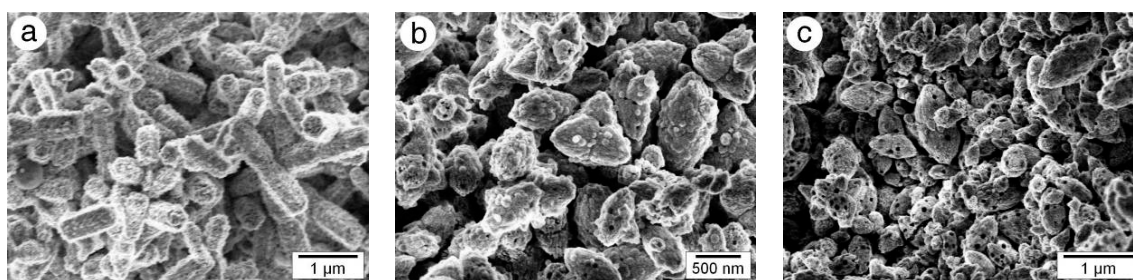


Figure 3.11. SEM micrographs of ZnO samples crystallized in the presence of 1 g L^{-1} of the P(S-AA) latex LTB1 (cf. Table 2.4), after adjusting the initial pH with a NaOH solution: **(a)** final product ($t = 90 \text{ min}$) after adjusting the initial pH to 5.8; **(b)** initial precipitate after adjusting the pH to 8, before the addition of HMTA (i.e., $t = 0 \text{ min}$); **(c)** final product ($t = 90 \text{ min}$) after adjusting the initial pH to 8.

Another ZnO sample was prepared by adjusting the initial pH to a higher value (8.0). In this case, rapid precipitation was observed after the addition of NaOH. Figure 3.11b shows the morphology of the precipitated powder, presumably ZnO. The final morphology, after addition of HMTA and a reaction time of 90 min, does not vary considerably from the initial, as shown in Figure 3.11c.

In conclusion, although an increase of the initial pH would optimize the surface charge of the latex particle, this leads to a rapid undesired precipitation of the ZnO and the controlling effect of the HMTA is cancelled. Therefore, no further pH control than that intrinsically provided by the reaction system was performed in the experiments of this work.

3.4.4 Effect of the latex ingredients

Monomers, oligomers, and small polymer chains can be present in the latex emulsions after a poor purification and they could have an influence in the final morphology of the ZnO crystals. In order to check the influence of the latex ingredients, separately from the emulsion, different precipitations were carried out in the presence of 1 g L^{-1} of acrylic acid (AA), maleic acid (MA), ethylene glycol methacrylate phosphate (EGMP), Lutensol AT50, and poly(acrylic acid) (PAA).

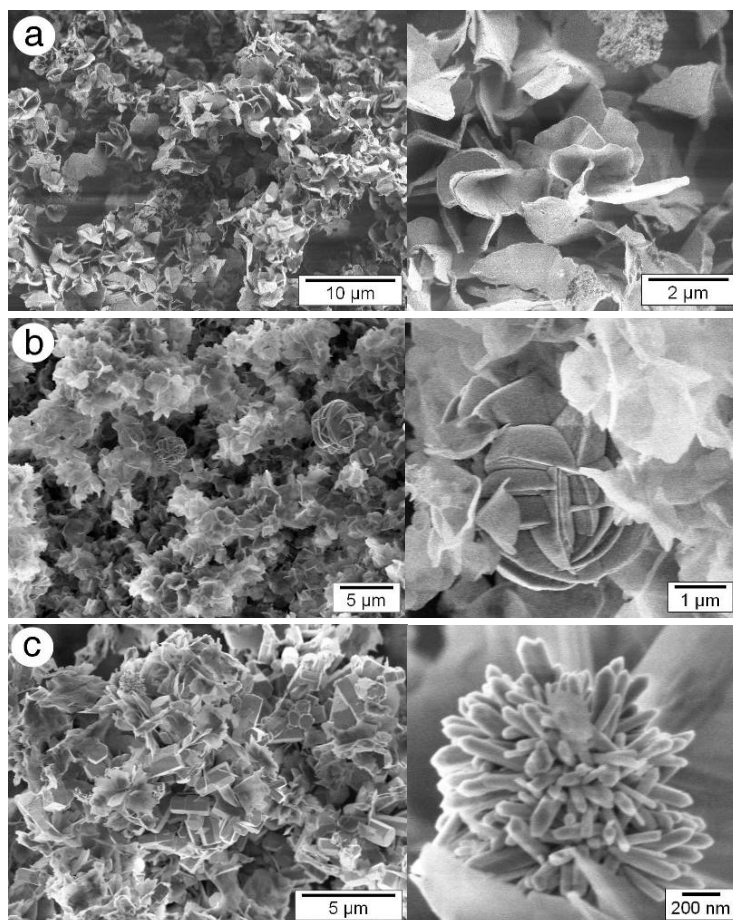


Figure 3.12. SEM images of the precipitation products obtained in the presence of 1 g L^{-1} of different monomers: (a) MA, (b) EGMP, and (c) AA.

The presence of all three monomers (AA, MA, and EGMP) leads to the formation of lamellar structures (see Figure 3.12), typical for zinc hydroxide species. Such species were confirmed by the X-ray diffraction (XRD) patterns, as it will be discussed in detail in the next chapter. Surprisingly, the presence of the MA monomer prevents completely the precipitation of ZnO, and no presence of zincite is found at all, neither by simple observation of the SEM images nor by XRD. In the product obtained in the presence of EGMP, some ZnO crystals were observed

in the micrographs, hidden between the sheetlike hydroxide structures and the aggregates of latex particles. In the case of AA, its presence leads to the formation of prismatic ZnO crystals that coexist with the laminar product. Smaller ZnO starlike crystals were also found.

The presence of the surfactant Lutensol AT50 has no significant effect, as it can be seen in Figure 3.13a, and the precipitated ZnO shows analogous morphologies to those obtained in the absence of any additive (cf. Figure 3.4). The effect of short chain PAA (molecular weight of 2000 g L^{-1}), shown in Figure 3.13b, was studied as an example of the influence of hydrophilic homopolymers. PAA shows a strong influence on the final morphology, but far away from that given by AA-derived latexes. At this point, it can be concluded that poly(styrene–acrylic acid) latex, taken as an example of surface-functionalized latex, has an effect on the crystallization of ZnO completely different from that shown by polystyrene latexes (Figure 3.6a) and that shown by the homopolymers.

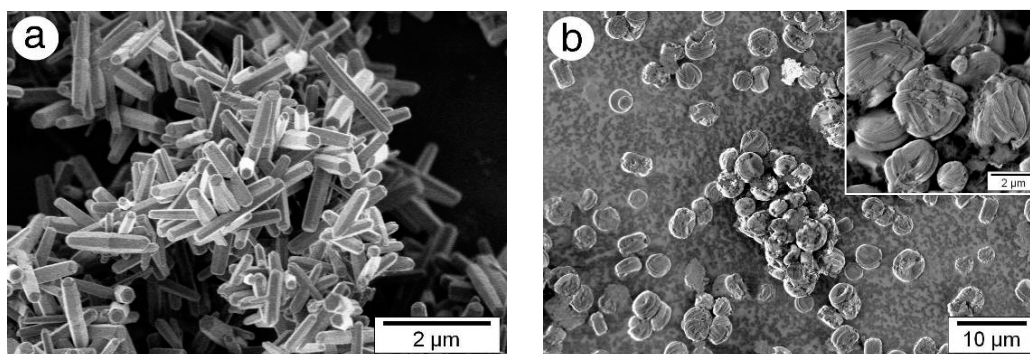


Figure 3.13. Micrographs of the ZnO precipitated in the presence of 1 g L^{-1} of (a) Lutensol AT50 and (b) poly(acrylic acid) ($M = 2000 \text{ g mol}^{-1}$).

3.4.5 Effect of the latex concentration

As it was found first for hydrophilic block and graft copolymers^[8,55,68,158] and later for latexes,^[8,9] the concentration of polymer during the crystallization has a significant effect on the morphology of the resulting ZnO crystal. The influence of the concentration for three selected latexes [i.e., P(S–AA), P(S–AA), and P(S–EGMP)] is shown in Figure 3.14.

As described in previous work,^[8,9] when an acrylic-acid-functionalized latex is used as crystallization additive, the length-to-width ratio of the resulting ZnO crystals decreases systemically by increasing the concentration. This is further studied in §3.5.

The maleic-acid-derived latexes produced a very strong effect in the crystals obtained. The significant differences in the morphologies for the P(S–AA) and the P(S–MA) latexes cannot be justified only in terms of number of carboxylic groups,

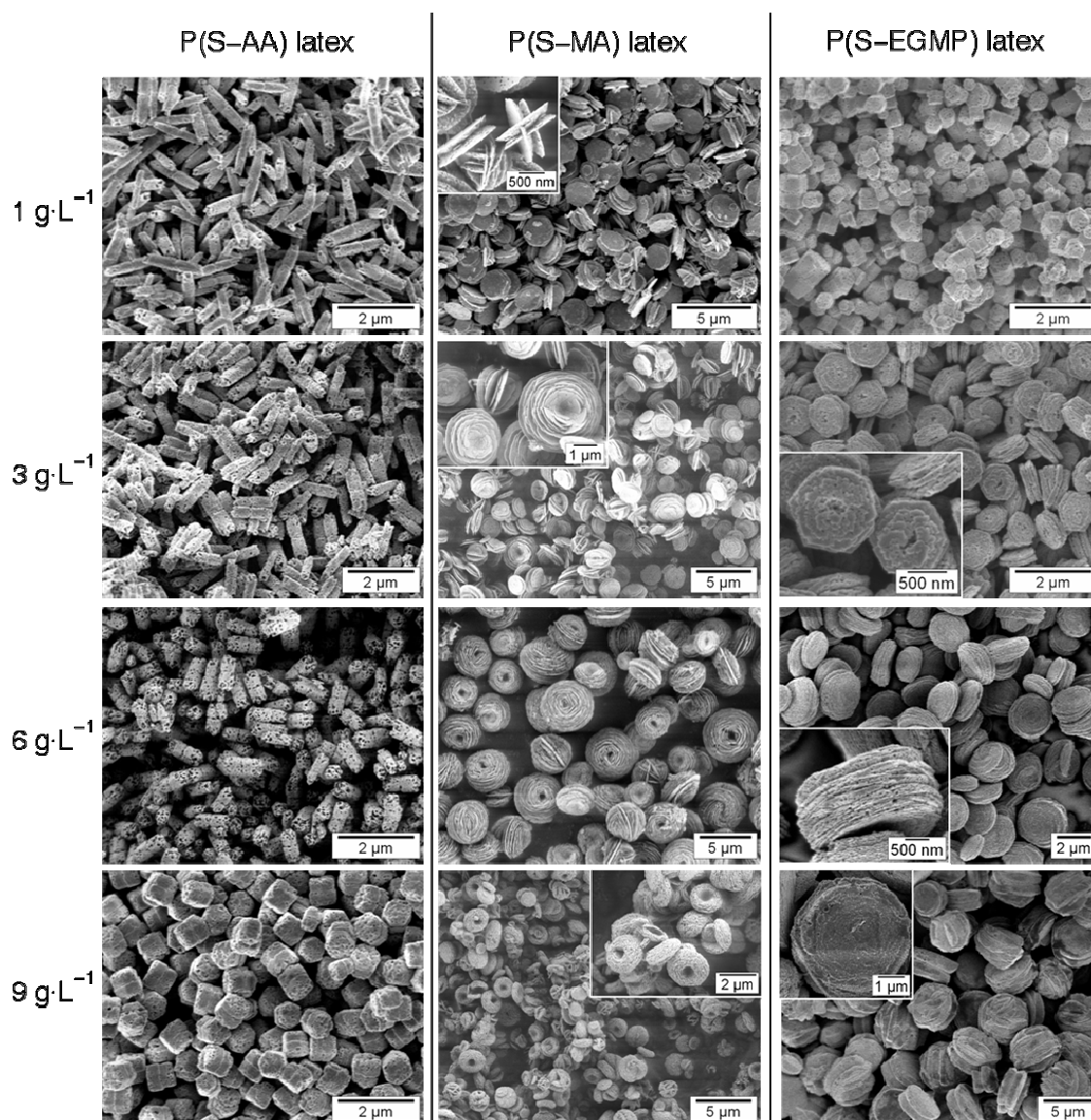


Figure 3.14. SEM micrographs of samples crystallized at different concentrations of latex functionalized on the surface with groups of different chemical natural: P(S-AA), P(S-AA), and P(S-EGMP) (latex samples LTB2, LT5, and LT17 of Table 2.4, respectively). The polymer has been removed by calcination at 600 °C.

because the effect is much higher than expected for such a surface charge densities. In the presence of an increasing concentration of the P(S-MA) latex, the growth in the *c*-axis is blocked and the crystals become wider until thin laminar structures are observed. If one naively assumes that the latex is reversibly adsorbed onto the (001) plane and that the rate of growth in *c*-direction is proportional to the actual coverage by the latex particles, then the absorption constant for the maleic-acid-functionalized latex must be much higher than that for the latex exposing acrylic acid groups towards the growth plane. In the latter case, prismatic crystals are obtained, and suppression of the growth of this plane

leads to platelike crystals. The strong affinity in the case of the maleic-acid-derived latex may be explained by taking into account the special conformation that the polymeric chains can take due to the *cis* position of the two carboxylic groups in the monomer. This conformation will not occur in the latex based on acrylic acid, in whose case very high concentrations of the latex (ca. 9 g L^{-1}) are required to substantively reduce the aspect ratio.

The phosphate groups attached to the surface in P(S–EGMP) latexes have an intermediate effect, not as strong as in the case of the maleic-acid-derived functionalities, but stronger than in the acrylic-acid-type residues. Comparing the effects of the acrylic-acid- and the phosphate-group-decorated latexes, one sees that a concentration of 1 g L^{-1} in the first case produces approximately the same effect as a concentration of 9 g L^{-1} in the latter. At a concentration of 6 g L^{-1} , laminar structures can be observed, similar to those obtained in the presence of P(S–AA) latexes.

In Chapter 1 it has been shown that crystal-growth mechanisms involve screw dislocations and growth spirals (see Figure 1.3). Latex particles may adsorb at active sites (cf. Figure 1.6) and “poison” the growth in certain directions. This possibility, which justifies the observed effects, was supported by scanning electron microscopy. Figure 3.15 shows a sample prepared in the presence of P(S–EGMP) latex particles before and after removing the polymer; clear evidences of growth spirals can be seen here.

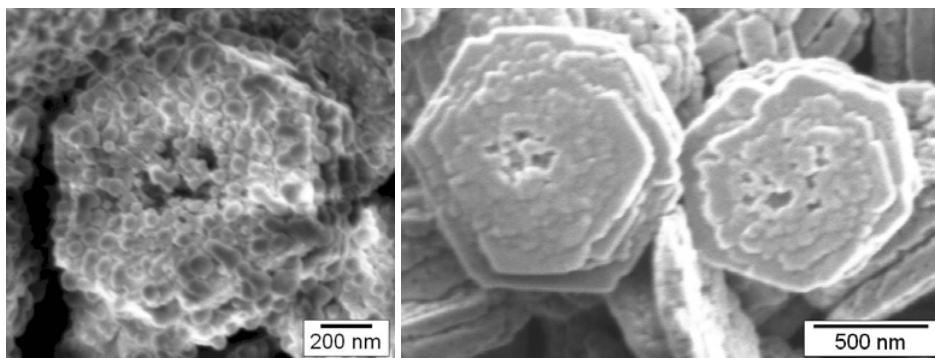


Figure 3.15. Scanning electron micrographs evidencing the presence of growth spirals in a ZnO sample prepared in the presence of 3 g L^{-1} of P(S–EGMP) latex particles (same latex as in Figure 3.14). The image on the left shows the sample as grown and the picture on the right shows the sample after calcination at $600 \text{ }^\circ\text{C}$.

3.5 Poly(styrene–acrylic acid) latex as a model for systematic studies

From the results of the screening experiments previously described, the P(S–AA) latex appears to be a convenient system for a more detailed study, because of

different reasons: (i) the particles are incorporated into the crystals without formation of large polymer aggregates; (ii) the prismatic form of the resulting crystals allows the measurement of width and length, facilitating the quantification of the effect of the additive; (iii) good estimation of the surface charge density of the latex can be obtained by titration with poly-DADMAC, whereas this may become more difficult for latex with other functional residues, for instance phosphate groups (see §2.5.2). Therefore, to analyze the influence of the latex concentration on the morphology and properties of the obtained ZnO, samples in the presence of different quantities of P(S-AA) latex were crystallized.

The yield of the precipitation reaction was estimated to be approximately constant, as deduced from the masses of the washed products, shown in Figure 3.16. Since the density of the latex (ca. 1 g cm^{-3}) is much lower than the density of the ZnO (5.61 g cm^{-3}) and the content of latex remaining after washing is up to 10 wt % (determined by thermogravimetric analysis), the differences in the mass caused by different content of latex are of less importance.

The first observation by SEM is the already indicated change on the crystal dimensions. The aspect ratio (A), defined as the quotient of the length and the width, undergoes a systematical decrease as the P(S-AA) latex concentration increases, as shown in the SEM micrographs of Figure 3.14. The width and length of the crystals (as defined in Figure 3.4b) in each sample were determined from statistical analysis of SEM images, after measuring at least 100 particles. Histograms of the length and width distributions were obtained for each sample and are plotted in Figure 3.17. The presence of the latex reduces the length distribution from multimodal to monomodal, even at the smallest concentration of 0.5 g L^{-1} . Further increase of the latex concentration reduces the length of the crystals taken at the maximum of the length distribution curve, which was used to describe the envelope of the histograms. Note that a single normal distribution is sufficient to describe the statistical data and that the width of the distribution becomes narrower as the latex concentration increases. The width distribution is rather narrow from the beginning, but the mean value increases systematically with increasing the latex concentration. In other words, the crystals become more isometric.

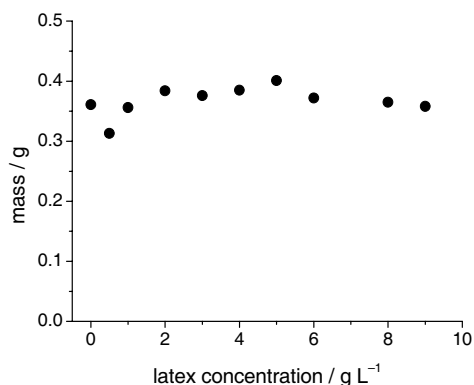


Figure 3.16. Masses of the washed product obtained in precipitations of ZnO in the presence of different concentrations of P(S-AA) latex additive (6.00 mmol of $\text{Zn}(\text{NO}_3)_2$ and 6.00 mmol of HMTA).

The aspect ratio A was calculated from the average length-to-width ratio of the data shown in Figure 3.17, and it is plotted in Figure 3.18a. The product of the square of the width and length of the crystals remains approximately constant within the limits of error, indicating that the volume of the growing crystals in the system is not significantly affected by the change in latex concentration. Considering that all data were obtained for comparable reaction yields, this implies that the number of crystals in the system remains the same for different latex concentrations.

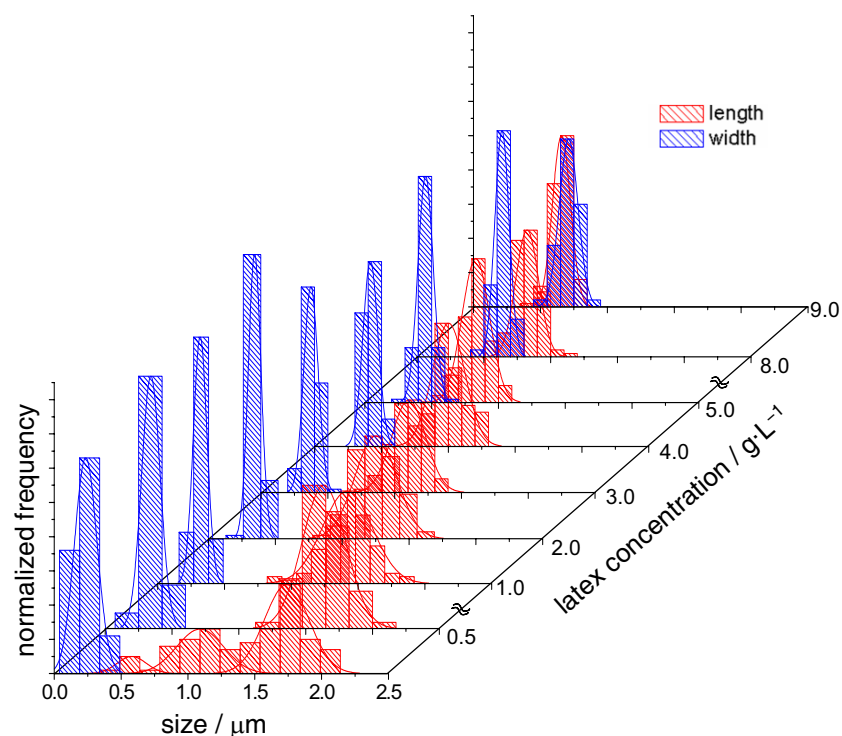


Figure 3.17. Histograms of lengths and widths of the crystals in samples grown in the presence of different concentrations of a P(S-AA) latex.

The explanation of the change of the morphology with increasing latex concentration requires a model of the interaction between the latex particles and the growing faces of the zinc oxide. Presumably, the latex particles, functionalized on the surface with carboxylic groups, are adsorbed preferentially onto the (001) face of the zincite, “poisoning” thereby the positions from which the crystal would normally tend to grow. Qi^[9] proposed a simple model in which the latex particles were assumed to adsorb to the basal plane (001) according to a Langmuir isotherm. According to this model, a surface coverage proportional to the overall concentration is achieved, and the fraction θ of the surface covered by latex, normalized to 1, is given by

$$\theta = \frac{kc}{1 + kc} \quad (3.21)$$

where k is the adsorption constant and c is the concentration of latex particles. Above a certain concentration, full coverage of the basal plane by the latex spheres is achieved and this determines the maximum of the effect. At lower concentrations, the crystals will grow along [001] in proportion to the fraction of free surface available for the addition of crystal-building species. The aspect ratio is assumed to be proportional to the free surface available at a certain coverage defined by θ . This gives rise to a rescaled aspect ratio, S , defined by the equation

$$S = 1 - \frac{A_c - A_\infty}{A_0 - A_\infty} \quad (3.22)$$

in which A_c is the aspect ratio at a certain latex concentration, A_∞ is the aspect ratio at infinitely large concentration, and A_0 is the aspect ratio obtained without latex. The rescaled aspect ratio S for the data of Figure 3.18a is plotted in Figure 3.18b, by adjusting the data to a function equivalent to the Langmuir isotherm:

$$S = \frac{k'c}{1 + k'c} \quad (3.23)$$

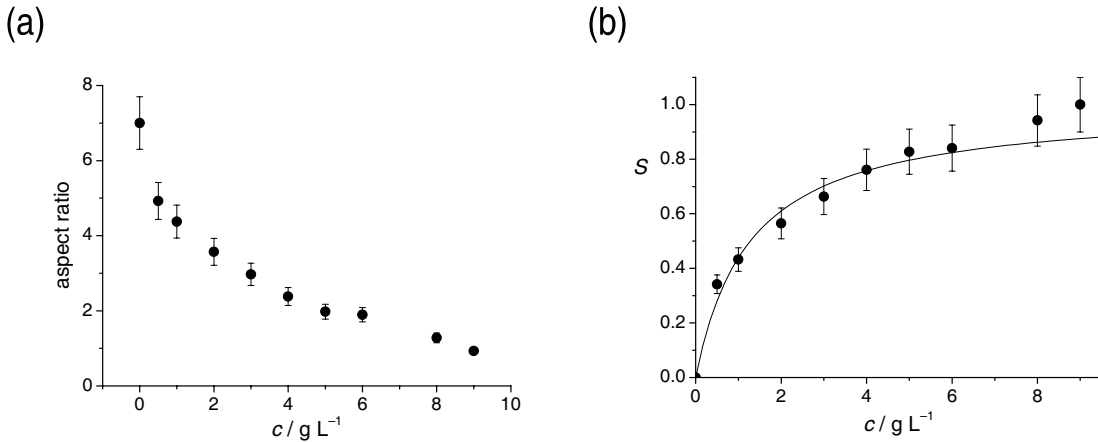


Figure 3.18. (a) Evolution of the aspect ratio with the concentration of P(S-AA) latex, c ; (b) Plot of the scaled aspect ratio S [see eq. (3.22)] versus the concentration of latex, following the algorithm of a Langmuir isotherm [see eq. (3.23)].

It can be observed that the model matches quite well with the data for latex concentrations below 6 g L^{-1} , but for higher concentrations the experimental values differ from the theoretical curve. At high concentration, more complex phenomena, such as multilayer adsorption, may occur, complicating the treatment. By excluding the points for $c > 6 \text{ g L}^{-1}$, the value obtained for the constant k' was 0.78 ± 0.05 . According to Qi, because the adsorption of the latex is related with the surface charge density, different values of k' would indicate different characteristics of the latex particles.^[9]

3.6 Conclusions

Zinc oxide represents a particularly suitable system for systematic studies because zincite is the only phase formed and it crystallizes, in general, in form of hexagonal prismatic crystals, which facilitates the qualitative and quantitative analysis of the effect of additives.

Polystyrene latex particles with a surface modified with hydrophilic groups have been used as controlling agents in the precipitation of ZnO from aqueous media. The presence of such functionalized latexes leads to higher monodispersity and narrower particle size distributions of the ZnO crystals. In addition, latex particles become incorporated into the growing crystal and organic–inorganic hybrid materials are obtained. From the analysis of the size distribution of the crystals at different concentration of the same type of additive, it can be deduced that the latex has very little, if at all, influence on the crystal nucleation. However, the width of the size distributions seems to become narrower at increasing latex concentration, which may indicate that Ostwald ripening is suppressed in the presence of the latex.

It has been observed that anchoring of the components of hydrophilic block and graft copolymers—which have been reported to influence effectively the crystallization of many inorganic crystals, including ZnO—to the surface of latex particles have similar effects to those shown by the copolymers. Nevertheless, functionalized latex particles are easily prepared by oil-in-water miniemulsion, while the synthesis of block and graft copolymers may be more complicated.

The screening of variations in the chemical composition of the corona of the latex particles reveals that both the chemistry of the functional groups and their concentration on the surface are important control parameters that allow the synthesis of zinc oxide with a wide variety of morphologies.

The systematic effect of the concentration of acrylic-acid-derived latexes in the aspect ratio (length-to-width ratio) of the crystals (i.e., the higher the concentration, the shorter and the narrower the crystals become) results in a convenient system for quantitative measurements, and this type of latexes will be use for further studies of this work. Latexes with other surface chemistry, for instance those derived from maleic acid and ethylene glycol methacrylate phosphate, have been also shown to influence effectively the ZnO crystal growth and will be also considered in the next chapters.

3.7 Experimental section

Chemicals and materials

The following chemicals were used in the crystallization experiments: zinc nitrate hexahydrate (Fluka, $\geq 99\%$), hexamethylenetetramine (HMTA, Aldrich, ACS reagent, $\geq 99.0\%$), acrylic acid (Aldrich, 99%), ethylene glycol methacrylate phosphate (Aldrich), poly(acrylic acid) (Aldrich, $M \cong 2000 \text{ g mol}^{-1}$), Lutensol AT50 (BASF AG). The latexes used were described in Chapter 2. The pH values were measured with a pH-meter Shott CG 843 equipped with a Pt/KCl glass electrode with an integrated temperature sensor (Blueline 14pH, Schott).

Crystallization experiments

Formulation 1: In a typical experiment, a solution of $\text{Zn}(\text{NO}_3)_2 \cdot 6\text{H}_2\text{O}$ (1.784 g, 6.00 mmol) in water ($195 - x \text{ mL}$) was placed in a jacketed reactor connected to thermostated water circulator, which allows a precise control of the temperature, under reflux and continuous magnetic stirring. The temperature was set at $95.0 \pm 0.1 \text{ }^\circ\text{C}$. The pertinent quantity of additive ($x \text{ mL}$, $x = 0$ in the case of the reference sample) was added into the reactor. After achieving the thermal equilibrium, the reaction was started by adding HMTA (0.840 g, 6.00 mmol) dissolved in water (5 mL). After 90 minutes, the reaction mixture was cooled down in an ice-water bath and the precipitate was separated by centrifugation, washed several times with water, and dried under vacuum at $40 \text{ }^\circ\text{C}$.

Formulation 2: All samples reported in this chapter were carried out according to the quantities and procedure of Formulation 1, with exception of those shown in Figures 3.4, 3.6, 3.7, and 3.9. In this case, the procedure was analogous, but the reaction was carried out in a 3-neck flask placed in an oil bath ($95 \text{ }^\circ\text{C}$), the total volume was half (the volume after the addition of HMTA was 100 mL), and the concentration of the reactants was divided by a factor two [$\text{Zn}(\text{NO}_3)_2 \cdot 6\text{H}_2\text{O}$: 0.446 g, 1.50 mmol; HMTA: 0.210 g, 1.50 mmol]. The reaction time and the product treatment were the same as in the conventional experiments.

Other experimental formulations (using the same reaction but with different concentration and procedures) were also investigated, but no samples corresponding to these experiments have been shown in this chapter.

Characterization of the crystals

Scanning electron microscopy (SEM) micrographs were taken with a field-emission microscope LEO EM1530 Gemini working at an accelerating voltage of

1–1.5 kV. Particle size histograms and distributions were obtained statistically by measuring the dimensions of at least 100 crystals with help of the software ImageJ (National Institute of Health, USA). In the indicated cases, samples were calcinated at 600 °C under an oxygen atmosphere (RT → 600 °C, 10 °C min⁻¹, TGA thermobalance Mettler TG50).

Chapter 4

Crystal characterization and growth kinetics of ZnO precipitated in the presence of latexes

The world of crystals proclaimed to me in distinct and unequivocal terms the laws of human life.

—Friedrich W. A. Fröbel (1782–1852)

4.1 Introduction

Although a large variety of shapes and morphologies are found in natural and synthetic crystals, all possible structures can be classified in a limited number of symmetry groups, which follow specific crystallographic rules. However, far from the theoretical ideality, real crystals do not fulfill these rules “perfectly” and grow with defects and internal strains. The study of crystal defects and their influence on the physical properties is considered in the next chapter; here, we focus on the long-range order.

So far it has been seen that when zincite is precipitated from aqueous medium in the presence of latexes with different surface chemistry, the morphology of the obtained crystals changes dramatically. A scenario with many morphologies (e.g., prismatic, platelike, needlelike, flowerlike crystals) has been presented. Some questions remain now open: Has this variety of morphologies a correspondence in the crystal perfection? Does the incorporation of latex lead to distortions and changes in the lattice structure? In the next pages, it is desired to answer these questions by characterizing the crystallinity of the precipitated products. X-ray diffractometry and vibrational spectroscopies are the basic tools used for this purpose. Finally, in a second part of the chapter, some kinetic considerations regarding the formation process of the crystals will be pointed out.

4.2 Crystal structure of zinc oxide

Zinc oxide crystallizes in the hexagonal system as zincite, which belongs to the point group C_{6v} (using the Schönflies notation, or $6mm$ in the Hermann–Mauguin

nomenclature) and to the space group C_{6v}^4 (or $P6_3mc$).[†] The cell parameters are $a = 3.2498 \text{ \AA}$ and $c = 5.2066 \text{ \AA}$, the number of formula unit is $Z = 2$, and the crystallographic density is 5.68 g cm^{-3} .^[164] The ratio c/a is 1.602, slightly smaller than

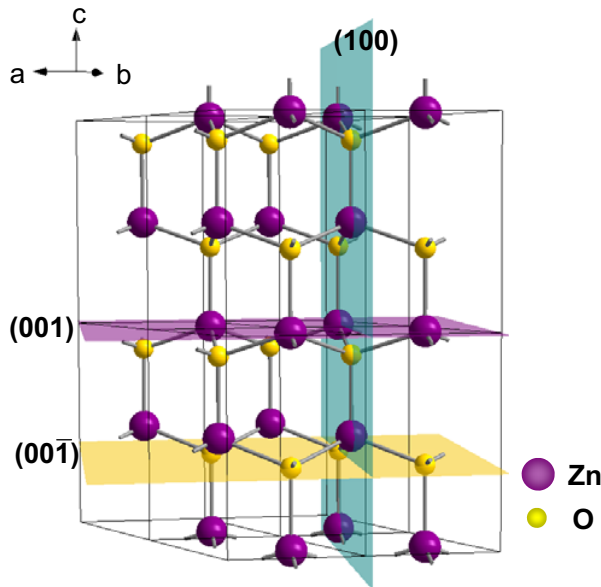


Figure 4.1. Crystal structure of ZnO (zincite).

the value for an ideal wurtzite lattice ($c/a = 2\sqrt{2/3} = 1.633$), that is, the ZnO lattice is contracted in the direction of the c -axis with respect to the ideal wurtzite structure.^[165]

The oxygen atoms are hexagonal close-packed and the zinc atoms occupy half of the tetrahedral interstices and are also hexagonal close-packed. This mode of packing is shown in Figure 4.1. The zinc and oxygen atomic planes, $\{001\}$ and $\{00\bar{1}\}$, alternating in the $[001]$ direction and perpendicular to the c -axis, exhibit a highly polar character and are not identical under

ideal conditions. A cut through one of these planes will lead to a dipole perpendicular to the surface, which has a physically unrealistic high surface energy.^[166] Under conditions of growth from an aqueous medium, these surfaces may be hydrated,^[167] but will still differ with regard to polarity and charge density. In fact, the twin formation reported in the previous chapter (see Figure 3.4b) may be caused by the different stability of these faces. The ZnO structure contains also a series of nonpolar faces $\{hk0\}$, electrically neutral, with equal number of oxygen and zinc atoms. An example of nonpolar faces is the family of planes $\{100\}$, represented in Figure 4.1.

4.2.1 X-ray diffractometry of ZnO

A powerful technique to investigate crystalline structures is X-ray diffraction (XRD), which gives information about the phases present in the sample and about the crystal order and perfection. Both the position and the width of peaks in the X-ray diffractograms offer crystallographic information about the analyzed

[†] Although zincite, with wurtzite structure, is the thermodynamically stable phase, cubic ZnO with rocksalt structure can be obtained at high pressures ($\geq 10 \text{ GPa}$). Also cubic ZnO with zincblende structure, a metastable phase, can be stabilized by epitaxial growth in cubic substrates.^[163]

structure: the line position allows to calculate the interplanar distances and the line width gives information about the crystallite size and the lattice distortions.^[168]

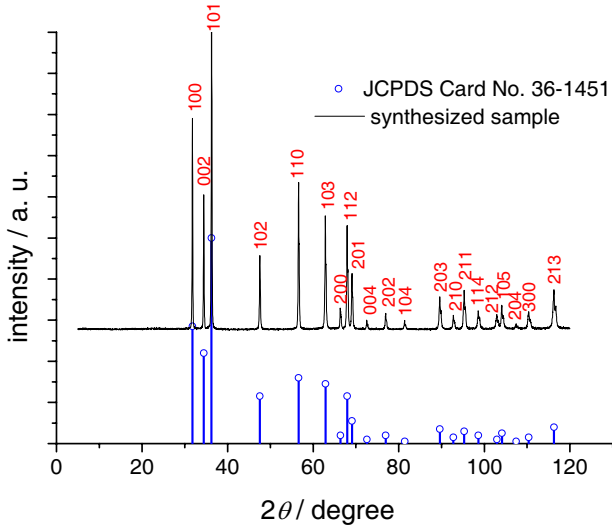


Figure 4.2. X-ray diffractogram of pure zincite (synthesized without any additive as indicated in §3.3), together with the pattern from the JCDs database and the corresponding indexing of the reflections.

Figure 4.2 shows the XRD pattern of a pure zincite sample with indication of the peak indexing. Considering the first two peaks, the (100) and (002) reflections, we can obtain a first estimation of the cell parameters as follows. From the position of the peaks in the diffractograms, the interplanar distances, d , can be calculated by Bragg's law

$$n\lambda = 2d \sin \theta \quad (4.1)$$

where λ is the wavelength of the radiation (1.54 Å for Cu K α radiation) and θ is the diffraction angle. For the hexagonal system, d_{hkl} is defined as^[168]

$$d_{hkl} = \left[\left(\frac{4}{3a^2} \right) (h^2 + k^2 + hk) + \left(\frac{l^2}{c^2} \right) \right]^{-\frac{1}{2}} \quad (4.2)$$

Substituting in this equation the values of h , k , and l for the reflection (100) ($h = 1$, $k = 0$, and $l = 0$), the cell constant a can be written as

$$a = \frac{2d_{100}}{\sqrt{3}} \quad (4.3)$$

Operating analogously for the reflection (002), the parameter c is given by

$$c = 2d_{002} \quad (4.4)$$

The cell parameters obtained by eqs. (4.3) and (4.4) are an approximation and take into consideration only the first two reflections. More precise calculations can be done by computational refinement of the whole diffractogram.

The broadening of the diffraction lines occurs for three main reasons: (i) an experimental contribution intrinsic to the instrumental equipment; (ii) a diffraction-order-independent broadening, related with the size of the crystal domains; and (iii) a diffraction-order-dependent broadening, caused by lattice strains (distortions). Since different common crystal defects cause a similar line broadening, it is often difficult to discern the type of defect dominating in a particular case. If the peak broadening is assumed to result only from the size of the coherently scattering domains, their size can be estimated using the Scherrer equation:

$$L_{hkl} = \frac{K\lambda}{\beta_{1/2} \cos \theta} \quad (4.5)$$

where K is a form factor ranging from 0.89 to 1.39 (commonly taken as 0.9 or approximated to unity), λ is the radiation wavelength, and $\beta_{1/2}$ is the full width at half maximum (FWHM) of the peak on the 2θ scale in radians. The dimension L_{hkl} obtained by the Scherrer equation is the length of the coherently scattering domains; it is often referred as *crystallite size*, although *coherence length* is probably more appropriate.

4.2.2 Lattice dynamics of ZnO: vibrational spectroscopies

Besides the XRD, other techniques that offer information about the structure of crystalline materials are the vibrational spectroscopies: the Fourier transform infrared (FTIR) spectroscopy and the Raman spectroscopy. With 4 atoms per unit cell, zincite (space group C_{6v}^4) has 12 vibration modes: one longitudinal-acoustic (LA), two transverse-acoustic (TA), three longitudinal-optical (LO), and six transverse-optical (TO).^[163] The group theory

Table 4.1. Infrared and/or Raman activity and frequency of the fundamental optical modes in zincite (from Raman measurements reported by Damen et al.^[169]).

symmetry character	activity (Raman, IR)	frequency [cm ⁻¹]
E_2	Raman	101
E_2	Raman	437
E_1 (transverse)	Raman and IR	407
A_1 (transverse)	Raman and IR	380
E_1 (longitudinal)	Raman and IR	583
A_1 (longitudinal)	Raman and IR	574

predicts the 9 optical modes: an A_1 mode, a doubly degenerate E_1 branch, two doubly degenerated E_2 branches, and two B branches. The A_1 and E_1 modes are both Raman- and infrared-active, the two E_2 modes are only Raman-active, and the B modes are inactive (silent modes).^[169] The active optical modes of zincite, together with the frequency reported in the literature for single crystals, are compiled in Table 4.1.

In addition to the crystal structure and the chemical composition, three factors affect the position and the form of the peaks in vibrational spectra: (i) the dielectric constant of the matrix in which the material is diluted, (ii) the particle aggregation, and (iii) the crystal shape.^[170] Morphological characteristics of small particles can influence the infrared and Raman spectra due to dipole oscillation induced by the vibrational modes. Andrés-Vergés et al.^[148,170,171] applied the so-called *theory of the average dielectric constant* (TADC) to analyze IR spectra of ZnO prepared by precipitation in a similar way to the here presented. In this theory, described in detail in articles of Ocaña et al.^[172] and Serna et al.^[173], the particles are considered to have an *average dielectric constant* (ϵ_{av}), which is a function of a *filling factor* (f) and a *depolarization or shape factor* (g):

$$\epsilon_{av} = f(f, g) \quad (4.6)$$

The filling factor, which ranges between 0 and 1, takes into consideration the aggregation of the particles and represents the fraction of the total occupied volume. The particle shape is assimilated to a revolution ellipsoid through a shape factor associated with the crystallographic axes. The shape factor associated with the c -axis, which is considered to be the revolution axis in the case of the ZnO crystal, is referred as g_1 and it ranges between 0 for the cylinder and 1 for the slab, being 0.33 for the sphere. From the average dielectric constant, the absorption coefficient K of the sample can be calculated by

$$K = \frac{\omega}{c} \frac{I(\epsilon_{av})}{\epsilon_{av}} \quad (4.7)$$

where $I(\epsilon_{av})$ represents the imaginary part of the average dielectric constant.

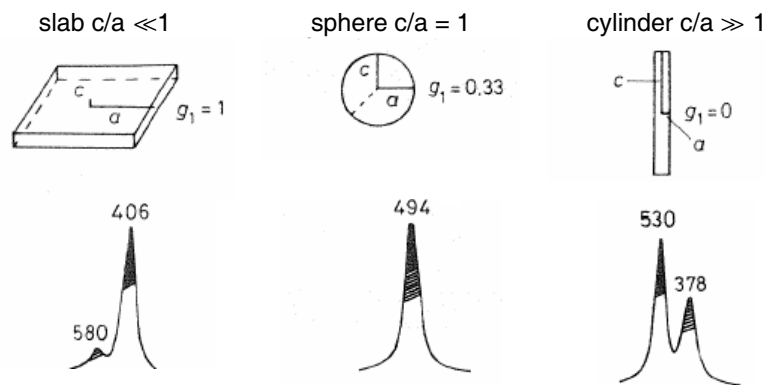


Figure 4.3. IR spectra of ZnO microcrystals calculated by Andrés-Vergés et al.^[170] for three ideal shapes (i.e., slab, sphere, and cylinder) using the theory of the average dielectric constant. (Reproduced by permission of The Royal Society of Chemistry.)

Using the TADC, Andrés-Vergés et al. calculated the position and the form of the IR absorption peaks corresponding to the two transverse optical modes $\omega_{T\parallel}$

and $\omega_{T\perp}$ (which should have positions at ca. 380 and 407 cm^{-1} , respectively, as indicated in Table 4.1) for the three ideal cases of the slab, the sphere, and the cylinder. They considered that the filling factor was negligible, with values of $f \leq 0.1$. Their results are represented in Figure 4.3, where it is observed that the two absorption bands move in opposite direction in going from the slab to the cylinder, overlapping for the case of the sphere.

4.3 Estimation of latex content by thermogravimetric analysis

As shown in Chapter 3, when zinc oxide is precipitated in the presence of latex additives, the polymer particles become incorporated into the crystalline structure. The latex content in the obtained ZnO–latex hybrid materials can be estimated by thermogravimetric analysis (TGA). Before TGA, the excess of latex (i.e., rests of nonincorporated latex and particles merely adsorbed at the crystal surface) should be removed by repetitive cleaning with water (or non-aggressive solvents like ethanol) or by other surface-cleaning methods, such as plasma-cleaning with Ar–O₂ gas mixtures, although the latter method was shown to be not sufficiently effective, especially in case of big quantities of latex or larger amounts of samples.

In the thermogravimetric analysis, the hybrid samples are heated under oxidative atmosphere up to the calcination of the polymer, suffering a weight loss, registered by a precision balance. Two steps can be pointed out in our samples: a first step of water elimination, at around 100 °C, and the step of latex combustion, in the range ~400–500 °C. This can be monitored by a TGA equipment coupled to a mass spectrometry (MS) detection system (abbreviated as TGA–MS). Figure 4.4a shows the weight loss for a ZnO–polymer hybrid sample containing acrylic-acid-derived latex particles, together with the MS signals corresponding to H₂O ($M_r = 18$) and CO₂ ($M_r = 44$). The water signal shows two peaks, corresponding to the two indicated steps. The CO₂ signal has an intense peak, coinciding with the second water peak and clearly ascribable to the latex combustion.

In Figure 4.4b it is shown the weight loss of samples synthesized in the presence of an increasing concentration of P(S–AA) latex, up to 6 g L⁻¹. It has to be noticed, that at high concentrations of latex (>6 g L⁻¹), a quantification of the latex content becomes difficult; the latex effect achieves a maximum and at high concentrations it does not follow the ideal Langmuir-type isotherm described in §3.5. When high concentration of latex are applied, further effects such as

aggregation or coagulation of the latex may also occur in the crystallization solution. Furthermore, if the amount of nonincorporated latex in the final product is too large, its removal becomes difficult and the TGA estimations may be erroneous. TGA results must be taken with care, but offer—when carried out properly—an adequate estimation of the latex content of the hybrid materials.

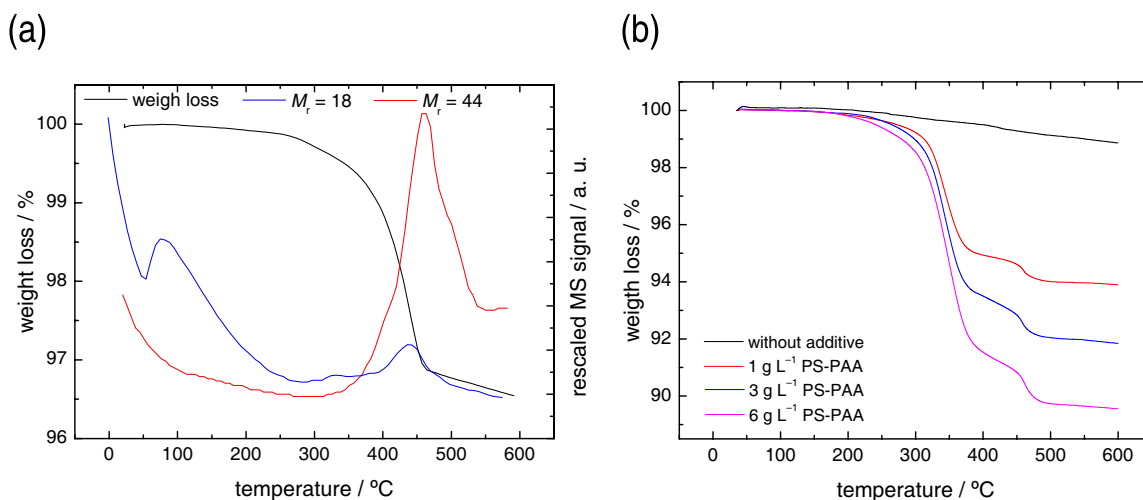


Figure 4.4. (a) Weight loss (black line) from TGA, with coupled MS detection of water (blue line, $M_r = 18$) and CO_2 (red line, $M_r = 44$) for a ZnO-latex hybrid sample synthesized in the presence of 1 g L^{-1} of the latex LT7 (cf. Table 2.4). (The intensities of the MS signals have been rescaled to fit both in the same graph.) (b) Weight loss as a function of the temperature for a sample prepared without any additive and for hybrid samples crystallized in the presence of different concentrations of the latex LT15 (cf. Table 2.4).

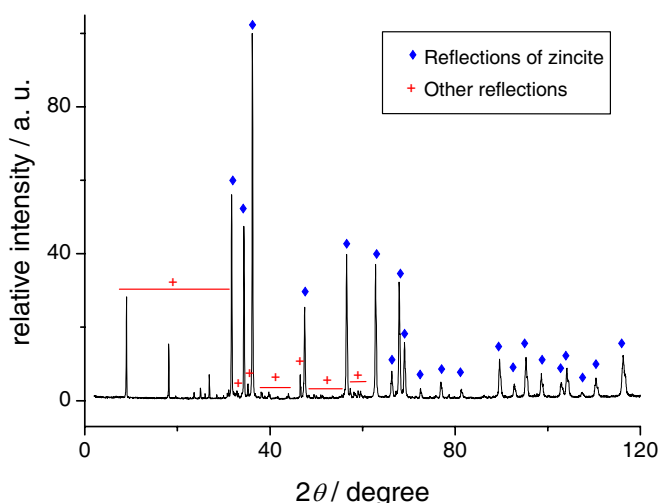
4.4 Crystal structure in the absence of additives

In the absence of additives, hexagonal zincite was typically the only phase identified by XRD. An example of the powder diffractogram of the synthesized samples has been shown in Figure 4.2. All observed peaks could be assigned to reflections of zincite. By applying Bragg's law [eq. (4.1)], the position of the peaks in the 2θ scale can be translated into interplanar distances. By substituting these distances in eqs. (4.3) and (4.4), values for the lattice parameters a and c (the first two reflections are considered) are obtained. Operating in this way, the lattice parameters for the reference sample (sample without additive) are $a = 3.249 \text{ \AA}$ and $c = 5.205 \text{ \AA}$, completely coincident with the reported crystallographic data of zincite.

Although uncommon in our experimental setup, in products synthesized at temperatures lower than $90 \text{ }^\circ\text{C}$ metastable hydroxide species may occur, as it was mentioned in §3.3. Figure 4.5a presents the XRD pattern of a sample prepared with an inappropriate temperature control (the same sample whose SEM image

was shown in Figure 3.5). It can be seen that, besides the zincite peaks, further reflections are found, of which the most significant (with higher intensity) appear at 2θ values of 9.02, 18.14, 26.90, 35.24, and 46.55°, having relative intensities of 28, 15.5, 7, 5, and 7, respectively (a value of 100 is taken for the peak (101) of zincite). According to reported data,[†] these additional reflections could not be ascribed either to crystalline zinc nitrate hydrate (the precursor) or to known phases of $\text{Zn}(\text{OH})_2$, and they are presumably attributable to intermediate metastable hydroxide species of unclear chemical composition. This assumption was supported by the observation that the non-zincite peaks disappear by heating the sample temperatures above 100 °C (at 100 °C the dehydration of hydroxo species should occur), as illustrated in Figure 4.5b.

(a)



(b)

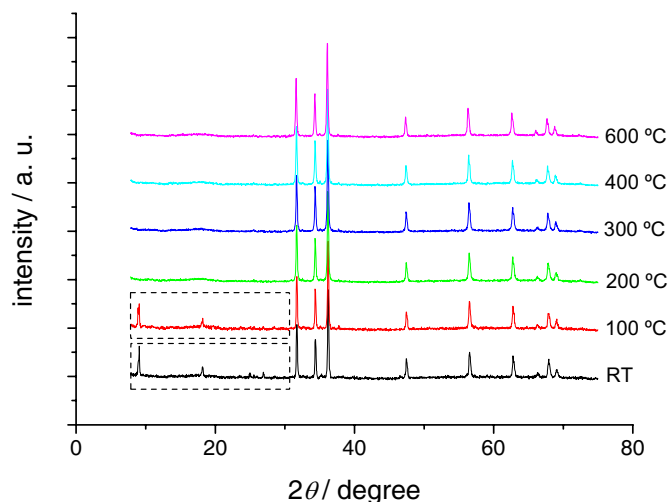


Figure 4.5. XRD powder diffractograms of a sample containing zincite and metastable species, presumably hydroxides (a scanning electron micrograph of this sample was shown in Figure 3.5): **(a)** diffractogram at room temperature with indication of zincite and additional reflection; **(b)** diffractograms at different temperatures, from room temperature (RT) to 600 °C.

[†] Data base of the JCPDS–ICDD (Joint Committee on Powder Diffraction Standards–International Center for Diffraction Data).

4.5 Crystal structure versus latex-surface chemistry

In the previous chapter, it was shown that the chemical nature of the latex used in the crystallization has a strong influence on the final morphology of the precipitated zinc oxide. The aim of this section is to analyze the crystalline structure of the obtained products as a function of the surface chemistry of the latex. ZnO samples crystallized in the presence of selected latexes with different chemical surface functionalization [i.e., PS, P(S-AA), P(S-MA), P(S-EGMP), and P(S-MAN)] were studied. The X-ray diffractograms of these samples are shown in Figure 4.6, where a ZnO sample obtained in the absence of additive is included as a reference.

The XRD reflections of all the samples correspond to pure zincite and no presence of other crystalline species was observed. A detailed analysis of the position and the broadening of the reflections (100) and (002) was carried out by normalizing the peaks and adjusting the data to Lorentzian (Cauchy)

curves, which may be taken as an approximation to fit XRD reflections.^[168] The contribution of the $K\beta$ to the peak form, especially recognizable in the reflection (002), was taken into account by fitting the peaks to double Lorentzian curves. These fittings are shown in Figure 4.7, where it can be observed that, for the different samples, the reflections (100) are more homogeneous than the reflections (002), in regard to position and breadth. The position and the full width at half maximum (FWHM) for the Lorentzian fittings, together with the coherence lengths, L_{hkl} , calculated for both reflections with the Scherrer equation [eq. (4.5)] are contained in Table 4.2. Also the ratio between the intensity of the (100) and (002) reflections is included. This ratio can give information about the aspect ratio of the crystals. However, the intensities in X-ray diffractograms may be strongly influenced by the so-called preferred orientation of crystals, which results from the different alignment that crystals can take, due to their different morphologies, when preparing powder samples. We are aware of this problem and we are not able to discern the differences in the intensity caused intrinsically

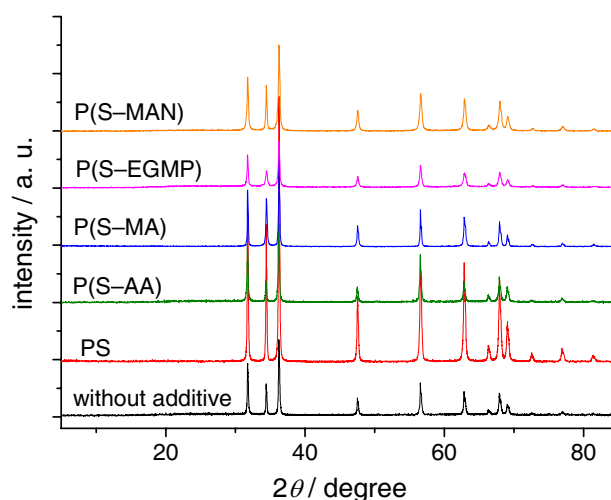


Figure 4.6. X-ray diffractograms of ZnO crystallized without additives and 1 g L^{-1} of different surface-functionalized latexes, as indicated in the graphs.

by the materials and those caused by the preferred orientations. Nevertheless, the ratios are given to allow the comparison with data reported in the literature.

The calculation by eqs. (4.3) and (4.4) of the lattice parameters for the samples prepared in the presence of latex particles gives a variation with respect to the reference sample (synthesized without additive) of only up to 0.2%. The fluctuations are close to the resolution of our diffractometer and any quantification of the effect becomes difficult. Consequently, it can be concluded that in spite of the different morphologies and the incorporation of the polymer into the crystal structure, the crystal order remains essentially undisturbed and the lattice parameters do not change significantly.

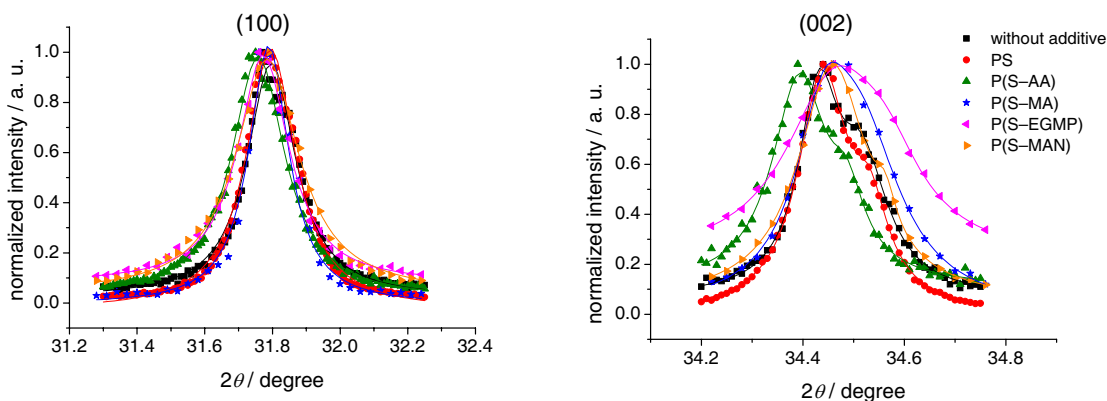


Figure 4.7. Normalized reflections (100) and (002) from the diffractograms shown in Figure 4.6. Experimental data are fitted to Lorentzian curves (represented in the graphs with solid lines).

Table 4.2. Parameters of the reflections (100) and (002) in ZnO crystals obtained without additives and in the presence of 1 g L^{-1} latexes with different surface chemistry. Coherence lengths (L_{hkl}) were calculated by eq. (4.5) The weight loss from the thermogravimetric analysis (TGA) allows to estimate the latex content in the samples.

latex ^[a]	TGA weight loss (%)	$\frac{I_{100}}{I_{001}}$	(100)			(002)		
			2θ [°]	$\beta_{1/2}$ [°]	L_{100} [nm]	2θ [°]	$\beta_{1/2}$ [°]	L_{002} [nm]
no latex	1.3	1.6	31.796	0.175	53	34.431	0.097	95
PS	3.0	1.1	31.795	0.177	52	34.439	0.118	78
P(S-AA)	6.1	1.9	31.758	0.192	48	34.493	0.132	70
P(S-MA)	11.1	1.2	31.789	0.143	64	34.441	0.134	69
P(S-EGMP)	23.3	1.8	31.773	0.184	50	34.459	0.236	39
P(S-MAN)	16.8	1.2	31.784	0.227	40	34.461	0.167	55

[a] Structure of the latex; the latexes used for the 2nd to 6th samples of this table were LT25, LT15, LT5, 02LH178, and LT4, respectively (cf. Table 2.4).

Further investigation of the crystalline powders was performed by Fourier transform infrared (FTIR) spectroscopy. The spectra of four representative samples are compared in Figure 4.8: a pure ZnO reference sample and samples

synthesized in the presence of 1 g L^{-1} of P(S-AA), P(S-AA), and P(S-EGMP) latexes.

The analysis of the FTIR spectra of zincite done by Andrés-Vergés et al.^[148,170,171] (see §4.2.2) appears to be applicable to our results. As these authors did, we do not consider the matrix effects for a relative comparison of the samples, because all of them were prepared using KBr as diluting agent. The particle aggregation is also considered to be of less importance, according to the SEM observations. Therefore, differences in the FTIR spectra are assumed to be caused basically by the differences in the morphology.

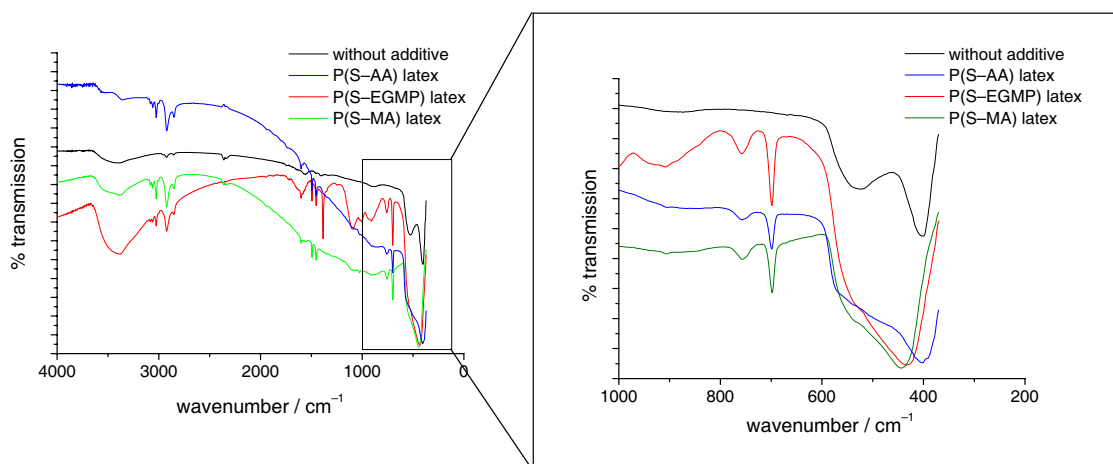


Figure 4.8. FTIR spectra of samples crystallized without additive and in the presence of 1 g L^{-1} of latex with different surface chemistry.

In the absence of additive, as described in the previous chapter, the samples are composed of polydisperse prismatic crystals. In this case, two FTIR peaks are observed at 401 and 524 cm^{-1} . In the presence of P(S-AA), the peak at 401 cm^{-1} is kept, but the one at higher wavenumber becomes a shoulder and cannot be clearly recognized. For the samples prepared with P(S-EGMP) and P(S-AA), the maximum absorption (minimum transmission) shifts to higher wavenumbers (432 and 442 cm^{-1} , respectively). According to the calculations of Andrés-Vergés et al., this would match with the change from prismatic shape to platelike morphology, coinciding with the SEM observations.

4.5.1 Effect of the independent monomers

The effect of the independent functional monomers on the crystallization can help to understand the effect of the surface chemistry of the latexes. In §3.4.1, SEM was used to analyze the morphology of the products obtained in the presence of 1 g L^{-1} of AA, EGMP, and MA. Now, we will analyze the X-ray diffractograms of these samples, shown in Figure 4.6 together with the XRD pattern of a reference

prepared without additives. Coinciding with the observations by microscopy, no presence of zincite is observed in the sample prepared with MA, and the X-ray diffractogram shows periodic peaks, typical for low-ordered turbostratic lamellar structures. This type of structures has been reported for a large number of metal-hydroxide species, among them:

- (i) hydroxides with inorganic anions, such as hydrozincite, $\text{Zn}_5(\text{OH})_6(\text{CO}_3)_2$ ^[174] and zinc hydroxide nitrate, $\text{Zn}_5(\text{OH})_8(\text{NO}_3)_2 \cdot 2\text{H}_2\text{O}$ ^[175]
- (ii) metal (Zn, Co, Ni) hydroxiacetates: $\text{M}(\text{OH})_{2-x}(\text{CH}_3\text{COO})_x \cdot n\text{H}_2\text{O}$ ^[176] (also reported for zinc as $\text{Zn}_5(\text{OH})_8(\text{CH}_3\text{COO})_2 \cdot 2\text{H}_2\text{O}$ ^[177]); nickel-zinc double hydroxiacetates, $\text{Ni}_{1-x}\text{Zn}_{2x}(\text{OH})_2(\text{CH}_3\text{COO})_{2x} \cdot n\text{H}_2\text{O}$; and
- (iii) hydroxides containing bigger organic molecules, such as dicarboxylic acids: compounds of zinc with 2,6-naphtalenedicarboxylic acid (ndc) and 4,4'-biphenyldicarboxylate (bpdc) presenting the chemical formulas $\text{Zn}_2\text{OH}_2(\text{ndc})$ and $\text{Zn}_3(\text{OH})_4(\text{bpdc})$, respectively,^[178] and terephthalate-based cobalt hydroxide, $\text{Co}_2(\text{OH})_2\text{C}_8\text{H}_4\text{O}_4$ ^[179]

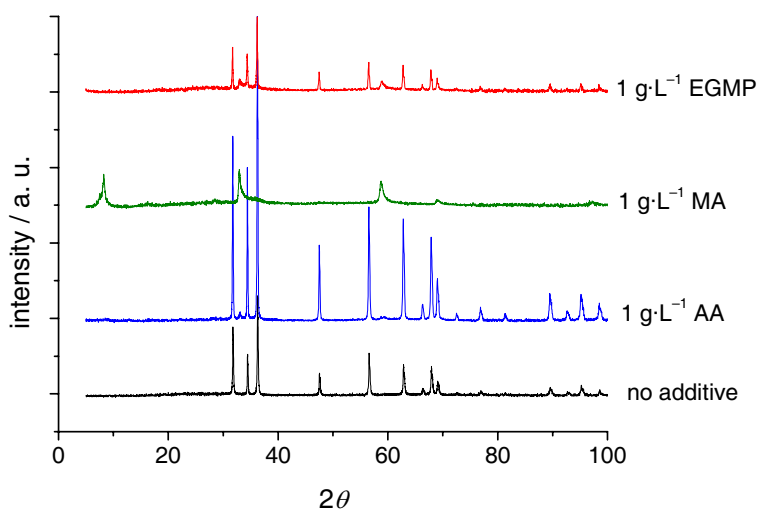


Figure 4.9. X-ray diffractograms of zincite crystallized without additive and of samples obtained in the presence of 1 g L^{-1} of different monomers: acrylic acid (AA), maleic acid (MA) and ethylene glycol methacrylate phosphate (EGMP).

Since $\text{Zn}(\text{NO}_3)_2 \cdot 6\text{H}_2\text{O}$ is used as precursor in our experiments, nitrate hydroxide species may occur, but analogously to the reported species for dicarboxylic acids, it is also reasonable to think in structures with formula $\text{Zn}_2(\text{OH})_2(\text{MA})$, or similar species with other stoichiometries. The three peaks at lower angles, corresponding to d_{hkl} values of 10.62, 5.464, and 3.106 Å, are indexed as (00*l*), and the three peaks at higher angles, corresponding to distances of 2.70, 1.57, and 1.36 Å are indexed as (*hk*0), accordingly to the literature.^[176,177,180] The (00*l*) peaks are supposed to be related with the interlayer distances. Thus, a interlayer distance of 10.6 Å can be estimated from the first (00*l*) peak. The XRD patterns of

the samples prepared with EGMG and AA show clearly the presence of zincite. The lamellar structure peaks at high angles can also be identified, but the (00 l) peaks do not appear.

The position and indexing of the peaks corresponding to lamellar structures for the three samples prepared with the monomers are listed in Table 4.3, which also include for comparison the values reported for layered zinc hydroxyacetate, $\text{Zn}(\text{OH})_{2-x}(\text{CH}_3\text{COO})_x \cdot n\text{H}_2\text{O}$, by Poul et al.^[176]

Table 4.3. Position of the peaks corresponding to lamellar structures in samples obtained in the presence of 1 g L^{-1} of MA, EGMP, and AA (cf. Figure 4.9), compared with the values reported by Poul et al.^[176] for layered zinc hydroxyacetate, $\text{Zn}(\text{OH})_{2-x}(\text{CH}_3\text{COO})_x \cdot n\text{H}_2\text{O}$.

hkl	MA sample		EGMP		AA		Poul et al.
	$2\theta / ^\circ$	$d_{hkl} / \text{Å}$	$2\theta / ^\circ$	$d_{hkl} / \text{Å}$	$2\theta / ^\circ$	$d_{hkl} / \text{Å}$	$d_{hkl} / \text{Å}$
001	8.31	10.62	–	–	–	–	14.68
002	16.20	5.464	–	–	–	–	7.36
003	28.71	3.106	–	–	–	–	4.91
100	33.10	2.703	33.11	2.703	33.16	2.703	2.717
110	58.75	1.570	58.75	1.570	58.75	1.570	1.569
200	69.02	1.359	–	–	–	–	1.359

4.6 Crystal structure versus latex concentration

The effect of the concentration on the crystal structure is analyzed next for the model case of poly(styrene–acrylic acid) latex. As previously shown, the increase of latex leads to a systematic decrease of the aspect ratio of the ZnO crystals. However, XRD patterns indicate that the microcrystalline structure is essentially conserved. Figure 4.10 shows the X-ray diffractograms of ZnO samples prepared with increasing concentration of P(S–AA) latex. The samples considered here are the same whose aspect ratio was studied in §3.5 (cf. Figures 3.17 and 3.18).

Proceeding in an analogous way to §4.5, the reflections

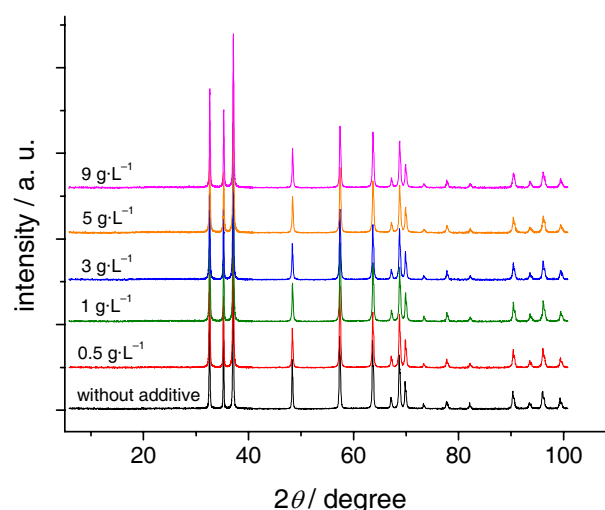


Figure 4.10. X-ray diffractograms of ZnO crystallized in the presence of different concentration of the poly(styrene–acrylic acid) latex LTB2 (cf. Table 2.4), as indicated in the graphs.

(100) and (002) were analyzed in detail. The fittings to Lorentzian curves for these peaks are shown in Figure 4.11, and the corresponding position and line width, together with the coherence length and the ratio between the intensity of both peaks, are compiled in Table 4.4. Also the latex content in the final product, that is, the quantity of incorporated latex, different from the initial latex concentration added during the crystallization, is contained in this table. The amount of latex occluded in the crystals was estimated from the weight loss determined by thermogravimetric analysis (TGA).

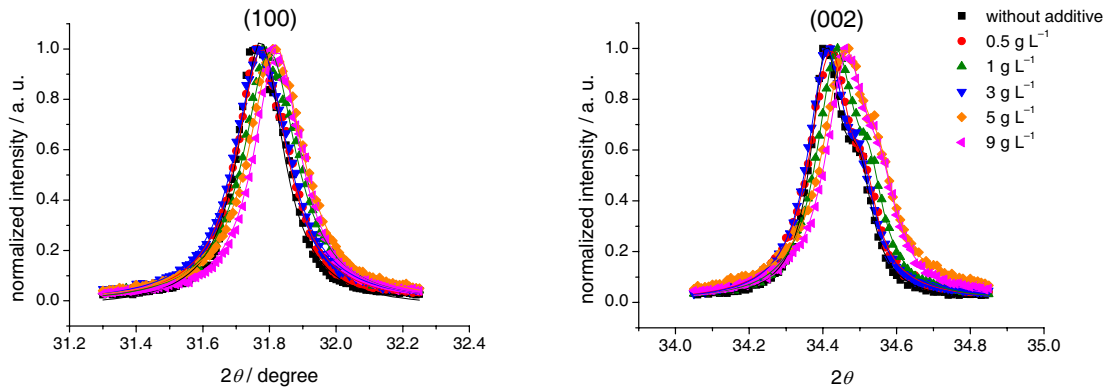


Figure 4.11. Normalized reflections (100) and (002) from the X-ray diffractograms shown in Figure 4.10. Experimental data are fitted to Lorentzian curves (represented with solid lines in the graphs).

Table 4.4. Parameters of the reflections (100) and (002) in ZnO crystals obtained in the presence of different amounts of the P(S-AA) latex LTB2 (cf. Table 2.4). Coherence lengths (L_{hki}) were calculated by eq. (4.5) and the latex content was estimated from the weight loss determined by TGA.^[a]

latex conc. [g L ⁻¹]	latex content [%]	$\frac{I_{100}}{I_{001}}$	(100)			(002)		
			2θ [°]	$\beta_{1/2}$ [°]	L_{100} [nm]	2θ [°]	$\beta_{1/2}$ [°]	L_{002} [nm]
0	0	1.2	31.750	0.1731	83	34.408	0.097	95
0.5	1.7	1.6	31.764	0.156	59	34.420	0.136	68
1.0	4.3	1.5	31.785	0.163	56	34.436	0.130	71
3.0	7.0	1.3	31.765	0.174	53	34.411	0.127	73
5.0	9.1	1.5	31.804	0.177	52	34.459	0.147	63
9.0	9.5	1.3	31.811	0.145	63	34.464	0.139	66

[a] Note that the samples shown here belong to a different experimental series than those shown in Table 4.2 (see §4.10 for experimental details); this explains small differences between values for the reference samples (prepared without additive) in both tables.

Roughly speaking, when the latex concentration increases, the 2θ values tend to shift to slightly smaller angles (considering the maximum of the Lorentzian fittings) and the peaks tend to broaden. Coherence lengths decrease when the additives concentration increases. However, as in the previous section, it should be mentioned that the shifts in the position are small and close to the resolution

of the X-ray diffractometer. In general, it can be concluded that the long-range order in the crystals is not disturbed. Thus, the use of latex as additive does not lead to any important change in the perfection of the crystals.

The effect of the latex concentration on zincite was also studied by vibrational spectroscopies, that is, by FTIR and Raman spectroscopy. All FTIR spectra of the samples prepared with different concentration of P(S-AA) latex were similar. However, a slight but systematic shift in the maximum absorption peak (minimum transmission) at around 400 cm^{-1} was observed, as shown in Figure 4.12. This shift, of up to 5 meV , appears to match with the morphological evolution from the prismatic shape to the more isometric crystals, considering once more the arguments and results of Andrés-Vergés et al.^[148,170,171]

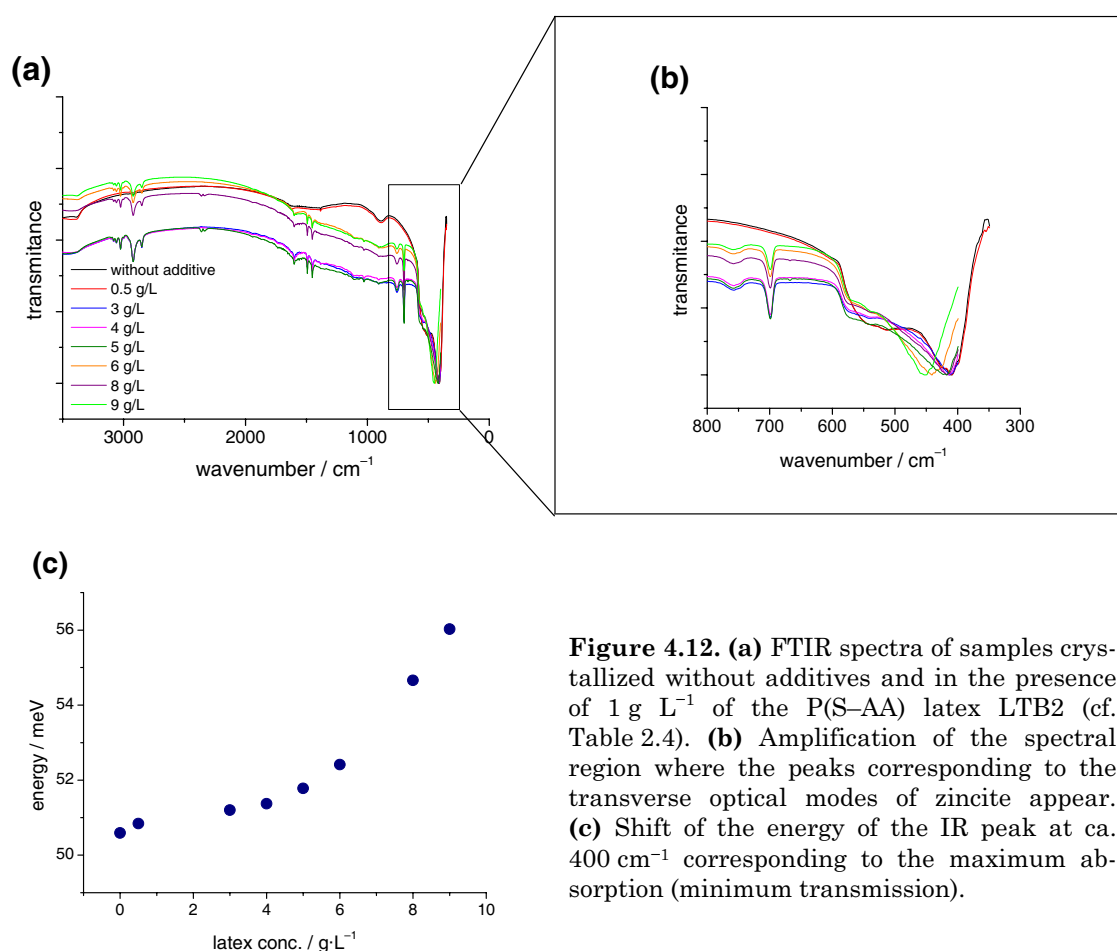


Figure 4.12. (a) FTIR spectra of samples crystallized without additives and in the presence of 1 g L^{-1} of the P(S-AA) latex LTB2 (cf. Table 2.4). (b) Amplification of the spectral region where the peaks corresponding to the transverse optical modes of zincite appear. (c) Shift of the energy of the IR peak at ca. 400 cm^{-1} corresponding to the maximum absorption (minimum transmission).

In the Raman spectra of the samples, shown in Figure 4.13, the two optical branches E_2 can be clearly identified at positions 100 and 436 cm^{-1} , in agreement with the reported values (compare to data of Table 4.1). For the different samples, no shift in the position of the peaks was detected. An additional interesting remark, regarding the lower energy spectral region (at around

3000 cm^{-1}), should be made. In this range a very strong luminescence was observed in the sample grown without additive, which is systematically quenched when the concentration of latex increases. Typically, luminescence is a non-desired feature in the vibrational spectroscopy that may interfere in the analysis of Raman spectra. However, in our case, the mentioned observation gives a preliminary information about the photoluminescence behavior of the samples, object of study in the next chapter.

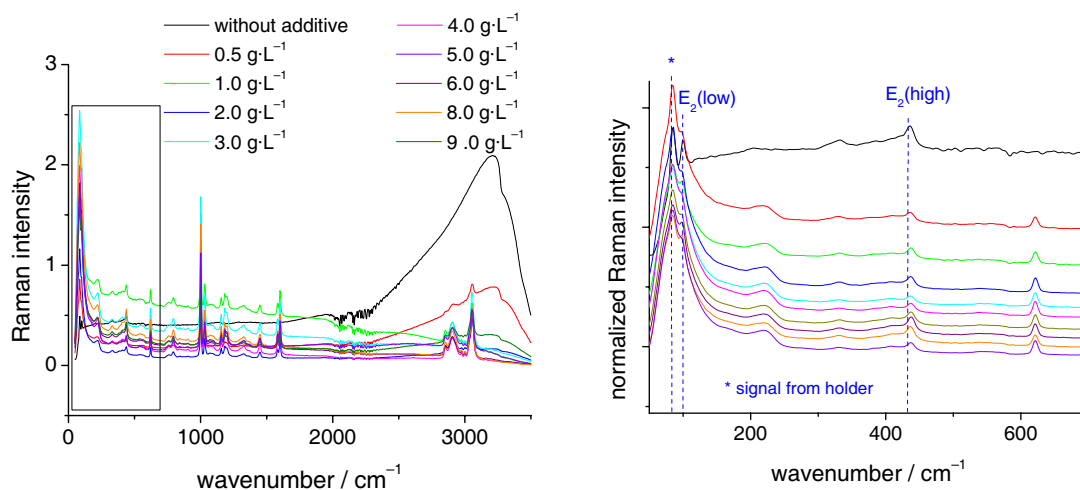


Figure 4.13 Raman spectra of samples crystallized without additives and in the presence of 1 g L^{-1} of the P(S-AA) latex LTB2 (cf. Table 2.4).

4.7 Effect of thermal annealing on the crystal structure

For the calculations of the coherence lengths by the Scherrer equation, it has been assumed that the broadening of the diffraction peaks comes essentially from the size of the scattering domains. However, strains in the lattice also cause broadening of the XRD reflections. Normally, the thermal annealing of crystals reduces the strains and the peaks become narrower.

To study the effect of thermal treatment on the crystal structure of materials, XRD powder diffractograms were registered before and after annealing for selected samples, synthesized in the absence and presence of different latex additives. The powders were heated at $600 \text{ }^\circ\text{C}$ ($\text{RT} \rightarrow 600 \text{ }^\circ\text{C}$, $10 \text{ }^\circ\text{C min}^{-1}$) under an O_2 atmosphere and annealed. The position and width of the (100) and (002) reflections, as well as the corresponding coherence length calculated by eq. (4.5), are contained in Table 4.5. The thermal annealing leads to broader rather than narrower peaks, although the effect is close to the resolution of the measurement and no quantification is possible. In general, no significant differences are observed between the values before and after polymer calcination.

Table 4.5. Comparison of the parameters of the XRD reflections (100) and (002) before and after thermal treatment (RT \rightarrow 600 °C).

peak	latex ^[a]	latex conc. [g L ⁻¹]	as grown			after annealing		
			2 θ [°]	$\beta_{1/2}$ [°]	L_{hkl} [nm]	2 θ [°]	$\beta_{1/2}$ [°]	L_{hkl} [nm]
(100)	no latex	0	31.796	0.177	52	31.753	0.188	49
	P(S-AA)	6	31.783	0.181	51	31.796	0.182	50
	P(S-MA)	3	31.759	0.142	65	31.752	0.144	64
	P(S-MA)	6	31.762	0.154	60	31.789	0.149	62
	P(S-EGMP)	3	31.743	0.267	34	31.779	0.291	32
	P(S-MAN)	6	31.761	0.156	59	31.777	0.152	60
(002)	–	0	34.460	0.179	52	34.413	0.185	50
	P(S-AA)	6	34.444	0.181	51	34.454	0.189	49
	P(S-MA)	3	34.425	0.174	53	34.415	0.175	53
	P(S-MA)	6	34.446	0.241	39	34.449	0.222	42
	P(S-EGMP)	3	34.419	0.383	24	34.440	0.374	25
	P(S-MAN)	6	34.430	0.171	54	34.435	0.168	55

[a] Structure of the latex; the latex used for the 2nd to 6th samples of this table were LT7, LT9, LT5, 02LH178, and LT4, respectively (cf. Table 2.4).

4.8 Kinetic considerations: morphogenesis of ZnO crystals in the presence of latexes

An experiment was designed to compare the morphogenesis of the zinc oxide crystals in the absence and in the presence of latex additives. Aliquots were taken from the crystallization reactor at different times between 1 and 90 min. The solids were cooled to stop the reaction, separated from the supernatant, and dried for subsequent SEM analysis. Figure 4.14 contains the micrographs of the products obtained for a reference sample, grown without polymer, and for samples synthesized with 1 and 3 g L⁻¹ of P(S-AA) latex. The figures show clearly the evolution with the time in the growth of the crystals.

In the absence of additive, zinc oxide crystals begin to form immediately after the addition of HMTA and can be already recognized after some seconds. As a general tendency, by addition of latex additive, the induction period of the crystal formation increases, and the higher the concentration is, the longer the necessary time for the begin of the particle formation will be. Regarding the formation of twin crystals, the micrographs show that in early steps the twins are not yet formed. The twinning becomes evident after several minutes.

Furthermore, in the presence of additive, lamellar structures can be easily recognized in early steps of the particle formation. In the absence of latex, some sheetlike structures are also observed at the shortest time studied (1 min), but in a minor proportion compared with the presence of latex. These observations

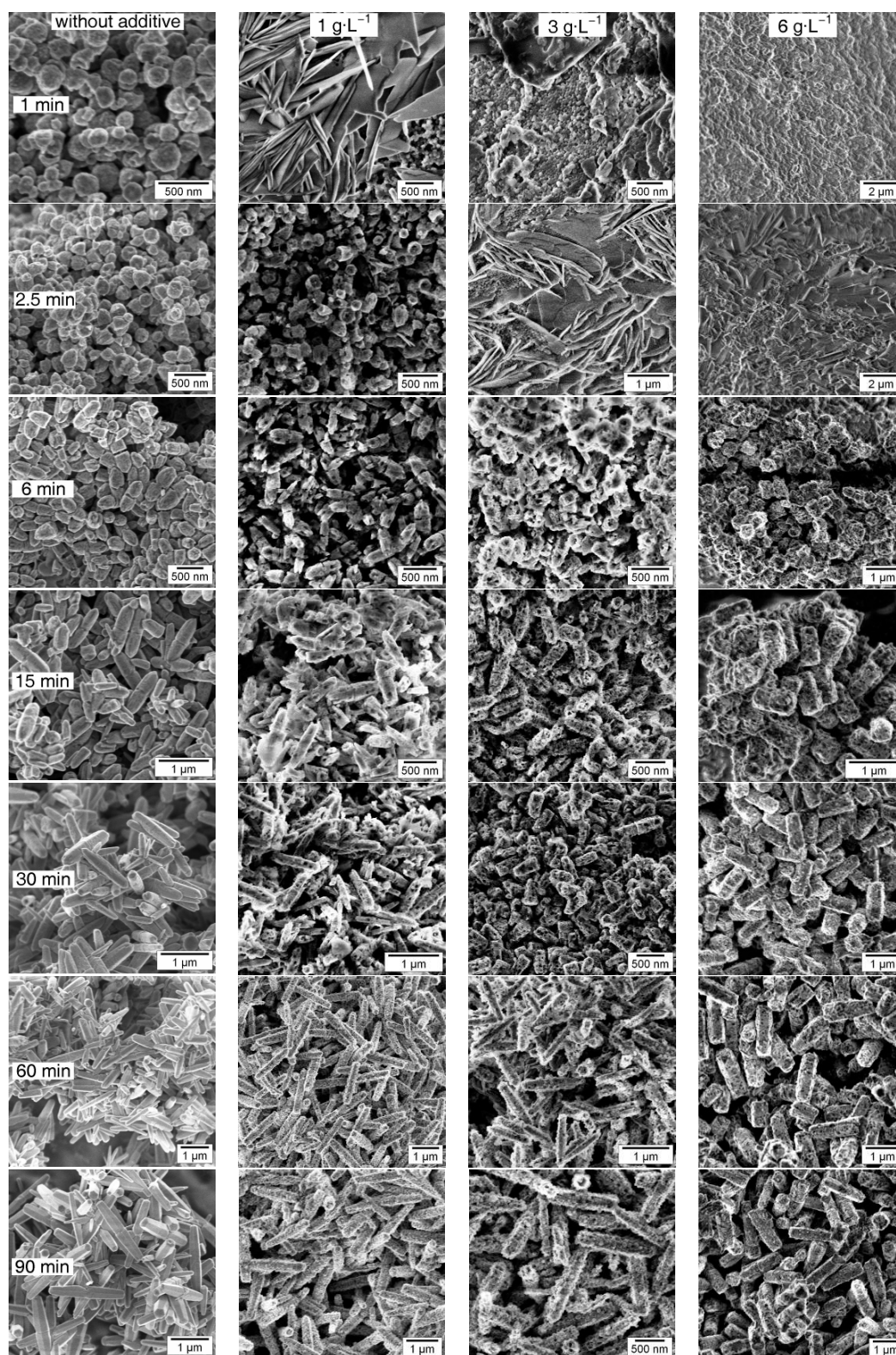


Figure 4.14 Morphogenesis of ZnO crystals precipitated in the absence and in the presence of different concentrations of the P(S-AA) latex LTB2 (cf. Table 2.4). SEM micrographs of the same column belong to the same sample and micrographs of the same row correspond to the same time.

suggest that the particle formation takes place through metastable intermediates that redissolve to form the most stable phase, zincite. The lamellar structures might be hydroxide species of zinc and nitrate, or species of zinc coordinated with the carboxylic groups from the latexes, or a mixture of the possible hydroxide species.

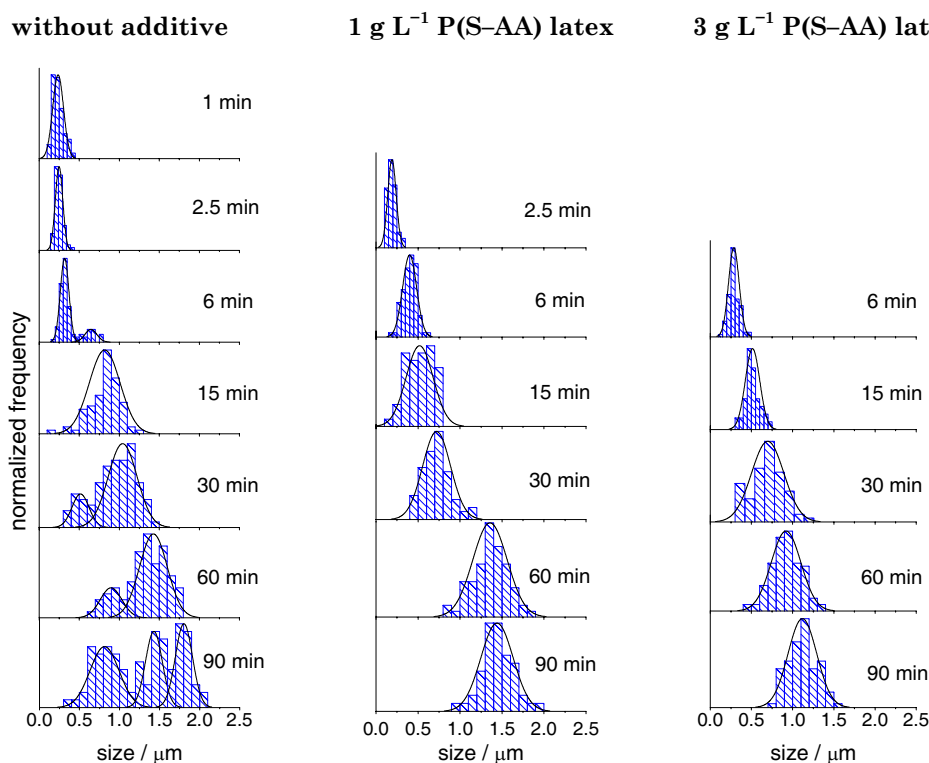


Figure 4.15. Histograms of crystal length at different reaction times in samples grown without additives and in the presence of 1 and 3 g L⁻¹ of the P(S-AA) latex LTB2 (cf. Table 2.4).

Particle size distributions were obtained for the different reaction times by statistical treatment of SEM micrographs and the results are presented in Figure 4.15. Only the length of the crystals (as previously defined) is considered, since it appears to be the most representative and evident magnitude for the kinetic analysis. The experimental difficulties to carry out kinetic studies make impossible any strictly quantitative measurement, but qualitatively it was observed that the particle size follows the expected tendency: the length increases with the time and decreases with the latex concentration. The evolution of the length (taken at the maximum of the normal curves enveloping the particle size distributions[†]) versus the time for the different concentrations is summarized in the graph of Figure 4.16. The variation of the particle size as a function of the latex concentration is in agreement with the previously described (see §3.4.5).

[†] In the case of multimodal distributions, the maximum of the peak with highest frequency was considered.

Average growth rates of 26, 22, and 16 nm min⁻¹ (calculated from the difference between the averages sizes at the first and the final time considered) can be estimated for the latex concentrations of 0, 1, and 3 g L⁻¹, respectively. Although the absolute values are only an estimation and must be taken with care, they evidence that the growth rate along the *c*-axis is reduced in the presence of latex.

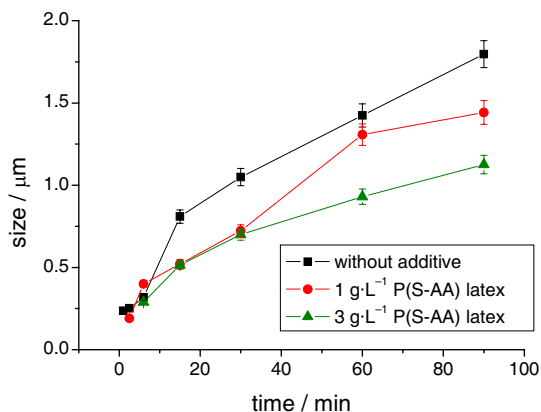


Figure 4.16. Evolution with the time of the size of crystals grown without additives and in the presence of 1 and 3 g L⁻¹ of the P(S-AA) latex LTB2 (cf. Table 2.4).

4.9 Conclusions

The crystallization of ZnO in the presence of latex particles leads to the formation of hybrid materials composed of inorganic and largely undisturbed crystalline material in which the organic polymer particles are embedded. The incorporation of the latexes in the growing crystals does not cause deterioration of the crystallinity, as proved by X-ray diffractometry. In spite of the strong influence that the latex structure (chemistry of the surface) and the latex concentration have on the external morphology, the microcrystalline structure is basically not affected. Therefore, it can be concluded that the use of latex additives do not lead to any important change in the long-range perfection of the crystals.

From infrared spectroscopy studies, the morphology of the precipitated micro- and submicrocrystals was found to affect the position and the form of the absorption peaks corresponding to the transverse optical vibration modes, in correlation with the variation of the aspect ratio in the samples.

Finally, we found clear evidences that the formation of the zincite takes places through lamellar intermediates, which seem to correspond to zinc hydroxide species containing nitrate groups from the precursor and/or carboxylic groups from the functionalized latexes. Furthermore, it was observed that the time required for beginning of the particle formation increases when latex additives are present.

4.10 Experimental section

Crystallization experiments

The samples considered in this chapter were prepared according to the formulations described in §3.7: the samples corresponding to Figures 4.2 and 4.6 to 4.8, and Tables 4.2 and 4.5 were synthesized according to Formulation 2, while the samples corresponding to Figures 4.4, 4.5, and 4.9 to 4.13, and Tables 4.3 and 4.4 were prepared according to Formulation 1.

Thermal treatment of samples

For the thermal treatment (§4.7), carried out in an oven (Linn High Term EVA-1700) under an O₂ atmosphere, the samples were placed in a porcelain combustion boat. The heating/annealing program was: (1) 5-min stabilization plateau at 25 °C (room temperature, RT); (2) RT → 600 °C, 10 °C min⁻¹; (3) 1-hour plateau at 600 °C; (4) 600 °C → RT, 10 °C min⁻¹. In some cases samples turn into yellowish or brown color after calcination. The brown color is an indication of carbon residues.

Characterization techniques

X-ray powder diffractograms were registered by a Seifert XRD 3000 TT diffractometer with Cu K α radiation ($\lambda = 1.54 \text{ \AA}$, voltage: 40 kV, current: 30 mA) in the range $2\theta = 5\text{--}120^\circ$ ($\Delta 2\theta = 0.01^\circ$ and $\Delta t = 3 \text{ s}$ in the ranges $30\text{--}50^\circ$ and $60\text{--}75^\circ$; $\Delta 2\theta = 0.03^\circ$ and $\Delta t = 1 \text{ s}$ in the ranges $5\text{--}30^\circ$, $50\text{--}60^\circ$, and $75\text{--}120^\circ$). For Figure 4.5a, the 2θ range was $2\text{--}120^\circ$ ($\Delta 2\theta = 0.03^\circ$ and $\Delta t = 3 \text{ s}$). Temperature-dependent diffractograms (Figure 4.5b) were measured in the range $5\text{--}75^\circ$ ($\Delta 2\theta = 0.03^\circ$ and $\Delta t = 2 \text{ s}$) in an analogous device equipped with an MRI TC radiation heating chamber (maximal error in the temperature measurement up to $\pm 5\%$). The heating rate was $10 \text{ }^\circ\text{C min}^{-1}$ and a stabilization time of 5 min was provided before the beginning of the measurements.

Thermogravimetric analysis (TGA) was carried out with a thermobalance Mettler TG50 (or alternatively with a Mettler Toledo ThermoSTAR TGA/SDTA 851) under an oxygen atmosphere (heating rate of $10 \text{ }^\circ\text{C min}^{-1}$, RT → 600 °C). TGA-MS curves were measured with a TGA/SDTA 851 coupled with a Balser MS/Netsch STA449 C mass detector (same heating rate as conventional TGA).

FTIR spectra were measured in a Nicolet Magna 850 spectrometer. The pellets used for the measurements were prepared as similar as possible to avoid differences caused by matrix effects, mixing homogeneously the sample (1–2 mg, weighed by a precision balance) with KBr (ca. 250 mg, Aldrich).

Raman spectra were registered from the original powders in a Bruker RFS100 spectrometer equipped with a Nd:YAG laser source (1064 nm, 510 mW), working at a power of 450 mW and accumulating 100 scans.

Morphogenesis experiments

A synthetic pathway analogous to Formulation 2, as reported §3.7, was carried out for the morphogenesis experiments (Figures 4.14 to 4.16). A 5-mL aliquot of the reactor content was taken with a syringe at different reaction times and immediately injected in a 10 mL round flask placed into an ice-water bath. A small portion of milliQ water was added to accelerate the cooling process and to stop the reaction as rapidly as possible. The aliquot was centrifuged and the product was dried under vacuum at 40 °C for later SEM observation. Scanning electron microscopy (SEM) micrographs were taken with a field-emission microscope (LEO EM1530 Gemini) applying an acceleration voltage of 1 kV. Particle size histograms and distributions were obtained as previously stated (§3.7).

Chapter 5

Influence of latex on the physical properties of zinc oxide: a spectroscopic investigation

The perfect crystal is one of the idealizations commonly found in theoretical physics and science fiction.

—A. M. Stoneham^[181]

5.1 Introduction

Physical properties of crystals, especially optical, magnetic, and electrical properties, may be strongly affected by the morphology, size, presence of impurities, or presence of defects in the crystal structure. In the previous chapter, it was concluded that, although latex particles become incorporated to give ZnO–polymer hybrid materials, the long-range order of crystalline ZnO is not disturbed by the presence of latexes. Here, we will focus on the local perfection of the materials (i.e., on the defect structure) and its relationship with the physical properties.

Beside all the known uses of zinc oxide (pigments, biomedicine, catalysis, etc.) new promising applications in optoelectronic devices, lasing, or solar cells—to mention some examples—seem to be possible. Therefore, the investigation of this semiconductor is the key issue of the research of many scientists. The study of the defects stays in the foreground of this scenario. Intrinsic or extrinsic defects can act as electron donors or acceptors and determine the physical features of semiconductors. In the past, the *n*-type conductivity conventionally observed in ZnO has been often attributed to oxygen vacancies (V_O) or interstitial zinc atoms (Zn_i) acting as donors, but now it is commonly believed that hydrogen and group-III elements are the most probable donors in ZnO under equilibrium conditions.^[182] Synthesis of *p*-type ZnO, although reported in the last years (see the review of Look^[182]), remains still a challenge and requires proper doping and defect control.

Energetic transitions responsible for absorption and emission are typically explained in terms of shallow and deep-level donors/acceptors. However, there is no consensus in the ascription of these donors and acceptors to concrete entities

in the zinc oxide structure, and many contradictions are found in literature. Especially controversial is the origin of the frequently observed visible emission. Depending on sample preparation, emission peaks in the whole visible range (blue, green, yellow, orange, and red emissions) have been reported and attributed without unanimity to all possible defects (i.e., interstitial zinc and oxygen, zinc and oxygen vacancies, antisites, and substitutional impurities). The discrepancy is even larger when the mechanisms of the absorption and emission processes are concerned. Thus, the defect structure of zinc oxide is a matter open to debate.

In this chapter, the ZnO–latex materials are studied by photoluminescence (PL) spectroscopy and electron paramagnetic resonance (EPR) to obtain information on defect centers and analyze the influence of latex particles on the optical and paramagnetic properties.

5.2 Fundamentals of defects in solids

5.2.1 Point defects in zinc oxide

In pure (*stoichiometric*) ZnO, point defects arise intrinsically through the translocation of zinc or oxygen atoms from their original place to an “incorrect” position. Experimentally, zinc- or oxygen-rich conditions result in nonstoichiometric ZnO, with slight excess of zinc or oxygen. The possible defects in both stoichiometric and nonstoichiometric ZnO are listed in Table 5.1 using the Kröger–Vink notation.^[28,183] Instead of using formal charges (represented with + or –, as conventional), it is usual to define *effective charges* with respect to the ideal unperturbed crystal. In this case, a positive charge on the defect is represented by superscript dot (\bullet),[†] and a negative charge is shown by a prime ($'$); neutral sites may be indicated explicitly with a superscript cross (\times). Defects in zinc oxide can be classified in the following types:

- (i) *vacancies*: empty sites in the oxygen sublattice (V_O) or in the zinc sublattice (V_{Zn}).[‡]
- (ii) *interstitial atoms (ions)*: oxygen (O_i) or zinc (Zn_i) atoms (ions) in interstices.
- (iii) *ions on lattice places*: zinc ions on zinc positions (Zn_{Zn}) or oxygen ions on oxygen positions (O_O).
- (iv) *antisites*: zinc atoms (ions) occupying oxygen lattice places (Zn_O) or vice versa (O_{Zn}).

[†] Not to be confused with the radical dot.

[‡] According to the IUPAC recommendations,^[183] the V symbolizing vacancies should be in italics, to avoid confusions with the symbol of vanadium, V.

Table 5.1. Nomenclature of defects in zinc oxide.

General notation	Specific notation in ZnO ^[a]
D, D [×] = Donor (of electrons) ^[b]	V _O = oxygen vacancy
D [•] = Singly ionized donor	V _{Zn} = zinc vacancy
D ^{••} = Doubly ionized donor	Zn _i = Zinc in an interstice
A, A [×] = Acceptor (of electrons) ^[b]	O _i = Oxygen in an interstice
A ['] = Singly ionized acceptor	O _O = Oxygen in oxygen lattice site
A ^{''} = Doubly ionized acceptor	Zn _{Zn} = Zinc in zinc lattice site
h [•] = free hole	O _{Zn} = Oxygen in zinc lattice site
e ['] = free electron	Zn _O = Zinc in oxygen lattice site

[a] Effective charges of each defect will be specified according to the general notation (e.g., V_O[×], O_i[']).

[b] According to the Kröger–Vink notation, defects with no effective charge (relative to the unperturbed lattice) may be indicated explicitly with a superscript cross.

5.2.1.1 Concentration of point defects

The concentration of intrinsic point defects can be estimated by statistical thermodynamics.^[184] The entropy of a system with N ions pairs containing n_S Schottky defects (see §5.2.1.2) at a certain absolute temperature T is given by the Boltzmann formula,

$$S = k_B \ln W \quad (5.1)$$

where k_B is the Boltzmann constant and W is the number of ways of distributing randomly n_S defects over N possible sites. Using the probability theory, the latter magnitude can be expressed as

$$W = \frac{N!}{(N - n_S)! n_S!} \quad (5.2)$$

Since cations and anions are present in the lattice, the overall value of W is the product of the anions contribution (W_a) and the cations contribution (W_c), that is, $W = W_a W_c$, and the entropy change is given by

$$\Delta S = k_B \ln W = k_B \ln \left(\frac{N!}{(N - n_S)! n_S!} \right)^2 = 2k_B \ln \frac{N!}{(N - n_S)! n_S!} \quad (5.3)$$

Applying the Stirling approximation ($\ln N! \approx N \ln N - N$), eq. (5.3) can be written as

$$\Delta S = 2k_B [N \ln N - (N - n_S) \ln(N - n_S) - n_S \ln n_S] \quad (5.4)$$

If the formation enthalpy of n_S Schottky defects is assumed to be $n_S \Delta H_S$, being ΔH_S the formation enthalpy of a single defect, the Gibbs free energy change is given by

$$\Delta G = n_S \Delta H_S - T \Delta S = n_S \Delta H_S - 2k_B [N \ln N - (N - n_S) \ln(N - n_S) - n_S \ln n_S] \quad (5.5)$$

At equilibrium conditions

$$\left(\frac{d\Delta G}{dn_S}\right) = 0 \quad (5.6)$$

Thus, differentiating eq. (5.5) and equating to zero,

$$\Delta H_S - 2k_B T [\ln(N - n_S) + 1 - \ln n_S - 1] = 0 \quad (5.7)$$

we obtain

$$\Delta H_S = 2k_B T \ln\left(\frac{N - n_S}{n_S}\right) \quad (5.8)$$

and solving for n_S yields

$$n_S = (N - n_S) \exp\left(-\frac{\Delta H_S}{2k_B T}\right) \quad (5.9)$$

As $N \gg n_S$, the number of Schottky defects can be approximated as

$$n_S \approx N \exp\left(-\frac{\Delta H_S}{2k_B T}\right) \quad (5.10)$$

Applying an analogous treatment, the number of Frenkel defects (see §5.2.1.2), n_F , is given by

$$n_F \approx (NN_i)^{1/2} \exp\left(-\frac{\Delta H_F}{2k_B T}\right) \quad (5.11)$$

Using first-principles pseudopotential methods, Kohan et al.^[185] calculated systematically the formation energy of all native point defects of ZnO (interstitials, vacancies, and antisites in their relevant charge states), concluding that, depending on the zinc partial pressure, the most abundant defects should be zinc and oxygen vacancies. At high zinc partial pressure, the formation energy of oxygen vacancies was found to be lower than the formation energy of zinc interstitials; therefore, oxygen vacancies should be predominant. At low zinc partial pressure (oxygen-rich conditions), zinc vacancies should predominate, since the calculated formation energies were lower than those calculated for other defects such as oxygen interstitials.

5.2.1.2 Defect equilibria in ZnO

A large number of defect equilibria can be written for zinc oxide. Here, following Neumann,^[186] they are briefly presented. First of all, equilibria corresponding to

the so-called Schottky and Frenkel defects, two classically considered types of point defects, have to be taken into account. A *Schottky defect*, schematically illustrated in Figure 5.1a, occurs when corresponding cations and anions are missing from their lattice sites. For singly ionized oxygen and zinc vacancies, this can be expressed as



A *Frenkel defect* is formed when an ion moves from its normal lattice position, creating a vacancy, and occupies an interstitial position (see Figure 5.1b). Two Frenkel-defect equilibria are possible in zinc oxide:

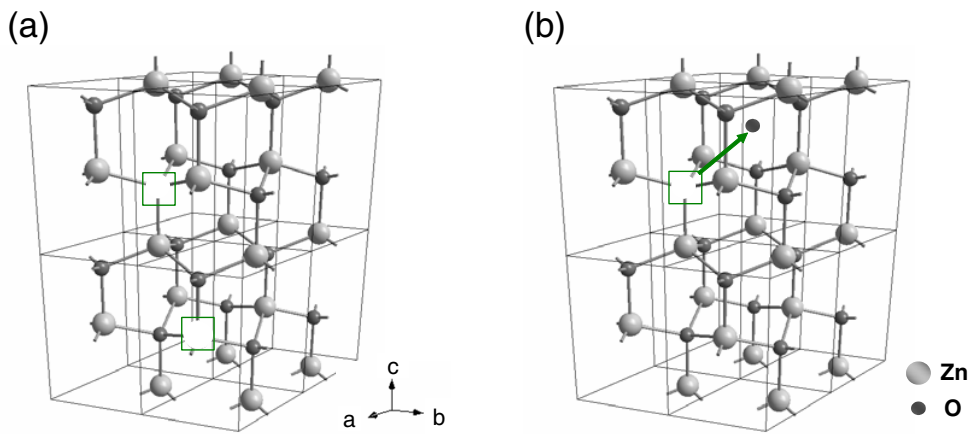
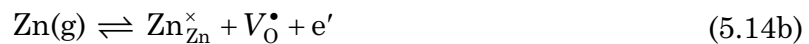


Figure 5.1. (a) Schottky and (b) Frenkel defects in a ZnO lattice.

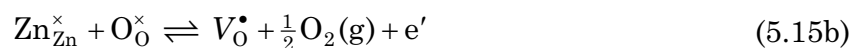
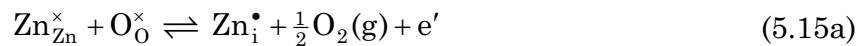
In addition to the previous equilibria, formal quasi-chemical reactions of formation of defects can be written. Zinc excess can be considered as the dissolution of zinc in ZnO to form singly ionized zinc interstitial



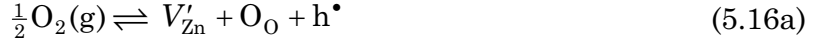
or singly ionized oxygen vacancies



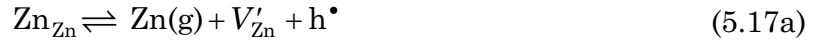
Alternatively, zinc excess can also be expressed as a partial vaporization of oxygen and the formation of Zn^{\bullet}_i and V^{\bullet}_{O} is given by



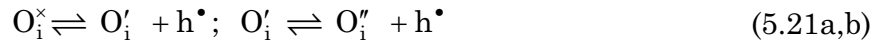
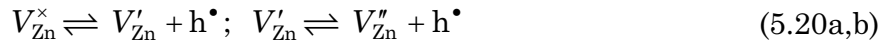
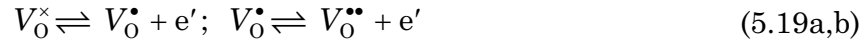
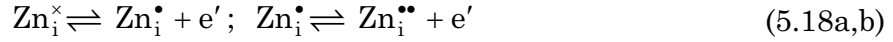
In an analogous way, the dissolution of oxygen in ZnO to form singly ionized zinc vacancies or oxygen interstitial can be formulated as



The formation of these defects can be expressed as a partial vaporization of zinc, according to the quasi-chemical reactions



All former defects can exist with no effective charge, singly ionized, or doubly ionized. This can be expressed by the equilibria



Although all these species are theoretically possible, not all have the same probability and some can be energetically less favored. This is an object of discussion and theoretical studies. For example, Van de Walle^[187] has pointed out after first-principles calculations that, for any Fermi-level position, V_0^\bullet is always higher in energy than either $V_0^{\bullet\bullet}$ or V_0^\times ; thus the singly ionized oxygen vacancy should never be thermodynamically stable. However, he indicated that it is possible to create this defect in a metastable manner by excitation, for instance by light.

5.2.2 Investigation of defects by photoluminescence spectroscopy

5.2.2.1 Basics of photoluminescence spectroscopy

Point defects have localized energy states within the band gap. Therefore, the defect structure of a solid determines the features of absorption and emission spectra. Unfortunately, the unambiguous assignment of an observed band with a particular defect is not a trivial task, because different defects can cause overlapping bands with similar energies.

The principles of photoluminescence (PL) spectroscopy are simple. The sample under observation is irradiated with light of known wavelength (a laser light or the light of a lamp going through a monochromator) and excited from the initial state to a state of higher energy. The sample can relax nonradiatively or emit

light spontaneously. This radiating emission is called *photoluminescence* (*luminescence* arising from *photoexcitation*) and can be classified in *fluorescence* and *phosphorescence*. From the mechanistic point of view, in the former case, the excited state and the final state have the same spin multiplicity, whereas in the latter the transition involves a change in spin multiplicity, typically from triplet to singlet or vice versa. Phenomenologically speaking, phosphorescence is used to describe long-lived luminescence (10^{-4} s or longer).^[188]

In ionic and semi-ionic crystals most defects are sensitive to the position of the atoms (ions) in the neighborhood and the absorption and emission depend on the vibration of these atoms. The processes of absorption and emission can be represented with the so-called *configuration-coordinate diagram*, illustrated in Figure 5.2. In this diagram, the total potential energy of the ground and excited states is approximated by parabolic curves (harmonic oscillator approximation) of the form

$$E = \frac{1}{2} KQ^2 \quad (5.22)$$

where K is a force constant and Q is the configuration coordinate, determined by the internuclear distance. After the absorption event, the electron distribution changes and the lattice relaxes to a next equilibrium position $Q_0 + \Delta Q$.^[189] According to the *Frank–Condon principle*, transitions from the ground to the excited state occur in a very short time (in the order of femtoseconds) and the configuration coordinate does not have time to change, so that transitions can be represented as vertical lines.

In the configuration-coordinate diagram, the vibrational states are schematically represented by horizontal lines. Different transitions between vibrational states of the ground and excited state are possible, although some transitions have higher probability than others. A typical transition is that from the lowest vibrational ground state to the vibrational excited state with the same configuration.

The system relaxes nonradiatively to a lower vibrational state of the excited state. Radiative emission may occur corresponding to the transition from this state to a vibrational level of the ground

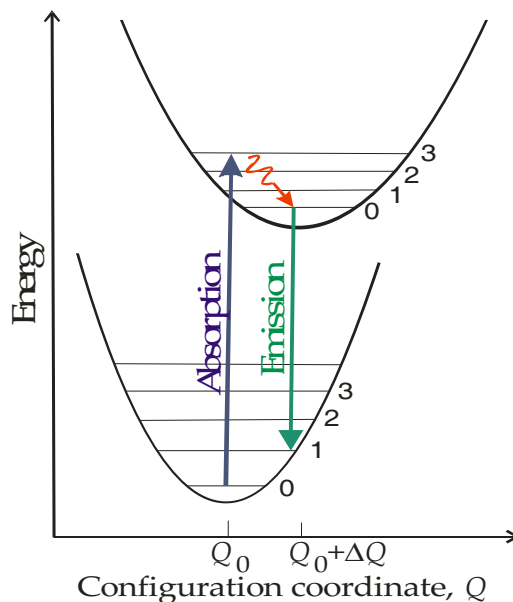


Figure 5.2. Configuration-coordinate diagram, according to the Frank–Condon principle.

state. In the described absorption–emission process, the energy corresponding to the emission is lower than that of the absorption; this is known as *Stokes shift*. Transitions between other vibrational states of the ground and excited state can originate as well the opposite situation, that is, emission energy higher than absorption energy; such a case, less common, is known as *anti-Stokes shift*.

Emission and excitation spectra: In photoluminescence, two types of spectra have to be considered:

- the photoluminescence *emission spectrum*, exciting the sample at a fixed wavelength and registering the emission intensity as a function of the emission wavelength; and
- the *photoluminescence excitation (PLE) spectrum*, fixing an emission wavelength (usually at an emission maximum) and registering the emission intensity as a function of the excitation wavelength. PLE spectra, differently from absorption spectra, are not influenced by absorption effects that do not lead to photoluminescence; excitation spectra show the absorption leading to radiative emission.

Excitons, donors, and acceptors: In a semiconductor, when a photon excites an electron to the conduction band, it leaves behind a hole in the valence band. This bound electron–hole pair can be considered as a quasi-particle called *exciton*, whose energy sits slightly below the band edge, at a distance determined by the *binding energy*. If the exciton possesses a low binding energy and a high mobility, it is called *free exciton (FE)*, also referred as *Mott–Wannier exciton*. The FE can move “freely” in the lattice until radiative or nonradiative recombination takes place (this process is often called *exciton annihilation*), but it can also meet a defect. In this latter case, the FE may recombine nonradiatively or it can lose some energy and form a so-called *bound exciton (BE)*. The binding energy of the BE depends not only on the Coulombic interaction between electron and hole, but also on the local potential created by the defect. Theoretically, BEs can be bound to neutral or charged donors/acceptors, but the binding to neutral donors/acceptors is by far the most important case.^[163]

Both intrinsic (or native) and extrinsic (impurities) defects can act as donors and acceptors of electrons. Donor or acceptor levels close to the conduction or the valence band are defined as *shallow*. If the energy of these levels is relatively far from the band edges, they are labeled as *deep*. Parallel to excitonic transitions (due to free and bound excitons), other defect-related emissions can be observed in photoluminescence spectra: (i) transition from the conduction band (or a shallow-donor level) to a deep-acceptor level; (ii) transition from a deep-donor level to

the valence band (or a shallow-acceptor level); and (iii) recombination of *donor–acceptor pairs* (DAP).

5.2.2.2 Excitonic transitions and UV emission in ZnO

Different exciton-related emissions have been reported for zincite in the photon energy range of 3.3–3.45 eV. A systematic overview of the optical transitions in zincite and the reported data is given by Özgür et al.^[163] in an extensive review published recently. In bulk ZnO at low cryogenic temperatures the free exciton is observed at about 3.377 eV.^[190] Other emission peaks in the UV range of 3.34–3.37 eV are assigned to excitons bound to shallow donors (shallow-donor-bound excitons) in a neutral or an ionized state. However, the nature of these donors remains unclear and many possibilities have been pointed out. Impurities such as halogen atoms or group-III elements (Al, Ga, In)^[191] can act as shallow donors. Oxygen vacancies^[28] and zinc interstitial^[192] have been also proposed, although the oxygen vacancy does not seem to be a probable candidate, since V_O is rather a deep donor than a shallow donor.^[182,187,192] In the last years a new possibility has been suggested: hydrogen. In other semiconductors, hydrogen is amphoteric and counteracts the prevailing type of conductivity, being used as passivating agent. In ZnO, contrarily, hydrogen is always positive and acts as a donor.^[187] According to some authors,^[187,193] hydrogen should be the prevalent shallow donor in ZnO and responsible of its intrinsic n -conductivity.

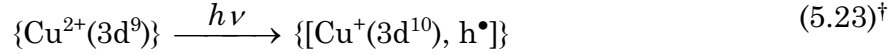
Besides the excitonic-related transitions an emission peak attributed to shallow-donor–shallow-acceptor recombination has been found at about 3.22 eV. Thonke et al.^[194] considered this peak to be related with nitrogen impurities and the shallow acceptor is assumed to be nitrogen on an oxygen site (N_O). Meyer et al.^[190] found a peak at the same position in intentionally N-doped ZnO, together with a peak at 3.235 eV. Differing from Thonke et al., they ascribed the peak at 3.235 eV to the N_O shallow acceptor and the peak at 3.22 eV to another residual unidentified.

5.2.2.3 Visible emission in ZnO

Additionally to the excitonic transitions in the UV region, a broad visible emission appears often in ZnO. As pointed out in the introduction of this chapter, the cause of this emission is controversial and has been debated for decades.

Green emission: A green band in the range 2.2–2.5 eV (typically 2.45–2.5 eV) is the visible emission most commonly found in ZnO, but there is no unanimity about the origin of this band.

A structured green-emission band was attributed by Dingle^[195] to residual copper impurities. Cu^{2+} has electronic structure $3d^9$ and can act as neutral acceptor, A^\times in Kröger–Vink notation (see Table 5.1), and capture an electron to give Cu^+ with electronic structure $3d^{10}$ (A), which bound with a hole gives the excited state:



Garces et al.^[196] found an unstructured green emission at 2.48 eV in their as-grown ZnO samples and a structured band at a nearby position (2.43 eV) after annealing at 900 °C. Before annealing Cu^+ was found to be the predominant species and they attributed the observed emission to a donor–acceptor pair (DAP) recombination between a singly ionized shallow donor, D^\bullet , and the singly ionized acceptor Cu^+ (A). After annealing, they agreed with the explanations of Dingle.

However, most authors ascribe the green emission in ZnO to intrinsic defects. Already in early studies, Kröger and Vink^[197] and Riehl and Ortmann^[198] proposed oxygen vacancies as centers responsible for the green emission, although the former authors suggested also Zn_i as an alternative. In an attempt to conciliate positions, Özgür et al.,^[163] have suggested that the green luminescence may be actually attributed to different origins: bands with characteristic fine structure are most probably ascribable to copper impurities, whereas similar structureless emission can be attributed to native point defects such as V_O or V_{Zn} . Since the first suggestions of Kröger and Vink, a large number of possibilities, invoking not only oxygen vacancies but also other types of defects, have been proposed:

- (i) Recombination of a photogenerated hole in the valence band with a donor V_O^\bullet .^[199,200]
- (ii) Transitions between different states of the oxygen vacancy. Leiter et al.^[201,202] proposed that the ground state of the neutral oxygen vacancy (V_O^\times), a diamagnetic singlet state, reaches after photoirradiation an excited singlet state, which relaxes nonradiatively to an emissive, paramagnetic triplet state.
- (iii) Transition of an electron close to the conduction band to a deep level $V_O^{\bullet\bullet}$.^[203–205]
- (iv) Recombination of a donor V_O^\bullet with an acceptor V_{Zn}' (DAP recombination).^[206,207]
- (v) Recombination of an electron in the conduction band with an acceptor V_{Zn}' .^[185,208]
- (vi) DAP recombination of an donor Zn_i with an acceptor V_{Zn}' .^[208]

[†] The braces $\{\}$ are used here to indicate that the process takes place in the solid state.

- (vii) Complex defects involving Zn_i .^[209]
- (viii) Antisites Zn_O ^[210] and O_{Zn} .^[211]

Furthermore, some other alternatives, such as chemisorbed oxygen^[212] or sulfur impurities,^[213,214] have also been suggested.

Yellow-to-orange emission: In addition to the green band, a yellow-to-orange band in the range 1.9–2.2 eV has been often reported, and its origins remains also unclear. In the previously mentioned work, Kröger and Vink,^[197] suggested the ascription of the orange band to V'_{Zn} centers. Yellow emission has been found in ZnO doped with lithium and other impurities (such as selenide^[213] or aluminum^[215]) and attributed to impurity acceptor levels. However, this band has also been found in undoped samples.^[163,216–221] Interstitial oxygen appears to be a probable candidate for this emission.^[216,218,220]

Other emission bands: Emission in the red region (1.55–1.75 eV) has also been sometimes reported.^[163,214,219] In the last years, furthermore, an unusual blue peak in the range 2.65 to 2.95 eV has been found in different ZnO samples.^[222–229] Some authors have attributed this blue emission to transitions from oxygen vacancies acting as shallow donors to the valence band,^[223,229] whereas others suggest a transition from Zn_i to the valence band.^[226]

5.2.3 Investigation of defects by electron paramagnetic resonance

Some defects in solids exhibit paramagnetism, as a result of unpaired electron spins. A useful instrumental technique to study paramagnetic defects is the electron spin resonance (ESR) or electron paramagnetic resonance (EPR). This technique is based on the transitions between spin states induced when a magnetic field is applied. EPR measures the resonance lines resulting from the interaction between the defect and the magnetic field, according to the resonance condition

$$h\nu = g\mu_B B_0 \quad (5.24)$$

where ν is the frequency of the applied magnetic field B_0 , μ_B is the Bohr magneton [$eh/(4\pi m_e)$], and g is a dimensionless scalar called g -factor (or g -value). For the free electron, the g -factor has a value of $g_e \approx 2.002319$. In anisotropic crystals, the g -factor is composed of two components, g_{\parallel} and g_{\perp} , parallel and perpendicular to the c -axis, respectively. The g -factor is then given by^[230]

$$g = \left(g_{\parallel}^2 \cos^2 \theta + g_{\perp}^2 \sin^2 \theta \right)^{1/2} \quad (5.25)$$

where θ is the angle between the magnetic field and the c -axis.

In ZnO, only singly ionized defects can be paramagnetic and show EPR signals, whereas neutral and doubly ionized defects will not give any signal. The defects can interact with the ^{67}Zn atoms, the only zinc isotope (isotopic abundance of 4.1% in natural zinc) with nuclear spin ($I = 5/2$), and give a hyperfine structure. The position of g is, in principle, characteristic for the type of defect, although, as in the case of the visible-emission bands, there is no agreement on the assignment of the lines and many contradictions can be found in literature.^[230] A characteristic signal at $g \approx 1.96$ ($g_{\parallel} = 1.957$ and $g_{\perp} = 1.956$), which seems to be attributable to shallow donors,^[187,193,231] is very often observed; its position seems to be independent of the shallow-donor identity.^[231] In a frequently cited work, Vanheusden et al.^[199,200] assigned this signal to singly ionized oxygen vacancies and correlated it with the green emission. However, this ascription is criticized by most authors. A signal at $g \approx 1.99$ ($g_{\parallel} = 1.9945$ and $g_{\perp} = 1.9960$) has been considered to be due to V_{O}^{\bullet} ,^[187,231] although it has been also attributed to O'_i .^[230] In addition, a further EPR signal assigned to V'_{Zn} has been found at g values of 2.00 to 2.02.^[230]

5.3 Optical properties of ZnO–latex hybrid materials

5.3.1 Room-temperature photoluminescence spectra

Photoluminescence (PL) excitation and emission spectra of pure ZnO and ZnO–latex hybrid samples were measured in the solid state, placing the crystalline powders between two quartz plates of a specially designed cell. Suspensions of the samples were not stable for the time required for the measurements; therefore, only solid-state spectra are considered. Slight differences in sample preparation are unavoidable in our solid-state procedure: since the samples contained changing quantities of polymer and had also different morphologies, they might be differently packed. However, considering that the preparation was similar in all cases, and taking into account that the latex introduces only small differences in the density—the density of ZnO is much higher than the density of the latex, and quantities up to 10% of the polymer do not imply large changes in the final density of the hybrid—, we are confident that the measurements are qualitatively comparable. Additionally, independent measurements confirmed the validity of our experimental method: PL spectra of suspensions of ZnO nanoparticles and solid-state spectra of the same samples following our method showed comparable results.^[232]

Following the strategy of previous chapters, a reference ZnO sample prepared in the absence of any additive was first studied and then compared with hybrid samples synthesized in the presence of latexes of different chemical nature. Next, the effect of the latex concentration was considered for the case of poly(styrene–acrylic acid) latexes.

PL spectra of pure-ZnO samples: The excitation spectrum of a pure ZnO reference sample,[†] registered at emission wavelength of 560 nm (2.21 eV), shows a pronounced peak at 384 nm (3.23 eV), after the onset of excitation, as it can be observed in Figure 5.3. This figure presents also emission spectra recorded at different excitation wavelength for the same sample. Two emission bands can be distinguished: a narrow and weak UV peak at 385 nm (placed at almost the same position as the excitation peak, with no significant Stokes shift) and a very broad and more intense green-yellow visible band centered at around 560 nm (~ 2.2 eV). From the experimental results shown in Figure 5.3, an excitation wavelength of 310 nm (4.00 eV) was selected for further experiments.

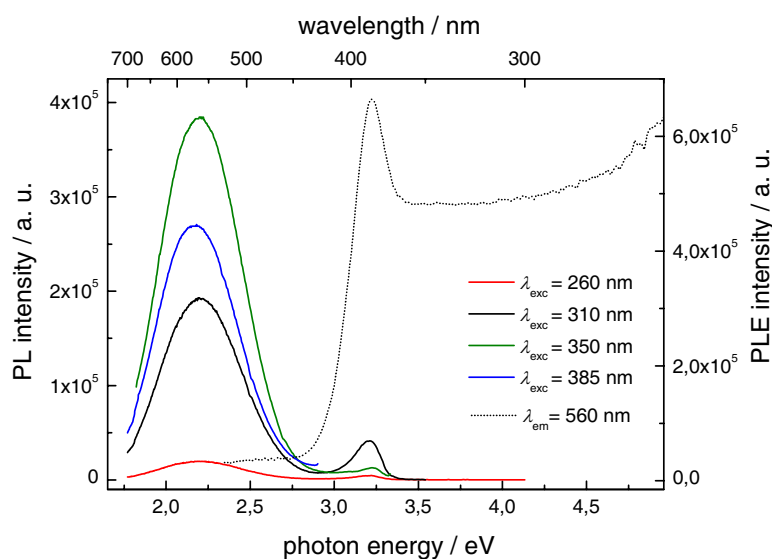


Figure 5.3. PL emission spectra (solid lines) of a pure ZnO reference sample registered at different excitation wavelengths (260, 310, 350, and 385 nm), together with the PL excitation (PLE) spectrum (dashed line) of the same sample registered at an emission wavelength of 560 nm.

The UV peak can be attributed to near-band-edge exciton annihilation, whereas the origin of the visible emission—as previously discussed—is less clear. The possible origin of the green emission through copper impurities, pointed out

[†] *Reference sample* refers here to a sample of zinc oxide precipitated from aqueous medium in the absence of any additive, as described in §3.3.

by some authors (see §5.2.2.3), was ruled out after comparing the spectra of a conventional ZnO reference sample (prepared with reagent-grade $\text{Zn}(\text{NO}_3)_2 \cdot 6\text{H}_2\text{O}$) and a sample synthesized analogously but employing a high-quality copper-free zinc nitrate (see Figure 5.4). While the conventional precursor has a purity of 99.4% and contains copper in the level of ≤ 50 ppm, the high-quality zinc nitrate had a purity of 99.999% and no detectable presence of copper.[†] However, the emission spectra do not show any appreciable difference, and the visible emission is similar in both cases. Therefore, the ascription of the visible emission to interstitial or vacancy defects in the crystal structure appears to be more reasonable than substitutional impurities.

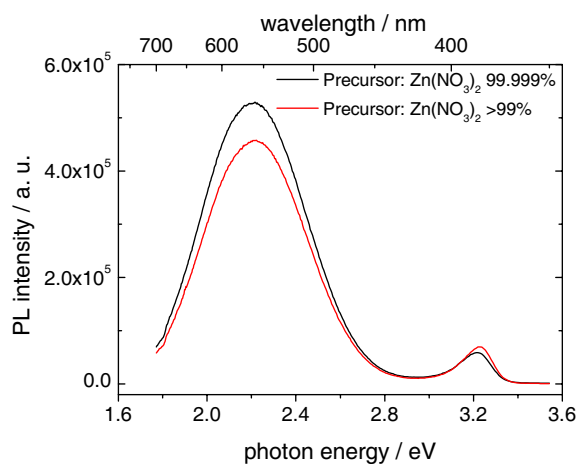


Figure 5.4. Comparison between PL emission spectra of ZnO sample prepared with zinc nitrate of different qualities: conventional reagent-grade $\text{Zn}(\text{NO}_3)_2 \cdot 6\text{H}_2\text{O}$ (purity = 99.4%) and high-quality copper-free $\text{Zn}(\text{NO}_3)_2 \cdot x\text{H}_2\text{O}$ (99.999%).

Photoluminescence versus chemical nature of the latex surface: As in previous chapters, samples prepared in the presence of poly(styrene–acrylic acid) [P(S–AA)], poly(styrene–maleic acid) [P(S–AA)], and poly(styrene–ethylene glycol methacrylate phosphate) [P(S–EGMP)] latexes are considered here. PL emission and excitation spectra of samples prepared with the same concentration (3 g L^{-1}) of these latexes are shown in Figure 5.5. The two bands observed in the pure ZnO appear as well in all samples. Additionally, in the case of the P(S–AA)-latex-containing sample, other peaks appear in the region 2.5–3 eV. This sample contains a considerable content of polymer and large aggregates of latex are not completely removed after washing, as it was judged by SEM. Thus, the additional peaks are reasonably attributable to the latex. This was confirmed by registering the spectra of pure latexes, shown in Figure 5.6. The graph presents the emission and excitation spectra of a P(S–AA) and a P(S–AA) latex, registered in the solid state after freeze-drying of the latex miniemulsion. For the analyzed latexes, the

[†] Details about further trace impurities present in the precursors are given in the experimental section, §5.6.

position of the peaks and the form of the spectra seem to be relatively independent of the surface chemistry. Very intensive emission appears in the range 2.5–3.5 eV when exciting at 4.00 eV (310 nm). In hybrid materials with low content of polymer, the emission of the latex is not significant with respect to the ZnO. In samples containing large aggregates of latex, on the contrary, emission due to the polymer can be recognizable in the spectra.

The differences in the excitation spectra of the different hybrids are also explained by the presence of polymer (compare the spectra of Figure 5.5b with the excitation spectra of the latexes in Figure 5.6).

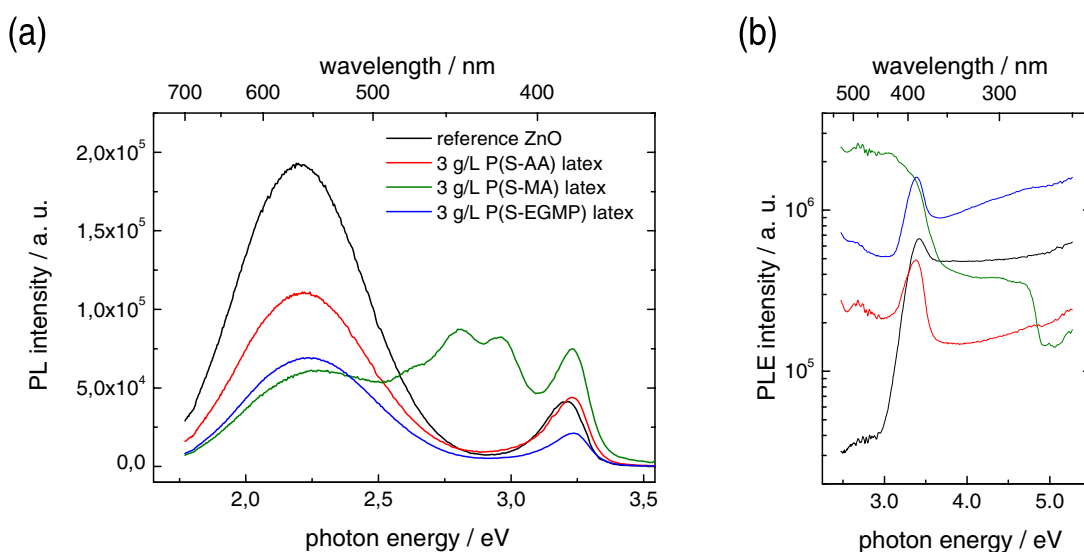


Figure 5.5. PL spectra of a pure ZnO sample (reference sample crystallized without any additive) and ZnO samples crystallized in the presence of 3 g L^{-1} of AA-, MA-, and EGMP-derived latexes (latexes LT7, LT9, and LT17 of Table 2.4): **(a)** PL emission spectra registered at an excitation wavelength of 310 nm (4.00 eV); **(b)** PL excitation spectra registered at an emission wavelength of 560 nm (2.21 eV).

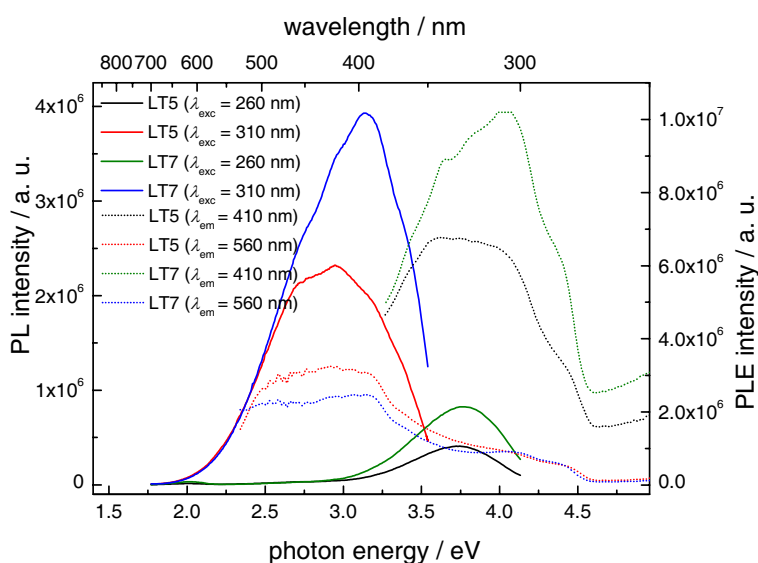


Figure 5.6. PL emission spectra (solid lines) and PL excitation spectra (dashed lines) of two representative latex samples: the P(S-AA) latex LT5 and the P(S-MA) latex LT7 (cf. Table 2.4). Spectra were registered in the solid state for the powder resulting after freeze-drying of the latex mini-emulsions.

When the polymer is removed by calcination (from room temperature to 600 °C, with a rate of 10 °C min⁻¹) under an oxygen atmosphere, the PL spectra of the samples change with respect to the nonannealed samples. This is to be observed in Figure 5.7. The visible emission is red-shifted from 560 nm (2.21 eV) in the as-grown pure ZnO sample to 603 nm (2.06 eV) in the O₂-annealed one. The visible peaks can be recognized after calcination in the sample synthesized in the presence of P(S-AA) latex: a yellow-orange peak at ~2.0–2.1 eV and a green peak at ~2.5 eV. In the sample prepared in the presence of P(S-AA) latex, the green contribution dominates the spectra after calcination. The UV-emission peak is slightly blue-shifted and, analogously, the excitation peak shifts also to higher energies (from 2.22 to 2.28 eV).

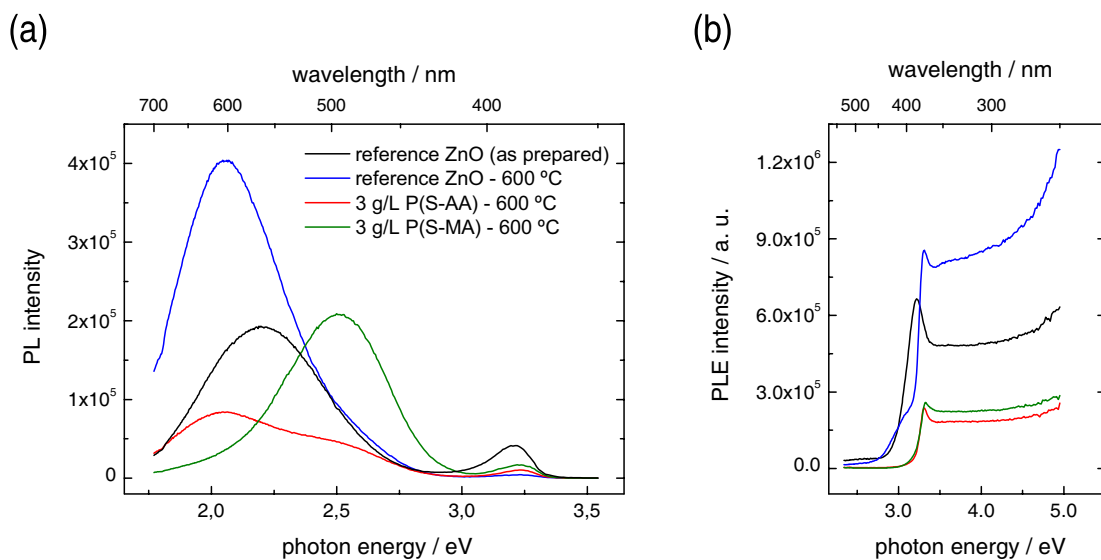


Figure 5.7. (a) PL emission spectra ($\lambda_{exc} = 310$ nm, 4.00 eV) and (b) PL excitation spectra ($\lambda_{em} = 560$ nm, 2.21 eV) of samples (the same samples of Figure 5.5) calcinated under O₂ atmosphere at 600 °C. The spectra of the pure ZnO sample before calcination is also included for comparison.

The observation of yellow-to-orange emission in ZnO samples annealed in oxidative atmosphere is not unusual and has often been reported. For instance, Studenikin et al.^[217] observed orange PL emission in ZnO films prepared by oxidative annealing, while samples annealed in a reductive atmosphere presented green emission. Yellow-orange emission appears to be related to an excess of oxygen and could be ascribed to interstitial oxygen.^[216] The almost disappearance of the excitonic emission and the parallel enhancement of the visible emission for samples thermally treated under O₂ atmosphere is also a frequent observation.^[220]

Our results suggest that the visible emission is composed of more than one contribution, probably two. Actually, the visible emission of all the samples can

be perfectly fitted to the sum of two Gaussian functions, centered in the green and in the yellow-orange regions. But why, if the oxidative atmosphere was similar for the different samples, strong yellow emission is observed in the reference sample after annealing, whereas the green band dominates the emission in the sample prepared with P(S-AA)? We can explain this as follows. Assume that both emissions are related to defects, but the concentration of defects responsible for the yellow peak increases in the presence of oxygen, while the green increases in oxygen deficient conditions. In the case of pure ZnO case, an excess of oxygen is available to create the interstitial oxygen required for the orange emission (assuming that this ascription is correct). For hybrid samples, the oxygen will be initially consumed in the combustion of the present polymer. Once the polymer has been burned out, the creation of interstitial oxygen is possible. Thus, in the sample prepared in the presence of P(S-AA), containing a reasonably low amount of latex, both bands are present, the orange being larger than the green. The sample synthesized with P(S-AA) contains large amounts of latex, and the oxygen will be consumed in its combustion. The latex material can work as a reducing agent towards ZnO in the heating/pyrolysis process; this is highly probable as ZnO can be reduced by carbon at high temperatures according to



Although the process takes place under continuous oxygen flux, the partial oxygen pressure can diminish if the amount of consumed oxygen is larger than the entrant. An involvement of oxygen vacancies in the green emission could be therefore speculated, since the concentration of this defect type should increase when the oxygen pressure decreases [consider Le Chatelier's principle in the equilibrium (5.15b)]. However, although it agrees with a "classical" assignment of the green emission, no unambiguous proves have supported this assumption.

Photoluminescence versus latex concentration: Samples precipitated in the presence of an increasing concentration of P(S-AA) latex were used to study the influence of the latex concentration on the PL spectra. The results are presented in Figure 5.8. Although both UV and visible emission are present in all the samples, their intensities and ratio change. For the reference sample, the UV peak is much smaller than the visible band, whereas for the hybrid samples, the maximum intensities of both peaks have the same order of magnitude. The main observation is that the visible emission is significantly quenched by the presence of latex. In addition, a noticeable decrease in the emission is observed when increasing the concentration of P(S-AA)-latex additive during the crystallization.

Excitation spectra of the samples, presented in Figure 5.8b, show the onset and the peak in approximately the same position, but the intensities change for the different latex concentrations.

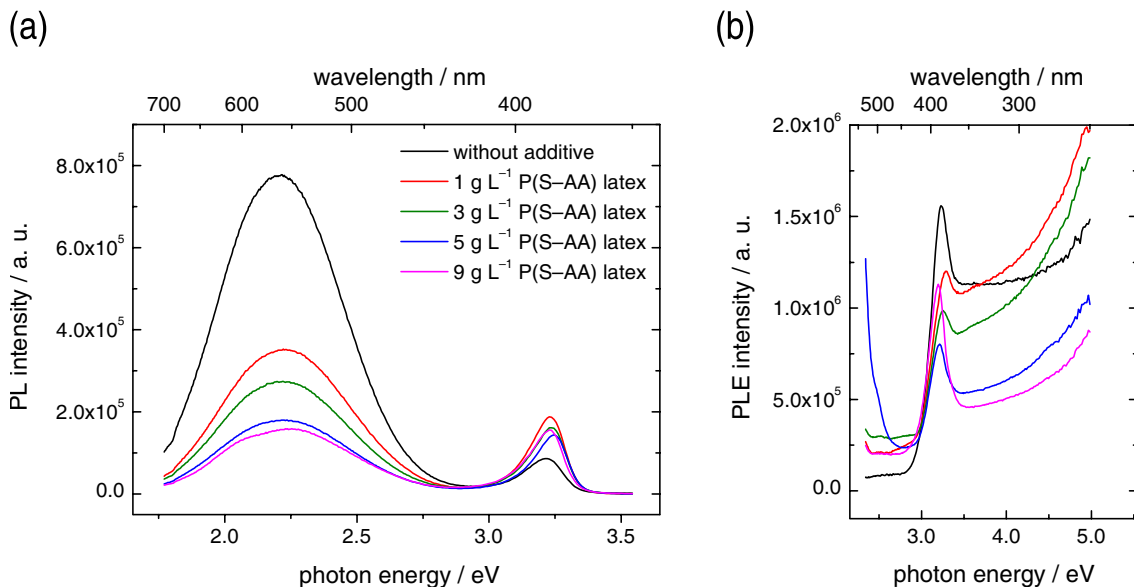


Figure 5.8. (a) PL emission spectra ($\lambda_{exc} = 310$ nm) and (b) PL excitation spectra ($\lambda_{em} = 560$ nm) of ZnO–latex hybrid samples crystallized in the presence of different concentrations of the P(S–AA) latex LTB2 (cf. Table 2.4), compared with a pure ZnO reference sample.

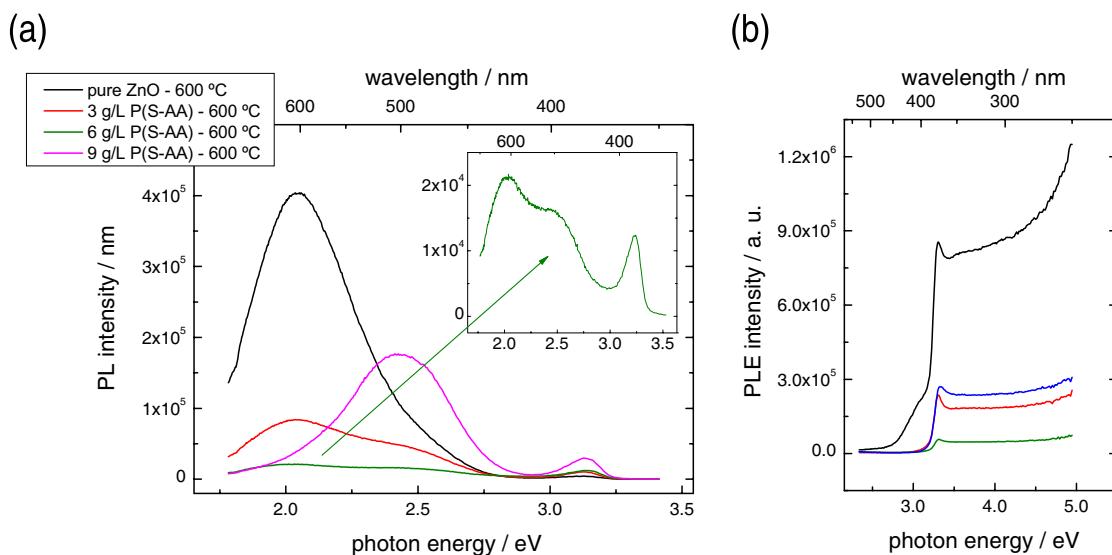


Figure 5.9. (a) PL emission spectra ($\lambda_{exc} = 310$ nm) and (b) PL excitation spectra ($\lambda_{em} = 560$ nm) of different ZnO samples after calcination under O₂ atmosphere at 600 °C. The samples were crystallized in the presence of different concentrations of the P(S–AA) latex LT7 (cf. Table 2.4).

The removal of the polymer by oxidative calcination (under an oxygen atmosphere) leads again to a split of the visible emission into two bands. As indicated before, the visible emission of the reference sample seems to shift to the red

(maximum at ~ 2.0 eV), while the UV peak slightly shifts to higher energies. Samples crystallized with intermediate latex concentration (3 and 6 g L⁻¹) show two visible components, as presented in Figure 5.9. The emission spectra of the sample obtained in the presence of the highest concentration (9 g L⁻¹) is dominated by the emission at ~ 2.5 eV, similarly to the case of the ZnO–P(S–AA) sample (cf. Figure 5.7). The explanations given above appear to be in complete accordance with these results. However, so far, it remains unclear if the peak observed in the nonannealed samples—apparently symmetrical—is a sum of the two components observed after annealing or, contrarily, is itself a peak with a different origin. Further experiments, presented in next sections, tried to give an answer to this question.

5.3.2 Dynamic behavior of the photoluminescence

Under the continuous monochromatic light of the spectrometer, a dynamic behavior of the PL emission was observed. A time-dependent increase of the UV emission occurs simultaneously to a decrease of the visible emission when the samples are studied under ambient conditions. This phenomenon is shown in Figure 5.10, where the PL-emission intensities for detection windows at 385 ± 1 nm and 560 ± 1 nm (under continuous excitation at 310 nm with a white lamp) are plotted versus the irradiation time. The dynamic effect appears to be less important for the pure ZnO samples, whose intensity change less than 10%, and is stronger for the hybrid materials, whose intensities may change up to more than 40% (compare normalized intensities in Figure 5.11). After ca. 20 s, the emission intensities remain approximately constant. The process was found to be reversible and the curves are reproducible if the measurements are taken with a difference of few minutes, to allow the complete relaxation of the samples.

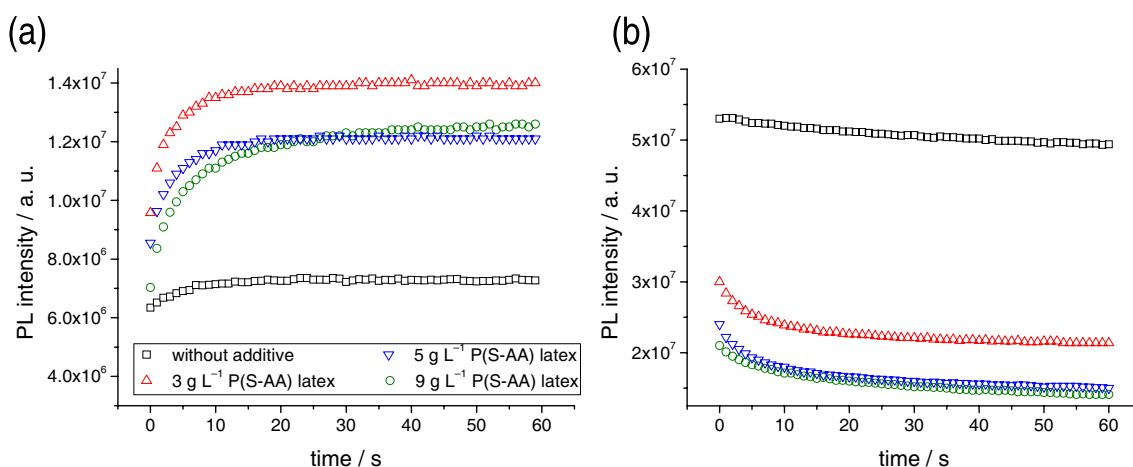


Figure 5.10. Dynamics of the PL emission under irradiation at 310 nm, detected at **(a)** $\lambda_{em} = 385 \pm 1$ nm and **(b)** $\lambda_{em} = 560 \pm 1$ nm.

Since the whole time to register a spectrum is around 3 min (scanning velocity of 2 nm s^{-1}) and the change in the intensity after several seconds is only a small percentage of that, the emission spectra previously presented (Figures 5.3–5.7) are assumed to show the situation of equilibrium of the mentioned dynamic process.

The shape of the curves shown in Figure 5.10 and the reversibility of the process suggested a photoinduced desorption of molecules adsorbed on the surface of the materials, presumably oxygen molecules from the medium. A fact that attracted our attention was that the curves fit well to adsorption-isotherm-like expressions. Somehow, the dynamic behavior of the luminescence appeared to mirror the assumed photodesorption process. Thus, the PL curves of Figure 5.10 might be rescaled and fitted to adsorption isotherms. For this purpose we assume that (i) the PL intensity is proportional to the coverage of the ZnO surfaces by oxygen molecules ($I \propto \theta$), and (ii) the oxygen concentration (partial pressure) is proportional to the time of photoirradiation ($c \propto t$). Although this empirical treatment could be questioned from a strict formal point of view, it offers an evident prove of the correlation of the PL with adsorption processes.

Several models have been proposed to describe the adsorption–desorption equilibria of gas molecules on a solid surface. One of these models is the *Langmuir–Freundlich isotherm*, sometimes called *Sips isotherm*,^[233,234] given by the equation

$$\theta = \frac{a(bc)^{1/m}}{1 + (bc)^{1/m}} \quad (5.27)$$

where θ is the surface coverage; a , b , and m are constants; and c is the adsorbent concentration (the gas, in our case). The Langmuir and Freundlich isotherms are limiting cases of this equation. If $m = 1$, we have a typical Langmuir isotherm,

$$\theta = \frac{abc}{1 + bc} \quad (5.28)$$

and if $m = 2$, we have a Langmuir isotherm for a dissociative adsorption (i.e., $X_2 \rightarrow 2X$, being X_2 the adsorbent molecule),^[235]

$$\theta = \frac{a(bc)^{1/2}}{1 + (bc)^{1/2}} \quad (5.29)$$

For $b \approx 1$ and very low concentrations, the term $(bc)^{1/m}$ becomes negligible with respect to 1, and eq. (5.27) can be simplified to a Freundlich isotherm:

$$\theta = ac^{1/m} \quad (5.30)$$

In Figure 5.11a, the dependence of the UV-emission intensity with the time of irradiation, t , is perfectly fitted with an expression analogous to the Langmuir–Freundlich isotherm:

$$I'_{\text{UV}} = \frac{a'(b't)^{1/m'}}{1 + (b't)^{1/m'}} \quad (5.31)$$

where a' , b' , and m' are the fitting parameters, and I'_{UV} is the rescaled intensity, calculated according to

$$I'_{\text{UV}} = \frac{I_t - I_0}{I_{\text{max}}} \quad (5.32)$$

where I_t is the PL intensity at a certain time and I_0 and I_{max} are the initial and maximum intensities, respectively.

In the case of the visible emission, the intensity decreases with the time, but the representation of $1 - I'_{\text{vis}}$ versus time (being I'_{vis} the visible emission normalized to 1) can also be adjusted to a Langmuir–Freundlich equation [eq. (5.33)], as illustrated in Figure 5.11b.

$$1 - I'_{\text{vis}} = \frac{a'(b't)^{1/m'}}{1 + (b't)^{1/m'}} \quad (5.33)$$

The parameters for the fittings of the rescaled experimental data of the UV and visible emissions [after eqs. (5.31) and (5.33)] are contained in Table 5.2.

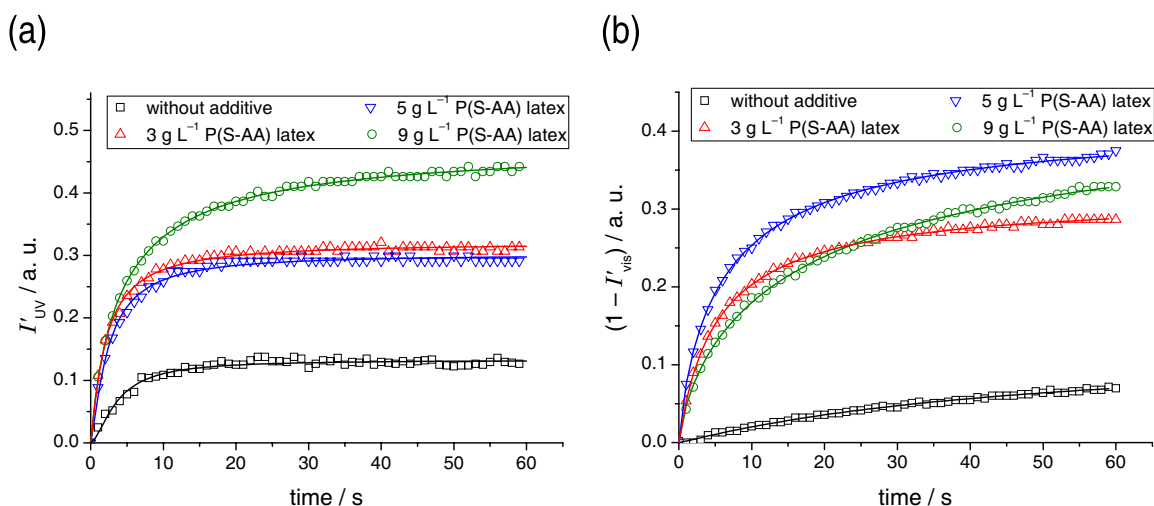
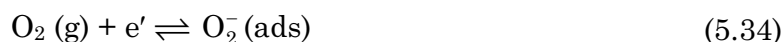


Figure 5.11. Adjustment of the rescaled experimental data of Figure 5.10 to Langmuir–Freundlich-type equations [eqs. (5.31) and (5.33)]: **(a)** detection at $\lambda_{\text{em}} = 385 \pm 1$ nm; **(b)** detection at $\lambda_{\text{em}} = 560 \pm 1$ nm. The fitting parameters are contained in Table 5.2.

Table 5.2. Langmuir–Freundlich-fitting parameters for the photoluminescence experimental data of ZnO samples crystallized in the presence of different concentrations of the P(S–AA) latex LTB2 (cf. Table 2.4).

latex conc. [g L ⁻¹]	$\lambda_{em} = 385 \text{ nm}$			$\lambda_{em} = 560 \text{ nm}$		
	a'	b'	m'	a'	b'	m'
0	0.133±0.001	0.18±0.01	0.62±0.04	0.13±0.01	0.021±0.003	0.95±0.05
3	0.321±0.001	0.50±0.01	0.87±0.03	0.318±0.002	0.183±0.002	1.06±0.01
5	0.303±0.002	0.42±0.01	0.78±0.03	0.424±0.003	0.160±0.003	1.19±0.02
9	0.480±0.003	0.237±0.004	1.10±0.02	0.468±0.009	0.053±0.003	1.35±0.03

Adsorption–photodesorption of oxygen on ZnO surfaces is an often observed phenomenon.^[236–243] In the dark, oxygen has a strong tendency to adsorb on the surface of ZnO, acting as an electron acceptor. Adsorbed O₂ can capture conducting electrons present in *n*-type ZnO according to the reaction (5.34) and a negatively charged layer with low conductivity is created near the surface, a so-called *depletion layer*.



When the material is irradiated with UV light of energy higher than the band gap, the photogenerated holes (of the electron–hole excitonic pair), with a positive effective charge, migrate to the negatively charged surface and neutralize the species O₂⁻:



Neutralized O₂ can be desorbed more easily than O₂⁻ and the depletion layer is destroyed. The photogenerated electron can move freely and the conductivity increases. The O₂ desorption continues until the equilibrium [eq. (5.36)] is achieved.



Keeping in mind these adsorption–desorption processes, which should take place at the surface of the particles, two different theories to explain the experimental observations are proposed in the following. The first one assumes interstitial oxygen as responsible for the visible emission. The second one is based in the model proposed by Bahnemann et al.,^[244] according to which the oxygen vacancy plays a mediating role in the tunneling of trapped electrons to preexisting trapped holes.

Model 1: Interstitial oxygen as responsible for visible emission

As pointed out, O₂ acts as an electron acceptor. Therefore, with the oxygen photodesorption fewer electrons are captured and the probability of excitonic

recombination increases, leading to an enhancement of the UV emission. Experimental curves of Figure 5.10a match with this description. Oppositely, curves of Figure 5.10b show that the O₂ photodesorption implies a parallel decrease of the visible emission. This could be understood with the following assumptions. According to the quasi-chemical reaction (5.16b), the concentration of interstitial-oxygen defects, [O_i], should be proportional to the square root of the O₂ partial pressure, p_{O_2} :

$$[O_i] \propto (p_{O_2})^{1/2} \quad (5.37)$$

The photodesorption of O₂ will reduce the concentration of interstitial oxygen. If it is postulated that interstitial oxygen is responsible, at least partially, for the visible emission, the photoluminescence should decrease simultaneously with the O₂ photodesorption.

However, our visible emission is centered at ~2.2 eV, and the yellow-orange emission assumed to be due to interstitial oxygen appears at 2.0 eV or even lower energies. This model can only explain partially, if at all, the observed visible emission. Therefore, a more complex theory seems to be necessary.

Model 2: Adsorbed species as “tunneling agents”

An alternative to the previous explanation is the model proposed by Bahnemann et al.,^[244] who—in agreement to our observations— reported a bleaching of the visible emission parallel to an increase of the UV peak. This model, depicted in Figure 5.12, assumes that “electron traps” are initially present in the system. Two competing radiative processes are considered: on one hand, the recombination of photo-generated electrons and holes; on the other hand, the trapping of photogenerated electrons followed by emission. The visible emission occurs after tunneling of trapped electrons from the conduction band to preexisting holes. Oxygen is supposed to play a crucial role in the electron tunneling. The adsorbed O₂ catches an electron from the conduction band and becomes O₂⁻ [eq. (5.34)]; afterwards, the electron is transferred to a preexisting trap (Tr):



Immediately after excitation, oxygen is adsorbed at the surface and can capture electrons, diminishing the probability of excitonic electron–hole recombination.

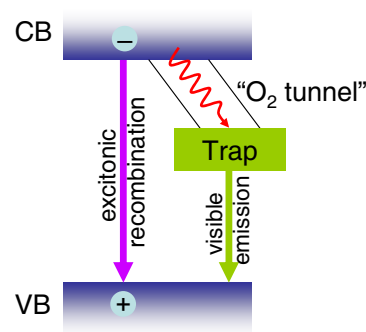


Figure 5.12. O₂-assisted tunneling of photogenerated electrons from the conduction band (CB) to a preexisting trap, followed by the radiative transition to the valence band (VB).

These electrons are tunneled to the traps and visible light is emitted. Under irradiation, the photogenerated holes begin to migrate to the surface and O_2 is photodesorbed. The disappearance of “tunneling agents” from the surfaces implies the decrease in the visible emission and a simultaneous growth of the excitonic recombination. The evolution of the photoluminescence is, therefore, parallel to the photodesorption process.

Two possible defects in zinc oxide could act as traps: oxygen vacancies and zinc interstitial. This model allows to explain the visible emission and its behavior without involving other less probable defects in *n*-type ZnO.

It is worthy to mention that van Dijken et al.^[203,204] proposed a similar model to explain the emission of nanocrystalline ZnO, but in which O^{2-} sites at the surface capture a hole ($O^{2-} + h^\bullet \rightarrow O^-$), which is transferred to a V_O^\bullet level ($V_O^\bullet + h^\bullet \rightarrow V_O^{\bullet\bullet}$). They assumed that the visible emission arises from the transition of photo-generated electrons of the conduction band to the deep trapped hole of $V_O^{\bullet\bullet}$.

With independence of the exact mechanism behind the process, photoluminescence appears to be dependent on adsorption–desorption processes at surface sites. In the presence of latex, the adsorption of O_2 is hindered and the visible emission decreases accordingly. Additionally, latex particles accelerate the photodesorption process, as judged from the slopes of the curves at initial times in Figure 5.11.

5.3.3 Temperature dependence of the photoluminescence

Investigations on the temperature dependence of the photoluminescence were carried out for further understanding of the optical properties of the prepared ZnO–latex hybrid materials. The measurement chamber of the spectrometer was progressively cooled by a liquid- N_2 circuit (cryostat) and PL emission spectra were registered at different temperatures in the range 77–305 K.

For all samples, including the pure-ZnO reference and the hybrid materials, the following features are observed as the temperature decreases: (i) both UV- and visible-emission intensities increase; (ii) the maximum of the UV peak shifts to higher energies (blue shift); (iii) the visible band, contrarily, shifts to lower energies (red shift); and (iv) both peaks become narrower (i.e., full width at half maximum decreases). An example of this behavior is presented in Figure 5.13 for a hybrid sample crystallized in the presence of 3 g L^{-1} of a P(S–AA) latex. The two recognizable bands of the spectra can be relatively well fitted with single Gaussian curves, but in the case of the visible emission, the fitting improves if two Gaussians are used. This suggests once more the possibility of two contributions in the visible emission: a green and a yellow-orange one. The evolution of

these two visible peaks with temperature seems to follow the same tendency as the envelop curve. However, since the exact position and the contribution of each component at different temperatures is not obvious and only mathematical speculations can be made, fittings of the whole visible emission to simple Gaussians are considered further on, keeping in mind that more than one energetic transition may be behind the visible emission.

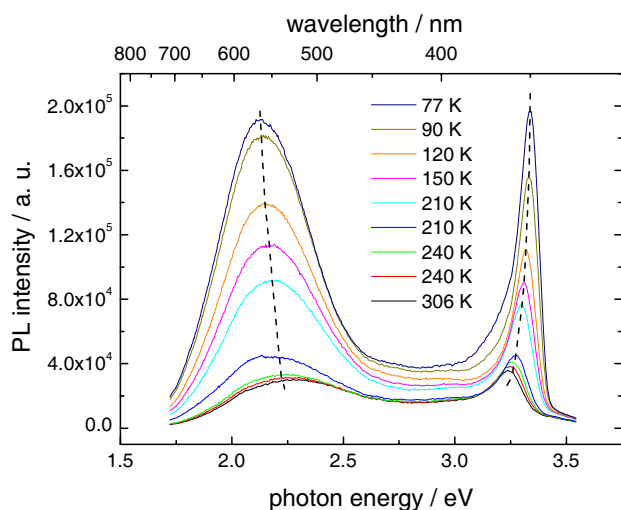


Figure 5.13. PL emission spectra ($\lambda_{\text{exc}} = 310$ nm, 4.00 eV) at different temperatures (RT \rightarrow 77 K) for a ZnO–latex hybrid sample crystallized in the presence of 3 g L⁻¹ of the latex LTB2 (cf. Table 2.4).

The growth of the integrated PL intensity when the samples are cooled down is the result of the freeze-out of phonons and quenching of nonradiative recombination processes.^[245] Figure 5.14 presents the evolution of the integrated PL intensity (normalized to 1) of the UV- and visible-emission bands for a set of hybrid samples, comparing them with a pure ZnO reference. It can be seen that the quenching of the UV peak is more important for the ZnO–latex materials than for pure ZnO: the thermal quenching from 77 K to room temperature is of $\sim 90\%$ for the hybrids, against a $\sim 20\%$ for the reference. The behavior appears to be opposite for the visible emission: thermal quenching is then less significant for samples prepared with increasing concentration of latex.

The temperature dependence of the PL intensity, $I(T)$, can be expressed by a simple thermal activation model according to the equation^[219,246–248]

$$I(T) = \frac{I_0}{1 + A \exp\left(\frac{-E_a}{k_B T}\right)} \quad (5.39)$$

where I_0 is the emission intensity at 0 K, A is a constant, and E_a is the activation energy of the thermal quenching process. The estimated activation energies for fitting of the data of Figure 5.14 according to eq. (5.39) are contained in Table 5.3.

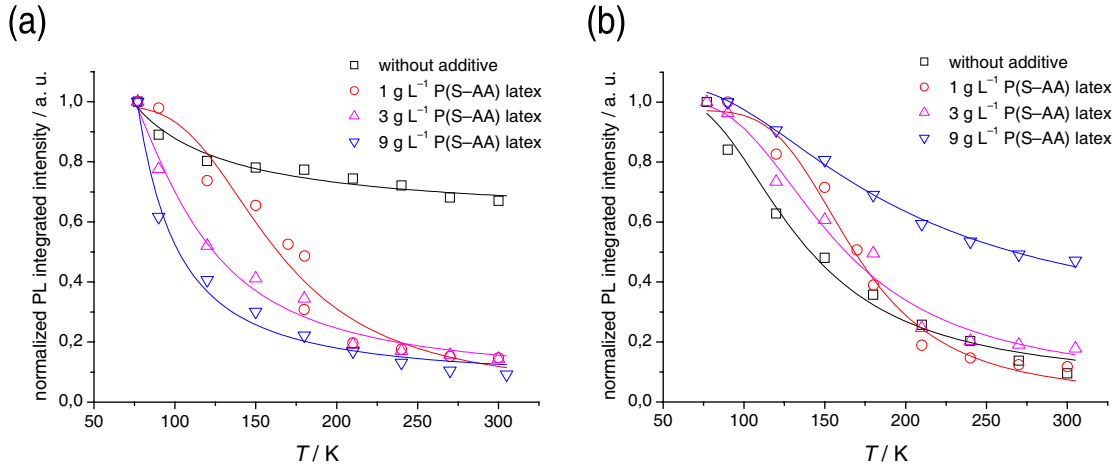


Figure 5.14. Temperature dependence of the PL emission bands (area of the peaks normalized to the unity) for pure ZnO and ZnO–latex hybrid samples, prepared with increasing concentration of the P(S–AA) latex LTB2 (cf. Table 2.4): **(a)** integrated intensity of the UV-emission peak; **(b)** integrated intensity of the visible emission. The solid lines are theoretical fittings according to the eq. (5.39).

Table 5.3. Activation energies (E_a) of the temperature-dependent quenching processes for the UV and visible emission bands, estimated from the theoretical fitting [cf. eq. (5.39)] of Figure 5.14.

latex concentration [g L ⁻¹]	0	1	3	9
$E_a(\text{UV})$ [meV]	3	62	28	19
$E_a(\text{vis})$ [meV]	41	84	51	35

The temperature dependence of energy bands at constant pressure originates from both thermal expansion of the lattice and renormalization of band energies by electron–phonon interactions.^[249] The blue shift of the UV excitonic emission which decreasing temperature arises essentially from a band gap shift, assuming the exciton binding energy to be independent of the temperature. Thermal expansion and electron–phonon interaction have a similar temperature dependence and all the phonons, in principle, contribute to the shift. The overall contribution to the shift can be reproduced by a Bose–Einstein distribution, using the effective phonon energy $\hbar\omega$. Thus, the temperature dependence of the excitonic emission can be expressed by the equation^[248,250]

$$E(T) = E_0 - \frac{\lambda}{\exp\left(\frac{\hbar\omega}{k_B T}\right) - 1} \quad (5.40)$$

where E_0 is the exciton energy at 0 K and λ is a proportional coefficient. Figure 5.15a shows that the evolution with the temperature of the UV-peak energy, taken at the maximum of emission, can be fitted to eq. (5.40). The corresponding fitting parameters are listed in Table 5.4.

A different tendency was observed for the visible emission: the band shifts systematically to lower energies as the temperature decreases, as can be seen in Figure 5.15b. This behavior, although not fully understood, has been sometimes reported in semiconductor crystalline materials. For instance, Leiter et al.^[202] reported a continuous blue shift of the excitonic emission as temperature decreases, parallel to a shift to higher energies of the oxygen-vacancy-related (according to their assignment) green emission (~ 2.45 eV). However, other authors have also observed different temperature dependence: van Dijken et al.^[204] reported a shift to higher energies with decreasing temperatures in the range $75 < T < 180$ K and a temperature independence of the energy position for $T < 75$ K and $T > 180$ K. In our case, the energy shift was found to fit well with an empirical Arrhenius-type equation of the form

$$E(T) = E_0 + A \exp\left(\frac{-\varepsilon}{k_B T}\right) \quad (5.41)$$

where E_0 is the energy at 0 K, A is a constant, and ε is an energetic parameter. Parameters corresponding to the fitting of the visible-emission data following this equation are contained in Table 5.4.

The opposite shift of the visible-emission energy with respect to the shift of the exciton-related peak could indicate, as proposed by Leiter et al.,^[202] that the visible PL involves intradefect transitions whose energy behaviors differently from the temperature dependence of the band gap.

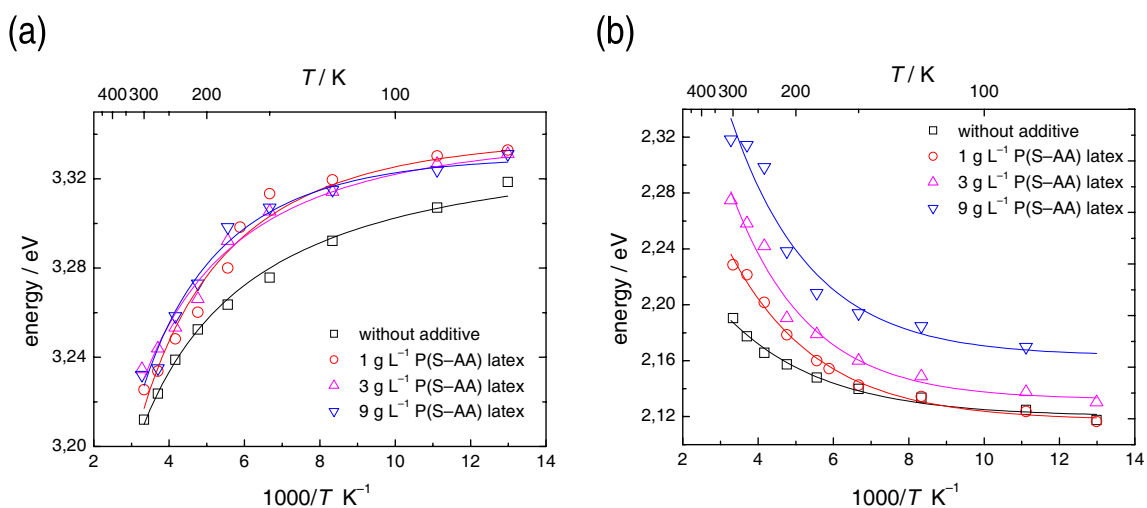


Figure 5.15. Temperature dependence of the energy of the maximum emission for pure ZnO and ZnO-latex hybrid products: **(a)** energy at the maximum of the UV emission; **(b)** energy at the maximum of the visible emission. The solid lines are theoretical fittings of the experimental data according to eqs.(5.40) and (5.41), for UV and visible emission respectively.

Table 5.4. Fitting parameters of the temperature-dependent experimental data of Figure 5.15 for the UV and visible emission, according to eqs. (5.40) and (5.41), respectively.

latex [g L ⁻¹]	UV emission			Visible emission		
	E_0 [eV]	λ [eV]	$\hbar\omega$ [meV]	E_0 [eV]	A [eV]	ε [meV]
0	3.32	0.07	12	2.12	0.25	33
3	3.34	0.18	23	2.12	0.49	37
5	3.34	0.10	17	2.13	0.74	42
9	3.33	0.22	29	2.16	0.79	40

5.3.4 Time-resolved spectroscopy

PL emission arising from excitonic recombination has been found to decay very rapidly (below nanosecond, in the scale of hundreds of picoseconds),^[251] while defect-related visible emission may have much longer lifetimes (in the microsecond scale).^[204,252] To obtain information about the lifetime of the visible emission in our samples, time-resolved spectra were registered at an excitation wavelength of 355 nm (3.49 eV) by using a pulse laser radiation (Nd:YAG laser).

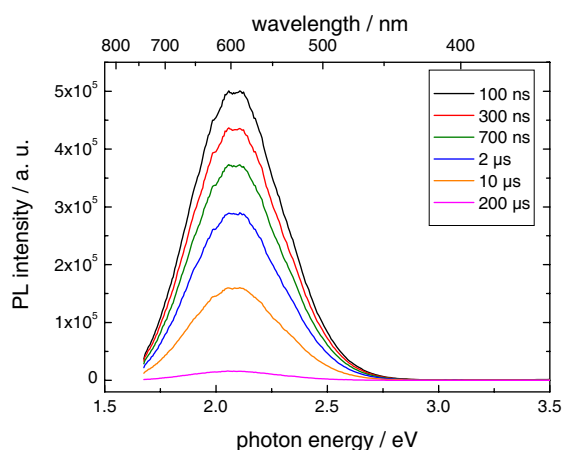


Figure 5.16. PL emission spectra for a pure ZnO sample after different delay times (0.1 to 200 μ s) under a laser excitation of 3.49 eV (355 nm, Nd:YAG laser) with a pulse of 10 ms.

Surprisingly, a red shift of the maximum of the visible emission was observed, with respect to the spectra obtained under continuous white light excitation (spectra of §5.3.1–5.3.3). An orange emission centered at ~ 2.1 eV (601 nm), which can be relatively well fitted with a Gaussian curve, appears in spectra of all samples, including pure ZnO and hybrids. As a representative example, Figure 5.16 shows the time-dependent emission spectra (delay times of 0.1 to 200 μ s) of a pure ZnO powder, prepared as usual in the absence of any latex additive. A band with the same shape centered at the same place is also found in the continuous wave (CW) spectra, exciting with the same laser source. The monochromatic radiation of the laser appears to “encounter” specifically certain energy levels, corresponding to the observed orange emission, while white light leads to a

broader visible emission, very probably originated by more than one energetic transition.

In the experimental setup used, an integrated intensity is registered for the different delay times. This means that, for a certain delay time t , the total radiation from the initial point (after the excitation pulse is finished) to t is detected. The study of absolute kinetics would require that the emitted light is detected for small windows of time. Consequently, integrated intensities do not allow quantitative determination of lifetimes, but a relative comparison with respect to the reference sample.

It was noticed that the representation of the integrated intensity of the orange emission versus the delay time does fit neither to a first-order nor to a second-order exponential decay, as illustrated in Figure 5.17, whereas the fitting is very good when a *Kohlrausch function* (or *stretched-exponential function*) is used. This function is an empirical expression originally proposed by Kohlrausch to describe structural relaxation of glassy fibers and later applied by Williams and Watts^[253] for dielectric relaxation of polymers (for this reason it is often called Kohlrausch–Williams–Watts or KWW function). The Kohlrausch function has been used to describe different physical relaxation phenomena, including luminescence decay processes of different complex systems.^[254–262]

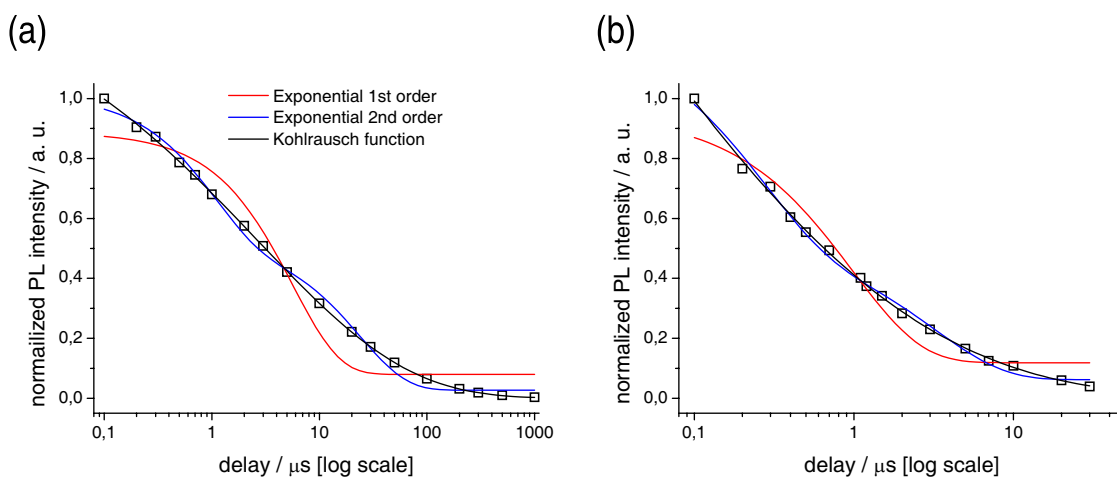


Figure 5.17. Comparison of different exponential fitting functions (first order, second order, and Kohlrausch function) for the photoluminescence decay of **(a)** a pure zinc oxide sample prepared in the absence of any additive and **(b)** a ZnO–latex hybrid material prepared in the presence of 9 g L^{-1} of the P(S–AA) latex LTB2 (cf. Table 2.4). The powder samples are excited at 3.49 eV (355 nm) for 10 ms with a Nd:YAG laser.

Assuming a Kohlrausch-type decay for the photoluminescence, the intensity $I(t)$ at a time t is given by

$$I(t) = I_0 \exp\left(-\frac{t}{\tau}\right)^\beta \quad (5.42)$$

where I_0 is the intensity at $t = 0$, τ is a parameter with the dimensions of time, and β is a parameter in the range $0 < \beta \leq 1$ ($\beta = 1$ yields a conventional first-order exponential decay). The Kohlrausch function implies a continuous distribution of lifetimes and eq. (5.42) can be mathematically written as

$$I(t) = \int_0^\infty \exp\left(-\frac{t}{\tau}\right) \rho(\tau) d\tau \quad (5.43)$$

where $\rho(\tau)$ is the distribution of lifetimes. An average lifetime, $\langle \tau \rangle$, is given by

$$\langle \tau \rangle = \frac{1}{\beta} \tau \Gamma\left(\frac{1}{\beta}\right) \quad (5.44)$$

being $\Gamma(1/\beta)$ the gamma function of the inverse of the parameter β .

The fact that our experimental data match with a stretched-exponential decay, unconventional for PL decay processes, can be justified by the dynamic behavior of the photoluminescence described in §5.3.2. If the visible emission under laser radiation is showing a similar dynamic decrease as under white light excitation, and taking into account—as previously mentioned—that the detected intensity for a delay time t is the integrated intensity from 0 to t , there will not be a unique lifetime, but a distribution of lifetimes, corresponding to the different decays of the PL at the infinitesimal time increments of the pulse. Figure 5.18 presents the PL decay of pure ZnO and ZnO–latex materials, adjusting the data to Kohlrausch functions. The corresponding fitting parameters, together with the correlation coefficient, and the average lifetimes are listed in Table 5.5. It is clearly seen that the luminescence has shorter lifetimes (about one order or magnitude) in the hybrid samples than in pure ZnO. Therefore, we consider that the latex acts as a quencher that increases the decay velocity of the PL visible emission.

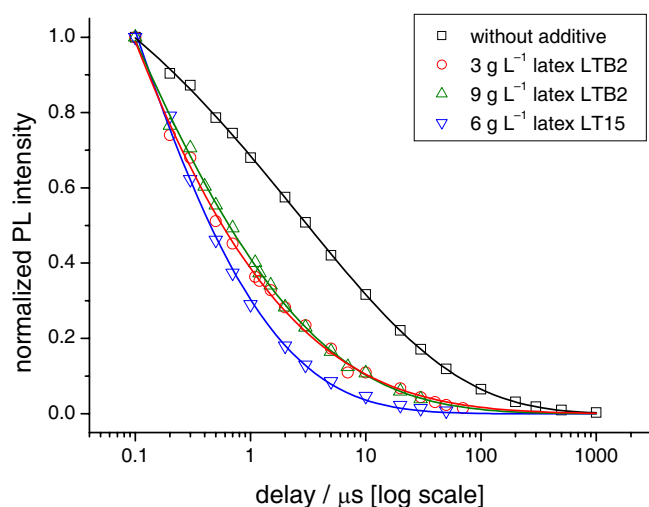


Figure 5.18. Photoluminescence decay of a pure zinc oxide sample and different ZnO–latex hybrid materials under excitation at 3.49 eV (355 nm) for 10 ms (Nd:YAG laser). The solid lines correspond to Kohlrausch functions.

Table 5.5. Parameters of the fittings of Figure 5.18 according to the Kohlrauch function [eq. (5.42)] and average lifetimes, $\langle \tau \rangle$, calculated with eq. (5.44). $\Gamma(1/\beta)$ represents the value of the gamma function for $1/\beta$ and r^2 is the square of the correlation coefficient.

latex additive ^[a]	I_0	τ [μs]	β	$\Gamma(1/\beta)$	r^2	$\langle \tau \rangle$ [μs]
no additive	1.43±0.02	2.7±0.2	0.311±0.006	2.464	0.9998	21.2
LTB2 [3]	11±5	(2±4)×10 ⁻⁴	0.14±0.02	767.506	0.9976	1.1
LTB2 [9]	4.6±0.9	0.012±0.009	0.20±0.02	26.696	0.9986	1.6
LT15 [6]	5.1±1.4	0.01±0.01	0.24±0.03	6.874	0.9984	0.4

[a] The sample reference is given first (cf. Table 2.4) and the quantity in gram per liter is given in square brackets (e.g., LTB2 [3] indicates 3 g L⁻¹ of the latex LTB2).

5.4 EPR investigation of ZnO–latex hybrid materials

Many authors have studied the correlation between the PL emission and the electron paramagnetic resonance (EPR) signals in ZnO, in an attempt to clarify the defect structure and the energetic levels. EPR spectra of all our samples showed a signal at $g \approx 1.96$, which is very strong compared to many spectra published. This signal seems to be attributable, according to literature (see §5.2.3), to shallow donors. No other peaks were observed in any case.

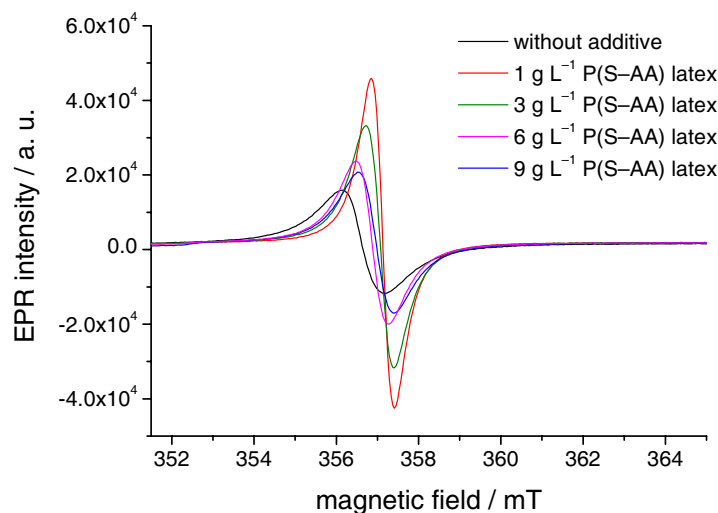


Figure 5.19. EPR spectra for a pure ZnO reference samples and for ZnO–latex hybrid samples prepared in the presence of different concentrations of the P(S-AA) latex LTB2 (cf. Table 2.4). Measurements were carried out in the presence of the free radical 4-oxo-TEMPO, used as an internal reference. The peaks of this organic radical, all below 351 mT, have been cut off. (See experimental details in Table 5.6.)

A quantification of the spin concentration was performed by using the free radical 4-oxo-2,2',6,6'-tetramethyl(piperidin-1-oxyl) (4-oxo-TEMPO) as an internal reference. Figure 5.19 shows the EPR spectra for the same batch of the

hybrid samples typically presented in previous sections, compared with the spectrum of a ZnO reference samples (conventional PL spectra of these samples have been shown in Figure 5.8). Here, the signals of the organic radical (that appear below 351 mT and do not interfere with the ZnO signals) have been cut off. Spin densities, represented in Figure 5.20a, were calculated taking into account the ratio between the mixed quantities of free radical and ZnO sample and the ratio between the intensities of the EPR signals. The EPR signal corresponds to the spin concentration in the total material. To obtain the concentration of paramagnetic defects in ZnO particles, the density of the samples was calculated by accounting the latex content, obtained from the weight loss in the thermogravimetric analysis (TGA), and approximating the density of the latex to 1.00 g cm^{-3} . A density of 5.606 g cm^{-3} was considered for the pure ZnO sample. The data used in the calculations are listed in Table 5.6. A spin density of $3.7 \times 10^{18} \text{ cm}^{-3}$ was calculated for the reference sample and values between 1.4×10^{18} and $3.2 \times 10^{18} \text{ cm}^{-3}$ were obtained for the hybrid samples.

Table 5.6. Experimental details of the samples prepared for quantitative EPR measurements (cf. Figures 5.19 and 20).

additive conc. [g L ⁻¹]	radical mixture [mg]	sample [mg]	latex content ^[a] [%]	density [g cm ⁻³]	EPR-signal ratio radical/ZnO
0	10.7	80.3	0.0	5.61	4.927
1	10.5	67.3	4.3	5.41	3.918
3	10.6	78.1	7.0	5.28	4.512
5	11.5	81.4	9.1	5.19	3.429
9	11.3	79.2	9.5	5.17	1.720

[a] Estimated from the weight loss by thermogravimetric analysis (RT → 600 °C, 10 °C min⁻¹).

In the PL visible emission, a difference up to more than a factor of 5 is observed in the integrated intensity (cf. Figure 5.8), while the concentrations of paramagnetic defects determined by EPR differ in less than a factor of 3 for the same batch of samples. Both intensities tend to decrease as latex concentration increases, but the quenching of the visible emission in the presence of latex is much more significant than the reduction of the EPR intensity. The evolution of both signals with the latex concentration is also different. Some samples showing lower PL emission than others can have, however, higher unpaired spin concentration. These facts indicate that, in our samples, the centers observed in the PL emission and the EPR spectra are different, contrarily to the findings of some authors (e.g., Vanheusden et al.^[199,200]).

The spectra of Figure 5.19 also show that the EPR signal becomes systematically narrower when the concentration of latex increases. Assuming that the

transverse electron spin relaxation time T_2 determines the peak width, Γ , these two magnitudes can be related with the expression

$$\Gamma = \frac{2}{\sqrt{3} \cdot T_2} \quad (5.45)$$

being Γ in megahertz (not in gauss) and T_2 in nanoseconds. Accordingly, values of T_2 can be estimated for the different samples. The calculated values, represented in Figure 5.20b, range from 38 ns for the pure ZnO to 75 ns for one of the hybrid samples.

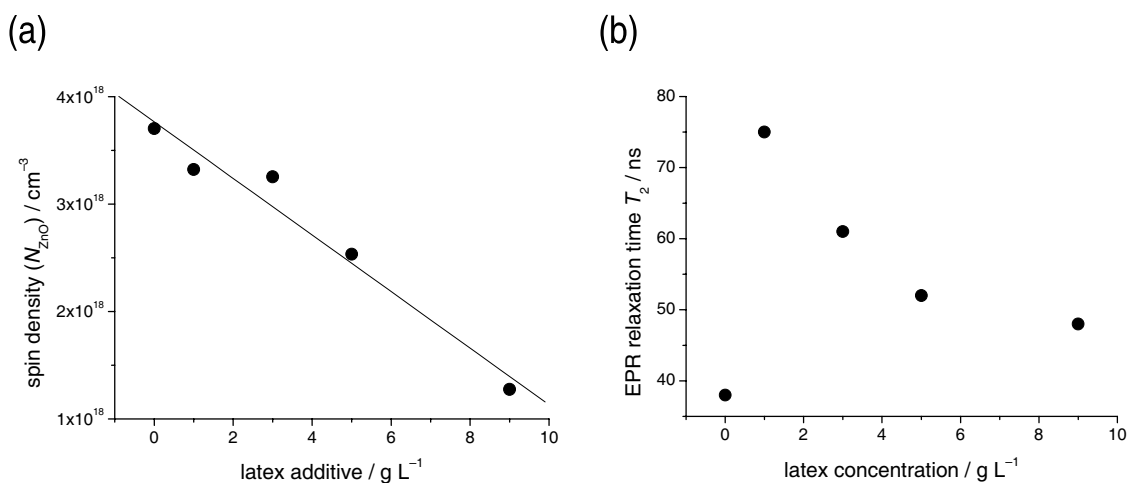


Figure 5.20. (a) Spin density calculated from the EPR measurements for samples prepared with different concentrations of the P(S-AA) latex LTB2 (cf. Table 2.4). The solid line is a linear fitting of the data. (b) Transverse electron spin relaxation times, T_2 , for the same set of samples, estimated from the line width of the EPR signal.

The definite evidence that the EPR signal and the visible emission in our samples have different origins came from comparing the temperature dependence of both types of spectra. Figure 5.21 presents the temperature dependence of the EPR signal for the reference and for a hybrid sample. In stark contrast to the intensity of the PL visible emission (cf. Figure 5.14b), the intensity of the EPR signal increases with increasing temperature. We assume that at low temperature, the shallow-donor centers have two paired electrons and are EPR-silent. With increasing temperature, more thermal energy is available to excite one of the two electrons from the shallow-donor level to the nearby conduction band. Assuming that the EPR signal at $g \approx 1.96$ is coming from unpaired electrons placed in the shallow-donor level, the increase of the signal with temperature would correspond to this excitation process. Accordingly, it should be possible to fit the temperature dependence to an Arrhenius-type activation expression with the form

$$I(T) = I_0 + A \exp\left(\frac{-E_a}{k_B T}\right) \quad (5.46)$$

where I_0 is the intensity at 0 K (that should be 0 if only one thermally activated paramagnetic center is present) and E_a is the activation energy. The fitting of the data appears to be clearly better if a $I_0 \neq 0$ is considered (compared solid and dashed in Figure 5.21). This suggests that two different paramagnetic centers are responsible for the observed signal. The first one should be initially paramagnetic and become diamagnetic by thermal activation. The second center type should be diamagnetic at 0 K and paramagnetic in the thermally activated state; this center is predominant and determines the general tendency of the EPR signal with temperature. Since the two centers appears in EPR spectra at the same position, which is attributed to shallow donors, the two components of the signal might correspond to two different shallow donors, placed at similar energies under the conduction band.

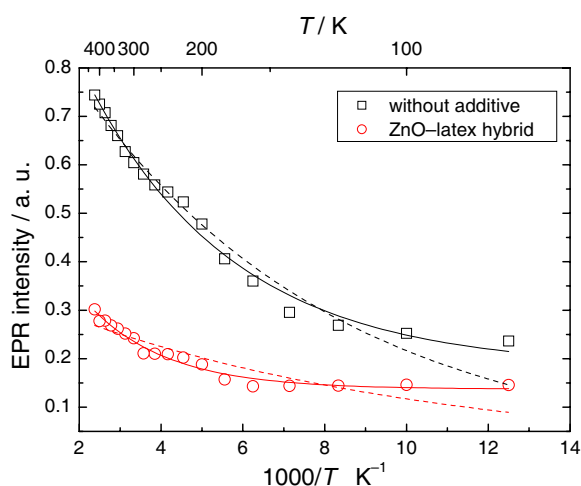


Figure 5.21. Temperature dependence of the EPR signal for a pure ZnO reference and a ZnO–latex hybrid sample prepared with 6 g L^{-1} of the P(S–AA) latex LT15 (cf. Table 2.4). The solid lines are theoretical fitting according to eq. (5.46) and the dashed lines are fittings to the same equation fixing $I_0 = 0$.

5.5 Conclusions

Latex nanoparticles have been shown to influence the optical and paramagnetic properties of ZnO precipitated from aqueous media. A weak UV peak and a more intense very broad visible emission appear in all PL emission spectra, but the ratio and intensity of the peaks changes considerably, depending on the concentration of latex added during crystallization. Latex appears to be a quencher of the visible emission.

Whereas the PL peak can be attributed to near-band-edge exciton annihilation, the visible emission, centered at $\sim 2.2 \text{ eV}$, appears to be more complicated to

understand. The observed broad band might be a sum of a green and a yellow-orange component. Under oxidative annealing of pure-ZnO powders, a strong 2.0-eV-centered emission appears, which could arise from the presence of interstitial oxygen. In similar conditions, hybrid ZnO–latex samples show a green (at ~ 2.5 eV) and a yellow band.

Surface-adsorbed species seem to have a determining influence on the optical properties. Under continuous irradiation, a noticeable dynamic behavior of the photoluminescence is observed. This has been explained in terms of photodesorption of adsorbed oxygen. It is assumed that O_2 plays a role as tunneling agent of electrons from the conduction band to a deep trap, probably related to oxygen vacancies or interstitial zinc and responsible for the green visible emission. When O_2 is photodesorbed, the “electron-shuttle” species disappears and visible emission is bleached, while the UV peak increases due to the higher probability of excitonic recombination. Latex particles seem to block possible adsorption sites and, consequently, the visible emission is quenched. Additionally, the latex promotes a faster oxygen photodesorption that implies a faster decay of the visible emission, confirmed by laser-pulsed time-resolved spectroscopy, although it has to be indicated that under laser excitation, only yellow-orange—and not green—emission (~ 2.0 eV) was observed.

Further information on the defects structure of the materials was obtained by electron paramagnetic resonance (EPR). EPR spectra of all samples show an intense signal at $g \approx 1.96$, the intensity of which tends to decrease as well with increasing latex concentration. However, no quantitative correlation was possible between PL and EPR; furthermore, temperature dependence of both signals follow opposite tendencies. Contrary to results of some authors,^[199,200] this indicates that in our samples, centers responsible for visible emission and centers responsible for the EPR signal are different.

The EPR signal may be ascribed to shallow donors placed near the conduction band. With high probability, two different centers with opposite temperature behavior contribute to this signal, one being initially paramagnetic at low temperatures and other one that achieves the paramagnetic state by thermal activation.

5.6 Experimental section

Materials

$Zn(NO_3)_2 \cdot 6H_2O$ (Aldrich, 99.4%) was typically used in the synthesis of ZnO. The following metal traces are present (certificate of analysis delivered by the

producer): ≤ 50 ppm of Ca, Cd, Co, Cu, Fe, K, Ni, and Pb; and ≤ 100 ppm of K and Na. The high-purity sample of Figure 5.4 was synthesized with copper-free $\text{Zn}(\text{NO}_3)_2 \cdot x\text{H}_2\text{O}$ (Aldrich, 99.999% based on trace metals analysis), containing the following traces (in ppm): B 0.40, Ni 0.23, Mn 0.20, Fe 0.19, Ca 0.11, Cs 0.05, Sr 0.04, Mo 0.04.

All samples of this chapter were synthesized according to Formulation 1 described in §3.7. Samples of Figures 5.7 and 5.9 were subjected to oxidative annealing under continuous O_2 stream following the program indicated in §4.10 (RT \rightarrow 600 °C \rightarrow RT, 10 °C min^{-1} ; 1-hour plateau at 600 °C).

Photoluminescence spectra

PL spectra were registered under atmospheric pressure using a Spex Fluorolog 212 spectrometer equipped with a Xe lamp. A scheme of the experimental setup of this equipment is represented in Figure 5.22. The measurements were carried out in a specially designed cell, comprised of two quartz plates placing the powder sample in between. A 345-nm high-pass filter was used for the emission spectra registered at $\lambda_{\text{exc}} = 310$ nm, as well as for the excitation spectra registered at $\lambda_{\text{em}} = 560$ nm. Similarly, 295-nm and 400-nm high-pass filters were used for emission spectra registered at excitation wavelengths of 260 and 350 nm, respectively. The scanning velocity was always of 2 nm s^{-1} .

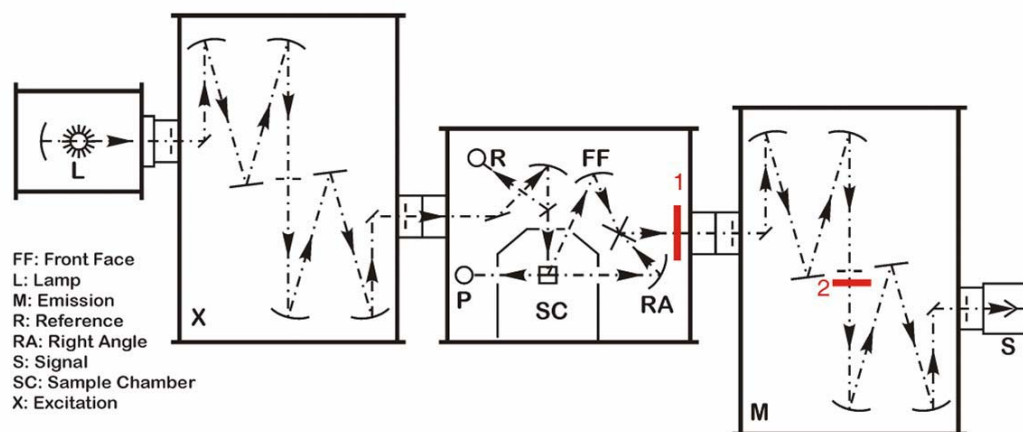


Figure 5.22. Scheme of the spectrometer used in the experiments (Spex Fluorolog 212). High-pass filters were placed (if necessary) in the positions labeled as 1 and 2, when working with front-face (FF) and right-angle (RA) geometry, respectively.

In conventional room-temperature spectra, front-face (FF) geometry was used, and the filters were placed in the position indicated as 1 in Figure 5.22. For the temperature-dependent spectra (§5.3.3), a cryostat was introduced into the sample chamber, and right-angle (RA) geometry was used (instead of FF). When working with RA geometry, the filters were placed in the position labeled as 2.

In the dynamic studies (§5.3.2), a time of not less than 3 min without irradiation elapsed between the different measurements to allow the complete relaxation of the samples.

Time-resolved spectroscopy

The spectra of prompt and delayed PL were recorded with an optical multichannel analyzer (EG&GOMA III) with a time-gated intensified diode array detector, after passing the emitted light through a spectrometer with a spectral resolution of 0.5 nm. Prompt PL was recorded with a gate width of 100 ns. A detection window of 10-ms width was used to detect the upconverted PL. Achromatic lenses were used for focusing the emitted PL. For excitation at 3.49 eV (355 nm), the third harmonic of a Nd:YAG laser was used. Typical excitation intensities were 10 mJ per pulse at 3.49 eV with a spot size of typically 5 mm in diameter. To increase the signal-to-noise ratio, the charge-coupled device (CCD) was cooled and the spectra were accumulated by averaging over 100 pulses.

Electron paramagnetic resonance

9.44 mg of 4-oxo-2,2',6,6'-tetramethyl(piperidin-1-oxyl) free radical (4-oxo-TEMPO, Aldrich) were mixed with 3.000 g of *o*-terphenyl (OTP, Fluka, $\geq 99\%$) and homogenized by melting the OTP at 80 °C. After cooling down, 0.301 g of this mixture were homogenized with 2.995 g of OTP and heated again to 80 °C. Known quantities of this final mixture (5–12 mg) were homogenized accurately with known quantities of the ZnO samples (50–90 mg). A part of the mixture was introduced in the EPR tubes for the quantitative measurements. All EPR measurements were performed on a Bruker Elexsys 580 spectrometer at frequencies of approximately 9.8 GHz, using a 4103TM cavity at room temperature and an MD4EN Bruker Flexline ENDOR resonator at low temperature. A microwave power of 2 mW was applied at room temperature. To avoid saturation of the nitroxide reference signal at lower temperatures, power was reduced to 20 μ W at 80 K and 0.2 μ W at 20 K. A modulation amplitude of 0.2 mT was used throughout. Spin concentration in the ZnO samples was determined from the ratio of the double integrals of the ZnO and nitroxide signals and the known spin concentration of the nitroxide.

Chapter 6

General conclusions and outlook

Hydrophilic and water soluble polymers are known to interfere with nucleation and growth of inorganic crystals in the course of precipitation from an aqueous medium. Double hydrophilic block or graft copolymers have been shown to be particularly effective when the functional groups (e.g., carboxylic groups) are spatially separated from other groups (e.g., ethylene oxide groups) which merely take care of water compatibility but do not show interactions with the surface of the inorganic material in the own right. In this work, it has been demonstrated for the precipitation of zinc oxide that anchoring of the components of double-hydrophilic block or graft copolymers to the surface of latex particles has similar effects. Whereas the synthesis of block or graft copolymer may be cumbersome, latex particles of defined diameter and varying composition of surface-anchored functional groups are readily and efficiently available by the miniemulsion polymerization technique. The application of such latexes offers new possibilities in the control of crystallization phenomena and, consequently, the properties of materials obtained in the course of precipitation. The crystallization of zinc oxide is particularly suited for systematic studies, because zincite is the only polymorph formed and it crystallizes in the form of hexagonal prismatic crystals. The length-to-width ratio of these crystals (aspect ratio) is the most important characteristic feature, and is subject to control by the polymer additive.

The systematic screening of variations in the chemical composition of the corona of the latex particles reveals that both the chemistry of the functional groups and their surface density are important control parameters that allow the modification of the shape of precipitated zincite from slender elongated to plate-like forms. Furthermore, the size distribution of the crystals becomes narrow and homogeneous. Polystyrene miniemulsion latexes with a corona composed of carboxylic groups (originating from acrylic acid used as comonomer) and oligo(ethylene oxide) residues (from the surfactant used in the preparation of the miniemulsion) have evolved as a model system from the screening procedure. The dependence of the aspect ratio on the overall latex concentration can be described satisfactorily by a model that assumes that latex particles adsorb to the growth centers at the basal plane of zincite according to a Langmuir isotherm.

A further conclusion is that the latex has a very little, if at all, influence on nucleation density. This is deduced from the study of the size distribution of the crystals obtained at different concentrations of the same type of latex. However, the width of the size distribution seems to grow narrower at increasing latex concentration which may be taken as an indication that Ostwald ripening is suppressed in the presence of the latex.

In addition, latex particles become incorporated into the growing crystals and polymer–inorganic hybrid materials are obtained. These materials are composed of an inorganic and largely undisturbed crystalline matrix in which organic latex particles (up to ca. 10 wt %) are embedded. Increasing amounts of latex particles become incorporated into the growing crystals at increasing overall concentration in the crystallizing system. The polymer can be removed by thermolysis or by dissolution in organic solvents leaving porous crystals of zinc oxide behind. These crystals might be the basis of materials suited for catalysis.

Some experimental evidence suggested that the formation of zincite takes place through lamellar intermediates, probably zinc hydroxide species containing groups from the precursor (nitrate groups) and/or from the functionalized latexes (carboxylic groups). The time required for beginning of the particle formation was observed to increase when latex particles are present. Further studies could focus on a more detailed analysis of the kinetics of the crystal growth.

Latex appears to be a quencher of the visible emission of zinc oxide. Thus, ZnO–latex hybrid materials show a significantly lower photoluminescence (PL) intensity in the visible range of the spectrum, with respect to pure zincite precipitated in the absence of any additive. Under continuous photoexcitation, a noticeable dynamic behavior of the photoluminescence is observed, which can be correlated with a photodesorption of adsorbed oxygen. These oxygen surface-adsorbed species seem to play a crucial role on the optical properties of the materials and may mediate the transport of electrons from the conduction band to preexisting deep-level traps, probably related to intrinsic defects (oxygen vacancies or interstitial zinc). The polymer particles can block the sites where oxygen adsorbs and the disappearance of the “electron-shuttle” species lead to the observed quenching of the visible emission. In addition, latex promotes a faster oxygen photodesorption, implying a faster decay of the visible emission.

Additional information about the defects arises from the electron paramagnetic resonance (EPR) spectra. An intense signal at $g \approx 1.96$, the intensity of which tends to decrease with increasing latex concentration, was observed for all samples. This signal can be attributed to shallow-donor levels (probably two centers of different chemical nature) near the conduction band. Contrary to results of some authors, no correlation was possible between the EPR signal and the visible

range of PL emission spectra; this indicates that centers responsible for the visible emission and the EPR signal are different. Optically detected electron paramagnetic resonance could provide in future work a better understanding of the relation between the defect centers in our materials and the optical and paramagnetic properties.

In summary, surface-functionalized latex particles have been shown to be efficient controlling agents for the mineralization of zinc oxide in aqueous medium. On one hand, the versatility of latex particles offers an interesting approach to polymer-controlled crystallization processes. Particles of chemically structured corona could even be good models to mimic the behavior of globular proteins in biomineralization. On the other hand, the precipitation of zincite in the presence of such polymer particles gives organic–inorganic hybrid materials, whose properties differ from those of the materials synthesized without additives. This could be the source of further developments in the materials science of zinc oxide. Furthermore, our studies could be extended to other metal oxides and II–VI compounds.

References

- [1] S. MANN. *Biomineralization*; Oxford University Press: New York, 2001.
- [2] *Biomineralization*; P. M. DOVE, J. J. DE YOREO, S. WEINER, Eds.; Mineralogical Society of America, Geochemical Society: Washington, 2003; Vol. 54.
- [3] *Biomineralization*; E. BAEUERLEIN, Ed.; Wiley-VCH: Weinheim, 2003.
- [4] E. MATIJEVIĆ. Preparation and Properties of Uniform Size Colloids. *Chem. Mater.* **1993**, *5*, 412–426.
- [5] E. MATIJEVIĆ. Uniform Colloid Dispersions. Achievements and Challenges. *Langmuir* **1994**, *10*, 8–16.
- [6] E. MATIJEVIĆ. Preparation and characterization of well defined powders and their applications in technology. *J. Eur. Ceram. Soc.* **1998**, *18*, 1357–1364.
- [7] W. TREMEL. Inorganic nanotubes. *Angew. Chem. Int. Ed.* **1999**, *38*, 2175–2179.
- [8] G. WEGNER, P. BAUM, M. MÜLLER, J. NORWIG, K. LANDFESTER. Polymers designed to control nucleation and growth of inorganic crystals from aqueous media. *Macromol. Symp.* **2001**, *175*, 349–355.
- [9] Y. QI. Crystallization of zinc oxide controlled by functional poly(styrene/acrylic acid) latex particles. Doctoral Thesis, Johannes Gutenberg-Universität Mainz, Germany, 2004.
- [10] D. PALMS. Kristallisation von Zinkoxid in Gegenwart funktionalisierter Oberflächen. Doctoral Thesis, Johannes Gutenberg-Universität Mainz, Germany, 2003.
- [11] M. FAATZ. Synthese und Anwendung von peptidfunktionalisierten Latexpartikeln mittels Miniemulsionspolymerisation. Diploma Thesis, Johannes Gutenberg-Universität Mainz, Germany, 2002.
- [12] L. HERSCHKE. Polymer controlled mineralization of zinc phosphate hydrates and applications in corrosion protection, catalysis and biomedicine. Doctoral Thesis, Johannes Gutenberg-Universität Mainz, Germany, 2004.
- [13] D. C. LOOK. Recent advances in ZnO materials and devices. *Mater. Sci. Eng. B* **2001**, *80*, 383–387.
- [14] C.-H. YAN, J. ZHANG, L.-D. SUN. Zinc Oxide Nanostructures. In *Encyclopedia of Nanoscience and Nanotechnology*; H. S. NALWA, Ed.; American Scientific Publishers: Stevenson Ranch, 2004; Vol. 10, pp 767–780.
- [15] S. J. PEARTON, D. P. NORTON, K. IP, Y. W. HEO, T. STEINER. Recent progress in processing and properties of ZnO. *Prog. Mater. Sci.* **2005**, *50*, 293–340.
- [16] W. STUMM, J. J. MORGAN. *Aquatic Chemistry: An Introduction Emphasizing Chemical Equilibria in Natural Waters*, 2nd ed.; John Wiley: New York, 1981.
- [17] J. W. MULLIN. *Crystallization*, 4th ed.; Butterworth-Heinemann: Oxford, 2001.
- [18] W. KLEBER. *Einführung in die Kristallographie*, 17th ed.; Verlag Technik: Berlin, 1990.
- [19] W. STUMM, J. J. MORGAN. *Aquatic Chemistry: Chemical Equilibria and Rates in Natural Waters*, 3rd ed.; John Wiley: New York, 1996.
- [20] M. VOLMER. *Kinetik der Phasenbildung*; Verlag von Theodor Steinkopff: Dresden and Leipzig, 1939.
- [21] W. KOSSEL. Zur Theorie des Kristallwachstums. *Nachr. Ges. Wiss. Göttingen, math.-phys. Kl.* **1927**, 135–143.
- [22] W. KOSSEL. Zur Energetik von Oberflächenvorgängen. *Ann. Phys. (Leipzig)* **1934**, *21*, 457–480.
- [23] I. N. STRANSKI. Zur Theorie des Kristallwachstums. *Z. Phys. Chem. (Leipzig)* **1928**, *136*, 259–278.
- [24] W. K. BURTON, N. CABRERA, F. C. FRANK. Role of Dislocations in Crystal Growth. *Nature* **1949**, *163*, 398–399.
- [25] W. K. BURTON, N. CABRERA, F. C. FRANK. The Growth of Crystals and the Equilibrium Structure of Their Surfaces. *Philos. Trans. R. Soc. London, Ser. A* **1951**, *243*, 299–358.
- [26] R. E. LIESEGANG. Über die Reifung von Silberhaloidemulsionen. *Z. Phys. Chem. (Leipzig)* **1911**, *75*, 374–377.
- [27] J. CORISH. Introduction to defects in solids. In *Defect in Solids: Modern Techniques*; A. V. CHADWICK, M. TERENZI, Eds.; Plenum Press: New York, 1985; Vol. B147, pp 1–36.

- [28] F. A. KRÖGER. *The Chemistry of Imperfect Crystals*; North-Holland Publishing Company: Amsterdam, 1964.
- [29] M. P. MARDER. *Condensed Matter Physics*; John Wiley: New York, 2000.
- [30] N. KUBOTA, J. W. MULLIN. A kinetic model for crystal growth from aqueous solution in the presence of impurity. *J. Cryst. Growth* **1995**, *152*, 203–208.
- [31] R. J. DAVEY, J. W. MULLIN. Growth of {100} faces of ammonium dihydrogen phosphate crystals in presence of ionic species. *J. Cryst. Growth* **1974**, *26*, 45–51.
- [32] R. J. DAVEY, J. W. MULLIN. Growth of {101} faces of ammonium dihydrogen phosphate crystals in presence of ionic species. *J. Cryst. Growth* **1974**, *23*, 89–94.
- [33] N. KUBOTA, M. YOKOTA, J. W. MULLIN. The combined influence of supersaturation and impurity concentration on crystal growth. *J. Cryst. Growth* **2000**, *212*, 480–488.
- [34] K. J. C. VAN BOMMEL, F. ARIANNA, S. SHINKAI. Organic Templates for the Generation of Inorganic Materials. *Angew. Chem. Int. Ed.* **2003**, *42*, 980–998.
- [35] F. ISKANDAR, MIKRAJUDDIN, K. OKUYAMA. In Situ Production of Spherical Silica Particles Containing Self-Organized Mesopores. *Nano Lett.* **2001**, *1*, 231–234.
- [36] C. A. MIRKIN. Programming the assembly of two- and three-dimensional architectures with DNA and nanoscale inorganic building blocks. *Inorg. Chem.* **2000**, *39*, 2258–2272.
- [37] D. RAUTARAY, A. KUMAR, S. REDDY, S. R. SAINKAR, M. SASTRY. Morphology of BaSO₄ crystals grown on templates of varying dimensionality: The case of cysteine-capped gold nanoparticles (0-D), DNA (1-D), and lipid bilayer stacks (2-D). *Cryst. Growth Des.* **2002**, *2*, 197–203.
- [38] A. TAUBERT, G. WEGNER. Formation of uniform and monodisperse zincite crystals in the presence of soluble starch. *J. Mater. Chem.* **2002**, *12*, 805–807.
- [39] N. JONGEN, P. BOWEN, J. LEMAITRE, J. C. VALMALETTE, H. HOFMANN. Precipitation of self-organized copper oxalate polycrystalline particles in the presence of hydroxypropylmethylcellulose (HPMC): Control of morphology. *J. Colloid Interface Sci.* **2000**, *226*, 189–198.
- [40] H. HOFMANN, P. BOWEN, N. JONGEN, J. LEMAITRE. Nano-composite powders, a new concept for their synthesis. *Scripta Mater.* **2001**, *44*, 2197–2201.
- [41] A. PEYTCHEVA, H. CÖLFEN, H. SCHNABLEGGER, M. ANTONIETTI. Calcium phosphate colloids with hierarchical structure controlled by polyaspartates. *Colloid Polym. Sci.* **2002**, *280*, 218–227.
- [42] S.-H. YU, H. CÖLFEN, A.-W. XU, W. F. DONG. Complex spherical BaCO₃ superstructures self-assembled by a facile mineralization process under control of simple polyelectrolytes. *Cryst. Growth Des.* **2004**, *4*, 33–37.
- [43] K. NAKA, D. K. KEUM, Y. TANAKA, Y. CHUJO. Control crystallization of calcium carbonate in aqueous solution with in-situ radical polymerization of sodium acrylate as a latent inductor for crystal nucleation and growth. *Bull. Chem. Soc. Jpn.* **2004**, *77*, 827–833.
- [44] M. BALZ, H. A. THERESE, J. X. LI, J. S. GUTMANN, M. KAPPL, L. NASDALA, W. HOFMEISTER, H. J. BUTT, W. TREMEL. Crystallization of vaterite nanowires by the cooperative interaction of tailor-made nucleation surfaces and polyelectrolytes. *Adv. Funct. Mater.* **2005**, *15*, 683–688.
- [45] L. M. QI, H. CÖLFEN, M. ANTONIETTI, M. LI, J. D. HOPWOOD, A. J. ASHLEY, S. MANN. Formation of BaSO₄ fibres with morphological complexity in aqueous polymer solutions. *Chem.—Eur. J.* **2001**, *7*, 3526–3532.
- [46] S.-H. YU, M. ANTONIETTI, H. CÖLFEN, J. HARTMANN. Growth and self-assembly of BaCrO₄ and BaSO₄ nanofibers toward hierarchical and repetitive superstructures by polymer-controlled mineralization reactions. *Nano Lett.* **2003**, *3*, 379–382.
- [47] R. B. BAGWELL, J. SINDEL, W. SIGMUND. Morphological evolution of barium titanate synthesized in water in the presence of polymeric species. *J. Mater. Res.* **1999**, *14*, 1844–1851.
- [48] H. WEI, Q. SHEN, Y. ZHAO, D. J. WANG, D. F. XU. Influence of polyvinylpyrrolidone on the precipitation of calcium carbonate and on the transformation of vaterite to calcite. *J. Cryst. Growth* **2003**, *250*, 516–524.
- [49] H. WEI, S. QIANG, Z. YING, D. J. WANG, D. F. XU. Crystallization habit of calcium carbonate in the presence of sodium dodecyl sulfate and/or polypyrrolidone. *J. Cryst. Growth* **2004**, *260*, 511–516 and 545–550.
- [50] M. BALZ, E. BARRIAU, V. ISTRATOV, H. FREY, W. TREMEL. Controlled crystallization of CaCO₃ on hyperbranched polyglycerol adsorbed to self-assembled monolayers. *Langmuir* **2005**, *21*, 3987–3991.

- [51] T. X. WANG, H. CÖLFEN, M. ANTONIETTI. Nonclassical crystallization: Mesocrystals and morphology change of CaCO_3 crystals in the presence of a polyelectrolyte additive. *J. Am. Chem. Soc.* **2005**, *127*, 3246–3247.
- [52] J. DONNERS, B. R. HEYWOOD, E. W. MEIJER, R. J. M. NOLTE, C. ROMAN, A. SCHENNING, N. SOMMERDIJK. Amorphous calcium carbonate stabilised by poly(propylene imine) dendrimers. *Chem. Commun.* **2000**, 1937–1938.
- [53] R. C. HEDDEN, B. J. BAUER, A. P. SMITH, F. GRÖHN, E. AMIS. Templating of inorganic nanoparticles by PAMAM/PEG dendrimer-star polymers. *Polymer* **2002**, *43*, 5473–5481.
- [54] K. NAKA, Y. TANAKA, Y. CHUJO. Effect of anionic starburst dendrimers on the crystallization of CaCO_3 in aqueous solution: Size control of spherical vaterite particles. *Langmuir* **2002**, *18*, 3655–3658.
- [55] P. BAUM. Kammförmige Polyelektrolyte als Additive in anorganischen Kristallisationsprozessen: Struktur-Wirkungs-Beziehungen. Doctoral Thesis, Johannes Gutenberg-Universität Mainz, Germany, 2000.
- [56] H. CÖLFEN. Double-hydrophilic block copolymers: Synthesis and application as novel surfactants and crystal growth modifiers. *Macromol. Rapid Commun.* **2001**, *22*, 219–252.
- [57] S.-H. YU, H. CÖLFEN. Bio-inspired crystal morphogenesis by hydrophilic polymers. *J. Mater. Chem.* **2004**, *14*, 2124–2147.
- [58] J. M. MARENTETTE, J. NORWIG, E. STOCKELMANN, W. H. MEYER, G. WEGNER. Crystallization of CaCO_3 in the presence of PEO-*block*-PMAA copolymers. *Adv. Mater.* **1997**, *9*, 647–651.
- [59] H. CÖLFEN. Precipitation of carbonates: recent progress in controlled production of complex shapes. *Curr. Opin. Colloid Interface Sci.* **2003**, *8*, 23–31.
- [60] S.-H. YU, H. CÖLFEN, M. ANTONIETTI. Polymer-controlled morphosynthesis and mineralization of metal carbonate superstructures. *J. Phys. Chem. B* **2003**, *107*, 7396–7405.
- [61] H. CÖLFEN, M. ANTONIETTI. Crystal design of calcium carbonate microparticles using double-hydrophilic block copolymers. *Langmuir* **1998**, *14*, 582–589.
- [62] H. CÖLFEN, L. M. QI. A systematic examination of the morphogenesis of calcium carbonate in the presence of a double-hydrophilic block copolymer. *Chem.—Eur. J.* **2001**, *7*, 106–116.
- [63] H. ENDO, D. SCHWAHN, H. CÖLFEN. On the role of block copolymer additives for calcium carbonate crystallization: Small angle neutron scattering investigation by applying contrast variation. *J. Chem. Phys.* **2004**, *120*, 9410–9423.
- [64] M. LEI, W. H. TANG, J. G. YU. Effect of a new functional double-hydrophilic block copolymer PAAL on the morphology of calcium carbonate particles. *Mater. Res. Bull.* **2005**, *40*, 656–664.
- [65] P. SHAKKTHIVEL, D. RAMESH, R. SATHIYAMOORTHY, T. VASUDEVAN. Water soluble copolymers for calcium carbonate and calcium sulphate scale control in cooling water systems. *J. Appl. Polym. Sci.* **2005**, *96*, 1451–1459.
- [66] N. NASSIF, N. GEHRKE, N. PINNA, N. SHIRSHOVA, K. TAUER, M. ANTONIETTI, H. CÖLFEN. Synthesis of stable aragonite superstructures by a biomimetic crystallization pathway. *Angew. Chem. Int. Ed.* **2005**, *44*, 6004–6009.
- [67] S.-H. YU, H. CÖLFEN, K. TAUER, M. ANTONIETTI. Tectonic arrangement of BaCO_3 nanocrystals into helices induced by a racemic block copolymer. *Nat. Mater.* **2005**, *4*, 51–55.
- [68] A. TAUBERT. Polymergesteuerte Fällungskristallisation von Zinkoxid. Doctoral Thesis, Johannes Gutenberg-Universität Mainz, Germany, 2000.
- [69] A. TAUBERT, D. PALMS, O. WEISS, M. T. PICCINI, D. N. BATCHELDER. Polymer-assisted control of particle morphology and particle size of zinc oxide precipitated from aqueous solution. *Chem. Mater.* **2002**, *14*, 2594–2601.
- [70] A. TAUBERT, G. GLASSER, D. PALMS. Kinetics and particle formation mechanism of zinc oxide particles in polymer-controlled precipitation from aqueous solution. *Langmuir* **2002**, *18*, 4488–4494.
- [71] A. TAUBERT, C. KUBEL, D. C. MARTIN. Polymer-induced microstructure variation in zinc oxide crystals precipitated from aqueous solution. *J. Phys. Chem. B* **2003**, *107*, 2660–2666.
- [72] S. F. CHEN, S. H. YU, B. YU, L. REN, W. T. YAO, H. CÖLFEN. Solvent effect on mineral modification: Selective synthesis of cerium compounds by a facile solution route. *Chem.—Eur. J.* **2004**, *10*, 3050–3058.
- [73] L. M. QI, H. CÖLFEN, M. ANTONIETTI. Control of barite morphology by double-hydrophilic block copolymers. *Chem. Mater.* **2000**, *12*, 2392–2403.

- [74] H. CÖLFEN, L. M. QI, Y. MASTAI, L. BÖRGER. Formation of unusual 10-petal BaSO₄ structures in the presence of a polymeric additive. *Cryst. Growth Des.* **2002**, *2*, 191–196.
- [75] M. LI, H. CÖLFEN, S. MANN. Morphological control of BaSO₄ microstructures by double hydrophilic block copolymer mixtures. *J. Mater. Chem.* **2004**, *14*, 2269–2276.
- [76] S.-H. YU, H. CÖLFEN, M. ANTONIETTI. Control of the morphogenesis of barium chromate by using double-hydrophilic block copolymers (DHBCs) as crystal growth modifiers. *Chem.—Eur. J.* **2002**, *8*, 2937–2945.
- [77] S.-H. YU, H. CÖLFEN, M. ANTONIETTI. The combination of colloid-controlled heterogeneous nucleation and polymer-controlled crystallization: Facile synthesis of separated, uniform high-aspect-ratio single-crystalline BaCrO₄ nanofibers. *Adv. Mater.* **2003**, *15*, 133–136.
- [78] D. B. ZHANG, L. M. QI, J. M. MA, H. M. CHENG. Morphological control of calcium oxalate dihydrate by a double-hydrophilic block copolymer. *Chem. Mater.* **2002**, *14*, 2450–2457.
- [79] S.-H. YU, M. ANTONIETTI, H. CÖLFEN, M. GIERSIG. Synthesis of very thin 1D and 2D CdWO₄ nanoparticles with improved fluorescence behavior by polymer-controlled crystallization. *Angew. Chem. Int. Ed.* **2002**, *41*, 2356–2360.
- [80] L. M. QI, H. CÖLFEN, M. ANTONIETTI. Synthesis and characterization of CdS nanoparticles stabilized by double-hydrophilic block copolymers. *Nano Lett.* **2001**, *1*, 61–65.
- [81] M. ANTONIETTI, M. BREULMANN, C. G. GÖLTNER, H. CÖLFEN, K. K. W. WONG, D. WALSH, S. MANN. Inorganic/organic mesostructures with complex architectures: Precipitation of calcium phosphate in the presence of double-hydrophilic block copolymers. *Chem.—Eur. J.* **1998**, *4*, 2493–2500.
- [82] R. M. FITCH. *Polymer Colloids: A Comprehensive Introduction*; Academic Press: London, 1997.
- [83] R. G. GILBERT. *Emulsion Polymerization: A Mechanistic Approach*; Academic Press: London, 1995.
- [84] J. M. ASUA. Emulsion polymerization: From fundamental mechanisms to process developments. *J. Polym. Sci. A* **2004**, *42*, 1025–1041.
- [85] F. A. BOVEY, I. M. KOLTHOFF, A. I. MEDALIA, E. J. MEEHAN. *Emulsion Polymerization*; Interscience Publishers: New York, 1955.
- [86] D. C. BLACKLEY. *Emulsion Polymerisation: Theory and Practice*; Applied Science Publishers: London, 1975.
- [87] *Emulsion Polymerization and Emulsion Polymers*; P. A. LOVELL, M. S. EL-AASSER, Eds.; John Wiley: Chichester, 1997;
- [88] *Scientific Methods for the Study of Polymer Colloids and Their Applications*; F. CANDAU, R. H. OTTEWIL, Eds.; Kluwer Academic Publishers: Dordrecht, 1990; Vol. 303.
- [89] M. S. EL-AASSER, C. D. SMITH, (EDS.). Emulsion Polymers. *Macromol. Symp.* **2000**, *155*, 1–237.
- [90] *Polymer Colloids: Science and Technology of Latex Systems*; E. S. DANIELS, E. D. SUDOL, M. S. EL-AASSER, Eds.; American Chemical Society: Washington, 2001.
- [91] *Polymeric Dispersions: Principles and Applications*; J. M. ASUA, Ed.; Kluwer Academic Publishers: Dordrecht, 1997.
- [92] Q. WANG, S. K. FU, T. Y. YU. Emulsion Polymerization. *Prog. Polym. Sci.* **1994**, *19*, 703–753.
- [93] M. ANTONIETTI, K. TAUER. 90 years of polymer latexes and heterophase polymerization: More vital than ever. *Macromol. Chem. Phys.* **2003**, *204*, 207–219.
- [94] M. NOMURA, H. TOBITA, K. SUZUKI. Emulsion polymerization: Kinetic and mechanistic aspects. In *Polymer Particles*, 2005; Vol. 175, pp 1–128.
- [95] K. LANDFESTER. Polyreactions in miniemulsions. *Macromol. Rapid Commun.* **2001**, *22*, 896–936.
- [96] M. ANTONIETTI, K. LANDFESTER. Polyreactions in miniemulsions. *Prog. Polym. Sci.* **2002**, *27*, 689–757.
- [97] J. M. ASUA. Miniemulsion polymerization. *Prog. Polym. Sci.* **2002**, *27*, 1283–1346.
- [98] F. J. SCHORK, Y. W. LUO, W. WSMULDERS, J. P. JRUSUM, A. BUTTÉ, K. FONTENOT. Miniemulsion Polymerization. *Adv. Polym. Sci.* **2005**, *175*, 129–255.
- [99] S. LELU, C. NOVAT, C. GRAILLAT, A. GUYOT, E. BOURGEAT-LAMI. Encapsulation of an organic phthalocyanine blue pigment into polystyrene latex particles using a miniemulsion polymerization. *Polym. Int.* **2003**, *52*, 542–547.
- [100] F. TIARKS, K. LANDFESTER, M. ANONIETTI. Encapsulation of carbon black by miniemulsion polymerization. *Macromol. Chem. Phys.* **2001**, *202*, 51–60.

- [101] N. BECHTHOLD, F. TIARKS, M. WILLERT, K. LANDFESTER, M. ANTONIETTI. Miniemulsion polymerization: Applications and new materials. *Macromol. Symp.* **2000**, *151*, 549–555.
- [102] L. P. RAMÍREZ, K. LANDFESTER. Magnetic polystyrene nanoparticles with a high magnetite content obtained by miniemulsion processes. *Macromol. Chem. Phys.* **2003**, *204*, 22–31.
- [103] K. LANDFESTER, L. P. RAMÍREZ. Encapsulated magnetite particles for biomedical application. *J. Phys.: Condes. Matter* **2003**, *15*, S1345–S1361.
- [104] E. D. SUDOL, M. S. EL-AASSER. Miniemulsion Polymerization. In *Emulsion Polymerization and emulsion polymers*; P. A. LOVELL, M. S. EL-AASSER, Eds.; John Wiley: Chichester, 1997; pp 699–722.
- [105] G. MOAD, D. H. SOLOMON. *The Chemistry of Free Radical Polymerization*; Pergamon: Oxford, 1995.
- [106] N. BECHTHOLD, K. LANDFESTER. Kinetics of miniemulsion polymerization as revealed by calorimetry. *Macromolecules* **2000**, *33*, 4682–4689.
- [107] M. S. EL-AASSER, E. D. SUDOL. Features of Emulsion Polymerization. In *Emulsion polymerization and emulsion polymers*; P. A. LOVELL, M. S. EL-AASSER, Eds.; John Wiley: Chichester, 1997; pp 37–58.
- [108] J. M. ASUA, V. S. RODRÍGUEZ, E. D. SUDOL, M. S. EL-AASSER. The Free-Radical Distribution in Emulsion Polymerization Using Oil-Soluble Initiators. *J. Polym. Sci. A* **1989**, *27*, 3569–3587.
- [109] C. M. MILLER, P. J. BLYTHE, E. D. SUDOL, C. A. SILEBI, M. S. EL-AASSER. Effect of the Presence of Polymer in Miniemulsion Droplets on the Kinetics of Polymerization. *J. Polym. Sci. A* **1994**, *32*, 2365–2376.
- [110] J. REIMERS, F. J. SCHORK. Miniemulsion copolymerization using water-insoluble comonomers as cosurfactants. *Polym. React. Eng.* **1996**, *4*, 135–152.
- [111] R. J. HUNTER. *Foundations of Colloid Science*, 2nd ed.; Oxford University Press: Oxford, 2001.
- [112] R. H. MÜLLER, S. RAIMUND. *Teilchengrößenmessung in der Laborpraxis*; Wissenschaftliche Verlagsgesellschaft: Stuttgart, 1996.
- [113] R. H. MÜLLER. *Zetapotential und Partikelladung ind der Laborpraxis*; Wissenschaftliche Verlagsgesellschaft: Stuttgart, 1996.
- [114] R. J. HUNTER. *Introduction to Modern Colloid Science*, 1st ed.; Oxford University Press: New York, 1999.
- [115] R. J. HUNTER. *Zeta potential in colloid science*; Academic Press: London, 1981.
- [116] F. TIARKS, K. LANDFESTER, M. ANTONIETTI. Preparation of polymeric nanocapsules by miniemulsion polymerization. *Langmuir* **2001**, *17*, 908–918.
- [117] K. LANDFESTER, N. BECHTHOLD, F. TIARKS, M. ANTONIETTI. Formulation and stability mechanisms of polymerizable miniemulsions. *Macromolecules* **1999**, *32*, 5222–5228.
- [118] K. LANDFESTER, N. BECHTHOLD, S. FORSTER, M. ANTONIETTI. Evidence for the preservation of the particle identity in miniemulsion polymerization. *Macromol. Rapid Commun.* **1999**, *20*, 81–84.
- [119] N. BECHTHOLD. Polymerisation in Miniemulsion. Doctoral Thesis, Universität Potsdam, Germany, 2000.
- [120] T. DING, E. S. DANIELS, M. S. EL-AASSER, A. KLEIN. Synthesis and Characterization of Functionalized Polymer Latex Particles Through a Designed Semicontinuous Emulsion Polymerization Process. *J. Appl. Polym. Sci.* **2005**, *97*.
- [121] P. PINCUS. Colloid Stabilization with Grafted Polyelectrolytes. *Macromolecules* **1991**, *24*, 2912–2919.
- [122] R. GRUNDER, Y. S. KIM, M. BALLAUFF, D. KRANZ, H. G. MULLER. Analysis of Polymer Lattices by Small-Angle X-Ray-Scattering. *Angew. Chem.-Int. Edit. Engl.* **1991**, *30*, 1650–1652.
- [123] H. TAMAI, M. HASEGAWA, T. SUZAWA. Surface Characterization of Hydrophilic Functional Polymer Latex-Particles. *J. Appl. Polym. Sci.* **1989**, *38*, 403–412.
- [124] D. CHARMOT, J. F. DALLEST, F. DOBLER. Carboxylated styrene-butyl acrylate and styrene-butadiene emulsion copolymers. Modelling the distribution of the acid monomer between serum, particle surface and the particle core. *Polymer* **1996**, *37*, 5237–5245.
- [125] L. VORWERG, R. G. GILBERT. Electrosteric stabilization with poly(acrylic acid) in emulsion polymerization: Effect on kinetics and secondary particle formation. *Macromolecules* **2000**, *33*, 6693–6703.

- [126] X. GUO, A. WEISS, M. BALLAUFF. Synthesis of spherical polyelectrolyte brushes by photoemulsion polymerization. *Macromolecules* **1999**, *32*, 6043–6046.
- [127] P. BORGET, F. LAFUMA, C. BONNET-GONNET. Characterizations and properties of hairy latex particles. *J. Colloid Interface Sci.* **2005**, *285*, 136–145.
- [128] B. HIRZINGER, M. HELMSTEDT, J. STEJSKAL. Light scattering studies on core–shell systems: determination of size parameters of sterically stabilized poly(methylmethacrylate) dispersions. *Polymer* **2000**, *41*, 2883–2891.
- [129] G. FRITZ, V. SCHADLER, N. WILLENBACHER, N. J. WAGNER. Electrosteric stabilization of colloidal dispersions. *Langmuir* **2002**, *18*, 6381–6390.
- [130] R. H. OTTEWILL. Small angle neutron scattering on polymer colloids. In *Scientific Methods for the Study of Polymer Colloids and Their Applications*; F. CANDAU, OTTEWILL, Eds.; Kluwer Academic Publishers: Dordrecht, 1990; Vol. 303.
- [131] R. H. OTTEWILL. Experimental Methods of Particle Characterization. *Pure Appl. Chem.* **1992**, *64*, 1697–1702.
- [132] H. DE BRUYN, R. G. GILBERT, J. W. WHITE, J. C. SCHULZ. Characterization of electrosterically stabilized polystyrene latex; implications for radical entry kinetics. *Polymer* **2003**, *44*, 4411–4420.
- [133] N. DINGENOUTS, C. NORHAUSEN, M. BALLAUFF. Observation of the volume transition in thermosensitive core–shell latex particles by small-angle X-ray scattering. *Macromolecules* **1998**, *31*, 8912–8917.
- [134] K. ISHIZU. Morphology of Core–Shell Type Polymer Microspheres on Carbon Substrates. *J. Colloid Interface Sci.* **1993**, *156*, 299–304.
- [135] M. A. WINNIK, C. L. ZHAO, O. SHAFFER, R. R. SHIVERS. Electron Microscopy Studies of Polystyrene–Poly(Methyl Methacrylate) Core–Shell Latex Particles. *Langmuir* **1993**, *9*, 2053–2065.
- [136] S. KIRSCH, A. DOERK, E. BARTSCH, H. SILLESCU, K. LANDFESTER, H. W. SPIESS, W. MAECHTLE. Synthesis and characterization of highly cross-linked, monodisperse core–shell and inverted core–shell colloidal particles. Polystyrene/poly(*tert*-butyl acrylate) core–shell and inverse core–shell particles. *Macromolecules* **1999**, *32*, 4508–4518.
- [137] I. PASTORIZA-SANTOS, B. SCHOLER, F. CARUSO. Core–shell colloids and hollow polyelectrolyte capsules based on diazoresins. *Adv. Funct. Mater.* **2001**, *11*, 122–128.
- [138] R. B. WANG, H. SCHMIEDEL, B. R. PAULKE. Isothermal titration calorimetric studies of surfactant interactions with negatively charged, 'hairy' latex nanoparticles. *Colloid Polym. Sci.* **2004**, *283*, 91–97.
- [139] X. WU, T. G. M. VAN DE VEN. Characterization of hairy latex particles with colloidal particle scattering. *Langmuir* **1996**, *12*, 3859–3865.
- [140] R. L. ROWELL. Characterization of Polymer Colloids. In *Scientific Methods for the Study of Polymer Colloids and Their Applications*; F. CANDAU, R. H. OTTEWILL, Eds.; Kluwer Academic Publishers: Dordrecht, 1990; pp 187–208.
- [141] ANA MORFESIS. Particle Sizing by Dynamic Light Scattering. Malvern Instruments; electronic document to be downloaded at <http://www.malvern.co.uk/common/webcasts/webcasts.htm> [or alternatively at: http://www.brainshark.com/malvern/particlesize_DLS] (accessed Aug 2005).
- [142] H. M. BUCHHAMMER, G. PETZOLD, K. LUNKWITZ. The Interaction between Oppositely Charged Polyelectrolytes in the Presence of Solid-Surfaces. *Colloid Surf. A* **1993**, *76*, 81–85.
- [143] S. K. KAM, J. GREGORY. Charge determination of synthetic cationic polyelectrolytes by colloid titration. *Colloid Surf. A* **1999**, *159*, 165–179.
- [144] K. BÖCKENHOFF, W. R. FISCHER. Determination of electrokinetic charge with a particle-charge detector, and its relationship to the total charge. *Fresenius J. Anal. Chem.* **2001**, *371*, 670–674.
- [145] H. TERAYAMA. Method of Colloid Titration (a New Titration between Polymer Ions). *J. Polym. Sci.* **1952**, *8*, 243–253.
- [146] K. H. WASSMER, U. SCHROEDER, D. HORN. Characterization and Detection of Polyanions by Direct Polyelectrolyte Titration. *Makromol. Chem.* **1991**, *192*, 553–565.
- [147] *PCD 03 pH, Particle Charge Detector: Instruction Manual*; Müttek Analytic: Herrsching (Germany), 1997.

- [148] M. ANDRÉS-VERGÉS, M. MARTÍNEZ-GALLEGO. Spherical and Rod-Like Zinc-Oxide Microcrystals - Morphological Characterization and Microstructural Evolution with Temperature. *J. Mater. Sci.* **1992**, *27*, 3756–3762.
- [149] S. MUSIĆ, D. ĐRAGČEVIĆ, M. MALJKOVIĆ, S. POPOVIĆ. Influence of chemical synthesis on the crystallization and properties of zinc oxide. *Mater. Chem. Phys.* **2002**, *77*, 521–530.
- [150] L. N. WANG, M. MUHAMMED. Synthesis of zinc oxide nanoparticles with controlled morphology. *J. Mater. Chem.* **1999**, *9*, 2871–2878.
- [151] H. Y. XU, H. WANG, Y. C. ZHANG, W. L. HE, M. K. ZHU, B. WANG, H. YAN. Hydrothermal synthesis of zinc oxide powders with controllable morphology. *Ceram. Int.* **2004**, *30*, 93–97.
- [152] J. E. RODRÍGUEZ-PAEZ, A. C. CABALLERO, M. VILLEGAS, C. MOURE, P. DURÁN, J. F. FERNÁNDEZ. Controlled precipitation methods: formation mechanism of ZnO nanoparticles. *J. Eur. Ceram. Soc.* **2001**, *21*, 925–930.
- [153] A. P. A. DE OLIVEIRA, J. F. HOCHÉPIED, F. GRILLON, M. H. BERGER. Controlled precipitation of zinc oxide particles at room temperature. *Chem. Mater.* **2003**, *15*, 3202–3207.
- [154] Z. S. HU, G. OSKAM, P. C. SEARSON. Influence of solvent on the growth of ZnO nanoparticles. *J. Colloid Interface Sci.* **2003**, *263*, 454–460.
- [155] S. A. VOROBYOVA, A. I. LESNIKOVICH, V. V. MUSHINSKII. Interphase synthesis and characterization of zinc oxide. *Mater. Lett.* **2004**, *58*, 863–866.
- [156] T. TRINDADE, J. D. PEDROSA DE JESUS, P. O'BRIEN. Precipitation of Zinc Oxide and Zinc Sulfide Powders by Controlled Precipitation from Aqueous Solution. *J. Mater. Chem.* **1994**, *4*, 1611–1617.
- [157] D. R. CHEN, X. L. JIAO, G. CHENG. Hydrothermal synthesis of zinc oxide powders with different morphologies. *Solid State Commun.* **1999**, *113*, 363–366.
- [158] M. ÖNER, J. NORWIG, W. H. MEYER, G. WEGNER. Control of ZnO crystallization by a PEO-*b*-PMAA diblock copolymer. *Chem. Mater.* **1998**, *10*, 460–463.
- [159] P. SCHINDLER, H. ALTHAUS, F. HOFER, W. MINDER. Löslichkeitsprodukte von Metalloxiden und -hydroxiden (10. Mitteilung): Löslichkeitsprodukte von Zinkoxid, Kupferhydroxid und Kupferoxid in Abhängigkeit von Teilchengröße und molarer Oberfläche. Ein Beitrag zur Thermodynamik von Grenzflächen fest-flüssig. *Helv. Chim. Acta* **1965**, *48*, 1204–1215.
- [160] C. F. BAES, R. E. MESMER. *The Hydrolysis of Cations*; John Wiley: New York, 1976.
- [161] P. SCHINDLER, H. ALTHAUS, W. FEITKNECHT. Löslichkeitsprodukte von Metalloxiden und -hydroxiden (9. Mitteilung): Löslichkeitsprodukte und Freie Bildungsenthalpien von Zinkoxid, amorphem Zinkhydroxid, β_1 -, β_2 -, γ -, δ - und ϵ -Zinkhydroxid. *Helv. Chim. Acta* **1964**, *47*, 982–991.
- [162] B. V. ENÜSTÜN, J. TURKEVICH. Solubility of Fine Particles of Strontium Sulfate. *J. Am. Chem. Soc.* **1960**, *82*, 4502–4509.
- [163] U. ÖZGÜR, Y. I. ALIVOV, C. LIU, A. TEKE, M. A. RESHCHIKOV, S. DOGAN, V. AVRUTIN, S.-J. CHO, H. MORKOÇ. A comprehensive review of ZnO materials and devices. *J. Appl. Phys.* **2005**, *98*, 041301 (1–103).
- [164] Powder diffraction file, card 36-1451, JCPDS–ICDD (Joint Committee on Powder Diffraction Standards–International Center for Diffraction Data), Swarthmore, 1996.
- [165] D. M. KOLB, H.-J. SCHULZ. Optical properties of zinc oxide. In *Current Topics in Materials Science*; E. KALDIS, Ed.; North-Holland Publishing Company: Amsterdam, 1981; Vol. 7, pp 226–268.
- [166] S. A. FRENCH, A. A. SOKOL, S. T. BROMLEY, C. R. A. CATLOW, S. C. ROGERS, P. SHERWOOD. Assignment of the complex vibrational spectra of the hydrogenated ZnO polar surfaces using QM/MM embedding. *J. Chem. Phys.* **2003**, *118*, 317–320.
- [167] P. PONASEWICZ, R. LITBARSKI. Adsorption phenomena. In *Current Topics in Materials Science*; E. KALDIS, Ed.; North-Holland Publishing Company, 1981; Vol. 7, pp 371–409.
- [168] H. P. KLUG, L. E. ALEXANDER. *X-Ray Diffraction Procedures for Polycrystalline and Amorphous Materials*, 2nd ed.; John Wiley: New York, 1974.
- [169] T. C. DAMEN, S. P. S. PORTO, B. TELL. Raman Effect in Zinc Oxide. *Phys. Rev.* **1966**, *142*, 570–574.
- [170] M. ANDRÉS-VERGÉS, A. MIFSUD, C. J. SERNA. Formation of Rod-like Zinc Oxide Microcrystals in Homogeneous Solutions. *J. Chem. Soc. Faraday Trans.* **1990**, *86*, 959–963.
- [171] M. ANDRÉS-VERGÉS, C. J. SERNA. Morphological Characterization of ZnO Powders by X-Ray and IR Spectroscopy. *J. Mater. Sci. Lett.* **1988**, *7*, 970–972.

- [172] M. OCAÑA, V. FORNÉS, J. V. GARCÍA-RAMOS, C. J. SERNA. Polarization Effects in the Infrared Spectra of α -Quartz and α -Cristobalite. *Phys. Chem. Minerals* **1987**, 1987, 527–532.
- [173] C. J. SERNA, M. OCAÑA, J. E. IGLESIAS. Optical properties of α -Fe₂O₃ microcrystals in the infrared. *J. Phys. C: Solid State Phys.* **1987**, 20, 473–484.
- [174] S. GHOSE. The Crystal Structure of Hydrozincite, Zn₅(OH)₆(CO₃)₂. *Acta Cryst.* **1964**, 17, 1051–1057.
- [175] W. STÄHLIN, H. R. OSWALD. The Crystal Structure of Zinc Hydroxide Nitrate, Zn₅(OH)₈(NO₃)₂·2H₂O. *Acta Cryst.* **1970**, B26, 860–863.
- [176] L. POUL, N. JOUINI, F. FIEVET. Layered hydroxide metal acetates (metal = zinc, cobalt, and nickel): Elaboration via hydrolysis in polyol medium and comparative study. *Chem. Mater.* **2000**, 12, 3123–3132.
- [177] E. HOSONO, S. FUJIHARA, T. KIMURA, H. IMAI. Growth of layered basic zinc acetate in methanolic solutions and its pyrolytic transformation into porous zinc oxide films. *J. Colloid Interface Sci.* **2004**, 272, 391–398.
- [178] K. O. KONGSHAUG, H. FJELLVAG. Organically pillared layered zinc hydroxides. *J. Solid State Chem.* **2004**, 177, 1852–1857.
- [179] Z. L. HUANG, M. DRILLON, N. MASCIOCCHI, A. SIRONI, J. T. ZHAO, P. RABU, P. PANISSOD. Ab-initio XRPD crystal structure and giant hysteretic effect (H-c=5.9 T) of a new hybrid terephthalate-based cobalt(II) magnet. *Chem. Mater.* **2000**, 12, 2805–2812.
- [180] J. H. CHOY, Y. M. KWON, K. S. HAN, S. W. SONG, S. H. CHANG. Intra- and inter-layer structures of layered hydroxy double salts, Ni_{1-x}Zn_{2x}(OH)₂(CH₃CO₂)_{2x}·nH₂O. *Mater. Lett.* **1998**, 34, 356–363.
- [181] A. M. STONEHAM. *Theory of defects in solids: electronic structure of defects in insulators and semiconductors*; Oxford University Press, 2001.
- [182] D. C. LOOK. Electrical and optical properties of p-type ZnO. *Semicond. Sci. Technol.* **2005**, 20, S55–S61.
- [183] *Nomenclature of Inorganic Chemistry: IUPAC Recommendations 2005*; N. G. CONNELLY, R. M. DAMHUS, R. M. HARSHORN, A. T. HUTTON, Eds.; The Royal Society of Chemistry: London, 2005;
- [184] L. SMART, E. MOORE. *Solid State Chemistry: An introduction*, 2nd ed.; Chapman & Hall: London, 1995.
- [185] A. F. KOHAN, G. CEDER, D. MORGAN, C. G. VAN DE WALLE. First-principles study of native point defects in ZnO. *Phys. Rev. B: Condens. Matter* **2000**, 61, 15019–15027.
- [186] W. HIRSCHWALD. In *Current Topics in Materials Science, Vol. 7*; E. KALDIS, Ed.; North-Holland Publishing Company: Amsterdam, 1981.
- [187] C. G. VAN DE WALLE. Defect analysis and engineering in ZnO. *Physica B* **2001**, 308–310, 899–903.
- [188] J. W. VERHOEVEN. Glossary of terms used in photochemistry: IUPAC Recommendations 1996. *Pure Appl. Chem.* **1996**, 68, 2223–2286.
- [189] J.-M. SPAETH. Spectroscopic studies of defects in ionic and semi-ionic solids. In *Defects in Solids: Modern Techniques*; A. V. CHADWICK, M. TERENCE, Eds.; Plenum Press: New York, 1985; Vol. B147, pp 205–241.
- [190] B. K. MEYER, H. ALVES, D. M. HOFMANN, W. KRIEGSEIS, D. FORSTER, F. BERTRAM, J. CHRISTEN, A. HOFFMANN, M. STRASSBURG, M. DWORZAK, U. HABOECK, A. V. RODINA. Bound exciton and donor–acceptor pair recombinations in ZnO. *Phys. Status Solidi B* **2004**, 241, 231–260.
- [191] B. K. MEYER, J. SANN, D. M. HOFMANN, C. NEUMANN, A. ZENNER. Shallow donors and acceptors in ZnO. *Semicond. Sci. Technol.* **2005**, 20, S62–S66.
- [192] D. C. LOOK, J. W. HEMSKY, J. R. SIZELOVE. Residual Native Shallow Donor in ZnO. *Phys. Rev. Lett.* **1999**, 82, 2552–2555.
- [193] D. M. HOFMANN, A. HOFSTAETTER, F. LEITER, H. J. ZHOU, F. HENECKER, B. K. MEYER, S. B. ORLINSKII, J. SCHMIDT, P. G. BARANOV. Hydrogen: A relevant shallow donor in zinc oxide. *Phys. Rev. Lett.* **2002**, 88, 045504(1–4).
- [194] K. THONKE, T. GRUBER, N. TROFILOV, S. R., A. WAAG, R. SAUER. Donor–acceptor pair transitions in ZnO substrate material. *Physica B* **2001**, 308–310, 945–948.
- [195] R. DINGLE. Luminescent Transitions Associated with Divalent Copper Impurities and Green Emission from Semiconducting Zinc Oxide. *Phys. Rev. Lett.* **1969**, 23, 579–581.
- [196] N. Y. GARCÉS, L. WANG, L. BAI, N. C. GILES, L. E. HALLIBURTON, G. CANTWELL. Role of copper in the green luminescence from ZnO crystals. *Appl. Phys. Lett.* **2002**, 81, 622–624.

- [197] F. A. KRÖGER, H. J. VINK. The Origin of the Fluorescence in Self-Activated ZnS, CdS, and ZnO. *J. Chem. Phys.* **1954**, *22*, 250–252.
- [198] N. RIEHL, H. ORTMANN. Über den Aufbau des lumineszierenden Zinkoxyds. *Z. Elektrochem.* **1956**, *60*, 149–151.
- [199] K. VANHEUSDEN, C. H. SEAGER, W. L. WARREN, D. R. TALLANT, J. A. VOIGT. Correlation between photoluminescence and oxygen vacancies in ZnO phosphors. *Appl. Phys. Lett.* **1996**, *68*, 403–405.
- [200] K. VANHEUSDEN, W. L. WARREN, C. H. SEAGER, D. R. TALLANT, J. A. VOIGT, B. E. GNADE. Mechanisms behind green photoluminescence in ZnO phosphor powders. *J. Appl. Phys.* **1996**, *79*, 7983–7990.
- [201] F. H. LEITER, H. ALVES, A. HOFSTAETTER, D. M. HOFMANN, B. K. MEYER. The Oxygen Vacancy as the Origin of a Green Emission in Undoped ZnO. *Phys. Status Solidi B* **2001**, *226*, R4–R5.
- [202] F. LEITER, H. ALVES, D. PFISTERER, N. G. ROMANOV, D. M. HOFMANN, B. K. MEYER. Oxygen vacancies in ZnO. *Physica B* **2003**, *340*, 201–204.
- [203] A. VAN DIJKEN, E. A. MEULENKAMP, D. VANMAEKELBERGH, A. MEIJERINK. The luminescence of nanocrystalline ZnO particles: the mechanism of the ultraviolet and visible emission. *J. Lumin.* **2000**, *87–89*, 454–456.
- [204] A. VAN DIJKEN, E. A. MEULENKAMP, D. VANMAEKELBERGH, A. MEIJERINK. The kinetics of the radiative and nonradiative processes in nanocrystalline ZnO particles upon photoexcitation. *J. Phys. Chem. B* **2000**, *104*, 1715–1723.
- [205] A. VAN DIJKEN, E. A. MEULENKAMP, D. VANMAEKELBERGH, A. MEIJERINK. Identification of the transition responsible for the visible emission in ZnO using quantum size effects. *J. Lumin.* **2000**, *90*, 123–128.
- [206] H.-J. EGELHAAF, D. OELKRUG. Luminescence and nonradiative deactivation of excited states involving oxygen defect centers in polycrystalline ZnO. *J. Cryst. Growth* **1996**, *161*, 190–194.
- [207] B. GUO, Z. R. QIU, K. S. WONG. Intensity dependence and transient dynamics of donor–acceptor pair recombination in ZnO thin films grown on (001) silicon. *Appl. Phys. Lett.* **2003**, *82*, 2290–2292.
- [208] E. G. BYLANDER. Surface Effects on Low-Energy Cathodoluminescence of Zinc Oxide. *J. Appl. Phys.* **1978**, *49*, 1188–1195.
- [209] N. O. KORSUNSKA, L. V. BORKOVSKA, B. M. BULAKH, L. Y. KHOMENKOVA, V. I. KUSHNIRENKO, I. V. MARKEVICH. The influence of defect drift in external electric field on green luminescence of ZnO single crystals. *J. Lumin.* **2003**, *102*, 733–736.
- [210] D. C. REYNOLDS, D. C. LOOK, B. JOGAI, H. MORKOÇ. Similarities in the bandedge and deep-centre photoluminescence mechanisms of ZnO and GaN. *Solid State Commun.* **1997**, *101*, 643–646.
- [211] B. X. LIN, Z. X. FU, Y. B. JIA. Green luminescent center in undoped zinc oxide films deposited on silicon substrates. *Appl. Phys. Lett.* **2001**, *79*, 943–945.
- [212] F. VAN CRAEYNES, W. MAENHOUT, W. DEKEYSER. Interpretation of yellow colour of heat treated ZnO powder. *Phys. Status Solidi* **1965**, *8*, 841.
- [213] S. M. THOMSEN. Sulfide in Zinc-Oxide Luminophors. *J. Chem. Phys.* **1950**, *18*, 770.
- [214] W. LEHMAN. Zinc Oxide and Zinc Cadmium Oxide Phosphors. *J. Electrochem. Soc.* **1968**, *115*, 538–540.
- [215] N. OHASHI, T. NAKATA, T. SEKIGUCHI, H. HOSONO, M. MIZUGUCHI, T. TSURUMI, J. TANAKA, H. HANEDA. Yellow emission from zinc oxide giving an electron spin resonance signal at $g=1.96$. *Jpn. J. Appl. Phys. Part 2* **1999**, *38*, L113–L115.
- [216] M. LIU, A. H. KITAI, P. MASCHER. Point defects and luminescence in zinc oxide and zinc oxide doped with manganese. *J. Lumin.* **1992**, *54*, 35–42.
- [217] S. A. STUDENIKIN, N. GOLEGO, M. COCIVERA. Fabrication of green and orange photoluminescent, undoped ZnO films using spray pyrolysis. *J. Appl. Phys.* **1998**, *84*, 2287–2294.
- [218] X. L. WU, G. G. SIU, C. L. FU, H. C. ONG. Photoluminescence and cathodoluminescence studies of stoichiometric and oxygen-deficient ZnO films. *Appl. Phys. Lett.* **2001**, *78*, 2285–2287.
- [219] L. E. GREENE, M. LAW, J. GOLDBERGER, F. KIM, J. C. JOHNSON, Y. F. ZHANG, R. J. SAYKALLY, P. D. YANG. Low-temperature wafer-scale production of ZnO nanowire arrays. *Angew. Chem. Int. Ed.* **2003**, *42*, 3031–3034.

- [220] X. LIU, X. H. WU, H. CAO, R. P. H. CHANG. Growth mechanism and properties of ZnO nanorods synthesized by plasma-enhanced chemical vapor deposition. *J. Appl. Phys.* **2004**, *95*, 3141–3147.
- [221] D. H. LIU, L. LIAO, J. C. LI, H. X. GUO, Q. FU. Preparation and photoluminescence of ZnO nanostructures by thermal evaporation growth without catalysts. *Mater. Sci. Eng. B* **2005**, *121*, 77–80.
- [222] L. DAI, X. L. CHEN, W. J. WANG, T. ZHOU, B. Q. HU. Growth and luminescence characterization of large-scale zinc oxide nanowires. *J. Phys.: Condes. Matter* **2003**, *15*, 2221–2226.
- [223] Z. Y. XUE, D. H. ZHANG, Q. P. WANG, J. H. WANG. The blue photoluminescence emitted from ZnO films deposited on glass substrate by rf magnetron sputtering. *Appl. Surf. Sci.* **2002**, *195*, 126–129.
- [224] D. H. ZHANG, Z. Y. XUE, Q. P. WANG. The mechanisms of blue emission from ZnO films deposited on glass substrate by r.f. magnetron sputtering. *J. Phys. D* **2002**, *35*, 2837–2840.
- [225] W. D. YU, X. M. LI, X. D. GAO. Catalytic synthesis and structural characteristics of high-quality tetrapod-like ZnO nanocrystals by a modified vapor transport process. *Cryst. Growth Des.* **2005**, *5*, 151–155.
- [226] Z. B. FANG, Y. Y. WANG, D. Y. XU, Y. S. TAN, X. Q. LIU. Blue luminescent center in ZnO films deposited on silicon substrates. *Opt. Mater.* **2004**, *26*, 239–242.
- [227] S. MONTICONE, R. TUFEU, A. V. KANAIEV. Complex nature of the UV and visible fluorescence of Colloidal ZnO nanoparticles. *J. Phys. Chem. B* **1998**, *102*, 2854–2862.
- [228] J. KUBOTA, K. HAGA, Y. KASHIWABA, H. WATANABE, B. P. ZHANG, Y. SEGAWA. Characteristics of ZnO whiskers prepared from organic zinc. *Appl. Surf. Sci.* **2003**, *216*, 431–435.
- [229] D. H. LIU, L. LIAO, J. C. LI, H. X. GUO, Q. FU. Preparation and photoluminescence of ZnO nanostructures by thermal evaporation growth without catalysts. *Mater. Sci. Eng. B* **2005**, *121*, 77–80.
- [230] G. NEUMANN. Paramagnetical properties. In *Current Topics in Materials Science*; E. KALDIS, Ed.; North-Holland Publishing Company: Amsterdam, 1981; Vol. 7, pp 269–278.
- [231] N. Y. GARCES, N. C. GILES, L. E. HALLIBURTON, G. CANTWELL, D. B. EASON, D. C. REYNOLDS, D. C. LOOK. Production of nitrogen acceptors in ZnO by thermal annealing. *Appl. Phys. Lett.* **2002**, *80*, 1334–1336.
- [232] M. M. DEMIR, R. MUÑOZ-ESPI, I. LIEBERWIRTH, G. WEGNER. Precipitation of monodisperse ZnO nanocrystals via acid-catalyzed esterification of zinc acetate. To be published.
- [233] R. SIPS. On the Structure of a Catalyst Surface. *J. Chem. Phys.* **1948**, *16*, 490–495.
- [234] R. SIPS. On the Structure of a Catalyst Surface (II). *J. Chem. Phys.* **1950**, *18*, 1024–1026.
- [235] P. ATKINS, J. DE PAULA. *Atkins' Physical Chemistry*, 7th ed.; Oxford University Press: Oxford, 2001.
- [236] D. A. MELNICK. Zinc Oxide Photoconduction, an Oxygen Adsorption Process. *J. Chem. Phys.* **1957**, *26*, 1136–1146.
- [237] R. J. COLLINS, D. G. THOMAS. Photoconduction and Surface Effects with Zinc Oxide Crystals. *Phys. Rev.* **1958**, *112*, 388–395.
- [238] D. B. MEDVED. Photodesorption in Zinc Oxide Semiconductor. *J. Chem. Phys.* **1958**, *28*, 870–873.
- [239] K. TANAKA, BLYHOLDE. G. Adsorbed Oxygen Species on Zinc Oxide in Dark and under Illumination. *J. Phys. Chem.* **1972**, *76*, 3184–3187.
- [240] Y. SHAPIRA, S. M. COX, D. LICHTMAN. Photodesorption from Powdered Zinc-Oxide. *Surface Science* **1975**, *50*, 503–514.
- [241] Y. TAKAHASHI, M. KANAMORI, A. KONDOH, H. MINOURA, Y. OHYA. Photoconductivity of Ultrathin Zinc-Oxide Films. *Jpn. J. Appl. Phys. Part 1* **1994**, *33*, 6611–6615.
- [242] D. H. ZHANG. Adsorption and photodesorption of oxygen on the surface and crystallite interfaces of sputtered ZnO films. *Mater. Chem. Phys.* **1996**, *45*, 248–252.
- [243] Q. H. LI, T. GAO, Y. G. WANG, T. H. WANG. Adsorption and desorption of oxygen probed from ZnO nanowire films by photocurrent measurements. *Appl. Phys. Lett.* **2005**, *86*, 123117(1–3).
- [244] D. W. BAHNEMANN, C. KORMANN, M. R. HOFFMANN. Preparation and Characterization of Quantum Size Zinc Oxide – A Detailed Spectroscopic Study. *J. Phys. Chem.* **1987**, *91*, 3789–3798.

- [245] L. E. GREENE, M. LAW, J. GOLDBERGER, F. KIM, J. C. JOHNSON, Y. F. ZHANG, R. J. SAYKALLY, P. D. YANG. Low-temperature wafer-scale production of ZnO nanowire arrays. *Angew. Chem. Int. Ed.* **2003**, *42*, 3031–3034.
- [246] P. O. HOLTZ, B. MONEMAR, H. J. LOZYKOWSKI. Optical properties of Ag-related centers in bulk ZnSe. *Phys. Rev. B: Condens. Matter* **1985**, *32*, 986–996.
- [247] D. S. JIANG, H. JUNG, K. PLOOG. Temperature dependence of photoluminescence from GaAs single and multiple quantum-well heterostructures grown by molecular-beam epitaxy. *J. Appl. Phys.* **1988**, *64*, 1371–1377.
- [248] X. T. ZHANG, Y. C. LIU, Z. Z. ZHI, J. Y. ZHANG, Y. M. LU, D. Z. SHEN, W. XU, X. W. FAN, X. G. KONG. Temperature dependence of excitonic luminescence from nanocrystalline ZnO films. *J. Lumin.* **2002**, *99*, 149–154.
- [249] P. B. ALLEN, M. CARDONA. Temperature dependence of the direct gap of Si and Ge. *Phys. Rev. B: Condens. Matter* **1983**, *27*, 4760–4769.
- [250] T. MAKINO, C. H. CHIA, N. T. TUAN, Y. SEGAWA, M. KAWASAKI, A. OHTOMO, K. TAMURA, H. KOINUMA. Exciton spectra of ZnO epitaxial layers on lattice-matched substrates grown with laser-molecular-beam epitaxy. *Appl. Phys. Lett.* **2000**, *76*, 3549–3551.
- [251] D. C. REYNOLDS, D. C. LOOK, B. JOGAI, J. E. HOELSCHER, R. E. SHERRIFF, M. T. HARRIS, M. J. CALLAHAN. Time-resolved photoluminescence lifetime measurements of the Γ_5 and Γ_6 free excitons in ZnO. *J. Appl. Phys.* **2000**, *88*, 2152–2153.
- [252] S. A. STUDENIKIN, M. COCIVERA. Time-resolved luminescence and photoconductivity of polycrystalline ZnO films. *J. Appl. Phys.* **2002**, *91*, 5060–5065.
- [253] G. WILLIAMS, D. C. WATTS. Non-Symmetrical Dielectric Relaxation Behaviour Arising from a Simple Empirical Decay Function. *Trans. Faraday Soc.* **1970**, *66*, 80–85.
- [254] X. CHEN, B. HENDERSON, K. P. O'DONNELL. Luminescence Decay in Disordered Low-Dimensional Semiconductors. *Appl. Phys. Lett.* **1992**, *60*, 2672–2674.
- [255] X. CHEN, D. UTTAMCHANDANI, D. SANDER, K. P. O'DONNELL. Luminescence Decay of Porous Silicon. *Physica B* **1993**, *185*, 603–607.
- [256] M. C. KO, G. J. MEYER. Dynamic Quenching of Porous Silicon Photoluminescence by Anthracene and 10-Methylphenothiazine. *Chem. Mater.* **1995**, *7*, 12–14.
- [257] I. DAG, E. LIFSHTIZ. Dynamics of recombination processes in PbI₂ nanocrystals embedded in porous silica films. *J. Phys. Chem.* **1996**, *100*, 8962–8972.
- [258] S. RINGHOFER, J. KALLEN, R. DUTZLER, A. BILLICH, A. VISSER, D. SCHOLZ, O. STEINHAUSER, H. SCHREIBER, M. AUER, A. J. KUNGL. X-ray structure and conformational dynamics of the HIV-1 protease in complex with the inhibitor SDZ283-910: Agreement of time-resolved spectroscopy and molecular dynamics simulations. *J. Mol. Biol.* **1999**, *286*, 1147–1159.
- [259] K. C. B. LEE, J. SIEGEL, S. E. D. WEBB, S. LEVEQUE-FORT, M. J. COLE, R. JONES, K. DOWLING, M. J. LEVER, P. M. W. FRENCH. Application of the stretched exponential function to fluorescence lifetime imaging. *Biophys. J.* **2001**, *81*, 1265–1274.
- [260] C. IM, J. M. LUPTON, P. SCHOUWINK, S. HEUN, H. BECKER, H. BASSLER. Fluorescence dynamics of phenyl-substituted polyphenylenevinylene-trinitrofluorenone blend systems. *J. Chem. Phys.* **2002**, *117*, 1395–1402.
- [261] J. LEE, M. LEE, K. J. B. LEE, D. S. KO. Scanning confocal fluorescence microscopy of single DNA-EtBr complexes dispersed in polymer. *Chem. Phys. Lett.* **2004**, *394*, 49–53.
- [262] M. N. BERBERAN-SANTOS, E. N. BODUNOV, B. VALEUR. Mathematical functions for the analysis of luminescence decays with underlying distributions 1. Kohlrausch decay function (stretched exponential). *Chem. Phys.* **2005**, *315*, 171–182.

List of abbreviations and symbols

Symbols with more than one character are entered according to the main letter (e.g., ΔG is entered in the position of G). Capitals are entered after lower-case letters. Values of physical constants are included in brackets after the corresponding symbol.

Abbreviations and acronyms

AA	acrylic acid	PL	photoluminescence
AIBN	2,2'-azobis(isobutyronitrile)	PLE	photoluminescence excitation
AMBN	2,2'-azobis(2-methylbutyronitrile)	poly-DADMAC	poly(diallyldimethylammonium chloride)
APh	2-allylphenol	PS	polystyrene
BCF	Burton–Cabrera–Frank	P(S–AA)	poly(styrene–acrylic acid)
BE	bound exciton	P(S–APh)	poly(styrene–2-allylphenol)
c.m.c.	critical micelle concentration	P(S–EGMP)	poly(styrene–ethylene glycol methacrylate phosphate)
DAP	donor–acceptor pair	P(S–MA)	poly(styrene–maleic acid)
DLS	dynamic light scattering	P(S–MAA)	poly(styrene–methacrylic acid)
EGMP	ethylene glycol methacrylate phosphate	P(S–MAN)	poly(styrene–methacrylonitrile)
EO	ethylene oxide	P(S–VBTMAC)	poly(styrene–vinylbenzyl trimethylammonium chloride)
EPR	electron paramagnetic resonance	RT	room temperature
FE	free exciton	S	styrene
FTIR	Fourier transform infrared	SCD	streaming current detector
FWHM	full width at half maximum	SEM	scanning electron microscope (microscopy)
HTMA	hexamethylenetetramine	TADC	theory of the average dielectric constant
IAP	ion activity product	TEM	transmission electron microscope (microscopy)
IHL	inner Helmholtz layer	4-oxo-TEMPO	4-oxo-2,2,6,6-tetramethyl-(piperidin-1-oxyl) free radical
IR	infrared	TGA	thermogravimetric analysis
KPS	potassium persulfate	TGA–MS	TGA–mass spectroscopy
MA	maleic acid	US	ultrasonication, ultrasound
MAA	methacrylic acid	VBTMAC	<i>ar</i> -vinylbenzyl trimethyl ammonium chloride
MAN	methacrylonitrile	XRD	X-ray diffraction
MMA	methyl methacrylate		
OHL	outer Helmholtz layer		
PCS	photon correlation spectroscopy		
PDI	polydispersity index		
PEO	poly(ethylene oxide)		

Greek symbols

β	parameter of the Kohlrausch function, eq. (5.42)
$\beta_{1/2}$	full width at half maximum
γ	interfacial (surface) tension
$\bar{\gamma}$	average interfacial tension
Γ	full width at half maximum, FWHM
$\Gamma(x)$	gamma function of the value x
ε	dielectric constant energetic fitting parameter in eq. (5.41)
ζ	zeta-potential (or ζ -potential)
η	viscosity
θ	diffraction angle angle between magnetic field and c -axis, eq. (5.25)
κ	Debye length
λ	wavelength constant in eq. (5.40)
λ_{em}	emission wavelength
λ_{exc}	excitation wavelength
μ	chemical potential of a crystal
μ_0	chemical potential of the bulk material (§3.2.2)
μ_B	Bohr magneton [$9.2740154 \times 10^{-24} \text{ J T}^{-1}$]
μ_E	electrophoretic mobility
ν	number of ions in a formula unit (§1.3.4) frequency
ν_A	stoichiometric coefficient of the species A
ρ	density
σ	surface charge density
σ_N	surface charge density (in charge groups per unit area)
τ	sample time (§2.3.1) Kohlrausch parameter (in unit time), eq. (5.42)
$\langle \tau \rangle$	average lifetime
ψ	potential (§2.3.2)

ω angular frequency ($\omega = 2\pi\nu$)

Latin symbols

a	area of a nucleus (§1.3.3) constant in eq. (2.8) and in §5.3.2 cell dimension in the a -axis
a'	Langmuir–Freundlich constant (§5.3.2)
A	acceptor
A	constant in eqs. (1.11), (2.7), and (5.39) area aspect ratio
A^\times, A', A''	neutral, singly, and doubly ionized acceptor, respectively (see §5.2.1)
A_0	aspect ratio for the reference sample (sample without additive)
A_1, A_2	symmetry characters of vibration mode
A_t	total surface of latex particles in a titrated sample, eq. (2.18)
A_∞	aspect ratio at infinitely large concentration
b	constant in eq. (2.8), eq. (2.9), and §5.3.2
b	Burgers vector
b'	Langmuir–Freundlich constant (§5.3.2)
B	constant in eq. (2.7) symmetry character of vibration mode
B_0	magnetic induction
c	concentration constant in eqs. (2.8) and (2.9) and §5.3.2 cell dimension in the c -axis

	light velocity [299 792 458 m s ⁻¹ , in vacuum]	ΔH_S	formation enthalpy of a Schottky defect
c^*	saturation concentration	I	intensity of scattered light
d	particle diameter		ionic strength
	interplanar distance		PL intensity (§5.3)
d_{hkl}	interplanar distance for the Miller indices hkl		EPR intensity (§5.4)
D	donor	I_0	initial PL intensity (§5.3.2 and §5.3.4)
D	diffusion coefficient		PL intensity at 0 K (§5.3.3)
$D^\times, D^\bullet, D^{\bullet\bullet}$	neutral, singly, and doubly ionized donor, respectively (see §5.2.1)	k	geometric constant depending on crystal shape (§3.2.2)
e	charge of the electron [1.60217733 × 10 ⁻¹⁹ C]		adsorption constant
e'	free electron		Miller index
E	magnitude of the electric field	k'	fitting constant in eq. (3.23)
	energy	k_B	Boltzmann constant [1.380658 × 10 ⁻²³ J K ⁻¹ ≡ 8.6174 × 10 ⁻²³ eV K ⁻¹]
E_0	energy at 0 K	K	form factor in eq. (4.5)
E_1, E_2	symmetry characters of vibration mode		absorption coefficient, eq. (4.7)
E_a	activation energy		force constant, eq. (5.22)
f	filling factor (§4.2.2)	K_{eq}	equilibrium constant
F	Faraday constant [9.6485309 × 10 ⁴ C mol ⁻¹]	K_{s0}	solubility product
g	depolarization or shape factor (§4.2.2)	K'_{si}	solubility product considering the reactions with protons, eq. (3.3)
	g -factor (see §5.2.4)	K_w	ion product of water
G	Gibbs free energy	l	geometric constant depending on crystal shape (§3.2.2)
$G(\tau)$	correlation function for a sample time τ (§2.3.1)		Miller index
ΔG_j^*	critical nucleation free energy	L_{hkl}	crystallite size or coherence length [in Scherrer equation, eq.(4.5)]
ΔG_v	difference of free energy between solution/melt and solid phase	m	constant in Freundlich and Langmuir–Freundlich isotherms (§5.3.2)
h	height of two-dimensional nucleus (§1.3.3)	m'	Langmuir–Freundlich constant (§5.3.2)
	Miller index	m_t	total mass of titrated latex sample
	Planck constant [6.626 0755 × 10 ⁻³⁴ J s]	M	molar mass
\hbar	Planck constant divided by 2π ($\hbar = h / 2\pi$)	n	mol number
h^\bullet	free hole		order [in Bragg's law, eq. (4.1)]
ΔH_F	formation enthalpy of a Frenkel defect	n_0	refractive index of the medium, eq. 2.3
		n_S	number of Schottky defects
		N	number of particles
			number of possible sites (§5.2.1.1)

N_A	Avogadro's number [$6.0221367 \times 10^{23} \text{ mol}^{-1}$]	t	time
N_{ch}	number of charged groups	T	absolute temperature
N_{part}	number of particles	T_2	transverse electron spin relaxation time
$O_1^{\times}, O_1^{\bullet}, O_1^{\bullet\bullet}$	neutral, singly, and doubly ionized oxygen vacancy, respectively (see §5.2.1)	U	potential (§2.5.2)
O_O	oxygen in an oxygen site (see §5.2.1)	v	volume of a nucleus/crystal (§1.3.2–1.3.3, §3.2.2) particle velocity (§2.3.3)
O_{Zn}	oxygen in a zinc lattice site (see §5.2.1)	V	consumed volume of titrating agent (§2.5.2) molar volume
P	partition coefficient (oil/water)	V_{emul}	volume of emulsion sample
q	magnitude of the scattering vector (§2.3.1) specific charge (in equivalent per unit mass) (§2.5.2)	$V_O^{\times}, V_O^{\bullet}, V_O^{\bullet\bullet}$	neutral, singly, and doubly ionized oxygen vacancy, respectively (see §5.2.1)
\mathbf{q}	scattering vector (§2.3.1)	$V_{\text{Zn}}^{\times}, V_{\text{Zn}}^{\bullet}, V_{\text{Zn}}^{\bullet\bullet}$	neutral, singly, and doubly ionized zinc vacancy, respectively (see §5.2.1)
Q	reaction quotient effective charge on a particle, eq. (2.11) configuration coordinate (§5.2.2.1)	w	solid part of the sample (in unit mass)
Q_0	configuration coordinate of the fundamental state in equilibrium (§5.2.2.1)	W	number of ways of distributing randomly a number of defects over the possible sites, eq. (5.1)
r	nucleus radius (§1.3.2) droplet radius, particle radius (Chapter 2) correlation coefficient	x	characteristic dimension of a crystal (§3.2.2)
r^*	critical nucleation radius	Z	number of formula unit
R	gas constant [$8.314510 \text{ J K}^{-1}$]	$Zn_i^{\times}, Zn_i^{\bullet}, Zn_i^{\bullet\bullet}$	neutral, singly, and doubly ionized interstitial zinc, respectively (see §5.2.1)
s	solid content of a latex emulsion (in percentage or per unit) surface of a particle (§3.2.2)	Zn_O	zinc in an oxygen lattice site (see §5.2.1)
\mathbf{s}_f	scattered wave vector (§2.3.1)	Zn_{Zn}	zinc ion a zinc lattice site (see §5.2.1)
\mathbf{s}_i	incident wave vector (§2.3.1)		
S	saturation level (or ratio) (§1.3.1–1.3.3) total molar surface (§3.2.2) rescaled aspect ratio (§3.5) entropy (§5.2.1.1)		

Index

- acceptor. *See* donor/acceptor
- acrylic acid, 33–36, 66–67
- active site, 7
- AIBN, 22–23, 33
- alkylperoxy radicals, 35
- alkyl radicals, 22–23
 - reaction with oxygen, 35
 - self-reaction, 23
- 2-allylphenol, 33–34, 36
- AMBN, 22–23, 32–33
- anchor block, 51
- antisite, 100, 108
- anti-Stokes shift, 106
- aspect ratio, 70–72
- Bohr magneton, 109
- Bragg's law, 79
- Brownian motion, 26
- Burgers vector, 10
- Burton–Cabrerá–Frank (BCF) theory, 8
- chain transfer, 21–22
- coalescence, 24–25
- coherence length, 80, 85–86, 90, 92–93
- colloid titration. *See* polyelectrolyte titration
- composite crystal, 15
- configuration-coordinate diagram, 105
- copper impurities. *See* impurity, copper
- core–shell latex, 36
- corona, latex, 36
- correlation function, 27–28
- costabilizer, 19–20, 25
- cosurfactant, 25
- crystal growth, 6–8
 - diffusion theories, 7
 - surface energy theories, 6–7
- crystal habit, 14
- crystallite size, *See* coherence length
- Debye length, 31
- defect, 10–11
 - equilibria (in ZnO), 102–104
 - extrinsic defect, 10
 - intrinsic defect, 10
 - linear defect. *See* dislocation
 - planar defect, 11
 - point defect, 10
 - point defects in ZnO, 100 ff
- depletion layer, 120
- dialkyldiazene initiator, 22
- dielectric constant, average, 81
- diffuse layer, 29
- diffusion coefficient, 9, 26
- dislocation
 - definition of, 10
 - dislocation line, 10–11
 - edge dislocation, 10–11
 - screw dislocation, 8, 10–11
- donor, *See* donor/acceptor
- donor/acceptor, 14, 99, 101, 106–107
 - deep/shallow, 99, 106, 131–132
 - donor–acceptor pair, 107–108
- Doppler effect, 26
- double layer, electric, 29
- double-hydrophilic block copolymer, 1, 16, 51–52
- double-hydrophilic graft copolymer, 1, 51–52
- dynamic light scattering (DLS), 26–28, 38–39
- effective charge, 29, 100
- electrokinetic potential. *See* zeta potential
- electrokinetics, 29–30
- electron paramagnetic resonance (EPR), 109–110, 129–132
- electron spin resonance (ESR). *See* electron paramagnetic resonance
- electro-osmosis, 30
- electrophoresis, 30–31, 46–47
- electrophoretic mobility, 30–31, 46–47
- emission spectrum, PL, 106, 110 ff
- emulsion, 19
 - inverse emulsion, 19
 - oil-in-water, 19
 - water-in-oil, 19
- ethylene glycol methacrylate phosphate, 33–34, 66–67, 87
- excitation spectrum, PL, 106, 110 ff
- exciton
 - definition of, 106
 - excitonic transitions in ZnO, 107
 - bound exciton, 106
 - free (or Mott–Wannier) exciton, 106
- filling factor, 81
- fluorescence, 105
- Fourier transform infrared (FTIR) spectroscopy, 80–82
- Frank–Condon principle, 105
- free energy of dissolution, 3
- free-radical polymerization, 20–24
- Frenkel defect, 102–103
 - concentration, 102
- Freundlich isotherm, 118
- g*-factor, 109
- grain boundary, 11
- growth spiral, 8, 69
- Helmholtz layer, 29
- Hermann–Mauguin notation, 77–78

- hexadecane, 25, 33
hexamethylenetetramine (HMTA), 57–58, 64–65
Hückel approximation, 31, 46
hydrodynamic radius, 27
hydroperoxide, 35
hydrophobic agent, 25, 32–33
impurity, 11–14
 compensated, 12
 copper impurity (in ZnO), 108, 111–112
 effect on crystal growth, 13
 effect on nucleation, 12
 effect on Ostwald ripening, 13
 effect on physical properties, 13–14
 effect on solubility, 12
 noncompensated, 13
induction period, 12, 93
initiation, 21–23
initiator, 22–23, 33
interfacial tension, 5 ff, 55 ff
interpenetration, 15
interstitial atom, 100 ff
 oxygen, 100 ff
 zinc, 100 ff
ion activity product, 3–4
Kohlrausch function, 127–129
Kröger–Vink notation, 100–101
KWW function. *See* Kohlrausch function
Langmuir isotherm, 13, 71, 118
Langmuir–Freundlich isotherm, 118 ff
latex, definition of, 17
lifetime, average PL, 126–129
Lutensol AT50, 32, 34, 66–67
macroemulsion, 19–20
maleic acid, 33–34, 66
methacrylic acid, 33–34
methacrylonitrile, 23, 33–34, 36
microemulsion, 19–20
mini-emulsion, 18 ff
morphogenesis, 93–96
n-type semiconductor, 14, 99
nucleation, 4–6, 23
 droplet nucleation, 24
 heterogeneous, 4, 12
 homogeneous, 4, 24
 micellar nucleation, 23
 primary, 4
 rate of nucleation, 6
 secondary, 4
 surface (two-dimensional) nucleation, 7–8
nucleus, 4–5
 surface nucleus, 7
Ostwald ripening. *See* ripening
Ostwald's rule of stages, 6
oxidative annealing, 92–93
 effect on photoluminescence, 114–117
oxygen photodesorption, 118–120
parallel growth, 15
particle size distribution, 28, 37–40
 from SEM, 37–39
 intensity distribution, 28, 39
 number distribution, 28, 39
 volume distribution, 28, 39
partition coefficient, 33
peroxide, 22
phosphorescence, 105
photoluminescence, 104–109, 110–128
 dynamics, 117–122
 room-temperature spectra, 110–117
 temperature dependence, 122–126
photon correlation spectroscopy. *See* dynamic light scattering
poly-DADMAC, 40–43
polydispersity index, 28, 39–40, 45
polyelectrolyte titration, 40–45
polymer colloid, 17
potassium persulfate, 22–23, 33, 45, 61–62
propagation, 21
p-type semiconductor, 14, 99
Raman spectroscopy, 80–82
Rayleigh approximation, 28
reinitiation, 21–22
relaxation time, transverse electron spin, 131
ripening, 4, 9, 24–25
saturation
 saturated solution, 4
 supersaturated solution, 4
 undersaturated solution, 4
saturation ratio (or level), 4–5
scattering vector, 27
Scherrer equation, 80
Schönflies notation, 77–78
Schottky defect, 101–103
 concentration, 101–102
sedimentation potential, 30
shape (or depolarization) factor, 81
shear plane, crystallographic, 11
Sips isotherm. *See* Langmuir–Freundlich isotherm
size, particle, 37–40, 45
 geometric size, 37
 hydrodynamic size, 37
 optical size, 37
Smoluchowski approximation, 31
solid content (of a latex emulsion), 44, 49
solution block, 52
spin density, 130–131
stability (of emulsions), 24–26
 electrostatic stabilization, 25–26
 electrosteric stabilization, 26
 steric stabilization, 26
stacking fault, 11
Stern potential, 29
Stokes shift, 106
Stokes–Einstein equation, 26

- streaming current detector, 40
streaming potential, 30, 40 ff
stretched-exponential function. *See*
 Kohlrausch function
styrene, 32–34
surface charge density, 40 ff, 44–45, 62 ff
surface diffusion, 7
surfactant, 23, 25, 34, 67
4-oxo-TEMPO, 129
termination, 21
TGA–MS, 82–83
theory of the average dielectric constant, 81–
 82
thermogravimetric analysis (TGA), 82–83,
 86, 90
tilt boundary, 11
time-resolved spectroscopy, 126–129
trap, electron, 121
turbostratic lamellar structures, 88
twin boundary, 11
twin formation, 15, 58
ultrasonication, 32, 48–49
urotropine. *See* hexamethylenetetramine
vacancy, 100 ff
 oxygen vacancy, 100 ff
 zinc vacancy, 100 ff
vibrational spectroscopies, 80–82
vinylbenzyl trimethyl ammonium chloride,
 33–34
visible emission (in ZnO), 107–109
wurtzite structure, 78
X-ray diffraction, 78–80, 83–93
zeta potential, 29–31, 46–47
zinc hydroxide, 53 ff
 polymorphs, 55, 57
 species, 53–55, 59, 84
zinc oxide
 crystal faces, 58, 78
 crystal phases, 77–78
 crystal structure, 77–78
 density, crystallographic, 78
 lattice parameters, 78–79
 precipitation, 53 ff
 solubility, 53–55, 57
 species diagram, 54
 vibration modes, 80
zincite. *See* zinc oxide

Lebenslauf

Rafael Muñoz-Espí

geb. am 7.12.1978 in Ontinyent (València)

- 1996 – 2001 Diplom in Chemie (*Llicenciat en Química*)
Universitat de València
- 2001 Diplomarbeit bei Prof. Dr. R. Tejero
Fachbereich Physikalische Chemie
Universitat de València
Titel: „Homology modeling of proteins by molecular dynamics:
fulfilling of homology constraints.“
- 2001 – 2002 Pädagogischer Befähigungsnachweis in Physik und
Chemie (*Certificat d’Aptitud Pedagògica, CAP*)
Universitat de València
- 2001 – 2003 Postgraduales Diplom in Physikalischer Chemie
(*Diploma d’Estudis Avançats, DEA*)
Fachbereich Physikalische Chemie
Universitat de València
- 2002 – 2006 Promotion
Max-Planck-Institut für Polymerforschung, Mainz